UNIVERSITY OF CALIFORNIA, SAN DIEGO

Synthetic Micro/Nanomachines and Their Applications: Towards 'Fantastic Voyage'

A dissertation submitted in partial satisfaction of the requirements for the degree

Doctor of Philosophy

in

Chemical Engineering

by

Wei Gao

Committee in charge:

Professor Joseph Wang, Chair
Professor Michael J. Heller
Professor Eric Lauga
Professor Deli Wang
Professor Liangfang Zhang

2014

The Dissertation of Wei Gao is approved, and it is acceptable in quality and form for publication on microfilm and electronically:

_____

_____

_____

_____

_____

Chair

University of California, San Diego

2014

DEDICATION

To my family.

EPIGRAPH

Life is like riding a bicycle. To keep your balance you must keep moving.

Albert Einstein

TABLE OF CONTENTS

LIST OF FIGURES

LIST OF TABLES

ACKNOWLEDGEMENTS

First of all, I would like to thank my thesis advisor professor Joseph Wang, for his advice, and support which made my dissertation possible. His enthusiasm and persistence have inspired me and have allowed me to accomplish more than I ever would have expected as a graduate student.

I would like to also thank my other committee members, professor Eric Lauga and professor Liangfang Zhang, professor Deli Wang and professor Michael Heller for guiding me through the journey. I also thank Professor Lauga and Professor Zhang for their important contributions to different aspects of this thesis through our close collobrations.

In the past five years, I have been fortunate to work with so many wonderful colleagues with whom I grow up academically and shared colorful life at UCSD. Here I would like to thank Dr. Sirilak Sattayasamitsathit, Dr. Kalayil Manian Manesh, Dr. Jahir Orozco, Dr. Daniel Kagan, Dr. Xiaomiao Feng, Mr. Allen Pei, Dr. Aysegul Uygun, Dr. Susana Campuzano, Dr. Filiz Kuralay, Dr. Miguel García, Dr. Maria Guix and many other friends in the lab for their and great help and for making me become a better scientist. I also thank all the undergraduate researchers who have worked with me for their great contributions I wish they all have promising careers ahead. Out of our lab, I would like to expecially thank my excellent collaborator Dr. On Shun Pak who really helped a lot with thesis.

I wish to thank my parents for their consistent support and countless sacrifices. I thank Yan Li for her her love and support throughout the past 5 years.

Finally, I would like to also thank the Howard Hughes Medical Institute and Jacobs fellowship from UC San Diego for the financial support over my PhD studies and the faculty and administration staff in department of Nanoengineering department at UCSD.

Chapter 1 is based, in part, on the material as it appears in ACS Nano, 2012, by Joseph Wang, Wei Gao; in part on the material as it appears in The Chemical Record, 2012, by Wei Gao, Sirilak Sattayasamitsathit, Joseph Wang. The dissertation author was the primary investigator and author of these papers.

Chapter 2.1, in full, is a reprint of the material as it appears in Journal of the American Chemical Society, 2014, by Wei Gao, Allen Pei, Renfeng Dong, Joseph Wang. Chapter 2.2, in full, is a reprint of the material as it appears in Journal of the American Chemical Society, 2013, by Wei Gao, Allen Pei, Xiaomiao Feng, Camille Hennessy, Joseph Wang. The dissertation author was the primary investigator and author of these papers.

Chapter 3.1, in full, is a reprint of the material as it appears in Journal of the American Chemical Society, 2011, by Wei Gao, Sirilak Sattayasamitsathit, Jahir Orozco, Joseph Wang. Chapter 3.2, in full, is a reprint of the material as it appears in Nanoscale, 2012, by Wei Gao, Sirilak Sattayasamitsathit, Aysegul Uygun, Allen Pei, Adam Ponedal, Joseph Wang. Chapter 3.3, in full, is a reprint of the material as it appears in Nanoscale, 2013, by Wei Gao, Sirilak Sattayasamitsathit, Jahir Orozco, Joseph Wang. The dissertation author was the primary investigator and author of these papers.

Chapter 4.1, is based, on the material as it appears in Nano Letters, 2012, by Susana Campuzano, Jahir Orozco, Daniel Kagan, Maria Guix, Wei Gao, Sirilak Sattayasamitsathit, Jonathan C. Claussen, Arben Merkoçi and Joseph Wang. Chapter 4.2, is based, on the material as it appears in Nanoscale, 2013, by Miguel García, Jahir Orozco, Maria Guix, Wei Gao, Sirilak

Sattayasamitsathit, Alberto Escarpa, Arben Merkoci and Joseph Wang. Chapter 4.3, is based on, the material as it appears in Journal of the American Chemical Society, 2012, by Filiz Kuralay, Sirilak Sattayasamitsathit, Wei Gao, Aysegul Uygun, Adlai Katzenberg, Joseph Wang. Chapter 4.4, is based on, the material as it appears in Journal of the American Chemical Society, 2013, by Jahir Orozco, Allan Cortés, Guanzhi Cheng, Sirilak Sattayasamitsathit, Wei Gao, Xiaomiao Feng, Yufeng Shen and Joseph Wang. The dissertation author was the primary investigator and author of these papers.

Chapter 5.1, is based, on the material as it appears in ACS Nano, 2014, by Wei Gao, Joseph Wang. Chapter 5.2, is based, on the material as it appears in ACS Nano, 2013, by Jahir Orozco, Victor García-Gradilla, Mattia D'Agostino, Wei Gao, Allan Cortés and Joseph Wang. Chapter 5.3, is based on, the material as it appears in ACS Nano, 2012, by Maria Guix, Jahir Orozco, Miguel Garcia, Wei Gao, Sirilak Sattayasamitsathit, Arben Merkoci, Alberto Escarpa, Joseph Wang. The dissertation author was the primary investigator and author of these papers.

Chapter 6.1, is based, on the material as it appears in Journal of the American Chemical Society, 2010, by Wei Gao, Sirilak Sattayasamitsathit, Kalayil Manian Manesh, Daniel Weihs, Joseph Wang. Chapter 6.2, is based, on the material as it appears in Soft Matter, 2011, by On Shun Pak, Wei Gao, Joseph Wang, Eric Lauga. Chapter 6.3, is based on, the material as it appears in Small, 2011, by Wei Gao, Kalayil Manian Manesh, Joe Hua, Sirilak Sattayasamitsathit, Joseph Wang. Chapter 6.4, is based on, the material as it appears in Nano Letters, 2014, by Wei Gao, Xiaomiao Feng, Allen Pei, Christopher R Kane, Ryan Tam, Camille Hennessy, Joseph Wang. Chapter 6.5, is based on, the material as it appears in Nanoscale, 2013, by Kalayil Manian Manesh, Susana Campuzano, Wei Gao, María Jesús Lobo-Castañón, Isao Shitanda, Kiarash Kiantaj, Joseph Wang. Chapter 6.6, is based on, the material as it appears in Small, 2012, by Wei Gao, Daniel Kagan, On Shun Pak, Corbin Clawson, Susana Campuzano, E. Chuluun-Erdene,

Erik Shipton, Eric E. Fullerton, Liangfang Zhang, Eric Lauga, Joseph Wang. The dissertation author was the primary investigator and author of these papers.

Chapter 7.1, is based, on the material as it appears in Journal of the American Chemical Society, 2012, by Wei Gao, Aysegul Uygun, Joseph Wang. Chapter 7.2, is based on, the material as it appears in Small, 2014, by Sirilak Sattayasamitsathit, Huanhuan Kou, Wei Gao, Walter Thavarajah, Kevin Kaufmann, Liangfang Zhang and Joseph Wang. Chapter 7.3, is based, on the material as it appears in Small, 2013, by Wei Gao, Mattia D'Agostin, Victor Garcia Gradilla, Jahir Orozco, Joseph Wang. Chapter 7.4, is based on, the material as it appears in ACS Nano, 2012, by Wei Gao, Allen Pei, Joseph Wang. Chapter 7.5, is based on, the material as it appears in Nanoscale, 2013, by Wei Gao, Xiaomiao Feng, Allen Pei, Yonge Gu, Jinxing Li, Joseph Wang. The dissertation author was the primary investigator and author of these papers.

VITA

2007	Bachelor of Science, Huazhong University of Science & Technology
2009	Master of Science, Tsinghua University
2014	Doctor of Philosophy, University of California, San Diego

PUBLICATIONS

1. Gao, W.; Sattayasamitsathit, S.; Manesh, K. M.; Weihs, D.; Wang, J. Magnetically Powered Flexible Metal Nanowire Motors. *J. Am. Chem. Soc.* **2010**, *132*, 14403–14405.

2. Sattayasamitsathit, S.; Gao, W.; Calvo-Marzal, P.; Manesh, K. M.; Wang, J. Simplified Cost-Effective Preparation of High Performance Pt-Ag Nanowire Motors, *ChemPhysChem* **2010**, *11*, 2802-2805.

3. Pak, O. S.; Gao, W.; Wang, J.; Lauga, E. High-Speed Propulsion of Flexible Nanowire Motors: Theory and Experiments. *Soft Matter* **2011**, *7*, 8169–8181.

4. Gao, W.; Manesh, K. M.; Hua, J.; Sattayasamitsathit, S.; Wang, J. Hybrid Nanomotor: A Catalytically/Magnetically Powered Adaptive Nanowire Swimmer. *Small* **2011**, 7, 2047–2051.

5. Gao, W.; Sattayasamitsathit, S.; Orozco, J.; Wang, J. Highly Efficient Catalytic Microengines: Template Electrosynthesis of Polyaniline/Platinum Microtubes. *J. Am. Chem. Soc.* **2011**, *133*, 11862–11864.

6. Orozco, J.; Campuzano, S.; Kagan, D.; Zhou, M.; Gao, W.; Wang, J. Dynamic Isolation and Unloading of Target Proteins by Aptamer-Modified Microtransporters, *Anal. Chem.* **2011**, *83*, 7962–7969.

7. Gao, W.; Sattayasamitsathit, S.; Wang, J. Catalytically propelled micro/nanomotors: how fast can they move? *Chem. Rec.* **2012**, *12*, 224–231.

8. Gao, W.; Sattayasamitsathit, S.; Uygun, A.; Pei, A.; Ponedal, A.; Wang, J. Polymer-based Tubular Microbots: Role of Composition and Preparation. *Nanoscale* **2012**, *4*, 2447–2453.

9. Campuzano, S.; Orozco, J.; Kagan, D.; Guix, M.; Gao, W.; Sattayasamitsathit, S.; Claussen, J. C.; Merkoci, A.; Wang, J. Bacterial Isolation by Lectin-Modified Microengines. *Nano Lett.* **2012**, *12*, 396–401.

10. Wang, J.; Gao, W. Nano/Microscale Motors: Biomedical Opportunities and Challenges. *ACS Nano* **2012**, *6*, 5745–5751.

11. Sattayasamitsathit, S.; O' Mahony, A. M.; Xiao, X.; Brozik, S. M.; Washburn, C. M.; Wheeler, D. R.; Gao, W.; Minteer, S.; Cha, J.; Burckel, D. B.; Polsky, R.; Wang, J. Highly Ordered Tailored Three-Dimensional Hierarchical Nano/Microporous Gold/Carbon Architectures. *J. Mater. Chem.* **2012**, *22*, 11950-11956.

12. Gao, W.; Kagan, D.; Pak, O. S.; Clawson, C.; Campuzano, S.; Chuluun-Erdene, E.; Shipton, E.; Fullerton, E. E.; Zhang, L.; Lauga, E.; Wang, J. Cargo-Towing Fuel-Free Magnetic Nanoswimmers for Targeted Drug Delivery. *Small* **2012**, *8*, 460–467.

13. Gao, W.; Uygun, A.; Wang, J. Hydrogen-Bubble-Propelled Zinc-Based Microrockets in Strongly Acidic Media. *J. Am. Chem. Soc.* **2012**, *134*, 897–900.

14. Kuralay, F.; Sattayasamitsathit, S.; Gao, W.; Uygun, A.; Katzenberg, A.; Wang, J. Self-Propelled Carbohydrate-Sensitive Microtransporters with Built-In Boronic Acid Recognition for Isolating Sugars and Cells. *J. Am. Chem. Soc.* **2012**, *134*, 15217–15220.

15. Guix, M.; Orozco, J.; Garcia, M.; Gao, W.; Sattayasamitsathit, S.; Merkoci, A.; Escarpa, A.; Wang, J. Superhydrophobic Alkanethiol-Coated Microsubmarines for Effective Removal of Oil. *ACS Nano* **2012**, *6*, 4445–4451.

16. Gao, W.; Pei, A.; Wang, J. Water-Driven Micromotors. *ACS Nano* **2012**, *6*, 8432–8438.

17. Gao, W.; Pei, A.; Feng, X.; Hennessy, C.; Wang, J. Organized Self-Assembly of Janus Micromotors with Hydrophobic Hemispheres. *J. Am. Chem. Soc.* **2013**, *135*, 998–1001.

18. Gao, W.; Sattayasamitsathit, S.; Orozco J.; Wang, J. Efficient Bubble Propulsion of Polymer-Based Microengines in Real-Life Environments. *Nanoscale* **2013**, *5*, 8909–8914.

19. Gao, W.; D'Agostino, M.; Garcia-Gradilla, V.; Orozco, J.; Wang J. Multi-Fuel Driven Janus Micromotors. *Small* **2013**, *9*, 467–471.

20. Gao, W.; Feng, X.; Pei, A.; Gu, Y.; Li, J.; Wang, J. Seawater-Driven Magnesium Based Janus Micromotors for Environmental Remediation. *Nanoscale* **2013**, *5*, 4696–4700.

21. Li, J.; Zhang, J.; Gao, W.; Huang, G.; Di, Z.; Liu, R.; Wang, J.; Mei, Y. Dry-Released Nanotubes and Nanoengines by Particle-Assisted Rolling. *Adv. Mater.* **2013**, *27*, 3715-3721.

22. Manesh, K. M.; Campuzano, S.; Gao, W.; Lobo-Castañón, M. J.; Shitanda, I.; Kiantaj, K.; Wang, J. Nanomotor-based Biocatalytic Patterning of Helical Metal Microstructures. *Nanoscale* **2013**, *5*, 1310–1314.

23. Gu, Y.; Sattayasamitsathit, S.; Kaufmann, K.; Vazquez-Duhalt, R.; Gao, W.; Wang, J. Self-Propelled Chemically-Powered Plant-Tissue Biomotors. *Chem. Commun.* **2013**, *49*, 7307-7309.

24. García, M.; Orozco, J.; Guix, M.; Gao, W.; Sattayasamitsathit, S.; Escarpa, A.; Merkoci, A.; Wang, J. Micromotor-Based Lab-on-Chip Immunoassays. *Nanoscale* **2013**, *5*, 1325–1331.

25. Orozco, J.; Cortes, A.; Cheng, G.; Sattayasamitsathit, S.; Gao, W.; Feng, X.; Shen, Y.; Wang, J. Molecularly Imprinted Polymer-based Catalytic Micromotors for Selective Protein Transport. *J. Am. Chem. Soc.* **2013**, *135*, 5336–5339.

26. Orozco, J.; García-Gradilla, V.; D'Agostino, M.; Gao, W.; Cortés, A.; Wang, J. Artificial Enzyme-Powered Microfish for Water-Quality Testing. *ACS Nano* **2013**, *7*, 818–824.

27. Olson, E. S.; Orozco, J.; Wu, Z.; Malone, C. D.; Yi, B. H.; Gao, W.; Eghtedari, M.; Wang, J.; Mattrey, R. F. Toward in vivo Detection of Hydrogen Peroxide with Ultrasound Molecular Imaging. *Biomaterials* **2013**, *34*, 8918-8924.

28. Garcia-Gradilla, V.; Orozco, J.; Sattayasamitsathit, S.; Soto, F.; Kuralay, F.; Pourazary, A.; Katzenberg, A.; Gao, W.; Shen, Y.; Wang, J. Functionalized Ultrasound-Propelled Magnetically-Guided Nanomotors: Towards Practical Biomedical Applications. *ACS Nano* **2013**, *7*, 9232-9240.

29. Gao, W.; Pei, A.; Dong, R.; Wang, J. Catalytic Iridium-Based Janus Micromotors Powered by Ultralow Levels of Chemical Fuels. *J. Am. Chem. Soc.* **2014**, *136*, 2276–2279.

30. Gao, W.; Wang, J. The Environmental Impact of Micro/Nanomachines: A Review. *ACS Nano* **2014**, *8*, 3170–3180.

31. Gao, W.; Feng, X.; Pei, A.; Kane, C. R.; Tam, R.; Hennessy, C.; Wang, J. Bio-Inspired Helical Microswimmer Based on Vascular Plant, *Nano Lett.* **2014**, *14*, 305–310.

32. Sattayasamitsathit, S.; Kou, H.; Gao, W.; Thavarajah, W.; Kaufmann, K.; Zhang, L.; Wang, J. Fully-Loaded Micromotors for Combinatorial Delivery and Autonomous Release of Cargoes. *Small* **2014**, DOI: 10.1002/smll.201303646.

33. Li, J.; Sattayasamitsathit, S.; Dong, R.; Gao, W.; Tam, R.; Ai, S.; Wang, J. Template Electrosynthesis of Tailored-Made Helical Nanoswimmers *Nanoscale* **2014**, *in press*.

34. Orozco, J.; Jurado-Sánchez, B.; Wagner, G.; Gao, W.; Vazquez-Duhalt, R.; Sattayasamitsathit, S.; Galarnyk, M.; Cortés, A.; Saintillan, D.; Wang, J. Bubble-Propelled Micromotors for Enhanced Transport of Passive Tracers. *Langmuir* **2014**, *30*, 5082-5087.

35. Xu, T.; Soto, F.; Gao, W.; Garcia-Gradilla, V.; Li, J.; Zhang, X.; Wang, J. Ultrasound-Modulated Bubble Propulsion of Chemically-Powered Microengines *J. Am. Chem. Soc.* **2014**, *136*, *in press*.

FIELDS OF STUDY

Major Field: Nanoengineering and Chemical Engineering

Studies in Nanoengineering

Professor Joseph Wang

ABSTRACT OF THE DISSERTATION

Synthetic Micro/Nanomachines and Their Applications: Towards 'Fantastic Voyage'

by

Wei Gao

Doctor of Philosophy in Chemical Engineering

University of California, San Diego, 2014

Professor Joseph Wang, Chair

The 1966 movie Fantastic Voyage captured the world's imagination, portraying a tiny submarine navigating through the human bloodstream and treating life-threatening medical conditions. My PhD research focuses on the synthetic nano/microscale machines to realize the Fantastic Voyage vision. Various biomedical and environmental areas would benefit from the developments of efficient fuel-free and fuel-driven nano/microscale machines.

The polymer-based catalytic tubular microengine is synthesized using a template based electrodeposition method. The oxygen bubble propelled microengine harvests the energy from chemical fuels (such as H_2O_2) and displays very efficient propulsion. It can serve as an ideal

platform for diverse biomedical and environmental applications. For example, lectin modified polyaniline based microengines can be used for selective bacteria (*E. Coli*) isolation from food, clinical and environmental samples; poly(3-aminophenylboronic acid)/Ni/Pt microengine itself provides the ‘built in’ glucose recognition capability for 'on-the-fly' capture, transport and release of yeast cells.

A series of micromotors which can be self-propelled in natural environments without additional chemical fuels are developed, holding great promise for *in vivo* biomedical applications: the polyaniline/zinc microrockets display effective autonomous motion in extreme acidic environments (such as human stomach); the Al-Ga/Ti based Janus micromotor can be propelled by the hydrogen bubbles generated from the rapid aluminum and water reaction; alkanethiols modified seawater-driven Mg Janus micromotors, which utilize macrogalvanic corrosion and chloride pitting corrosion processes, can be used for environmental oil remediation.

Magnetically powered nanoswimmers have attracted considerable attention due to their great biocompatibility. A high-speed magnetically-propelled nanowire swimmer which mimics swimming microorganisms by exploiting the flexible nanowire as artificial flagella under rotating magnetic field is illustrated. New bioinspired microswimmers can also be prepared directly from isolated spiral vessels of plants, harnessing the intrinsic biological structures of nature. Potential applications of these cargo-towing nanoswimmers are demonstrated by the directed delivery of drug-loaded microparticles to HeLa cancer cells in biological media.

With such innovations and developments, along with careful attention to key challenges and requirements, nano/microscale motors are expected to have tremendous impact on diverse biomedical and environmental applications, providing unlimited opportunities limited only by one’s imagination.

Chapter 1 Introduction of Micro/Nanomotors

1.1 The propulsion of at micro/nanoscale

1.1.1 The life at low Reynolds number

The 1966 movie *Fantastic Voyage* captured the world's imagination, portraying a tiny submarine navigating through the human blood stream and treating life-threatening medical conditions. Nearly five decades later, science is starting to catch up to the fiction of Hollywood. Recent advances in synthetic nano/microscale machines may help to realize the *Fantastic Voyage* vision of delivering therapeutic and diagnostic agents to previously inaccessible areas of the body.

Nanomotors are nanoscale devices capable of converting energy into movement and forces. Movement is essential for life in the macroscopic and nanoscopic scales. For example, animals run away fast from dangers while protein nanomotors shuttle cargo along intracellular microtubule tracks. However, the nanoscale propulsion through a fluid environment currently represents one of the major challenges of nanotechnology due to the absence of the inertial forces exploited by biological organisms on macroscopic scales. The difficulties are summarized by Purcell's famous "scallop theorem",[1-3] which states that a reciprocal motion (a deformation with time-reversal symmetry) cannot lead to any net propulsion at low Reynolds numbers. The Reynolds number, which measures the relative importance of inertial to viscous forces, can be expressed as,

$$\mathrm{Re} = \rho UL/\mu$$

where ρ and μ are the density and shear viscosity of the fluid, while U and L are the characteristic velocity and length scales of the self-propelling body. A swimming person has a Reynolds

number of around 10^4 while bacteria inhabit a world where Reynolds number ~ 10^{-5} to 10^{-4}. The swimming strategies at macroscale may not be applicable to nanoscale due to the domination of viscous forces. However, Nature has created efficient biomotors through millions of years of evolution and uses them in numerous biological processes and cellular activities. Some of these biological nanomotors move extremely fast relative to their size, with speeds exceeding 100 body lengths s^{-1} (bl s^{-1}).[4-6] Inspired by the sophistication of nature biomotors and driven by pioneering contributions of Sen & Mallouk's team and Ozin's group,[7-9] major efforts are currently being devoted to the design of efficient high-speed synthetic micro/nanoscale motors that convert diverse energies into autonomous motion.[10-19] A variety of fuel-driven and fuel-free microscale motors, developed during the past decade (Figure 1.1.1),[10–13,19,20] offer great promise for diverse biomedical applications. The sophistication of these tiny man-made machines has been increasing rapidly over the past five years and provides unlimited opportunities. As new capabilities are developed and proper attention is given to key challenges, these nanovehicles could realistically be used for a broad range of important biomedical applications, ranging from directed drug delivery to biopsy and from cleaning clogged arteries to precision nanosurgery or transport of radioactive seeds to tumor locations.

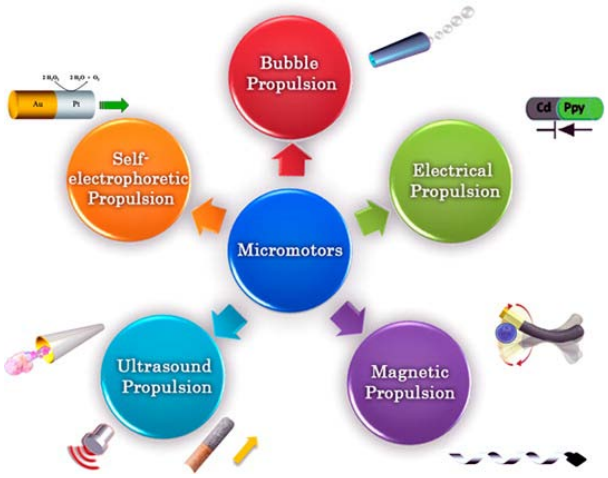

Figure 1.1.1 Micro/nanomotors powered by different mechanisms.

1.1.2 Catalytic nanowire motors

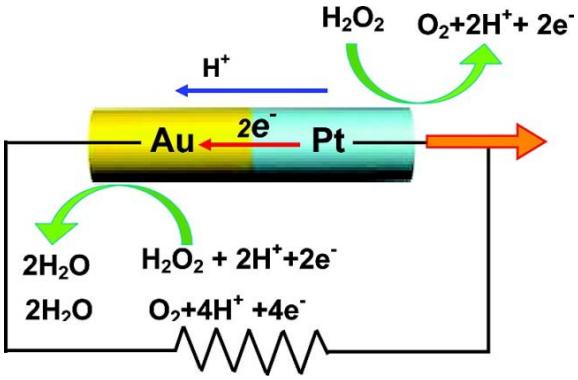

Figure 1.1.2 Self-electrophoresis (bipolar electrochemical) mechanism for the propulsion of catalytic nanowire motors in the presence of hydrogen peroxide. The mechanism involves an internal electron flow from one end to the other end of the nanowire, along with migration of protons in the double layer surrounding the wires. (Reprinted with permission from ref. 11. Copyright 2009 American Chemical Society.)

Chemically powered nanowire motors, particularly bisegment Au-Pt wires (**Figure 1.1.2**), firstly proposed by Ozin's and Sen & Mallouk groups, exhibit autonomous propulsion due to the electrocatalytic decomposition of the hydrogen peroxide fuel.[7-15] Specifically, the platinum segment of the nanowire oxidizes the peroxide fuel, creating electrons that travel through the wire towards the gold segment where hydrogen peroxide is reduced. The internal electron flux leads to electromigration of protons in the electrical double layer (surrounding the nanowire) from the platinum end to the gold end that causes a self-electrophoretic movement.[7] These bimetallic Pt-Au catalytic nanowire motors are commonly prepared by a template-directed sequential electrodeposition within the cylindrical nanopores of a porous membrane followed by the template removal, to form nanowire with 2 μm length and 200 nm diameter.[10,11] Motion control, which is another important requirement for diverse biomedical applications of catalytic nanomotors. Recent advances have demonstrated a precise (temporal and spatial) motion control of catalytic nanowires in connection to different stimuli,[21] and their ability to capture and direct cargo toward a predetermined destination.[15,22] These and other advances have created new opportunities for novel applications of catalytic nanowire motors.[23] Unfortunately, the self-

electrophoretic mechanism of catalytic nanowires is not compatible with high-ionic-strength biological fluids.[24]

1.1.3 Catalytic Janus micro/nanomotors

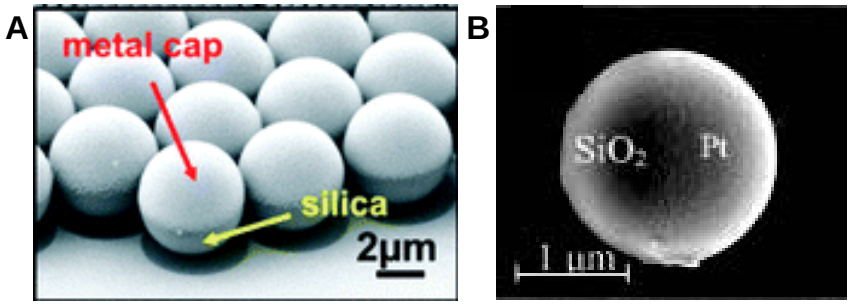

Figure 1.1.3 The catalytically-powered Pt-coated spherical silica Janus micromotors based on diffusiophoretic mechanism. (A, reprinted with permission from ref. 27. Copyright 2012 American Chemical Society; B, reprinted with permission from ref. 26. Copyright 2009 American Institute of Physics.)

Particular recent attention has been also given to chemically-powered Janus micromotors based on diffusiophoretic mechanism.[25-27] Janus particles, named after the Roman god Janus, are nano/microscale particles with two distinct surfaces each exhibiting differing physical properties.[28-31] Janus particle nanomotors with catalytic and noncatalytic faces, reported by Howse's group[25] and Zhao's group[26], have been made from polystyrene and silica spheres partially coated by platinum. Such catalytic Janus particles can move autonomously in a hydrogen peroxide fuel solution (Figure 1.1.3).[25-27] The platinum catalyzes the reduction of a ''fuel'' of hydrogen peroxide to oxygen and water, which produces more molecules of reaction product than consumed fuel. The gradients of oxygen formed by decomposition of the fuel can cause the osmotic propulsion toward the inert side. However, recently reports have also claimed the self-electrophoresis plays a major role for the propulsion of Janus micromotors.[32,33]

1.1.4 Bubble propelled catalytic microengines

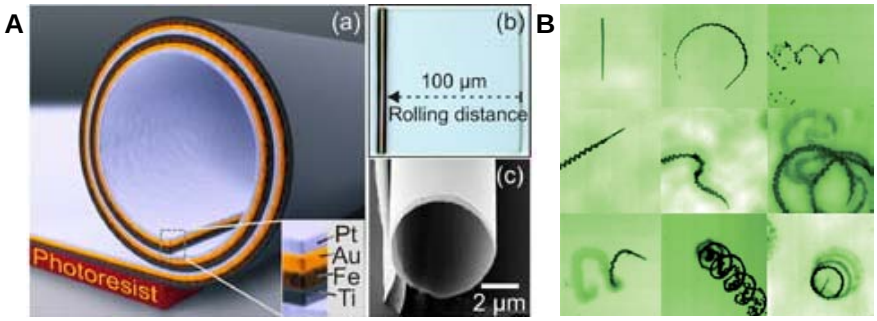

Figure 1.1.4 A) a) Schematic diagram of a rolled-up microtube consisting of Pt/Au/Fe/Ti multilayers on a photoresist sacrificial layer. b) Optical microscopy and c) SEM images of a rolled-up Pt/Au/Fe/Ti microtube. B) Trajectories of microbubble tails for different motions. (Reprinted with permission from ref. 17. Copyright 2009 Wiley.)

Catalytic microtube engines (Figure 1.1.4), pioneered by Mei and Schmidt, are extremely powerful catalytically-propelled micromotors.[16-18] These microtube engines commonly have an inner (catalytic) Pt surface, are typically 50-100 µm in length, and have an opening diameter of 5-10 µm.[16] The oxygen-bubble propulsion mechanism of these tubular microengines is associated with the catalytic decomposition of the hydrogen peroxide fuel at the inner platinum surface which produces oxygen gas that nucleates into bubbles. The conical shape of these microtubes and corresponding pressure differential assist the unidirectional expansion of the catalytically-generated oxygen bubbles, and their release from one of the tubular openings. Small amounts of surfactant are used to sustain the bubble development and promote their release. The bubble propulsion of these microtube engines addresses the ionic-strength limitation and the limited scope of catalytic nanowire motors to allow efficient propulsion in relevant biological media.[34-36] Microtube engines are commonly prepared by top-down photolithography, glancing angled e-beam deposition and the stress-assisted rolling of functional nanomembranes on polymers into conical microtubes. The incorporation of an intermediate ferromagnetic (Ni, Fe or Co) layer during the fabrication process offers a precise magnetic guidance of their movement.[16-18,34-36] Another approach for preparing microengines, involving sequential electrodeposition of platinum

and gold layers onto an etched silver wire template, offers a low yield and inferior propulsion behavior.[19]

1.1.5 Fuel free micro/nanomotors

To enhance biocompatibility, several groups have also explored fuel-free micro/nanomachine propulsion mechanisms based on externally applied magnetic or electric fields.[37–41] Magnetically driven micromotors, which swim under externally applied magnetic fields, are particularly attractive for a variety of biomedical applications because they can perform complex maneuvers and demanding tasks while obviating fuel requirements. Dreyfus *et al.*[39] were the first to realize the idea experimentally by fabricating a 24 μm long swimmer based on a flexible filament, made of paramagnetic beads linked by DNA, and attached to a red blood cell. Actuation was distributed along the filament by the paramagnetic beads; the presence of the red blood cell broke the front–back symmetry, and allowed the propagation of a traveling wave along the filament, leading to propulsion. Nelson[37] and Fischer[38] reported recently the fabrication and magnetically-controlled motion of efficient artificial flagella consisting of helical tails (Figure 1.1.5). These cork-screw swimmers offer attractive propulsion but require specialized ‘top down’ self-scroll or shadow-growth preparation routes along with advanced microfabrication facilities. The steep instrumental demands of these preparation routes restrict their production only to labs with such advanced fabrication facilities and greatly hinder their widespread use. In addition, biocompatible materials are desired for a variety of *in vivo* biomedical applications.

1. 2 Micro/nanomotors: how fast can they move?

As we discussed above, particular recent attention has been given to catalytically-propelled micro/nanomotors that display efficient locomotion due to electrocatalytic decomposition of hydrogen peroxide fuel. Such chemically-powered catalytic nanowires and microtube motors display high speed and power, along with precise motion. The new capabilities of catalytically-propelled micro/nanomotors have been the subject of several recent review articles,[7-10] and hold considerable promise for important and diverse applications. Many of these future applications require high force and power, as reflected by their speed. For example, for a catalytic nanowire motor, the drag force can be estimated by using the Stokes' drag theory:[3]

$$\mathrm{F} = \frac{2\pi\mu LU}{\ln(L/a) - 1/2}$$

where F is the drag force, U is the speed of the nanomotor, μ is the fluid dynamic viscosity, and L and a are the length and radius of the nanowire, respectively. Since the power (P) normally corresponds to FU, the fluid drag force F and P are thus proportional to U and U^2, respectively, i.e., high speed means higher power and higher cargo towing ability. The absolute speed of these nanomotors can be normalized with respect to the body lengths to obtain the relative speed: body lengths per second (bl s^{-1}).

Considerable attention has been given to improve the propulsion efficiency of catalytically-propelled micro/nanomotors in the past decade. Generally, high-performance propulsion of catalytic micro/nanomotors can be accomplished via three different ways: a) control of the motor design and composition; b) control of the fuel composition; c) use of external stimuli. Table 1.1 summarizes the recent research efforts aimed at enhancing the speed and power of different catalytically-propelled micro/nanomotors. In this section, we will address the question: "what is the fastest catalytic micro/nanomotor relative to its size?" For an even better comparison, we will introduce a new speed definition: relative speed (bl s^{-1})/fuel level (%). This speed

definition allows a more critical and direct comparison of the speed of various catalytic micro/nanomotors reported to date (under similar conditions, i.e., fuel level). We will also introduce efforts to improve the fuel economy and hence to lower the required fuel level, as desired for diverse biomedical applications. For example, a lower hydrogen peroxide concentration can greatly reduce the cell toxicity.[34,42]

Table 1.1 Speeds of common catalytically-propelled micro/nanomotors.

Type of motors	**References**	**Schematic**	**Size (μm)**	**Max Speed (μm s^{-1})**	**Relative Speed (bl s^{-1})**	**Speed/Fuel (bl s^{-1} $\%^{-1}$)**
Au-Pt Bisegment Nanowires	Sen & Mallouk et al.[7]	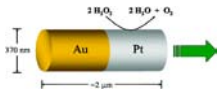	2	8	4	N/A
Bipolar Nanowires	Sen & Mallouk[43]		2	30	15	3
Pt-CNT/Au Nanowires	Wang et al.[44]	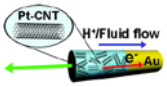	2	50-60	30	12
Pt-Alloy Nanowires	Wang et al.[45]	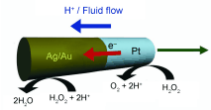	2	150	75	5
Pt-Ag bimetallic nanowires	Wang et al.[46]	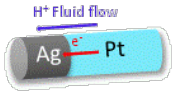	1.8	41	23	N/A
Pt based Rolled-up Microengines	Mei and Schmidt et al.[17,18]	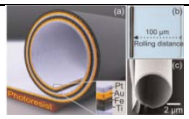	50-100	2000	40	~2.7
Templated Au/Pt Microengines	Wang et al.[19]	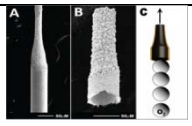	150-200	450	2.5	~0.25

1.2.1 Motor design and composition

Designing efficient fuel-driven micro/nanomotors requires detailed understanding of the fundamental electrochemistry and fluid flow physics that propel catalytic micro/nanomotors. Achieving such understanding requires theoretical modeling of fundamental mechanisms that propel the micro/nanomotors along with critical experimental evaluation and identification of efficient catalytic materials and optimal motor designs, which can have a dramatic influence on the speed of micro/nanomotors.

The asymmetrical flow of electrons causes a self-electrophoretic movement of conventional bimetallic Pt-Au nanowire motors with speeds of around 10-12 μm s^{-1} in 5-10% hydrogen peroxide solutions.[7] Various studies have led to increased speed and power of nanowire motors through a rationale selection of the catalytic material.[43-46] For example, Sen and Mallouk[43] reported that Pt/Ru nanowires can move at a speed of 30 μm s^{-1}, while Sattayasamitsathit et al.[46] demonstrated recently on Pt/Ag nanowire motors with speeds approaching 40 μm s^{-1}.

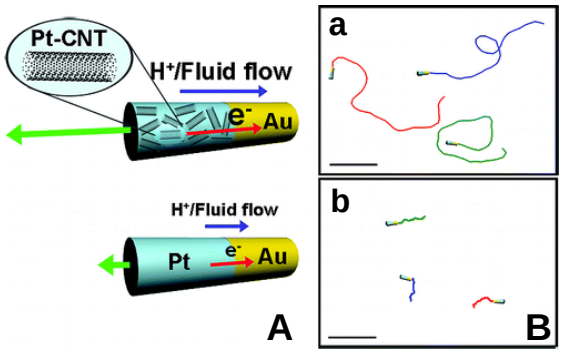

Figure 1.2.1 (A) A schematic representation of the self-electrophoresis mechanism of Au/Pt-CNT (top) and Au/Pt (bottom) bipolar nanomotors. B) Track lines illustrating the typical speeds of Au/Pt-CNT (a) and Au/Pt (b) nanomotors measured from the movement of the nanomotors in a 15% hydrogen peroxide fuel over a 4 s period. (B) (Reprinted with permission from ref. 44. Copyright 2008 American Chemical Society.)

Figure 1.2.1 illustrates that the incorporation of carbon nanotubes (CNT) into the platinum (Pt) segment of Pt/Au nanowire motors leads to dramatically accelerated movement in hydrogen peroxide solutions, with average speeds (50~60 μm s^{-1}).[44] Such enhancement has been

attributed to the higher electrocatalytic reactivity of the CNT-Pt segment towards the oxidation of hydrogen peroxide (although it may involve iron impurities of the carbon nanotube).[47]

A dramatic acceleration of bisegment nanowire motors to over 120 μm s^{-1} can also be achieved by using a cathodic Ag/Au alloy instead of a gold segment.[45] Ag-Au alloys are efficient catalysts for the reduction of the hydrogen peroxide fuel. The speed of these alloy nanowire motors is strongly affected by the alloy composition, increasing in a nearly linear fashion upon increasing the silver level in the growth solution from 0 to 75% (v/v) (a-d). Ultrafast nanomotors, travelling at speeds of 100 μm s^{-1}, have thus been developed though a judicious engineering of the composition of the nanowire as well as of the fuel (as will be discussed below).[44,45]

The morphology of the nanowire motor can also influence their speed. For example, Ozin's group has shown that replacing the nickel segment with a porous nickel segment increases the speed of Au-Ni nanowire by 30~50%.[48]

Bubble-propelled rolled-up microengines normally move at speeds of 50 and 2000 μm s^{-1} using 1.5 and 15% H_2O_2 solutions, respectively.[17] With a typical length of 50 μm, these speeds correspond to 1 and 50 bl s^{-1}, respectively. Sanchez et al. demonstrated that the speed of rolled-up microtube engines can be increased dramatically to 10 bl s^{-1} (~226 μm s^{-1}) in a 1.5% H_2O_2 solution by replacing the inner Pt layer with a biocatalytic (catalase) one.[49]

The propulsion of microtube engines also requires proper attention to optimal geometry of these microengines based on critical design considerations.[50] Various geometries of tubular micromotors (cylindrical, step cone, and smooth cone) have been examined in connection to various inlet/outlet diameter ratios and different length/width ratios.[19]

1.2.2 Fuel composition

Control of the fuel composition and concentration can also have a profound effect upon the nanomotor speed. Various fuel additives, such as silver ions,[51,52] surfactant,[16,17,19] hydrazine,[44] as well as the fuel level itself,[44,45] can offer substantial acceleration of the speed of different

nanomotors. For example, adding hydrazine to the peroxide fuel has led to a dramatic acceleration of catalytic nanowire motor's speed. The Pt-CNT based nanomotor can achieve an average speed of 94 μm s^{-1} with hydrazine (c), compared to 40-50 μm s^{-1} without hydrazine (b).[44] Silver ions represent another fuel additive that can greatly influence the speed of common Au/Pt nanowire motors.[51] A dramatic speed acceleration from 10 μm s^{-1} to 50~60 μm s^{-1} has been observed in the presence of 100 μM Ag. Such remarkable silver effect has been attributed to the underpotential deposition of silver onto catalytic Au/Pt nanowires.[51] In contrast, the presence of most other ions usually leads to reduced speed, as expected from the self-electrophoretic propulsion mechanism of catalytic nanomotors.[53] Proper attention should thus be given to the fuel purity, and particularly to it salt content.

Figure 1.2.2 Nanomotor racing: Optical images, superimposed with track lines, illustrating the speed of magnetically-guided Au/Ni/Au/Pt (a, d) and Au/Ni/Au/Pt-CNT (b, c) nanomotors, using 2.5% hydrogen peroxide, with (c, d) and without (a, b) 0.15% hydrazine. (Reprinted with permission from ref. 44. Copyright 2008 American Chemical Society.)

A key factor affecting the propulsion of microtube engines is the surfactant concentration The presence of surfactants, such as sodium cholate or benzalkonium chloride, reduces the surface tension and facilitates formation of the microbubbles.[16,17,19] The appropriate concentration can greatly enhance the speed. Sanchez and Mei *et al.* demonstrated that the surfactant level can greatly influence the speed of the rolled-up microengine.[54] This effect can be attributed to the lowering of the surface tension, smaller bubble size, and a much higher bubble frequency.

1.2.3 External stimuli

As mentioned before, one can also control the motion of catalytic micro/nanomotors using different external stimuli, including light, magnetic or electrical fields or elevated

temperatures.[21,55] For example, temperature has a profound influence on the speed of catalytic micro/nanomotors through effect on the electrochemical reactivity of hydrogen peroxide decomposition.[42, 56] We demonstrated a dramatically accelerated motion observed during the heat pulses, which is attributed primarily to the thermal activation of the redox reactions of the H_2O_2 fuel at the Pt and Au segments and to the decreased viscosity of the aqueous medium at elevated temperatures.[56] The thermally modulated motion during repetitive temperature on/off cycles is highly reversible and fast, with speeds of 14 and 45 μm s^{-1} at 25 and 65 °C, respectively.

Electrochemical (potential) control of the fuel concentration can also be used for modulating the speed of nanowire motors. Wang's group show that by stepping the potential from +1.0 V to -0.4 V, the speed of Au/Pt nanomotor increase from 4 to 22 μm s^{-1}, reflecting the reduction of oxygen to hydrogen peroxide at the negative potential.[57]

As we discussed in this section, tremendous progresses have been made toward increasing the speed and power of the micro/nanomotors. However, coupled with optimal surface morphology and microporosity, these efficient electrocatalytic materials could result with new ultrafast nanomotors and lead to new world records. The further increase in nanomotor power and speed will facilitate more demanding tasks such as pickup and transport of 'heavy' cargo (e.g., cellular or therapeutic payloads). Equally important, the improved fuel economy should lower the fuel concentration requirements.

1.3 The potential applications of micro/nanomotors

1.3.1 Cargo loading and transport

Micro/nanomotors-based cargo delivery represents a novel approach for transport various payloads in a target specific manner.[59] In the past decade, different approaches have been used for loading and releasing cargo to the motors.[15,22,23,54,58] Figure 1.3.1Aa show that nanomotors can capture positively-charged polymeric cargo through an electrostatic interactions with a negatively-charged polypyrrole (PPy) end. The polymeric-bead cargo can be coated with streptavidin which can interact with biotin modified nanomotors (Figure 1.3.1Ab).[22] Another important nanomotor cargo-loading route is magnetic interactions between the nickel part of nanowire motors or microengines and iron-oxide nanoparticles encapsulated cargos. Figure 1.3.1B demonstrated the dynamic magnetic pickup of the magnetic microspheres and their directed transport within a complex PDMS microchannel network along predetermined paths.[15]

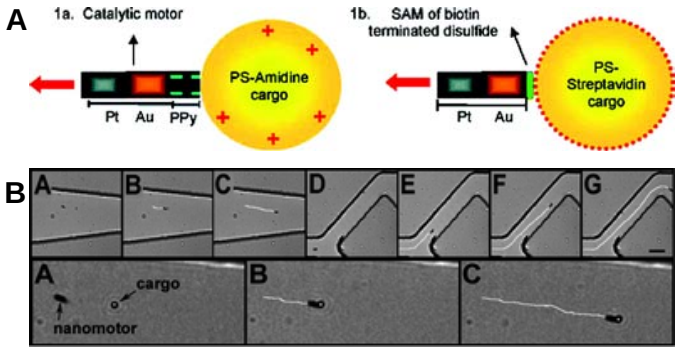

Figure 1.3.1 A) Cargo attachment by (a) electrostatic interaction between the negative-charged nanowire motor and a positively-charged micro-sphere; (b) biotin–streptavidin binding between biotin functionalized nanowires and a streptavidin-coated cargo. (Reprinted with permission from ref. 22. Copyright 2009 American Chemical Society.) B) 'On-the-fly' pickup and directed transport of microsphere cargo along predetermined paths within a polymeric microchip channel network. (Reprinted with permission from ref. 15. Copyright 2008 American Chemical Society.)

1.3.2 Motion based sensing

The idea of motion as a new transduction mechanism for sensing application was first introduced in connection to the detection of silver ions. For example, we reported on a motion-

enabled sensing of trace silver ions based on the dramatic and specific acceleration of bimetal nanowire motors in the presence of this toxic ion (Figure 1.3.2A).[51] The specific acceleration has been attributed to the underpotential deposition of silver onto a platinum segment, which increases the electrocatalytic activity. The resulting silver sensing protocol relies on the use of an optical microscope for tracking changes in the speed of the nanomotors in the presence of the target analyte. The highly selective motion-based response is characterized with a defined concentration dependence, with the speed (or distance) providing the quantitative information down to the nanomolar level. Such changes in the in the swimming behavior indicates promise for tracing plumes of hazardous chemicals. The silver-based acceleration has formed the basis for a motion-based detection of DNA hybridization in connection to silver nanoparticle tags (Figure 1.3.2B).[59] Dissolution of the silver nanoparticles, in the presence of the hydrogen peroxide fuel, lead to well-defined dependence of the speed signal on the concentration of the target DNA, down to femtomolar level.

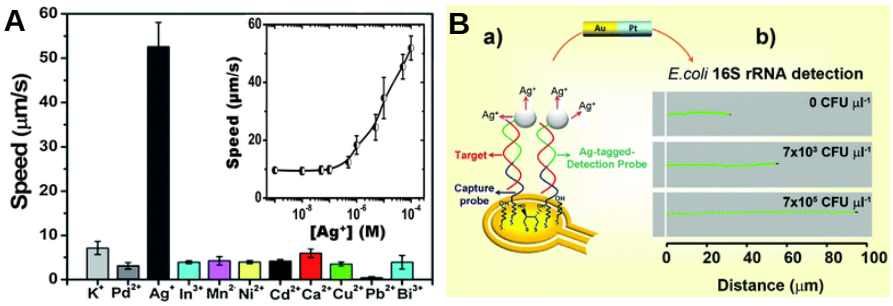

Figure 1.3.2 A) Motion-based silver detection by utilizing a unique nanomotor speed to Ag^{+} concentration relationship. (Reprinted with permission from ref. 51. Copyright 2009 American Chemical Society.) B) Motion-based nucleic acid detection. Microscopic images shows visual detection of speed/distance changes of the catalytic nanowire motors in the resulting Ag^{+}-enriched fuel obtained after hybridization with *E. coli* 16S rRNA. (Reprinted with permission from ref. 59. Copyright 2010 Nature Publishing Group.)

1.3.3 Isolation of biological targets

Artificial nano/microscale motors hold considerable promise for diverse medical diagnostic applications.[34-36] Particularly attractive for such bioanalytical applications are new

artificial nanomotors, which are capable of capturing and isolating biological targets from unprocessed biological media.[34–36] Such capture and transport of biological targets offer an attractive alternative to current (time-consuming and laborious) sample-processing protocols. Selective on-the-fly isolation of biological targets—ranging from nucleic acids to circulating tumor cells—from raw biological fluids has thus been realized through the rational functionalization of catalytic tubular microengines with different bioreceptors (Figure 1.3.3).[34] Such motion-based isolation routesenabledirect visualization of the binding events based on the movement of the microtransporters. Such motion-based isolation routes enable direct visualization of the binding events based on the movement of the microtransporters. Receptor-functionalized synthetic nanomotors are particularly promising for enhancing bioanalytical microchip systems. Functionalized nanomotors could be guided through the microchip channels, picking up and transporting target biomolecules to isolation compartments for subsequent analysis and quantification. By transporting captured analytes without bulk fluid flow, such microscale motors can eliminate the need for external pumps or power sources common in lab-on-chip systems. This application represents a major step toward designing integrated biomedical microsystemsthat perform a series of tasks for diverse diagnostic and therapeutic applications.

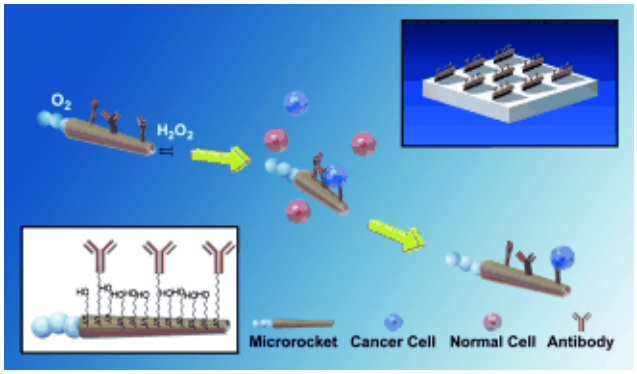

Figure 1.3.3 Microengines for capture and isolation of cancer cells. Upon encountering the cells, the anti-CEA mAb-modified microengines recognize the CEA surface antigens on the target cancer cells, allowing their selective pickup and transport. The top-right and bottom-left insets illustrate the preparation of the Ab-modified microengines and their functionalization, respectively. (Reprinted with permission from ref. 34. Copyright 2011 Wiley.)

1.3.4 Drug delivery

A bottleneck in nanoparticle-mediated drug delivery is the poor tissue penetration of the nanoparticle carrier and its therapeutic cargo.[23] To combine active targeting with precise guidance and control, future generation drug-delivery vehicles will require powerful propulsion and navigation capabilities in order to deliver payloads to predetermined body locations. Major research efforts have thus been devoted to searching for the magic bullets to target and to treat cancer. Nanoshuttle carriers, transporting their drug payloads directly to diseased tissues, hold considerable promise for improving the therapeutic efficacy and reducing the side effects of toxic drugs.[23] Such nanoshuttles can be functionalized to carry large payloads of drugs, along with imaging moieties and targeting ligands to confer tissue specificity.

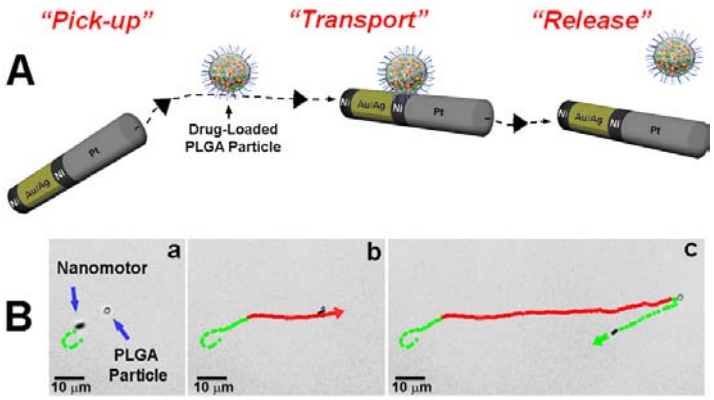

Figure 1.3.4 Transport and release of PLGA drug carriers by catalytic nanowire motors. Schematic (A) and microscopic time lapse-images (B) depicting the dynamic pick-up (a), transport (b), and release (c) of drug-loaded PLGA particles using a nanoshuttle. (Reproduced from ref. 23, Copyright 2010 Wiley)

Several intial proof-of-concept studies of nanoshuttle drug carriers have been carried out over the past three years.[23,54,60,61] Figure 1.3.4 illustrated that the catalytic nanowire shuttles can readily pickup drug-loaded poly(D,L-lactic-co-glycolic acid) (PLGA) particles and liposomes and transport them over predefined routes toward predetermined target destinations.[23] Powerful alloy and carbon-nanotube (CNT)-based nanowire motors have thus been used to provide the high force necessary to transport "heavy" therapeutic cargo. In comparison to the PLGA particles, the

liposome transport has been relatively slower due to its large size. Catalytic microtube engines have also been shown to be useful for transporting heavy cargo.[54] Imparting asymmetry into rolled-up InGaAs/GaAs/(Cr)Pt microtubular structures was shown to be useful inproviding a corkscrew-like motion thatwas employed for drilling and embedding into fixed cells (Figure 3a),[60] suggesting potential use of these catalytic nanostructures as microtools. The extent of asymmetry of the shape of these microtube drillers has a profound effect upon their trajectory.

Despite this recent progress in nanoshuttle drug carriers, tremendous challenges remain for translating these intial proof-of-concept studies into practical drug delivery for *in vivo* applications. Firstly, nanowire motors can not move in ionic solution while almost all the biofluids contain high concentrations of salts.[24] Secondly, the requirement of the common hydrogen peroxide fuel hinders some practical biomedical applications of catalytically propelled micro/nanomotors. These challenges also include limited tissue penetration, autonomous release of the therapeutic payload, swimming against the dynamic blood flow, and use of biocompatible materials. Eventually, such externally driven nanoshuttles will provide an attractive new approach for delivering drug payloads directly to predetermined destinations in a target-specific manner.

1.4 The objectives of the thesis

The objectives of the thesis are:

- To develop catalytic micromotors which can be powered by extremely low levels of chemical fuels (Chapter 2): the requirement of high fuel concentrations greatly hinders the practical utility of catalytically-powered nanomotors.
- To develop highly efficient catalytic micromotors which can display high-speed propulsion at real world environments (Chapter 3): the current nanowire or Janus motors cannot operate in ion-rich solutions while most real world samples contain high concentrations of ions.
- To develop proof-of-concept of using micromotors for biomedical applications such as targeted drug delivery and bioisolation (Chapter 4).
- To develop proof-of-concept of using micromotors for environmental monitoring and remediations (Chapter 5).
- To address the challenges of the propulsion in biofluids or nature environments (Chapter 6). Extending the scope of chemically powered nanomotors to diverse biomedical operations and different biological fluids would require the identification of new *in situ* fuels in connection with new materials and reactions.
- To develop next generation fuel-free micro/nanomotors for practical applications to eliminate the requirement of chemical fuels (Chapter 7).

Chapter 1 is based, in part, on the material as it appears in ACS Nano, 2012, by Joseph Wang, Wei Gao; in part on the material as it appears in The Chemical Record, 2012, by Wei Gao, Sirilak Sattayasamitsathit, Joseph Wang. The dissertation author was the primary investigator and author of these papers.

1.5 References

1. Wang, J. *Nanomachines: Fundamentals and Applications*; Wiley-VCH: Weinheim, Germany, **2013**.

2. Purcell, E. M. *Am. J. Phys.* **1977**, *45*, 3.

3. Lauga, E.; Powers, T. *Rep. Prog. Phys.* **2009**, *72*, 096601.

4. Stocker, R.; Seymour, J. R.; Samadani, A.; Hunt, D. E.; Polz, M. F. *Proc. Natl. Acad. Sci. U.S.A.* **2008**, *105*, 4209.

5. Mitchell, J. G.; Pearson, L.; Bonazinga, A.; Dillon, S.; Khouri, H.; Paxinos, R. *Appl. Environ. Microbiol.* **1995**, *61*, 877.

6. Barbara, G. M.; Mitchell, J. G. *FEMS Microbiol. Ecol.* **2003**, *44*, 79.

7. Paxton, W. F.; Kistler, K. C.; Olmeda, C. C.; Sen, A.; St. Angelo, S. K.; Cao, Y.; Mallouk, T. E.; Lammert, P. E.; Crespi, V. H. *J. Am. Chem. Soc.* **2004**, *126*, 13424.

8. Fournier-Bidoz, S.; Arsenault, A. C.; Manners, I.; Ozin, G. A. *Chem. Commun.* **2005**, *4*, 441.

9. Ozin, G. A.; Manners, I. Fournier-Bidoz, S.; Arsenault, A. *Adv. Mater.* **2005**, *17*, 3011.

10. Mallouk, T. E.; Sen, A. *Sci. Amer.* **2009**, *300*, 72.

11. Wang, J. *ACS Nano* **2009**, *3*, 4.

12. Sanchez, S.; Pumera, M. *Chem. Asian J.* **2009**, *4*, 1402.

13. Mirkovic, T.; Zacharia, N. S.; Scholes, G. D.; Ozin, G. A. *ACS Nano* **2010**, *4*, 1782.

14. Kline, T. R.; Paxton, W. F.; Mallouk, T. E.; Sen, A. *Angew. Chem. Int. Ed.* **2005**, *44*, 744.

15. Burdick, J.; Laocharoensuk, R.; Wheat, P. M.; Posner, J. D.; Wang, J. *J. Am. Chem. Soc.* **2008**, *130*, 8164.

16. Mei, Y. F.; Solovev, A. A.; Sanchez, S.; Schmidt, O. G. *Chem. Soc. Rev.*, **2011**, *40*, 2109.

17. Solovev, A. A.; Mei, Y. F.; Urena, E. B.; Huang, G. S.; Schmidt, O. G. *Small* **2009**, *5*, 1688.

18. Mei, Y. F.; Huang, G. S.; Solovev, A. A.; Urena, E. B.; Monch, I., Ding, F.; Reindl, T.; Fu, R. K. Y.; Chu, P. K.; Schmidt, O. G. *Adv. Mater.* **2008**, *20*, 4085.

19. Manesh, K. M.; Yuan, R.; Clark, M.; Kagan, D.; Balasubramanian, S.; Wang, J. *ACS Nano* **2010**, *4*, 1799.

20. Wang, J.; Gao, W. *ACS Nano* **2012**, *6*, 5745.

21. Wang, J.; Manesh, K. M. *Small* **2010**, *6*, 338.

22. Sundararajan, S.; Lammert, P. E.; Zudans, A. W.; Crespi, V. H.; Sen, A. *Nano Lett.* **2008**, *8*, 1271.

23. Kagan, D.; Laocharoensuk, R.; Zimmerman, M.; Clawson, C.; Balasubramanian, S.; Kang, D.; Bishop, D.; S. Sattayasamitsathit, L. Zhang, J. Wang, *Small* **2010**, *6*, 2741.

24. Paxton, W. F.; Sundararajan, S.; Mallouk, T. E.; Sen, A. *Angew. Chem. Int. Ed.* **2006**, *45*, 5420.

25. Howse, J. R.; Jones, R. A.; Ryan, A. J.; Gough, T.; Vafabakhsh, R.; Golestanian, R. *Phys. Rev. Lett.* **2007**, *99*, 048102.

26. Gibbs, J. G.; Zhao, Y. –P. *Appl. Phys. Lett.* **2009**, *94*, 163104.

27. Baraban, L.; Makarov, D.; Streubel, R.; Monch, I.; Grimm, D.; Sanchez, S.; Schmidt, O. G. *ACS Nano* **2012**, *6*, 3383.

28. Hu, J.; Zhou, S. X.; Sun, Y. Y.; Fang, X. S.; Wu, L. M. *Chem. Soc. Rev.* **2012**, *41*, 4356.

29. Jiang, S.; Chen, Q.; Tripathy, M.; Luijten, E.; Schweizer, K. S.; Granick, S. *Adv. Mater.* **2010**, *22*, 1060.

30. Walther, A.; Muller, A. H. E. *Soft Matter* **2008**, *4*, 663.

31. Loget, G.; Roche, J.; Kuhn, A. *Adv. Mater.* **2012**, *24*, 5111.

32. Ebbens, S.; Gregory, D.A.; Dunderdale, G.; Howse, J.R. **2013**, arXiv:1312.6250.

33. Brown, A.; Poon, W. *Soft Matter* **2014**, DOI: 10.1039/c4sm00340c.

34. Balasubramanian, S.; Kagan, D.; Hu, C. J.; Campuzano, S.; M. Jesus Lobo-Castañon, Lim, N.; Kang, D. Y.; Zimmerman, M.; Zhang, L.; Wang, J. *Angew. Chem. Int. Ed.* **2011**, *50*, 4161.

35. Kagan, D.; Campuzano, S.; Salasubramanian, S.; Kuralay, F.; Flechsig, G. U.; Wang, J. *Nano Lett.* **2011**, *11*, 2083.

36. Orozco, J.; Campuzano, S.; Kagan, D.; Zhou, M.; Gao, W.; Wang, J. *Anal. Chem.*, **2011**, *83*, 7962.

37. Zhang, L.; Abbott, J. J.; Dong, L. X.; Kratochvil, B. E.; Bell, D.; Nelson, B. J. *Appl. Phys. Lett.* **2009**, *94*, 064107.

38. Ghosh, A.; Fischer, P. *Nano Lett.* **2009**, *9*, 2243.

39. Dreyfus, R.; Baudry, J.; Roper, M. L.; Fermigier, M.; Stone, H. A.; Bibette, J. *Nature* **2005**, *437*, 862.

40. Tottori, S.; Zhang, L.; Qiu, F.; Krawczyk, K. K.; Franco-Obregon; A.; Nelson, B. J. *Adv. Mater.* **2012**, *24*, 811.

41. Peyer, K. E.; Tottori, S.; Qiu, F.; Zhang, L.; Nelson, B. J. *Chem. Eur. J.* **2012**, *19*, 28.

42. Sanchez, S.; Ananth, A. N.; Fomin, V. M.; Viehrig, M.; Schmidt, O. G. *J. Am. Chem. Soc.* **2011**, *133*, 14860.

43. Wang, Y.; Hernandez, R. M.; Bartlett, D. J.; Bingham, J. M.; Kline, T. R.; Sen, A.; Mallouk, T. E. *Langmuir* **2006**, *22*, 10451.

44. Laocharoensuk, R.; Burdick, J.; Wang, J. *ACS Nano* **2008**, *2*, 1069.

45. Demirok, U. K.; Laocharoensuk, R.; Manesh, K. M.; Wang, J. *Angew. Chem. Int. Ed.* **2008**, *120*, 9489.

46. Sattayasamitsathit, S.; Gao, W.; Calvo-Marzal, P.; Manesh, K. M.; Wang, J. *ChemPhysChem* **2010**, *11*, 2802.

47. Pumera, M.; Iwai, H. *Chem. Asian J.* **2009**, *4*, 554.

48. Zacharia, N. S.; Sadeq, Z. S.; Ozin, G. A. *Chem. Commun.* **2009**, *39*, 5856.

49. Sanchez, S.; Solovev, A. A.; Mei, Y. F.; Schmidt, O. G. *J. Am. Chem. Soc.* **2010**, *132*, 13144.

50. Li, J. X.; Huang, G. S.; Ye, M. M.; Li, M. L.; Liu, R.; Mei, Y. F. *Nanoscale* **2011**, *3*, 5083.

51. Kagan, D.; Calvo-Marzal, P.; Balasubramanian, S.; Sattayasamitsathit, S.; Manesh, K. M.; Flechsig, G. U.; Wang, J. *J. Am. Chem. Soc.* **2009**, *131*, 12082.

52. Gao, W.; Manesh, K. M.; Hua, J.; Sattayasamitsathit, S.; Wang, J. *Small* **2011**, *7*, 2047.

53. Paxton, W. F.; Baker, P. T.; Kline, T. R.; Wang, Y.; Mallouk, T. E.; Sen, A. *J. Am. Chem. Soc.* **2006**, *128*, 14881.

54. Solovev, A. A.; Sanchez, S.; Pumera, M.; Mei, Y. F.; Schmidt, O. G. *Adv. Funct. Mater.* **2010**, *20*, 2430.

55. Solovev, A. A.; Smith, E. J.; Bof′ Bufon, C. C.; S. Sanchez, O. G. Schmidt. *Angew. Chem. Int. Ed.* **2011**, *50*, 10875.

56. Balasubramanian, S.; Kagan, D.; Manesh, K. M.; Calvo-Marzal, P.; Flechsig, G. U.; Wang, J. *Small* **2009**, *5*, 11569.

57. Calvo-Marzal, P.; Manesh, K. M.; Kagan, D.; Balasubramanian, S.; Cardona, M.; Flechsig, G. U.; Posner, J.; Wang, J. *Chem. Comm.* **2009**, *45*, 4509.

58. Wang, J. *Lab Chip* **2012**, *12*, 1944.

59. Wu, J.; Balasubramanian, S.; Kagan, D.; Manesh, K. M.; Campuzano, S.; Wang, J. *Nat. Commun*. **2010**, *1*, DOI: 10.1038/ ncomms1035.

60. Solovev, A. A.; Xi, W.; Gracias, D. H.; Harazim, S. M.; Deneke, C.; Sanchez, S.; Schmidt, O. G. *ACS Nano***2012**, *6*, 1751.

61. Zhang, L.; Petit, T.; Peyer, K. E.; Nelson, B. J. *Nanomed.-Nanotechnol. Biol. Med.* **2012**, *8*, 1074.

Chapter 2 Catalytic Janus Micromotor and Their Self-Assembly

2.1 Iridium-based Janus micromotors powered by ultralow levels of chemical fuels

2.1.1 Introduction

Achieving autonomous motion of nano-/microscale objects in the low Reynolds number regime is an exciting yet challenging research area.[1-10] Particular attention has been given over the past decade to chemically-powered micromotors that exhibit self-propulsion in the presence of hydrogen peroxide fuel. These include primarily bimetallic catalytic nanowires,[11-13] microtubular microengines,[14-17] and Janus microparticles.[18-21] These chemically-powered micromotors commonly require high concentrations of the chemical fuel. Despite extensive efforts to lower the required fuel level, such catalytic micromotors still rely on at least 0.2% (~60 mM) hydrogen peroxide for their operation.[16,22] The requirement of high fuel concentrations greatly hinders the practical utility of catalytically-powered nanomotors. In addition, the repertoire of chemical reactions that can impact momentum remains limited primarily to hydrogen peroxide.

Here we introduce a catalytic Janus micromotor that displays efficient propulsion in the presence of extremely low levels of chemical fuel, 10^{-7} to 10^{-4} %, *i.e.*, over a 10,000-fold decrease compared to common catalytic motors. Such low-fuel micromotors have been realized using iridium (Ir)-based Janus microparticles (with an Ir layer on an oxide support surface) in the presence of hydrazine as the sole fuel (Figure 2.2.1A). At the macroscale, hydrazine (N_2H_4) is a

well-known monopropellant, commonly used in rocket motors.[23] On the other end of the spectrum, a bimetallic catalytic microfluidic pumping system, based on very high hydrazine fuel levels (2%), has been reported.[24] We have previously shown that a hydrazine additive within a high hydrogen peroxide fuel level results in dramatically increased speed for both catalytic nanowire motors and tubular microengines.[13,25]

In the following sections, we will demonstrate that efficient autonomous propulsion of Janus micromotors can be achieved even at trace (ppb) levels of hydrazine alone. The influence of fuel concentrations on the motor speed is investigated and compared to common peroxide-based catalytic Janus micromotors which display autonomous propulsion due to the oxygen product gradient.[18-21] The propulsion mechanism of the new Ir-based motors is discussed and its dependence on the composition of the particle support is evaluated. Collective swarming and the resulting micropumping behaviors at low fuel concentrations are also demonstrated.

2.1.2 Experimental section

Synthesis of Janus micromotors

The Janus micromotors were prepared using silica microparticles (1.21 μm and 4.74 μm mean diameter, Bangs Laboratories, Fishers, IN, USA) and polystyrene microparticles (0.91 μm mean diameter, Spherotech, Lake Forest, IL, USA) as the base particles. 10 μL of silica particles were first dispersed into ethyl alcohol (A407-4, Fisher, Pittsburgh, PA, USA) and centrifuged. Then, the silica particles were redispersed in 150 μL ethyl alcohol. The sample was then spread onto glass slides and dried uniformly to form particle monolayers. The particles were sputter coated with a very thin Ir layer (~20 nm) using an Emitech K575X Sputter Coater for 3 cycles with 10 s per cycle (5 cycles for particles with a diameter of 4.74 μm). Pt-SiO_2 Janus particles were sputter coated with a 20 nm Pt layer using a Denton Discovery 18 sputter coater. The deposition was performed at room temperature with a DC power of 200 W and Ar pressure of 2.5 mT for 15 s. In order to obtain a uniform Janus half-shell coating, rotation was turned off

and the sample slides were set up at an angle to be parallel to the Pt target. The resultant optimal thicknesses of Pt and Ir layers of the Janus micromotors (1.2 diameter) are 20 nm and 10 nm, respectively (as measured by Veeco DEKTAK 150 Profilometer). After the fabrication, the Janus particles were detached from the substrate *via* sonication or pipette pumping and were mixed with an aqueous solution of hydrazine. For the magnetic Janus motors, silica particle monolayers were prepared as above. A 10 nm layer of Ti followed by a 15 nm layer of Ni were sequentially deposited on half of the particles by electron beam evaporation (Temescal BJD 1800 Ebeam Evaporator). Then, a conformal coating of TiO_2 was deposited on the particles by atomic layer deposition (ALD) (Beneq TFS200) at 100°C for 1000 cycles. The final Ir coating was sputter coated as above. Polystyrene S particles (AP-08-10 and CM-08-10 from Spherotech, Lake Forest, IL) with an Ir Janus layer were prepared similarly.

Reagents and solutions

Hydrazine and hydrogen peroxide solutions are purchased from Sigma (# 309400) and Fischer (# H325-100), respectively. In order to propel the catalytic Janus particles, aqueous hydrazine and hydrogen peroxide solutions with concentrations ranging from 0.00000001% to 10 % were prepared and used as chemical fuels. The propulsion experiments were carried out by mixing 3 µL of the motors (taken from glass slides by pipette) and 3 µL hydrazine solutions.

Equipment

Images were captured by an inverted optical microscope (Nikon Instrument Inc. Ti-S/L100), coupled with 40× objectives, and a Hamamatsu digital camera C11440 using the NIS-Elements AR 3.2 software. pH values of the aqueous solutions were measured with Five-Easy pH meter (Mettler Toledo, Inc., Columbus, OH, USA).

2.1.3 Results and discussions

The Janus micromotors consist of plain silica particles (1.2 µm diameter) with one hemisphere coated with iridium metal. Iridium metal catalyst beds are commonly utilized to

decompose hydrazine fuel in monopropellant rockets.[26,27] The Ir surface catalyzes the decomposition of hydrazine to form nitrogen gas (N_2), hydrogen gas (H_2), and ammonia (NH_3) as products (Figure 2.1.1A) in accordance to reactions 1 and 2: [26,27]

$$3\ N_2H_4 \rightarrow N_2 + 4\ NH_3 \qquad (2.1.1)$$

$$3\ N_2H_4 \rightarrow 2\ N_2 + 3\ H_2 + 2\ NH_3 \qquad (2.1.2)$$

As a result, a high local concentration of products is formed around the Ir surface, leading to an osmotic gradient and a fluid slip velocity. The diffusiophoretic mechanism causes water to flow from regions of low to high solute concentrations. The induced fluid flow is thus directed around the motor, from the SiO_2 side to the Ir side, propelling the Janus micromotor towards the SiO_2 side. The micromotors are easily fabricated by a directional Ir sputter deposition onto a monolayer of silica microparticles (Figure 2.1.1B). As illustrated from the track-lines of Figure 2.2.1C, the resulting Ir-SiO_2 Janus motors move rapidly at an average speed of 21 μm/s in a 0.001% hydrazine solution.

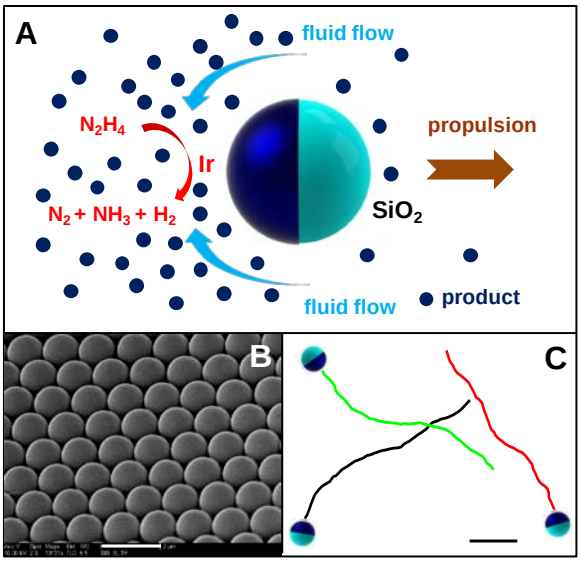

Figure 2.1.1 A) Schematic of catalytic Ir/SiO_2 Janus micromotors powered by hydrazine. N_2, H_2, and NH_3 molecules are generated at the Ir surface, creating a zone of high product concentrations. Fluid flows from the SiO_2 side to the Ir side due to the product gradient. As a result, the motor moves towards the SiO_2 side. B) Scanning electron microscope (SEM) image of an array of assembled spherical Ir/SiO_2 micromotors. Scale bar, 2 μm. C) Tracking lines illustrating the distances traveled by three micromotors in a 0.001% hydrazine solution over 1 s. Scale bar, 5 μm.

In general, diffusiophoretic movement of a particle is caused by a gradient of uncharged (non-electrolyte) solutes, such as N_2, H_2, and NH_3 in the present system, across the particle surface. This interaction is determined by the absorption strength (Gibbs' absorption length, K), and the length of the solute-surface interaction, L. The velocity of the particle (*U*) resulting from the solute gradient is described by:[28,29]

$$U = \frac{kT}{\eta} KL\nabla C \tag{2.1.3}$$

where *k* is the Boltzmann constant, *T* is the solution temperature, η is the fluid viscosity, and ∇C is the solute concentration gradient. However, in the case of hydrazine, the products contain not only neutral (N_2, H_2, NH_3) molecules but also a cationic (NH_4^+) species, resulting from the protonation of NH_3 in water. As a result, there are two possible diffusiophoretic mechanisms for the directional propulsion: chemophoretic and osmophoretic, corresponding to electrolyte and non-electrolyte products, respectively. These mechanisms are opposing, with chemophoretic movement towards higher concentrations and osmophoretic movement directed to lower concentrations.[30] For the present Ir Janus motors, the directional locomotion towards the SiO_2 side confirms the dominating role of the osmotic effects. As the motors continue to move, more hydrazine is reacted and additional cations are produced, resulting in a stronger chemophoretic influence, responsible for the gradual decrease in motor speed over time.

The propulsion of the new Ir-SiO_2 micromotors involves a similar mechanism as that of Pt-based Janus motors which utilize the O_2 gradient resulting from Pt-catalyzed decomposition of hydrogen peroxide. The track-lines of Figure 2.1.2A illustrate the motion of common Pt-SiO_2 micromotors in the presence of a high concentration of hydrogen peroxide fuel (10%) with an average speed of 12 μm/s. Using 1% hydrogen peroxide, these Pt-SiO_2 micromotors display no apparent displacement (inset of Figure 2.1.2A), analogous to the behavior of common Au-Pt bimetallic nanowire motors.[11-13] In contrast, and as indicated from Figure 2.1.2B, the new Ir-SiO_2 Janus motors move with greatly increased speeds of over 20 μm/s in just 0.001% hydrazine fuel.

The 10,000-fold excess of fuel required to propel the Pt-Janus motors vs. Ir-based Janus motors (Figure 2.1.2A vs. 2.1.2B), highlights the significant advantage of using remarkably low levels of the hydrazine fuel. It should be pointed out that while Pt-SiO_2 Janus motors also displayed directional propulsion at low hydrazine concentrations, other metal catalytic layers (*e.g.*, Pd, Ag) resulted in a greatly diminished movement.

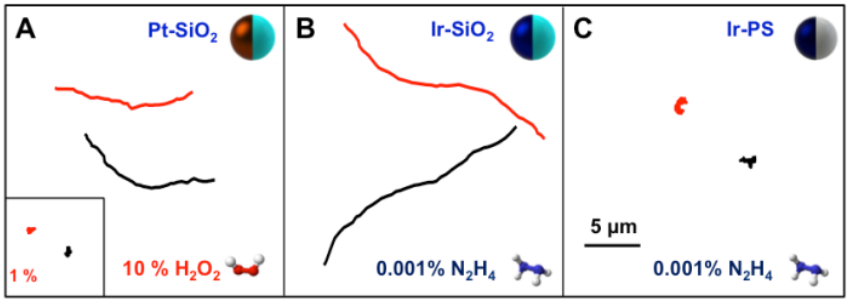

Figure 2.1.2 Tracking lines illustrating a typical motion and moving distances of Pt/SiO_2 Janus micromotors (a) in the presence of 10 % and 1 % (inset) hydrogen peroxide fuel, and of Ir/SiO_2 (b) and Ir/PS (c) micromotors in the presence of 0.001% hydrazine fuel over a 1 s period.

Interestingly, Ir-coated polystyrene (PS) Janus microparticles hardly move under the same conditions, and instead display extremely low movement speeds and short lifetimes (Figure 2.1.2C). It is well established that high surface-area oxide surfaces enhance the reactivity of Ir catalysts toward the hydrazine decomposition reaction.[24] Iridium-based Janus micromotors made with PS particles coated with a layer of alumina or titania show improved movement behavior (with a directional speed of 12 µm/s) compared to plain Ir-PS motors. Such strong dependence of the movement upon the surface conditions suggests the critical role of the oxide surface supporting the Ir catalytic layer.

The Ir Janus motors are able to retain directional propulsion over a wide range of fuel concentrations and during long periods of more than 10 min. Figure 2.1.3 shows the influence of fuel concentration on the micromotor speed. The motors exhibit a high average speed of 21 µm/s in 0.001% fuel. As expected, the speed decreases upon lowering the fuel level; yet, it remains higher than Brownian motion even at concentrations as low as 0.0000001%. Inset (a) of Figure

2.1.3 displays the actual tracked paths of the motors, demonstrating their significant net displacement at extremely low fuel concentrations compared to randomly moving Brownian particles (1-4 vs. 0). Enhanced diffusion and increased directional mobility are observed even at ppb fuel levels. To clearly indicate the directional movement of the Janus motors at extremely low fuel concentrations, we experimentally estimated the enhanced diffusion coefficients of the motors. The motors ($n \geq 40$) were tracked over 10 s, and the mean squared displacement was calculated at different fuel levels and plotted against time using MATLAB to obtain the diffusion coefficient from the slope. The mean squared displacement, ΔL^2, of the Janus motors has contributions from both directional propulsion and Brownian diffusion. The rotational diffusion coefficient, τ_R, of a particle with radius R can be found from the Stokes-Einstein relation:

$$\tau_R{}^{-1} = \frac{kT}{8\pi\eta R^3} \tag{2.1.4}$$

The mean squared displacement can be approximated by two characteristic equations for time scales far from τ_R:[18]

$$\Delta L^2 = \begin{cases} 4D\Delta t + V^2\Delta t^2\,, & \Delta t \ll \tau_R \\ (4D + V^2\tau_R)\Delta t\,, & \Delta t \gg \tau_R \end{cases} \tag{2.1.5}$$

where D is the diffusion coefficient for a plain particle, Δt is the time, and V is the velocity. For $\Delta t << \tau_R$, the propulsion of the particle dominates and ΔL^2 increases quadratically with time, while when $\Delta t >> \tau_R$, the rotational diffusion of the particle randomizes the 2-dimensional directional movement of the particle, resulting in a random walk with ΔL^2 increasing linearly with time. For these Janus motors with a diameter of 1.2 μm, τ_R is found to be 1.38 s, and the plot of the mean squared distance over 10 s is easily linearly fitted. Inset (b) of Figure 2.1.3 shows the increase in diffusion coefficient from 0.24 $\mu m^2/s$ to 0.48 $\mu m^2/s$ and to 0.67 $\mu m^2/s$ upon increasing the hydrazine level from 0% to 0.0000001% to 0.00001%, respectively, illustrating the high mobility of the motors (relative to Brownian motion) even in extremely low fuel levels. It should be pointed out that these ppb-ppm hydrazine fuel levels have been shown to exert negligible toxicity

on different animals.[31,32] Similar to other chemical fuels, the level of hydrazine may change during practical applications due to reactions with co-existing species.

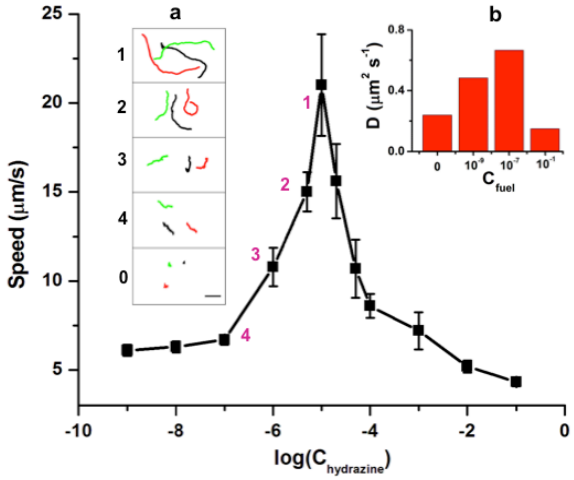

Figure 2.1.3 Dependence of the speed of Ir/SiO_2 Janus micromotors upon the hydrazine concentration over the 0.0000001%–10% range ($n \geq 50$). Inset a), tracking lines illustrating the travel distances of the Janus micromotors over a 1 s period in the presence of 0.001% (1), 0.0005% (2), 0.0001% (3), 0.00001% (4) hydrazine, as well as without hydrazine (0). Scale bar, 5 μm. Inset b), histogram of the diffusion coefficients of the Ir-based Janus micromotors, compared to Brownian motion, in the presence of extremely low levels of hydrazine.

As illustrated in Figure 2.1.3, the speed of Janus micromotors decreases upon increasing the fuel concentrations above 0.001%. This is contrary to the common behavior of catalytic micromotors and is likely due to the inhibiting effects of the ionic species associated with the hydrazine decomposition reaction, namely partial protonation of the NH_3 to form NH_4^+ (pK_a = 9.25). Solutions containing high hydrazine concentrations also have high pH values (11.58, 10.64, 10.13 for 10%, 1% and 0.1% hydrazine, respectively) due to the formation of $N_2H_5^+$ and OH^- ions:

$$N_2H_4 + H_2O \rightarrow [N_2H_5]^+ + OH^- \qquad (2.1.6)$$

As a result, the speed and diffusion coefficient of the motors in 10% (0.15 $\mu m^2/s$) hydrazine is even lower than the diffusion coefficient observed without the fuel (0.24 $\mu m^2/s$), i.e., for Brownian motion. Additional experiments indicated reduced speed with increasing salt concentrations. Such ionic-strength effect is consistent with the behavior of H_2O_2-powered Pt-

based micromotors.[33] Note that no apparent bubble generation was observed throughout these experiments.

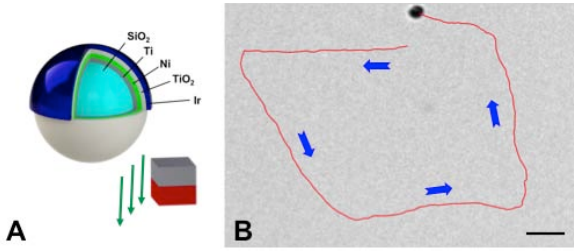

Figure 2.1.4 A) Schematic of the magnetic control of multi-layer Ir-TiO_2-Ni-Ti-SiO_2 Janus micromotors. B) Time-lapse images showing the magnetically-guided propulsion of an Ir-TiO_2-Ni-Ti-SiO_2 micromotor in the presence of 0.001% hydrazine. Scale bar, 5 μm.

Magnetic control of the directionality of the new Janus micromotor can be achieved through the deposition of a paramagnetic Ni layer. Coating the entire particle with a TiO_2 layer (through atomic layer deposition, ALD) after the Ni the deposition, results in a uniform oxide support which can facilitate the Ir based catalytic reaction. Figure 2.1.4A illustrates the layered coatings on the microparticle used for achieving magnetic guidance of the Janus micromotors. These Janus motors can be precisely navigated using an external magnetic field to follow predetermined trajectories (Figure 2.1.4B). Such magnetic guidance thus offers high spatial and temporal resolution essential for a variety of practical applications. The resulting motors display a high speed of over 30 μm/s, which is higher than that of Ir-SiO_2 micromotors, and can be attributed to the increased surface area of the ALD-fabricated TiO_2 layer.

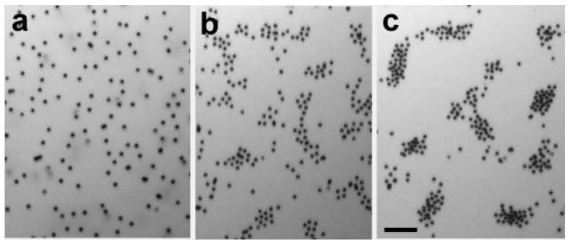

Figure 2.1.5 The swarming behavior of the Ir-based micromotors (diameter: 4.74 μm). (a-c) Microscopic images illustrating the time-dependent schooling of the Janus micromotors in presence of 0.001% hydrazine fuel at 0, 2, 4 min, respectively. Scale bar, 50 μm.

We also observed that the new hydrazine-driven Janus micromotors display a collective swarming behavior in response to their environment (Figure 2.1.5). While a limited aggregation of the 1.2 μm micromotors was observed in the 0.001% hydrazine solution, increasing the motor size to 4.74 μm resulted in a rapid formation of densely ordered swarms. The gradient-induced swarming of gold microparticles in the presence of high levels of H_2O_2 coupled with N_2H_4 has been reported previously.[34] The new Janus motors autonomously swarm with the sole presence of extremely low levels of hydrazine fuel. The time-lapse images in Figure 2.1.5 illustrate the spatially-organized schooling of the Janus motors at 0, 2 and 4 min after the addition of 0.001% hydrazine (a, b and c, respectively). This behavior is attributed to the diffusioosmotic and diffusiophoretic effects resulting from the accumulation of non-electrolyte reaction products. The larger schools of Ir motors remained aggregated for up to 1 hour and then began to disperse due to the diminished fuel level and product gradient. However, new school formation can be triggered by re-adding the hydrazine fuel, indicating a reversible swarming behavior.

Due to the product concentration gradient and limited propulsion speed of 4.74 μm motors, an inward fluid flux is generated, facilitating the formation of motor swarms. As a result, the smaller schools can continuously attract and draw in neighboring motors, resulting in larger and more tightly packed schools (c). The fluid flows generated around these motor swarms has been visualized using smaller passive tracer microparticles (1.2 μm in diameter), illustrating the capability of using these motor swarms as efficient micropumps.[35] These micropumps retain their pumping ability over the entire schooling period, indicating considerable promise for nanoscale delivery applications.[36]

2.1.4 Conclusions

In conclusion, we have demonstrated that catalytic micromotors can be powered by extremely low concentrations of chemical fuels. Such hydrazine-propelled iridium-based micromotors display efficient propulsion of over 20 μm/s and require substantially (10,000 fold)

lower fuel levels compared to commonly-used peroxide-based Pt-based micromotors. This study also represents the first example of the use of hydrazine as the sole fuel for catalytic micromotors. As these Janus micromotors can operate in such low fuel levels, additional studies to further understand their propulsion behavior and efficiency could be extremely useful for designing more efficient micro/nanomachines.[37] Further studies are desired for elucidating the fundamental principles of the propulsion mechanism of such hydrazine-driven Janus micromotors involving both electrolyte and non-electrolyte products. Future efforts will also aim at exploiting the defined dependence on the hydrazine concentration for sensing applications and for following concentration gradients *via* chemotaxis. The attractive propulsion and near fuel-free requirements of the new catalytic Janus micromotors hold considerable promise for the design of practical chemically-powered nanomachines towards a wide range of important future applications ranging from targeted drug delivery,[38] bioisolation[39] to environmental remediation.[40]

2.2 Organized self-assembly of Janus micromotors with hydrophobic hemispheres

2.2.1 Introduction

Locomotion of synthetic nano/microscale objects through fluid environments is one of the most exciting and challenging areas of nanotechnology.[1-10] Self-propelled nano/microscale machines have demonstrated considerable potential for performing diverse operations and important tasks, including isolation of biomaterials,[39,41] nanotool-based drilling,[42] cell manipulation,[43,44] delivery of therapeutic payloads,[45] and environmental remediation.[40] Particular recent attention has been given to chemically-powered Janus micromotors[18-20] that exhibit autonomous self-propulsion in the presence of hydrogen-peroxide fuel. Janus particles, named after the Roman god Janus, are nano/microscale particles with two distinct surfaces each exhibiting differing physical properties.[46-49] Catalytic Janus particles which are half-coated with a Pt layer move autonomously in a hydrogen peroxide fuel solution in response to gradients of oxygen formed by decomposition of the fuel.[18-20]

Inspired by animal interactions, the ability of synthetic microscale motors to produce self-organized structures is of considerable interest, owing to their future implications in nanomedicine, nanomachinery, transport systems, and chemical sensing.[50-52] For example, translating microscale movement to the macroscopic level would require cooperative action of multiple micromotors. Such coordinated action holds particular promise towards multiple-motor driven transport of large cargo. While many aspects of such coordinated movement of animals are still not fully understood, they have inspired substantial research efforts towards the self-organization of synthetic nanomaterials. Mallouk and Sen studied the schooling behavior of light-powered AgCl micromotors in water due to the diffusiophoresis mechanism.[53] Howse's team reported that doublets of catalytic Janus particles can rotate with different orientations,[54]

while Sanchez *et al.* described the transport of cargo by pairs of Janus micromotors.[55] However, such interactions between catalytic motors have been induced by random aggregation and not by controlled directed assembly and specific attachments. To our knowledge, there are no reports on the controlled guided formation, organization and motion of dynamic assemblies of multiple Janus particle motors based on specific and directional interactions. Recent reports from Granick and his colleagues described methods for the directed self-assembly of non-motor Janus microparticles involving hydrophobic poles (hemispeheres).[56-60] Various distinct assembly patterns, in which each Janus sphere was coordinated with other neighbors through hydrophobic interactions, were demonstrated,[56-60] but not in connection to motion.

Here we introduce the first example of spatially guided organization of chemically-powered Janus motors induced by hydrophobic surface interactions involving multiple motor/motor and motor/non-motor interactions. We demonstrate the controlled propulsion of such highly-ordered micromotor assemblies, and that the self-assembly process can occur dynamically during the movement. The influence of the self-assembled structures upon the coordinated movement of multiple Janus motors is investigated. The self-organization of motor microparticles with opposite hydrophobic and catalytic faces leads to controlled high-order motor assemblies where the hydrophobic sides of neighboring particles face each other, in a manner analogous to the orientation-dependent particle organization described by Granick's team.[57] In addition to the directed organization of multiple motors, we will illustrate the dynamic assembly of multiple-motors and multiple-cargo particles using mixtures of catalytic and non-catalytic microparticles towards organized cargo loading and delivery.

2.2.2 Experimental section

Synthesis of Janus micromotors

The micromotors were prepared using silica microparticles (1.21 μm mean diameter, Bangs Laboratories, Fishers, IN, USA) as the base particles. 20 μL of silica particles were first

dispersed into ethyl alcohol (A407-4, Fisher, Pittsburgh, PA, USA) and centrifuged. Then, the silica particles were redispersed in a small amount of ethyl alcohol, to which 200 µL of methylene chloride (D143-4, Fisher, Pittsburgh, PA, USA) and 15 µL of n-octadecanetrichlorosilane (OTS) (104817, Sigma-Aldrich, St Louis, MO, USA) were added. The particles were then stirred for 3 minutes at room temperature for the reaction to occur. To remove any unreacted OTS, the particles were then centrifuged and washed four times in anhydrous hexane (H292-500, Fisher, Pittsburgh, PA, USA) to a final volume of 400 µL. The sample was then spread onto glass slides and dried uniformly to form particle monolayers. The particles were sputter coated with a 20 nm Pt layer using a Denton Discovery 18. The deposition was performed at room temperature with a DC power of 200 W and Ar pressure of 2.5 mT for 15 s. In order to obtain a uniform Janus half-shell coating, rotation was turned off and the sample slides were set up at an angle to be parallel to the Pt target. After the fabrication, the Janus particles were detached from the substrate via sonication or pipette pumping and were mixed with an aqueous solution of hydrogen peroxide. The suspension was placed onto a glass substrate where the particles settle due to gravity. Previous work on hydrophobic interactions of SAM/Au/polystyrene Janus particles found that the range of allowed attractive bonding angles increases with the ionic strength of the solution. However, our Janus particle motor assemblies are observed to assemble in a wide range of possible rotational orientations even in deionized water due to the decreased inter-particle coulomb repulsion effects between the Janus particles associated with the hydrophobic modification of the silanol groups.

Reagents and Solutions

In order to propel the catalytic Janus particles, aqueous hydrogen peroxide solutions with concentrations ranging from 10 % were used as chemical fuels. The motor-motor assembly experiments were carried out by mixing 5 µL motors (taken from glass slides by pipette) and 20% hydrogen peroxide solutions, while the motor/non-motor assembly experiments by mixing the 5

μL motors, 5 μL non-motor and 30% hydrogen peroxide solutions. The non-motor solution was prepared by adding 1 mL ultrapure water (18.2 MΩ·cm) to the modified silica particles after the hexane dry. For the motor/single non-motor interaction experiments, 50 times diluted particles were used. The original concentration was used for the motor/multiple non-motor interaction.

2.2.3 Results and discussions

In this work, the Janus motors consist of hydrophobic octadecyltrichlorosilane-modified silica microspheres that are capped with a catalytic Pt hemisphere patch. As illustrated in Figure 2.2.1A, neighboring motors thus experience attractive hydrophobic interactions between their exposed OTS-modified silica hemispheres, leading to defined spatial assemblies. The catalytic Pt patch restricts the interparticle attraction to the hydrophobic hemisphere while maintaining a wide range of orientational freedom for each motor in the assembly.

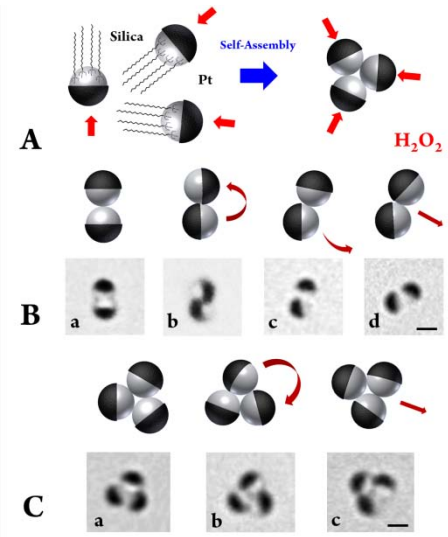

Figure 2.2.1 A) Schematic of the assembly of OTS modified Janus micromotors, with the hydrophobic OTS sides facing one another; B) Typical doublet Janus motor assemblies: (a-c) movement of Janus motor doublet assemblies with different orientations. C) Typical assemblies of Janus motor triplet assemblies: (a-c) movement of triple-motor assemblies with different orientations. Scale bar, 1 μm. Conditions, 5% hydrogen peroxide.

The asymmetric distribution of the catalyst on the surface of such assemblies thus imparts a net force and net torque to the system. As expected, different bonding orientations between

these hydrophobic Janus motors induce different forms of motion. The relative orientation of each motor in the assembly changes its contribution to the net propulsion force and rotational moment. Figure 2.2.1 illustrates different movement behaviors of doublet (B) and triplet (C) motor-motor assemblies with various bonding orientations. Figure 2.2.1B(a) shows that the symmetric bonding of two such motors results in a non-directional Brownian motion due to the opposing symmetric forces. In contrast, translational and rotational motion can be observed for motors with angled bonding orientations (Figure 2.2.1B(b-d)). In Figure 2.2.1B(b), representing an extreme case of minimal contact, the opposite-facing motor doublet displays a very fast, stationary rotation corresponding to a very high angular velocity (of over 30 rad/s) and near-zero rotational radius. The intermediate-angled motor doublet, shown in Figure 4.2.1B(c), displays a slow angular velocity (2.5 rad/s) with a larger rotational radius (11 μm). The angled bilaterally-symmetric dual motor of Figure 2.2.1B(d) displays a nearly linear motion, with a very large rotational radius and near-zero angular velocity (the rotational radius and angular velocity would be ideally infinite and zero in this case). These microscope images clearly indicate that the interactions between the individual motors of the doublets occur between their hydrophobic hemispheres, reflecting the controlled assemblies of the Janus micromotors. These motor doublets retain their distinct motion pattern throught the experiments. Previous randomly-formed doublets[54] have been connected also through their catalytic patches. Similar movement characteristics are observed in Figure 2.2.1C for organized triplet motor assemblies. For example, Figure 2.2.1C(a) demonstrates that a highly symmetric assembly of three motors, formed by hydrophobic interactions, leads to a non-directional Brownian motion with no net translational movement. In contrast, a rotational symmetric assembly of the three motors, with an offset angle (Figure 2.2.1C(b)), results in fast spinning motion about the centroid (13.5 rad/s). Figure 2.2.1C(c) illustrates a triplet assembled with bilateral symmetry that moves in a directional linear path. Any orientational deviation of a single motor will change the moment of the assembly as a whole and affect the translational and

angular velocity of the assembly, as illustrated in the doublets of Figure 2.2.1B(c) and Figure 2.2.1B(d).

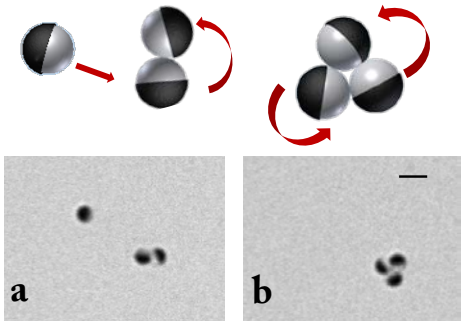

Figure 2.2.2 Janus motor assembly: dynamic 'switch' from doublet to triplet configurations. Scale bar, 2 μm. Conditions, as in Figure 2.2.1.

The hydrophobic interactions between individual micromotors and micromotor assemblies can promote a continuous growth of the assembly during its movement and lead to dynamic changes in the motion behavior. For example, Figure 2.2.2 illustrates an 'on-the-fly' doublet-to-triplet switching due to the self-attachment of a moving single Janus motor. Prior to this capture, the doublet travels in a circular path with a large radius. However, the resulting symmetric triplet assembly rotates (spins) rapidly around its centroid (with a minimal radius). These data clearly illustrate that the self-assembly mechanism can occur dynamically during the continuous movement of motors and their assemblies.

Figure 2.2.3 compares the behavior of Janus micromotors with (A) and without (B) the hydrophobic coating. As expected, the control experiment without such hydrophobic coating shows multiple randomly moving unassembled single Janus motors (B). Such lack of assembly for the uncoated microparticles can be attributed to the electrostatic repulsion between the charged surface regions.[54] In contrast, the hydrophobic hemispheres lead to the formation of multi-motor assemblies (A). A simultaneous dynamic movement of different single, doublet, and triplet motor assemblies can thus be observed over a small area. Overall, these data clearly

illustrate that hydrophobic forces are crucial for the formation of distinct assembly patterns and further support their role in the motor organization process.

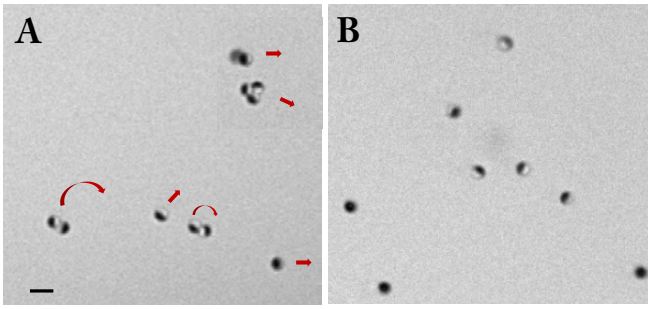

Figure 2.2.3 Control experiments: Janus micromotors with (A) and without (B) hydrophobic coating. The latter offers simultaneous movement of single, doublet, and triplet motor assemblies. Scale bar, 2 μm. Conditions, as in Figure 2.2.1.

In addition to the doublet and triplet assemblies, multiple Janus motors can form additional structural patterns. For example, four motors can self-assemble into a 3-D tetrahedral structure. Due to the symmetric contributions of the driving force from each motor, such a quartet displays only Brownian motion. It is possible to control the specific orientation and cluster shape of the assembled Janus particles by controlling the colloidal valence through optimization of the hydrophobic surface area.[58,59] For example, particles with different half opening angles will form different cluster shapes.[59] Smaller hydrophobic patches can restrict the motor assembly to clusters of up to four particles.[56] However, increasing the patch size would allow the growth of larger assemblies.

In addition to assemblies of multiple Janus micromotors, the new concept allows a directed assembly of motors/non-motors using non-catalytic hydrophobic microparticles acting as cargo. Such capability of organized loading of multiple cargo particles onto a single motor or assembly of multiple motors holds considerable promise for tailor-made cargo pickup towards optimal active transport and delivery. The Janus motor/non-motor particles assemble into configurations that maximize the hydrophobic interactions with each other in order to form structures that minimize the potential energy.[60] Figure 2.2.4a demonstrates the formation and

movement of a doublet consisting of a single Janus particle motor with a single non-motor particle. As expected, the doublet moves in a direction perpendicular to the hemispherical boundary. Figure 2.2.4b demonstrates a triplet assembly with dual motors and a single non-motor which again demonstrates a nearly translational motion. The structure of Figure 2.2.4c (formed from three motors and one non-motor particle) differs slightly from the ideal tetrahedral assembly for a quadruplet. This planar quadruplet assembly species commonly exists since deviations from the ideal configurations are possible as a result of the larger valence of the hydrophobic hemisphere and the spontaneous deformation of structures from the relatively weak attractive forces and Brownian motion.[60] In order to obtain ideal multiple motor/single non-motor assemblies that travel linearly, it is necessary to control the bonding orientation of the motors to the bare cargo particle. This can be achieved by tailoring the size of the hydrophobic patch.[60] Owing to the dynamic nature of the self-organization process, the relative population of each assembly depends on the incubation time. During the experimental time scale used in this study (up to 10 min) the relative frequency of the observed assembly follows the: doublet>triplet>quadruplet trend. The resulting doublet, triplet, and quadruplet motor/single non-motor assemblies display speeds of 12, 4 and 4 μm/s, respectively (n=5), reflecting the tradeoff between increased propulsion force and larger fluid drag. The speed of such assemblies remains stable in a dilute particle solution containing a given fuel level.

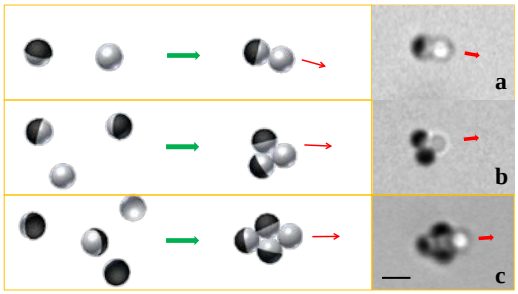

Figure 2.2.4 Assemblies of Janus motor/non-motor microparticles. (Left) Schematic and (Right) microscopic images (Right) of (a) doublet, (b) triplet, (c) quadruplet motor/non-motor assemblies. Scale bar, 2 μm. Conditions, as in Figure 2.2.1.

Figure 2.2.5 illustrates a triplet of micromotors (shown in Figure 2.2.1Cc) capturing 'on-the-fly' a single non-motor particle. The hydrophobic interaction between the motor triplet and the non-motor particle can be clearly seen from the dynamic uptake of the non-motor. The resulting assembly has a lower angular velocity and rotational radius as a result of the hydrophobic attachment of the non-motor particle. The motor/non-motor interactions allow a continuous pickup of additional cargo while maintaining a well-organized cargo loading process.

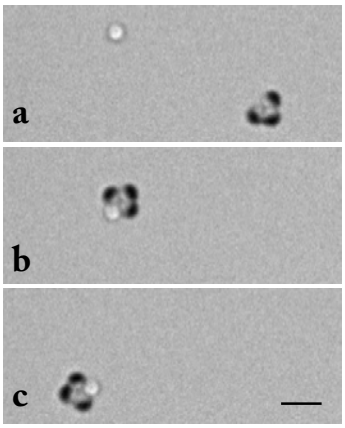

Figure 2.2.5 'On-the-fly' capture of a non-motor particle by a triplet micromotor assembly. Time-lapse images of a, b, and c are in 1 second intervals. Scale bar, 3 μm. Conditions, 5% hydrogen peroxide.

Figure 2.2.6 illustrates a single Janus motor carrying multiple non-motor particles (3 in (a) and 6 in (b)) to form organized motor/cargo assemblies through hydrophobic interactions. The single Janus motor is usually self-propelled at a fast speed of 15 μm/s in a 5% w/v hydrogen peroxide solution, corresponding to 12.5 body lengths/s. The speed decreases to 6 and 3 μm/s upon assembling with 3 and 6 non-motor particles, respectively, reflecting the increased fluid drag force associated with the larger assembly. Such dynamic cargo pickup can continue until the movement stops. A well-defined loading and organization of multiple cargoes on a single motor, in a packed 'flower' type arrangement, can be clearly observed in Figure 2.2.6b. Compared to previously reported randomly-formed motor/cargo systems[54,55] the new directed assembly method

leads to defined motor/multi-cargo assemblies that minimize the potential energy to offer optimal cargo transport for diverse applications such as targeted drug delivery.

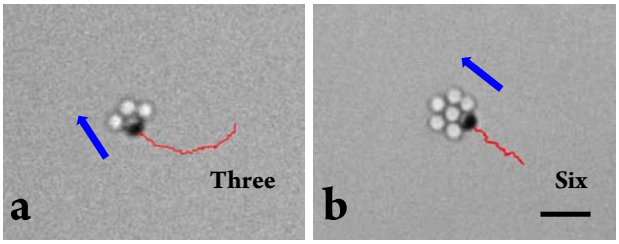

Figure 2.2.6 Organized cargo loading. Time-lapse images (over 2 seconds) of the track-lines of motor/non-motor assemblies: transport of 3 (a) and 6 (b) non-motor spheres. Scale bar, 5 μm. Conditions, as in Figure 2.2.1.

An interesting phenomenon has been observed with some triplet assemblies consisting of a motor doublet and a single non-motor. As illustrated in Figure 2.2.7, such motor/non-motor triplet assemblies can rotate around the non-motor particle which serves as the fixed axis of rotation. The hydrophobic interactions between the three particles allow them to remain bonded together, while other interactions between the non-motor particle and the glass-slide surface (e.g., electrostatic, hydrogen-bonding, and van der Waals interactions) allow the assembly to be anchored to the glass surface to form the fixed-point rotation.[61] The direction of rotation is determined by the orientation of the doublet motor assembly. Note, in this case, that the non-motor particle is also rotating with the motors, but without a net displacement.

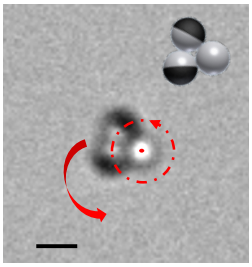

Figure 2.2.7 Motor/non-motor interaction: rotational motion with the non-motor anchored to the glass surface. Scale bar, 2 μm. Conditions, as in Figure 2.2.1.

2.2.4 Conclusions

In summary, we have demonstrated that hydrophobic interactions provide a new approach for constructing defined assemblies of chemically-powered Janus particle motors. These assemblies were prepared by octadecyltrichlorosilane (OTS) modification of the surface of a silica microparticle and addition of a catalytic Pt hemispheric coating. This represents the first example of preparing defined assemblies of micromotors based on specific and directional interactions. The assembly structure along with the individual particle orientations has a profound influence on the movement of such defined micromotor assemblies. Extended higher-order structures are expected by tuning the size and position of the hydrophobic patch beyond the traditional two-faced Janus particle geometry of uniform particle and patch size. A theoretical model will be developed for predicting the dynamics of such self-propelled particle assemblies. This attractive assembly strategy allows the cooperative action and coordinated movement of multiple Janus motors, making it promising for diverse future applications ranging from advanced transport to targeted drug delivery. In addition, probing the limits of such autonomous motor assembly systems could help to understand the behavior of biological systems involving multiple moving and interacting components such as fish schooling.

Chapter 2.1, in full, is a reprint of the material as it appears in Journal of the American Chemical Society, 2014, by Wei Gao, Allen Pei, Renfeng Dong, Joseph Wang. Chapter 2.2, in full, is a reprint of the material as it appears in Journal of the American Chemical Society, 2013, by Wei Gao, Allen Pei, Xiaomiao Feng, Camille Hennessy, Joseph Wang. The dissertation author was the primary investigator and author of these papers.

2.3 References

1. Wang, J. Nanomachines: Fundamentals and Applications, Wiley-VCH, Weinheim, 2013.
2. Mallouk, T. E.; Sen, A. *Sci. Amer.* **2009**, *5*, 72.
3. Mirkovic, T.; Zacharia, N. S.; Scholes, G. D.; Ozin, G. A. *ACS Nano* **2010**, *4*, 1782.
4. Wang, J.; Gao, W. *ACS Nano* **2012**, *6*, 5745.
5. Sanchez, S.; Pumera, M. *Chem.–Asian J.* **2009**, *4*, 1402.
6. Ozin, G. A.; Manners, I.; Fournier-Bidoz S.; Arsenault, A. *Adv. Mater.* **2005**, *17*, 3011.
7. Wang, W.; Duan, W.; Ahmed, S.; Mallouk T. E.; Sen, A. *Nano Today* **2013**, *8*, 531.
8. Wilson, D. A.; Nolte, R. J. M.; van Hest, J. C. M. *Nat. Chem.* **2012**, *4*, 268.
9. Loget, G.; Kuhn, A. *J. Am. Chem. Soc.* **2010**, *132*, 15918.
10. Loget, G.; Kuhn, A. *Nat. Commun.* **2011**, *2*, 535.
11. Paxton, W. F.; Kistler, K. C.; Olmeda, C. C.; Sen, A.; St. Angelo, S. K.; Cao, Y.; Mallouk, T. E.; Lammert, P. E.; Crespi, V. H. *J. Am. Chem. Soc.* **2004**, *126*, 13424.
12. Fournier-Bidoz, S.; Arsenault, A. C.; Manners, I.; Ozin, G. A. *Chem. Commun.* **2004**, 441.
13. Laocharoensuk, R.; Burdick, J.; Wang, J. *ACS Nano* **2008**, *2*, 1069.
14. Mei, Y. F.; Huang, G. S.; Solovev, A. A.; Urena, E. B.; Monch, I.; Ding, F.; Reindl, T.; Fu, R. K. Y.; Chu, P. K.; Schmidt, O. G. *Adv. Mater.* **2008**, *20*, 4085.
15. Mei, Y. F.; Solovev, A. A.; Sanchez, S.; Schmidt, O. G. *Chem. Soc. Rev.* **2011**, *40*, 2109.
16. Gao, W.; Sattayasamitsathit, S.; Orozco, J.; Wang, J. *J. Am. Chem. Soc.* **2011**, *133*, 11862.
17. Zhao, G.; Pumera, M. *RSC Adv.* **2013**, *3*, 3963.
18. Howse, J. R.; Jones, R. A.; Ryan, A. J.; Gough, T.; Vafabakhsh, R.; Golestanian, R. *Phys. Rev. Lett.* **2007**, *99*, 048102.
19. Gibbs, J. G.; Zhao, Y. –P. *Appl. Phys. Lett.* **2009**, *94*, 163104.
20. Baraban, L.; Makarov, D.; Streubel, R.; Monch, I.; Grimm, D.; Sanchez, S.; Schmidt, O. G. *ACS Nano* **2012**, *6*, 3383.
21. Gao, W.; Pei, A.; Feng, X.; Hennessy, C.; Wang, J. *J. Am. Chem. Soc.* **2013**, *135*, 998.

22. Sanchez, S.; Ananth, A. N.; Fomin, V. M.; Viehrig, M.; Schmidt, O. G. *J. Am. Chem. Soc.* **2011**, *133*, 14860.

23. Schmidt, E. W. Hydrazine and Its Derivatives; Wiley-Interscience: New York, 2001.

24. Ibele, M. E.; Wang, Y.; Kline, T. R.; Mallouk, T. E.; Sen, A. *J. Am. Chem. Soc.*, **2007**, *129*,7762.

25. Gao, W.; Sattayasamitsathit, S.; Uygun, A.; Pei, A.; Ponedal, A.; Wang, J. *Nanoscale* **2012**, *4*, 2447.

26. Contour, J. P.; Pannetier, G. *J. Catal.* **1972**, *24*, 434.

27. Escard, J. *J. Cat.* **1973**, *29*, 31.

28. Keh, H. J.; Luo, S. C. *Phys. Fluids* **1995**, *7*, 2122.

29. Pavlick, R. A.; Sengupta, S.; McFadden, T.; Zhang, H.; Sen A. *Angew. Chem. Int. Ed.* **2011**, *50*, 9374.

30. Anderson, J. L. *Ann. Rev. Fluid Mech.* **1989**, *21*, 61.

31. Re-Evaluation of Some Organic Chemicals, *IARC Monographs on the Evaluation of the Carcinogenic Risks to Humans*, IARC: Lyon, **1999**, *71*, 991.

32. Choudhary, G.; Hansen, H. *Chemosphere* **1998**, *37*, 801.

33. Ebbens, S.; Gregory, D. A.; Dunderdale, G.; Howse, J. R.; Ibrahim, Y.; Liverpool, T. B.; Golestanian, R. **2013**, arXiv:1312.6250.

34. Kagan, D.; Balasubramanian, S.; Wang, J. *Angew. Chem. Int. Ed.* **2011**, *50*, 503.

35. Patra, D.; Zhang, H.; Sengupta, S.; Sen, A. *ACS Nano* **2013**, *7*, 7674.

36. Zhang, H.; Yeung, K.; Robbins, J. S.; Pavlick, R. A.; Wu, M.; Liu, R.; Sen, A.; Phillips, S. T. *Angew. Chem., Int. Ed.* **2012**, *51*, 2400.

37. Wang, W.; Chiang, T.; Velegol, D.; Mallouk, T. E. *J. Am. Chem. Soc.* **2013**, *135*, 10557.

38. Gao, W.; Kagan, D.; Pak, O. S.; Clawson, C.; Campuzano, S.; Chuluun-Erdene, E.; Shipton, E.; Fullerton, E. E.; Zhang, L.; Lauga, E.; Wang, J. *Small* **2012**, *8*, 460.

39. Campuzano, S.; Orozco, J.; Kagan, D.; Guix, M.; Gao, W.; Sattayasamitsathit, S.; Claussen, J. C.; Merkoci, A.; Wang, J. *Nano Lett.* **2012**, *12*, 396.

40. Guix, M.; Orozco, J.; Garcia, M.; Gao, W.; Sattayasamitsathit, S.; Merkoci, A.; Escarpa, A.; Wang, J. *ACS Nano* **2012**, *6*, 4445.

41. Orozco, J.; Campuzano, S.; Kagan, D.; Zhou, M.; Gao, W.; Wang, J. *Anal. Chem.* **2011**, *83*, 7962.

42. Solovev, A. A.; Xi, W.; Gracias, D. H.; Harazim, S. M.; Deneke, C.; Sanchez, S.; Schmidt, O. G. *ACS Nano* **2012**, *6*, 1751.

43. Zhang, L.; Petit, T.; Peyer, K. E.; Nelson, B. J. *Nanomed.-Nanotechnol. Biol. Med.* **2012**, *8*, 1074.

44. Sanchez, S.; Solovev, A. A.; Schulze, S.; Schmidt, O. G. *Chem. Commun.* **2011**, *47*, 698.

45. Kagan, D.; Laocharoensuk, R.; Zimmerman, M.; Clawson, C.; Balasubramanian, S.; Kang, D.; Bishop, D.; Sattayasamitsathit, S.; Zhang, L.; Wang, J. *Small* **2010**, *6*, 2741.

46. Hu, J.; Zhou, S. X.; Sun, Y. Y.; Fang, X. S.; Wu, L. M. *Chem. Soc. Rev.* **2012**, *41*, 4356.

47. Jiang, S.; Chen, Q.; Tripathy, M.; Luijten, E.; Schweizer, K. S.; Granick, S. *Adv. Mater.* **2010**, *22*, 1060.

48. Walther, A.; Muller, A. H. E. *Soft Matter* **2008**, *4*, 663.

49. Loget, G.; Roche, J.; Kuhn, A. *Adv. Mater.* **2012**, *24*, 5111.

50. Kagan, D.; Balasubramanian, S.; Wang, J. *Angew. Chem., Int. Ed.* **2011**, *50*, 503.

51. Sen, A; Ibele, M.; Hong, Y.; Velegol, D. *Faraday Disc.* **2009**, *143*, 15.

52. Solovev, A. A.; Sanchez, A.; Schmidt, O. G. *Nanoscale* **2013**, *5*, 1284.

53. Ibele, M.; Mallouk, T. E.; Sen, A. *Angew. Chem., Int. Ed.* **2009**, *481*, 3308.

54. Ebbens, S.; Jones, R. A. L.; Ryan, A. J.; Golestanian, R.; Howse, J. R. *Phys. Rev. E* **2010**, *82*, 015304.

55. Baraban, L.; Tasinkevych, M.; Popescu, M. N.; Sanchez, S.; Dietrich, S.; Schmidt, O. G. *Soft Matter* **2012**, *8*, 48.

56. Chen, Q.; Whitmer, J. K.; Jiang, S.; Bae, S. C.; Luijten, E.; Granick, S. *Science* **2011**, *331*, 199.

57. Jiang, S.; Chen, Q.; Tripathy, M.; Luijten, E.; Schweizer, K. S.; Granick, S. *Adv. Mater.* **2010**, *22*, 1060.

58. Chen, Q.; Diesel, E.; Whitmer, J.; Bae, S. C.; Luijten, E.; Granick, S. *J. Am. Chem. Soc.* **2011**, *133*, 7725.

59. Hong, L.; Cacciuto, A.; Luijten, E.; Granick, S. *Langmuir* **2008**, *24*, 621.

60. Chen, Q.; Yan, J.; Zhang, J.; Bae, S. C.; Granick, S. *Langmuir* **2012**, *28*, 13555.

61. Valadares, L. F.; Tao, Y. G.; Zacharia, N. S.; Kitaev, V.; Galembeck, F.; Kapral, R.; Ozin, G. A. *Small* **2010**, *6*, 565.

Chapter 3 Polymer-based Catalytic Microengines

3.1 Template based electrosynthesis of PANI/Pt microengines

3.1.1 Introduction

Inspired by the sophistication of nature biomotors and driven by recent nanotechnological advances, major efforts are currently being devoted to the design of efficient synthetic micro/nanoscale motors that convert various energies into autonomous motion.[1-5] Particular recent attention has been given to self-propelled chemically-powered catalytic nanomotors based on the decomposition of hydrogen peroxide.[1-5] Although catalytic nanowire motors (described in Chapter 1) and Janus micromotors (described in Chapter 2) have shown diverse capabilities including cargo transport and self-assembly, catalytic microtube engines - pioneered by Mei and Schmidt[5-7]- are particularly attractive for practical applications due to their efficient bubble-induced propulsion in relevant biological fluids and salt-rich environments.[8-10] The oxygen-bubble propulsion mechanism of tubular microengines, associated with their conical shape and inner Pt surface, thus addresses the ionic-strength limitation and the limited scope of catalytic nanowire motors.[11] Such powerful microengines are commonly prepared by top-down photolithography, e-beam evaporation and stress-assisted rolling of functional nanomembranes on polymers into conical microtubes. While offering an extremely attractive performance, their practical utility is greatly hindered by the complexity of the fabrication process and related (clean-room) costs. Another approach for preparing microengine, involving sequential electrodeposition of platinum and gold layers onto an etched silver wire template,[12] offers a low yield and inferior propulsion behavior.

Here we demonstrate a greatly simplified membrane-template mass production of high performance catalytic microtubular engines. The resulting microtubes have significantly smaller size than commonly used rolled-up microengines (8 vs. 50~100 μm), require very low fuel concentrations (down to 0.2% H_2O_2 vs. 1.5%) and move at a very high speed (over 350 body lengths s^{-1}). The template electrodeposition method has been widely used for preparing different types of nanowires,[13] and is commonly employed for preparing bimetallic catalytic nanowire motors.[2,3] To realize the synthesis of efficient conical microtube engines we relied here on a unique combination of commercial microporous membranes, containing a huge number of uniform double conical pores (Whatman Catalog No. 7060-2511), with the plating of polymeric/metal bilayers with a highly catalytic inner platinum surface. Martin[14] and Whitesides[15] demonstrated the successful template synthesis of cylindrical conducting-polymer microtubes, while Wan and Bai[16] described the template preparation of Sn/Pt bimetallic nanotubes based on evaporation and electrodeposition methods. Template electrosynthesis of microstructures of different shapes, including conical and double conical nanowires and microtubes, was also described[17, 18] but not in connection to nanomotors.

3.1.2 Experimental section

Synthesis of multilayer microtube rocket

The multilayer microtubes were prepared using a common template directed electrodeposition protocol. A cyclopore polycarbonate membrane, containing 2 μm diameter conical-shaped micropores (Catalog No 7060-2511; Whatman, Maidstone, U. K.), was employed as the template. A 150 nm gold film was first sputtered on one side of the porous membrane to serve as working electrode. A Pt wire and an Ag/AgCl with 3 M KCl were used as counter and reference electrodes, respectively. The membrane was then assembled in a plating cell with an aluminum foil serving as contact. Polyaniline microtubes were prepared by modifying the previously described method.[15] Briefly, polyaniline (Sigma-Aldrich, St Louis, MO) was distilled

before used at a vapor temperature of 100 °C and a pressure of 13 mm Hg. It should be pointed out that such freshly distilled aniline solution should be used within 3 days. Polyaniline microtubes were electropolymerized for 5 sec at +0.80 V from a plating solution containing 0.1 M H_2SO_4, 0.5 M Na_2SO_4 and 0.1 M aniline; subsequently, the inner Pt tube was deposited galvanostatically at -2 mA for 3600 sec from a commercial platinum plating solution (Platinum RTP; Technic Inc, Anaheim, CA). For PANI/Ni/Pt trilayer microtube, polyaniline microtubes were deposited from a plating solution containing 0.1 M H_2SO_4, 0.5 M Na_2SO_4 and 0.1 M aniline and electropolymerized at +0.8 V for 5 sec; then a nickel layer was deposited from a nickel plating solution containing 20 g L^{-1} $NiCl_2 \cdot 6H_2O$, 515 g L^{-1} $Ni(H_2NSO_3)_2 \cdot 4H_2O$, and 20 g L^{-1} H_3BO_3 at -1.0 V (vs. Ag/AgCl) for 1 C; finally, the inner Pt tube was deposited galvanostatically at -2 mA for 1800 s. The sputtered gold layer was completely removed by hand polishing with 3-4 μm alumina slurry (as indicated by visual inspection of the membrane color). Incomplete removal will result in bubbles emerging from the smaller opening (yet without compromising the performance). The membrane was then dissolved in methylene chloride for 10 min to completely release the microtubes. The microtubes were collected by centrifugation at 6000 rpm for 3 min and washed repeatedly with methylene chloride (three times), followed by ethanol and ultrapure water (18.2 MΩ cm), twice of each, with a 3 min centrifugation following each wash. All microtubes were stored in nanopure water at room temperature when not in use. The microrocket preparation method is characterized with good reproducibility. For example, two batches tested from different membranes yielded average speeds of 286 and 281 μm s^{-1}, with relative standard deviations of 16.4 and 18.2%, (n=30 for each batch, using 1.0% H_2O_2 and 1.6% sodium cholate). Typically, such microengine can propel continuously for over 20 min in 15 μL mixed solution (until the sample solution dries up).

Equipments

Template electrochemical deposition of microtube was carried out with a CHI 621A potentiostat (CH Instruments, Austin, TX). Scanning electron microscopy (SEM) images were obtained with a Phillips XL30 ESEM instrument, using an acceleration potential of 20 kV. Mapping analysis was investigated by Oxford EDX attached to SEM instrument and operated by Inca software. An inverted optical microscope (Nikon Instrument Inc. Ti-S/L100), coupled with a 40x objective, a Photometrics QuantEM 512/SC camera (Roper Scientific, Duluth, GA) and a MetaMorph 7.6 software (Molecular Devices, Sunnyvale, CA) were used for capturing movies at a frame rate of 30 frames per second. The speed of the microengines was tracked using a Metamorph tracking module and the results were statistically analyzed using Origin software.

Reagents and Solutions

In order to self-propel catalytic microengines, aqueous hydrogen peroxide solutions with concentrations ranging from 0.2–5.0% were used as chemical fuels, containing 0.33-5.0% (w/v) sodium cholate (Sigma-Aldrich, St Louis, MO) to reduce the surface tension, hence facilitating the engine propulsion. Below 0.5% peroxide, the fraction of moving microengines decreases greatly due to the lower bubble frequency (i.e., weaker bubbling thrust). The experiments of the microengines in human serum samples from human male AB plasma (Sigma-Aldrich, St. Louis, MO) and cell culture media (Catalog No. 15-040-CV, Mediatech Inc, Manassas, VA) were carried out by mixing sequentially 5 μL microengine solution, 5 μL 10% sodium cholate, 10 μL biological media and 5 μL 7.5% H_2O_2, i.e., a final solution corresponding to 40% of the raw samples.

3.1.3 Results and discussions

Figure 3.1.1A depicts the process of template preparation of the polyaniline (PANI)/platinum bilayer microtubular engines. The template used in this process is a commercially available 20 μm-thick Cyclopore polycarbonate membrane, which has a symmetrical double cone pore structure of 2 μm of diameter in both sides and 1 μm in its center.

By using one portion of their double cone (Figure 3.1.1A), such membrane provides an attractive asymmetric template structure required for the bubbling propulsion mechanism. Due to the solvophobic effect and electrostatic effect,[14] aniline monomers initially polymerize on the inner wall of the membranes, leading to a rapid formation of a PANI film. A platinum tube layer is subsequently plated inside the PANI tube using a galvanostatic method. The resulting conical bilayer microtube structure is preserved after the template dissolution. Figure 3.1.1B shows the side-view (a) and cross-view (b) SEM images of a typical 8-μm long conical microtube. The PANI/Pt bilayer tube has a defined geometry with outer diameters of 2 μm and 1.1 μm, along with inner openings of 1.5 and 0.5 μm, and a taper angle of 3.2°. The PANI and Pt layers are easily visualized from the cross-view image, with a thickness of 180 and 80 nm, respectively. Common rolled-up microengines have significantly larger openings of 5-10 μm in diameter.[5-7] An EDX mapping analysis, carried out to confirm the bilayer content (e.g., Figure 3.1.2b and 3.1.2c), shows clearly the presence of both platinum and carbon (from PANI) within the conical microtube.

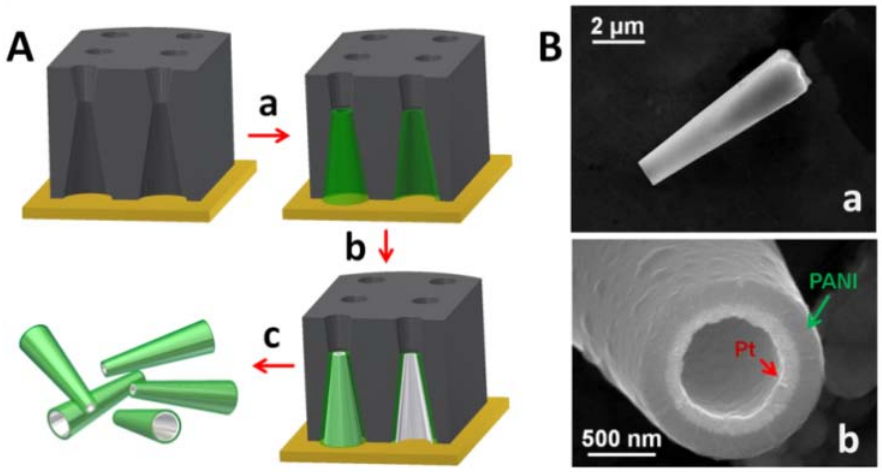

Figure 3.1.1 A) Preparation of bilayer PANI/Pt microtubes using Cyclopore polycarbonate membranes: a) deposition of the polyaniline (PANI) microtube; b) deposition of the Pt microtube; c) dissolution of the membrane and release of the bilayer microtubes. B) SEM images of the microtube engines: a) side view of a bilayer PANI/Pt microtube; b) cross view of a bilayer PANI/Pt microtube.

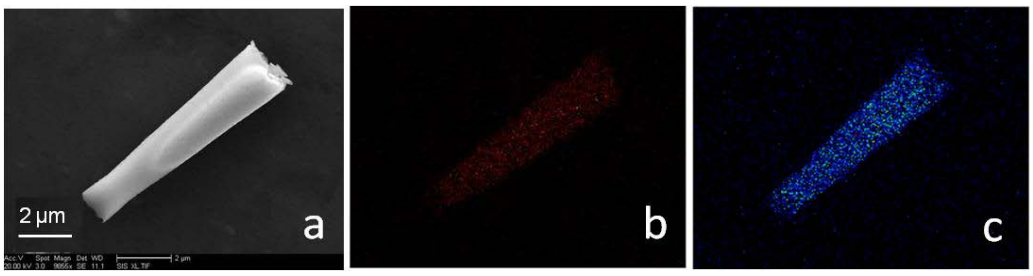

Figure 3.1.2 EDX mapping analysis of a bilayer PANI/Pt microtube. a) the SEM image of a bilayer microtube; b) EDX Mapping result of the distribution of carbon; c) EDX mapping result of the distribution of platinum.

The high propulsion power of the template-prepared PANI/Pt microtube engines is illustrated in Figure 3.1.3. For example, Figure 3.1.3 A (a, b), show the movement of two microengines in a 1% H_2O_2 solution (containing 0.33% of the sodium cholate surfactant) during a 3 s period. The two microengines move rapidly in spiral and circular trajectories, with an average speed of 120 µm s^{-1}. Similar motion trajectories were reported for larger rolled-up microengines.[7] Long oxygen bubble tails, released from the wider tubular openings, can be easily visualized, with individual microbubble of 2.5 µm. While the bilayer microengines of Figure 3.1.3A move randomly, it is also possible to guide them magnetically by depositing an intermediate ferromagnetic Ni layer and forming a trilayer PANI/Ni/Pt microengine. Figure 3.1.3B shows time lapse images (200 ms intervals) of the motion of a PANI/Ni/Pt microengine under the magnetic field in the presence of 1% H_2O_2 solution. The speed of the trilayer microengine decreases to 80 µm s^{-1}, compared to 120 µm s^{-1} of the bilayer PANI/Pt microtubes (under the same conditions), reflecting the smaller pore diameter associated with the Ni layer. Our further experimental results show that the opening size of PANI/Pt microengines has a profound effect on their speed. For example, reducing the inner opening diameter from 500 to 150 nm (measured from smaller side of the tube) resulted in a lower speed of 60 µm s^{-1} (vs. 120 µm s^{-1}, using 1% H_2O_2 and 0.33% sodium cholate).

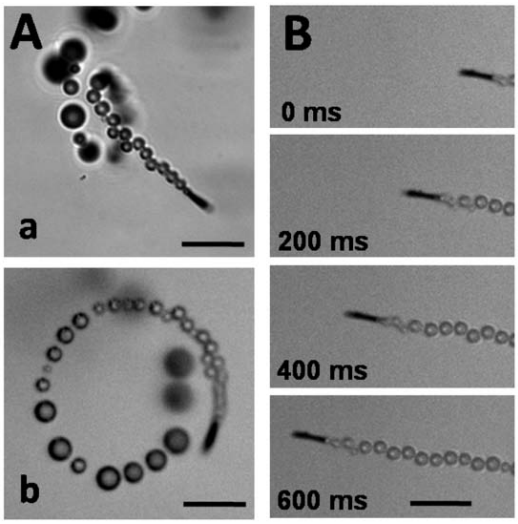

Figure 3.1.3 A) Highly efficient tubular catalytic PANI/Pt microengines: spiral (a) and circular (b) motion. Trajectories are visualized by microbubble tails in a 1% H_2O_2 solution. B) Time lapse images (200 ms intervals) of the motion of a PANI/Ni/Pt trilayer microengine under the magnetic field in the presence of 1% H_2O_2 solution. Sodium cholate level (A, B), 0.33% (w/v). Scale bars, 20 µm.

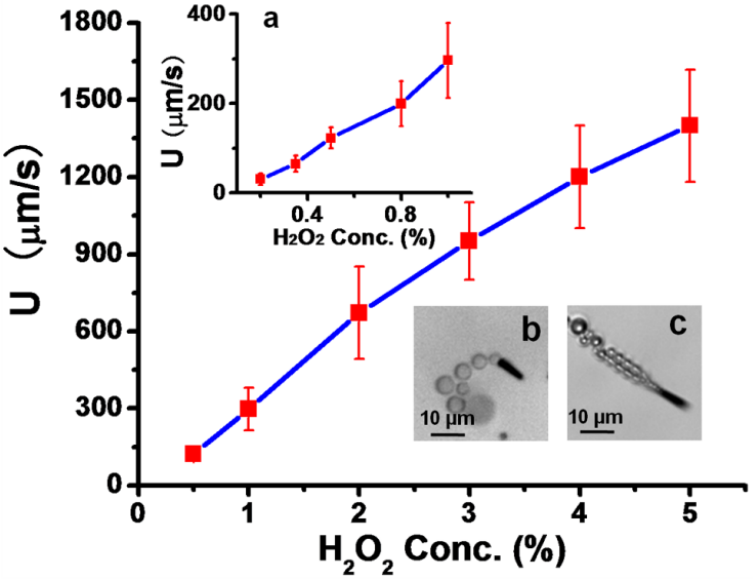

Figure 3.1.4 Dependence of the PANI/Pt-microengine speed upon the hydrogen peroxide concentration over the 0.2 to 5.0% range, in the presence of 1.6% (w/v) sodium cholate (n=60). Inset a), speed profile over the 0.2–1.0% peroxide range. Insets b) and c), propulsion in the presence of 0.3% and 0.5% hydrogen peroxide, respectively.

The concentration of hydrogen peroxide fuel strongly influences the velocity of the catalytic microengines. As illustrated in Figure 3.1.4, the average speed of the PANI/Pt

microtubular engines increases from 123 ± 21.4 μm s^{-1} (15 body-lengths s^{-1}) in a 0.5% hydrogen peroxide to 1410 ± 172 μm s^{-1} (~180 body lengths s^{-1}) at 5% peroxide (using 1.6% of the sodium cholate surfactant; n=60). The greatly increased speed of the PANI/Pt microengines over the entire range of H_2O_2 fuel (0-5%) reflects the higher pressure experienced by the bubbles.[7] However, using a low peroxide level (below 5%), the template bilayer microengines display a much faster speed than the rolled-up microengines.[7,20] The fastest observed speed of the microengines exceeds 3 mm s^{-1}, i.e., more than 375 body lengths s^{-1}. Such ultrafast speed is attributed primarily to increased electrocatalytic reactivity of the inner platinum surface associated with the higher surface roughness [Figure 3.1.1B(b)], compared to the smooth platinum surface of rolled-up microengines. Increasing the area of Pt electrode sensors was shown previously to increase their catalytic reactivity toward the decomposition of hydrogen peroxide.[21] Our experiments also show that such microengines can move in very low peroxide levels. Inset (a) of Figure 3.1.4 shows the dependence of the microengine speed upon the hydrogen peroxide concentration over the 0.2-1.0% range. Well defined propulsion is observed over this range of low peroxide concentrations, with speed ranging between 25 and 285 μm s^{-1}. For example, the microengine can move at ~25 μm s^{-1} (over 3 body length s^{-1}) in a 0.2% peroxide solution. Even further lowering of the peroxide concentration down to 0.05% can be achieved by adding 0.05% hydrazine. In contrast, the lowest peroxide level reported for propelling catalytic rolled-up microengines is 1.5% (resulting in a low speed of 1 body-lengths s^{-1}).[19]

The radius and frequency of the generated oxygen bubbles are influenced by the level of peroxide fuel. The inset of Figure 3.1.4 illustrates the representative bubble size of microtubular engines in the presence of 0.3 (b) and 0.5 (c) % H_2O_2, and 1.6% (w/v) sodium cholate surfactant. The bubble frequency is increasing greatly (from 16 Hz to 60 Hz) upon raising the peroxide level from 0.3 to 0.5%, while the bubble size decreases from 2.6 μm to 2.0 μm, respectively. As expected,[7] larger bubbles with a lower frequency lead to a lower speed (e.g., 40 μm s^{-1} in 0.3%

hydrogen peroxide as compared to 120 μm s^{-1} in 0.5% peroxide). We also observed that the average moving steps are close to the bubble radius. For example, in 0.5% hydrogen peroxide - where the bubble radius is around 2 μm and the frequency around 60 Hz - the microengine speed is 122 μm s^{-1}, i.e., nearly corresponding to the product of the bubble and frequency, indicating that the drag forces on the engines and bubbles are comparable. Similar effects were reported for the rolled-up microtubes.[7]

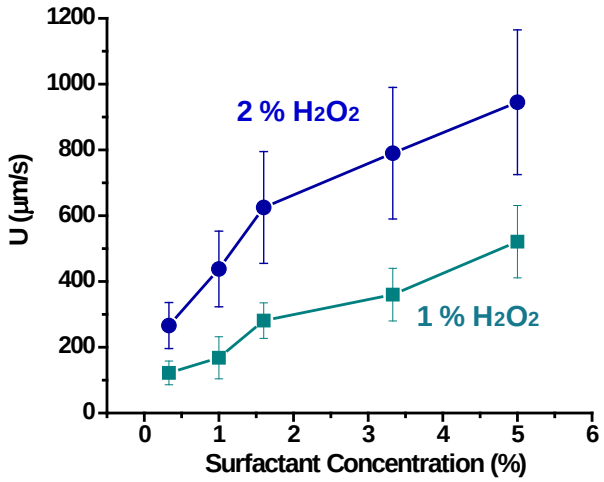

Figure 3.1.5 Influence of sodium cholate concentration on the speed of the microengines in the presence of 1% and 2% hydrogen peroxide.

The influence of the surfactant concentration (sodium cholate in this work) upon the speed of microengines was also examined (Figure 3.1.5). Increased speed is observed upon raising the surfactant concentration over the 0-5% range. Using a 1% H_2O_2 solution containing 0.33% sodium cholate, the microengines have an average speed of 120 μm s^{-1}; the speed increases to around 300 μm s^{-1} in 1.6% sodium cholate and to 520 μm s^{-1} in 5% sodium cholate. In the presence of 2% H_2O_2 (along with 5% sodium cholate), the microengine move at 1.0 mm s^{-1}. Such surfactant-induced increase of the speed is attributed to the lowering of the surface tension smaller bubble size and a much higher bubble frequency, in a mannar analogous to those reported for rolled-up microrckets.[6, 7]

Common catalytic nanowire motors operate only in low ionic-strength aqueous solutions[11] and hence cannot be applied to realistic biological environments. Microtubular engines address this ionic-strength limitation and can expand the scope of nanomotors to salt-rich environments.[9,10,12] For example, Figures 3.1.6A and 3.1.6B illustrate the movement of the template-prepared microengine in realistic biological environments, such as cell culture media and human serum, respectively (containing 1.5% H_2O_2 and 2 % sodium cholate). The new microengines propel efficiently using physiological conditions, with high average speeds of 150 (cell culture) and 95 (serum) μm s^{-1}. The decrease of the speed (vs. more than 300 μm s^{-1} in water, under similar conditions) is attributed to viscosity effects (e.g. ~1.5 mPa·s for human serum). A slower speed (~200 μm s^{-1}) was also observed in a high ionic aqueous solution (3 M NaCl, viscosity ~1.2 mPa·s).

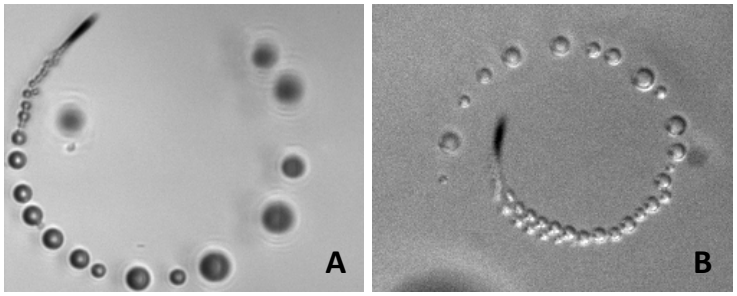

Figure 3.1.6 Motion of the bilayer microrocket in different biological media: A) Cell Culture Media; B) Human Serum, spiked with 1.5% H_2O_2, 2% sodium cholate.

Assuming the microengine as a cylinder microrod (since the fluid cannot freely flow through microengine because of the oxygen bubbles), with 8 μm in length and 2 μm in diameter moving at the speed of 1400 μm s^{-1}, we can roughly estimate the drag force by using the Stokes' drag theory

$$F_d = \frac{2\pi\mu LU}{\ln(L/a) - 1/2}$$

where F_d is the fluid resistance, *U* is the speed in the microengine, μ is the fluid dynamic viscosity, and *L* and *a* are the length and radius of the microtubes, respectively. The estimated drag force of the microengines, 45 pN, is sufficient for transporting large cargos such as cells.[8, 9, 20]

3.1.4 Conclusions

In conclusion, we demonstrated that remarkably efficient microtube engines can be mass produced by a greatly simplified low-cost membrane template electrodeposition. The resulting PANI/Pt microtubes are significantly smaller than rolled-up microengines, move at a greatly higher speed (of over 350 body-length s^{-1}) and require very low fuel concentrations. Reducing the peroxide level leads to greatly improved cell viability in connection to relevant biomedical applications.[9] While the concept has been illustrated in connection to PANI/Pt microengines, the template electrodepostion allows plating of different outer or inner layer materials (polymers, metals, etc.) to meet specific needs and different applications, and expanding the scope of catalytic micro/nano machines. The attractive properties of these new template-prepared microtube engines, along with their bioenvironmental compatibility, hold considerable promise for the design of practical nanomachines for a wide range of important future applications.

3.2 The role of composition on the performances of the microengines

3.2.1 Introduction

In the previous section, a greatly simplified template-membrane based synthesis of highly efficient and smaller microtube engines was reported recently.[22] The new template electrodeposition protocol has led to ultrafast (>350 body lengths s^{-1}) PANI/Pt bilayer tubular microengines (8-μm long), requiring very low fuel concentrations (down to 0.2% H_2O_2).[22] Such ultrafast nanomotor speed reflects a large force and power essential to execute different tasks. Here we report on a critical evaluation of template-prepared polymer-metal tubular microengines based on different materials and synthesis conditions and on the dramatically improved propulsion performance achieved by identifying new compositions and optimizing their preparation protocol. We indicate that when polymer-based microstructures are prepared by template-directed electrochemical synthesis, there is an opportunity to control the morphology. In particular, we critically compare microengines based on different electropolymerized outer layers and various metallic and alloy inner layers. As excepted for template directed electrochemical synthesis, the preparation conditions, particularly the electropolymerization conditions, are shown to have a profound effect upon the morphology and propulsion behavior. The movement is also shown to be greatly influenced by the choice of monomer structure that affects the diameter and shape. This detail study has thus led to useful insights into the preparation and composition of high-performance biocompatible low-cost template-prepared tubular microengines and facilitated the rational design of ultrafast PEDOT/Pt bilayer microengines with a record-breaking speed of over 1400 body lengths per second. In addition to pursuit the ultrafast propulsion, we also describe the first example of microengines based on an inner Pt-Ni alloy surface combining (within the same layer) catalytic and magnetic properties for the peroxide decomposition and

magnetic alignment, respectively. Bimetallic Au-Pt microengines are also presented here for the first time, with the presence of a gold outer layer facilitating surface functionalization towards potential biomedical applications.

Particular attention is given to the role of the electropolymerized outer layer and to the influence of different inner catalytic layers. Compared to common metallic materials, conducting polymers, such as polyaniline (PANI), polypyrrole (PPy), polythiophene (PT) and poly(3,4-ethylenedioxythiophene) (PEDOT) offer considerable promise for various practical applications due to their light weight, conductivity, mechanical flexibility, and unique chemical and redox properties, along with minimal structural defects, high aqueous stability and biocompability.[23-29] Functionalized-polymer microstructures have thus found a growing role as microscale actuators, drug carriers or metabolite and genetic biosensors.[30-32] For sensing applications of conducting polymers, the tubular forms of conducting polymers have been shown advantageous (over film, fibrillar or wire forms) owing to their high surface area and fast response.[33] Conducting polymer nanotubes, suitable for self-propelled tubular microengines, can be prepared by both oxidative-chemical, soft-template and hard-template electrochemical polymerization methods; although little attention has been given to electrochemical preparation of conducting-polymer microtubes, the electropolymerization route is preferred since it offers precise control of the deposition conditions and hence of the dimensions and morphology of the resulting microtubes.[34,35] The exact microstructures and morphologies of the resulting conducting polymers have a profound effect on their physical and chemical properties.[36,37] Here we investigate the preparation of self-propelled microengines based on different conducting polymers and electropolymerization conditions (e.g., monomer, surfactant, supporting electrolyte and monomer concentration). The influence of these conditions upon the structure and behavior of the resulting microengines is investigated in connection to PPy-, PEDOT- and PANI-based microtubes. The systematic optimization of the composition and preparation of such polymer-based tubular microengines,

reported in the following sections, offers useful insights towards the rational preparation of high-performance microengines with distinct advantages over existing microscale motors.

3.2.2 Experimental section

Synthesis of various tubular microengines

The various microtubes were prepared using a common template directed electrodeposition protocol. A Cyclopore polycarbonate membrane, containing 2 μm diameter conical-shaped micropores (Catalog No 7060-2511; Whatman, Maidstone, U. K.), was employed as the template. A 75 nm gold film was first sputtered on one side of the porous membrane to serve as working electrode using the Denton Discovery 18. The sputter was performed at room temperature under vacuum of 5 x 10^{-6} Torr, DC power 200 W and flow Ar to 3.1 mT. Rotation speed is 65. Sputter time 90 s. A Pt wire and an Ag/AgCl with 3 M KCl were used as counter and reference electrodes, respectively. The membrane was then assembled in a plating cell with an aluminum foil serving as a contact. Polyaniline microtubes were prepared by modifying the previously described method.[22] Briefly, aniline and pyrrole (Sigma-Aldrich, St Louis, MO) were distilled before use at a vapor temperature of 100 °C and a pressure of 13 mm Hg. Polyaniline (PANI) microtubes were electropolymerized at +0.80 V for 0.02 C from a plating solution containing 0.1 M H_2SO_4, 0.5 M Na_2SO_4 and 0.1 M aniline; subsequently, the inner Pt tube was deposited galvanostatically at -2 mA for 600 s from a commercial platinum plating solution (Platinum RTP; Technic Inc, Anaheim, CA).

Poly(3,4-ethylenedioxythiophene) (PEDOT) microtubes were electropolymerized at +0.80 V for a charge of 0.06 C from a plating solution containing 15 mM EDOT, 7.5 mM KNO_3 and 100 mM sodium dodecyl sulfate (SDS); subsequently, the inner Pt tube was deposited galvanostatically at -2 mA for 600 s. The smaller microengines (4 μm in length) were synthesized using a Cyclopore polycarbonate membrane, containing 1 μm diameter micropores (Catalog No 7060-2510; Whatman, Maidstone, U. K.) PEDOT microtubes were electropolymerized at +0.80

V using a charge of 0.04 C while the corresponding inner platinum layer was deposited galvanostatically at -2 mA for 600 s.

Polypyrrole (PPy) microtubes were electropolymerized at +0.80 V for a charge of 0.8 C from a plating solution containing 37 mM pyrrole and 7.5 mM KNO_3. Subsequently, a metal tube layer was plated inside the polymer layer. Different metallic layers were examined for this purpose. For PPy/Pt, the inner Pt tube was deposited galvanostatically at -2 mA for 600 s from a commercial platinum plating solution (Platinum RTP; Technic Inc, Anaheim, CA); for PPy/Ag, silver was plated subsequently at -0.9 V (vs. Ag/AgCl) for a total charge of 1 C using a commercial silver plating solution (1025 RTU @ 4.5 Troy/gallon; Technic Inc., Anaheim, CA); for PPy/Pt-Ni alloy, platinum-nickel alloy is plated at -1 V for a total charge of 2 C using a 1:1 mixed solution of a commercial platinum solution and a nickel plating solution containing 20 g L^{-1} $NiCl_2 \cdot 6H_2O$, 515 g L^{-1} $Ni(H_2NSO_3)_2 \cdot 4H_2O$, and 20 g L^{-1} H_3BO_3; for PPy-Au, gold is plated at -0.9 V for 1 C from a commercial gold plating solution (Orotemp 24 RTU RACK; Technic Inc.).

The sputtered gold layer was completely removed by hand polishing with 3-4 μm alumina slurry. The membrane was then dissolved in methylene chloride for 10 min to completely release the microtubes. The latter were collected by centrifugation at 6000 rpm for 3 min and washed repeatedly with methylene chloride, followed by ethanol and ultrapure water (18.2 MΩ cm), three times of each, with a 3 min centrifugation following each wash. All microtubes were stored in ultrapure water at room temperature when not in use. The microengine preparation method provides a good reproducibility.

Catalase modification

The inner Au layer from the bilayer microtubes was functionalized with a mixed MUA/MCH monolayer. A solution of 2.5 mM MUA and 7.5 mM MCH was prepared in ethanol. The microengines were incubated in the solution overnight. After rinsing the tubes with ethanol for 5 min, they were transferred to an Eppendorf vial containing a 200 μl PBS buffer (pH 5.5)

solution with the coupling agents 1-Ethyl-3-[3-dimethylaminopropyl] carbodiimide hydrochloride (EDC), N-hydroxylsulfosuccinimide (Sulfo-NHS) at 0.4 M and 0.1 M respectively, and the enzyme catalase (2 mg mL^{-1}). This incubation was carried out 7 hours at 37ºC and thereafter rinsed with PBS with a pH of 7.4 and SDS 0.05 wt % for 15 min at each step. Finally the microengines were washed repeatedly by centrifugation at 6000 rpm for 3 min with water for three times to remove extra catalase in solution before testing.

3.2.3 Results and discussions

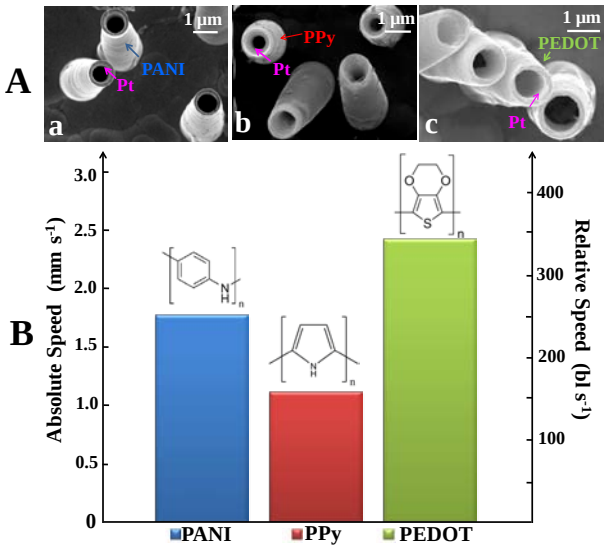

Figure 3.2.1 A) SEM images of polymer-based template growth of the bilayer microtubes: a) PANI/Pt; b) PPy/Pt; c) PEDOT/Pt. B) The absolute and relative speeds of the polymer-based bilayer microtubes in a 5% H_2O_2 solution containing 2.67% sodium cholate.

Various polymer-based bilayer microtubes have been successfully fabricated in this study using template-electrodeposition method in connection to a Cyclopore polycarbonate membrane, with conical-shaped micropores. The nucleation and growth of conducting polymer microtubes involve electrostatic and solvophobic interactions between the polymers and pore wall.[34] Poly(3,4-ethylenedioxythiophene) (PEDOT), polyaniline (PANI) and polypyrrole (PPy) were selected for the present microengine work owing to their inherent chemical stability.[38] As expected and will be illustrated below, the thickness (and hence opening side) and the length of

the polymer-based microtubes depends on the synthesis conditions. The most favorable electrochemical growth conditions of PEDOT, PANI and PPy (described below) were optimized for their microtubes bilayer structures. Figure 3.2.1A displays the SEM images of the three different template-prepared bilayer microtubes under the optimized conditions: PANI/Pt (a), PPy/Pt (b) and PEDOT/Pt (c). In general, such bilayer microtubes were prepared following the previously described method.[22] PPy and PEDOT microtubes were electrosynthesized at +0.8 V using 7.5 mM KNO_3 as the electrolyte, and charges of 0.8 C and 0.06 C, respectively; PANI microtube was prepared using the same potential in a plating solution containing 0.1 M H_2SO_4, 0.5 M Na_2SO_4 and 0.1 M aniline for a charge of 0.02 C. Subsequently, the inner Pt layer was deposited galvanostatically at -2 mA for 600 s from a commercial platinum plating solution. The presence of HSO_4^- anion, acidic media, and sodium cations provides a high PANI polymerization rate, conductivity and electroactivity.[38,39] The electropolymerization of PPy and PEDOT commonly involves plating solutions containing the sodium dodecyl sulfate (SDS) surfactant for improving the monomer solubility in aqueous solution and lowering the oxidation potential[40,41] resulting in improved the opening size and surface morphology of the microtubes. The images of Figure 3.2.1, involving these 3 different monomers, clearly indicate that the template electrodeposition method leads to bilayer microtubes with uniform morphology. The resulting bilayer PANI/Pt (a), PPy/Pt (b) and PEDOT/Pt (c) microtubes (~7 μm long) are characterized with different front opening diameters of 0.8 μm, 0.6 μm and 1 μm respectively. Such different openings can be attributed to differences in the sizes of the polymer chains, electropolymerization rate and in the packing patterns of the different polymers.[42] The morphological features of the polymer films have a profound effect upon their electrochemical and electrochromic properties.[43] Comparing the formation of PEDOT, PANI and PPy structures, it can be observed that the PANI and PEDOT tubules have larger opening and do not close up, even after a long polymerization time. In contrast, the PPy tubules usually have a thicker layer, and form wire or fibers after long

polymerization time, filling the pores completely.[44] EDX mapping analysis, shown in Figure 3.2.2, confirmed the presence of Pt, N of the PPy/Pt (a) and Pt, S of the PEDOT/Pt (b), and the successful growth of the bilayer microtubes.

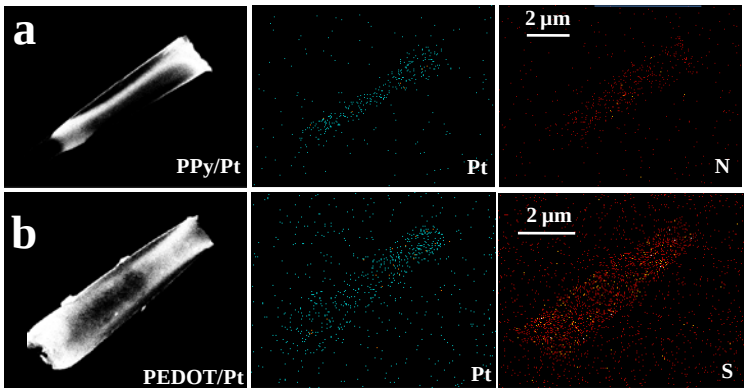

Figure 3.2.2 The EDX analysis results of the polymer based bilayer microtubes: a) PEDOT/Pt; b) PPy/Pt.

Figure 3.2.1B compares the speeds of the various polymer-based microengines (in the presence of 5% hydrogen peroxide along with 2.67% (w/v) sodium cholate as surfactant). The PPy/Pt, PEDOT/Pt and PANI/Pt bilayer microengines display ultrafast speeds of 1120, 2400 and 1700 µm s^{-1} (corresponding to 160, 340 and 240 body lengths s^{-1}), respectively. Such differences in the speed are attributed primarily to the size of the opening diameter.[22,45] Considering the tubular microengine as a cylinder microrod (since the fluid cannot freely flow through microengine because of the oxygen bubbles), the fluid drag coefficient is expected to be the same for the microengines with the same outer diameter and different inner opening diameters;[22,45] however, the larger inner opening is coupled with a larger catalytic surface area, hence facilitating the bubble evolution and leading to a faster speed.[45] Additional experiments using a higher (10%) peroxide level showed that the PEDOT/Pt microengines can achieve an ultrafast average speed of 3350 µm s^{-1} (around 480 body lengths s^{-1}). As will be illustrated below, even further acceleration and a new speed record (of 1400 body lengths s^{-1}) can be achieved by operating these PEDOT/Pt microengines at a physiological temperature. It should also be pointed out that the preparation of

the PEDOT-based bilayer microtubes provides more reproducible yields and consistent batch-to-batch morphology and length, especially compared to fast growing PANI-based tubular microengines (involving a very rapid aniline electropolymerization).[22] Overall, PEDOT-based miccrobots provide the most favorable preparation and propulsion performance.

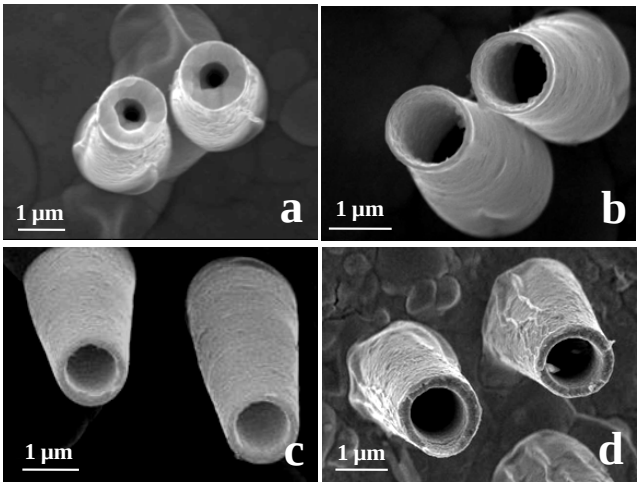

Figure 3.2.3 The SEM images of PEDOT based bilayer microtube prepared under different conditions: a) 100 mM EDOT and 100 mM SDS; b) 15 mM EDOT and 100 mM sodium dodecyl sulfate; c) 15 mM EDOT and 2 mM SDS; d) 15 mM EDOT alone. Supporting electrolyte (during the electropolymerization): 7.5 mM KNO_3.

Scanning electron microscope (SEM) images show useful insights into the morphological features of PEDOT/Pt tubular microengines, grown in the different synthesis media. As indicated from the images of Figure 3.2.3(a-d), the monomer concentration and the presence of surfactant in the electropolymerization media have a profound effect upon the morphology and opening diameter of the resulting polymer microtubes. The effect of the monomer concentration was investigated by comparing morphology of the microengines in electrochemical template systems using 15 and 100 mM EDOT (in the presence of 100 mM SDS). The higher monomer concentration led to less uniform, rougher tubular structures with thicker walls (i.e., smaller opening pore) (Figure 3.2.3, a *vs.* b). It can be concluded that solvophobic and electrostatic interactions between the pore wall of membrane and reacting species can result in the preferential nucleation and growth of PEDOT onto the pores of the membrane wall, producing microtube

structure with a thicker polymer layer.[46] PEDOT/Pt microtubes prepared using 15 mM EDOT solution are characterized with a smoother more regular surface morphology, along with thinner walls. Such improved microtube structures containing a wider opening pore, lead to faster speed compared with PEDOT/Pt microengines prepared in presence of higher monomer concentration.

The surfactant effect was also examined for the preparation of PEDOT/Pt microengines using the same monomer concentration. Due to the low solubility of EDOT in water, the electropolymerization of EDOT was usually carried out in organic solvents (which may deteriorate the polycarbonate membrane pores).[47] Recently, the surfactants were used to control the morphology of the PEDOT film with electrochemical methods in an aqueous solution.[48] Herein, the surfactant effect upon the PEDOT/Pt microtube structures was investigated using plating solutions containing different surfactant concentrations (2 and 100 mM) and 15 mM of the EDOT monomer. The film thickness increased (from 150 to 100 nm) upon decreasing the surfactant concentrations from 100 to 2 mM (Figure 3.2.3(b) and (c)). Without the surfactant, the polymerization created a non-uniform and thicker polymer layer, displayed in Figure 3.2.3(d), leading to a smaller inner diameter which greatly hinders the microengine propulsion. Most favorable surface morphology was obtained by the polymerization using a low monomer concentration in the presence of proper surfactant (100 mM). The improvement of the surface quality in presence of surfactant like long-chain alkyl sulfonate groups can be mainly attributed to the decreased oxidation potential of the monomer under the same conditions.[49] Furthermore, the addition of surfactant has improved both the solubility of the monomer and the morphological properties of the polymer because of its dopant anion role in the polymer chain structure.[50,51] Thus, the surfactant/monomer ratio is also an important parameter for controlling the surface morphology and physical properties in PEDOT/Pt microtubes for diverse applications.

Another variable that had an effect on the yield, conductivity and morphology of the polymer microtube structure and growth was the nature of the electrolyte. For example, we

compared the growth of PEDOT/Pt microtubes in the presence of lithium perchlorate ($LiClO_4$) and potassium nitrate (KNO_3) in the same aqueous media. The polymer growth in $LiClO_4$ was not well repeatable under similar polymerization conditions yielding different lengths (not shown). In contrast, KNO_3 offered a greatly improved surface morphology, stability and thickness in the PEDOT/Pt microtube structures. The advantage of KNO_3 comes from the fact that the charges were consumed more rapidly in the presence of nitrate ions than with chlorate ions, indicating the faster deposition of the PEDOT doped with nitrate ions.[39] In the presence of KNO_3, a homogenous polymer (PEDOT) surface was deposited onto membrane template in a short polymerization time.

The use of membranes with different pore diameters allowed for increased control on the size of the mirotubes. For example, with a membrane with a 1 μm pore size, one can obtain smaller bots that are half the size of usual microtubes. Figure 3.2.4 shows a single (a) and multiple (b) smaller PEDOT/Pt microtubes with lengths of only 4 μm and opening diameters of less than 800 nm (half the body length of the normal template based bilayer microengines). The experiments show that the smaller microengines can also achieve a very high speed. For example, they can move at a fast speed of 325 μm s^{-1} in a 4% H_2O_2 (containing 5% sodium cholate), corresponding to a relative speed of over 80 body lengths s^{-1}.

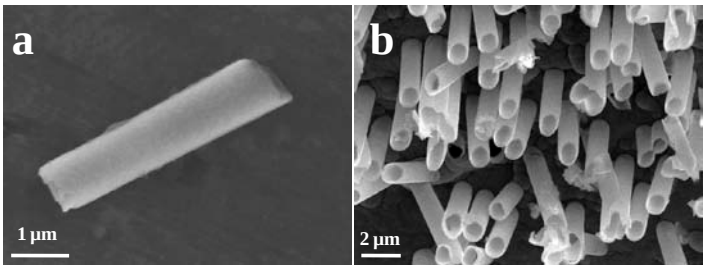

Figure 3.2.4 The PEDOT/Pt microtube with smaller size: 4 μm in length, outer 1 μm vs. 1.1 μm, inner diameter 700-800 nm.

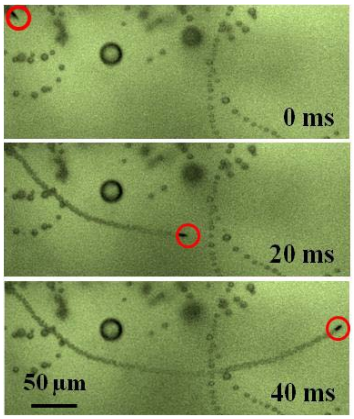

Figure 3.2.5 The ultrafast propulsion (over 1400 body lengths s^{-1}) of the PEDOT/Pt microengine in 10% H_2O_2 and 5% sodium cholate surfactant in physiological temperature of 37ºC.

Previous studies have shown that temperature has a profound influence on the speed of catalytic micro/nanomotors through its effect on the electrochemical reactivity of hydrogen peroxide decomposition.[52,53] A similar phenomenon was observed here for the new polymer-based microtubes. At a physiological temperature of 37 °C, such template-based PEDOT/Pt microengines can achieve an ultrafast speed of over 1400 body lengths s^{-1} (10 mm s^{-1} in absolute speed), compared to around 500 body lengths s^{-1} in room temperature. Such speed represents the fastest relative speed of any artificial nanomotors reported up to date.[54] Figure 3.2.5 shows the time lapse images of one superfast PEDOT/Pt microengine at 37 °C over a 40 ms period. The microengine travels at a speed of around 10 mm s^{-1} within 10% H_2O_2/5% sodium cholate solution, which corresponds to around 1400 body lengths s^{-1}, considering its 7 µm body length. Under the same conditions, PANI/Pt based microengines can also achieve a superfast speed of over 730 body lengths s^{-1} (compared to 350 body lengths s^{-1} in room temperature). We observed that besides increasing temperature, adding hydrazine can also lead to a dramatic increase in the speed of catalytic tubular microengines, analogous to the hydrazine effect upon the speed of catalytic nanowire motors.[55] An ultrafast propulsion, at around 5 mm s^{-1} at room temperature - corresponding to around 700 body lengths s^{-1} - of a PANI/Pt microengine in a 10% H_2O_2 solution spiked with only 0.25% hydrazine was observed. In fact, the propulsion of the platinum-based

microengines using hydrazine fuel alone (without any hydrogen peroxide) has also been observed along with the corresponding N_2 bubbles generation;[56] yet, such propulsion is short-lived and usually lasts only 1-2 seconds.

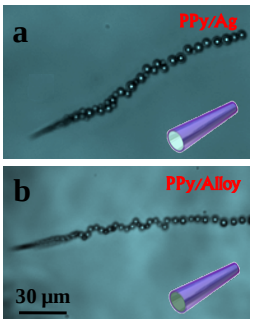

Figure 3.2.6 Propulsion images of PPy-based tubular microengine a) PPy/Ag in 15% H_2O_2 and 5% sodium cholate; b) PPy/Pt-Ni alloy in 10% H_2O_2 and 5% sodium cholate.

While platinum is commonly used as the inner catalytic layer of tubular microengines, we examined the potential use of various alternative catalytic metals. For example, silver is another good catalyst for hydrogen peroxide decomposition, and can therefore be used as the inner catalytic layer of the microengines. Figure 3.2.6A shows that a PPy/Ag bilayer microengine moving efficiently at a speed of 500 µm s^{-1} in the presence of 15% hydrogen peroxide and 3% sodium cholate surfactant. Although the speed of the PPy/Ag microengine is obviously slower than of the platinum-based polymer ones (under same conditions), it is still very fast considering the relative speed of more than 70 body length s^{-1}, compared to common rolled-up platinum-based microengines (50 body lengths s^{-1} in 15% H_2O_2).[17, 18] Although the silver layer can be partially dissolved in hydrogen peroxide,[57, 58] ultrafast propulsion was observed for over 40 min without considerable speed variations.

Magnetic guidance is essential for the many practical applications of the catalytic micro/nanomotors. As reported before, trilayer microengines with the addition of an inner nickel layer can provide magnetically-guided propulsion, but their preparation requires a 3-step electrodeposition process.[22] Here we illustrate that a simplified Pt/Ni alloy inner layer, instead of

separate platinum and nickel layers, can provide simultaneously both the catalytic activity and desired magnetic navigation. Figure 3.2.6B shows a time lapse image of the propulsion of a PPy/Pt-Ni-alloy microengine in a 10% hydrogen peroxide solution. The PPy/alloy microengine displays efficient propulsion at a high speed of 470 μm s^{-1} (67 body lengths s^{-1}). However, this is obviously slower than trilayer microengines due to the lower catalytic surface area.

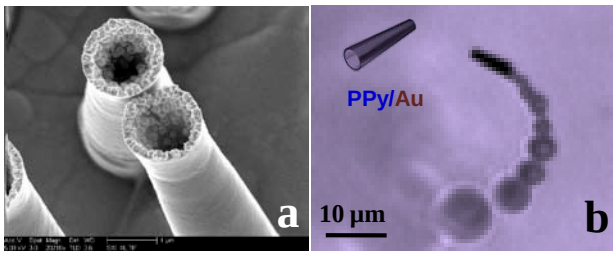

Figure 3.2.7 a) SEM of PPy/Au_{rough} bilayer micro tubular microengine. b) Time-lapse image of biocatalytic propulsion of PPy/Au-catalase in 0.5% H_2O_2 and 2% sodium cholate.

Biocatalytic layers based on immobilized catalase have can serve as attractive alternatives to electrocatalytic metals for propelling peroxide-driven nano/microscale motors.[59,60] Sanchez et al. showed that catalase-modified rolled-up catalytic microjets can move in 1.5% hydrogen peroxide at a speed of 10 body lengths s^{-1}.[60] Similarly, a gold inner layer electrodeposited inside the outer polymeric tube layer can be used to immobilize the catalase biocatalyst. Template electrodeposition of the polymer-Au microtube results in a very rough surface (shown in Figure 3.2.7A) desired for immobilizing large amounts of the enzyme. As illustrated in Figure 3.2.7B, the resulting biocatalytic bilayer microengines propel favorably in the presence of a low peroxide level (0.5% H_2O_2), at a speed of 8 body lengths s^{-1}. PPy/Au microtubes (without catalase modification) displayed no directed motion under the same conditions (not shown).

We also examined the possible replacement of the catalytic Pt layer with inner palladium (Pd) or iridium (Ir) catalytic layers. Unfortunately, it was very difficult to deposit defined

palladium or iridium microtubes within the polymer layer. Unlike Pt, Ag or Au, Pd and Ir usually grow on the top of the tube and block the pore, thus eliminating the tubular bubble propulsion.

Diverse biological applications may require an outer gold layer owing to its facile functionalization and excellent biocompatibility.[9,10] Here, we demonstrate the template synthesis of Au/Pt bilayer microengines coupling these advantages of an outer Au layer with the effective catalytic activity of the inner Pt layer. The Au outer layer was electrodeposited from a Au plating solution containing 0.1 M $NaNO_3$ using DMSO as an electrolyte (without addition of any other surfactants),[61] followed by a subsequent deposition of an inner platinum layer. However, we can see clearly that the resulting gold outer surface is relatively rough. This can be attributed to the interaction of DMSO and the polycarbonate membrane. DMSO slowly dissolves the polycarbonate membranes, making the pores shrink as the microtube is growing. This resulted in a lower yield of viable microtubes and a non-uniform, rough outer layer. As shown in Figure 2.2.8, such Au/Pt bimetallic microengines propel very rapidly at a speed of 1.5 mm s^{-1} in a 10% H_2O_2 (2.67% sodium cholate) solution. An improved method for depositing the gold microtube layer should lead to a better microengine performance and yield.

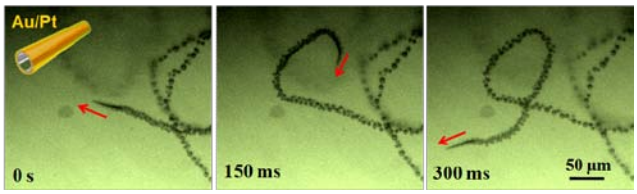

Figure 3.2.8 Ultrafast propulsion of Au/Pt bimetallic tubular microengine in 5% H_2O_2 and 2% sodium cholate.

3.2.4 Conclusions

In conclusion, we evaluated and characterized template-synthesized tubular microengines containing different materials, including various conducting polymers and metals. The critical comparison of different materials and plating conditions used for microengine synthesis had led to the considerate difference on the propulsion and capability for various applications. Template

electrodeposition has been shown to be particularly attractive for preparing such new polymer-based catalytic microengines. The influence of the preparation conditions, particularly the electropolymerization conditions, has shown to have a profound effect upon the morphology and propulsion behavior. The new insights into the preparation and composition of template-prepared tubular microengines have facilitated the rational design of high-performance PEDOT/Pt bilayer microengines with a record-breaking speed of over 1400 body lengths per second at *37ºC*. The remarkable speed of the new microengines also reflects their high towing capacity, as desired for diverse biomedical applications. Lower speeds are expected in biological media owing to the the increased viscosity. The morphology of the conducting polymer microtube is greatly influenced by the nature and concentration of monomer and of the supporting electrolyte, as well as by the surfactant present. The inherent advantages of easy fabrication of conducting polymer/metal microtubes make them attractive candidates to advanced sensor systems to diverse chemicals such as biomaterials, hydrogen peroxide or methanol fuel cell systems. Moreover, conducting polymer/metal microtubes are inexpensive and versatile because of their properties can be readily modified by the use of a wide range of molecules that can be entrapped or used as dopants. Recently, the polymer microengine have been successfully used for bacteria isolation based on the lectin modifications.[62] Polymers with different functional groups (such as -OH or -COOH) can be chosen as the outer layer for different applications, hence facilitating different surface functionalization processes. These properties and advantages make the new polymer-based tubular microengines extremely attractive alternatives to current bimetallic microtube systems and hold considerable promise for diverse future applications.

3.3 Efficient propulsion in real world environments

3.3.1 Introduction

As we discussed the Chapter 3.1 and 3.2, catalytic microtube engines have been shown to be extremely useful for addressing the ionic-strength limitation of bimetal catalytic nanowire motors.[6,7] Such bubble-propelled microengines thus display efficient propulsion in salt-rich environments due to electrocatalytic decomposition of hydrogen peroxide fuel.[12,22] Early studies have also indicated facile motion of polymer-based micromotors or rolled up microjets in various diluted (3-4 fold diluted) real-life media.[8-10,62-65] However, recent reports claimed that the movement of bubble-propelled Cu-Pt microengines is greatly hindered in various diluted real samples, and even completely stopped in highly diluted serum or seawater.[66,67] Such observations may have profound implications upon the scope of future applications of microscale machines. The impeded movement in such samples has been attributed to high viscosity of these media and to co-existing molecules that passivate the catalytic Pt surface.[66,67] Since bubble-propelled microengines can be prepared by different fabrication methods and using different materials,[1] it is essential to carefully examine this important issue, in connection to other common protocols for fabricating bubble-propelled microtube engines, and to gain understanding of the role of the motor design and composition upon the propulsion efficiency in different media.

In this section, we wish to demonstrate that polymer-Pt microtube engines display efficient propulsion even in undiluted seawater and serum matrices, and to examine the effect of various undiluted (and slightly diluted) real-life environments upon their movement. Template electrodeposition has been shown to be particularly attractive for preparing polymer-based catalytic microengines (Figure 3.4.1a).[22,68] Such polymer-based microengines have been shown recently to display a record-breaking speed of over 1400 body lengths/s.[54,68] The preparation conditions, particularly the electropolymerization parameters, have been shown to have a

profound effect upon the morphology and propulsion behavior of polymer-based microengines.[21] Such motor morphology and performance are thus greatly influenced by the nature and concentration of monomer and of the supporting electrolyte, as well as by the surfactant present. Such preparation conditions can be used to tailor and optimize the composition and geometry of the microengine (including its two openings), and hence to tune the propulsion efficiency. Due to their remarkable intrinsic speed and force, such polymer-based microengines still display a highly efficient (although diminished) propulsion behavior in raw viscous real-life media, reflecting that the Reynolds number is a measure of the ratio of inertial forces to viscous forces.

To examine the effect of various matrices upon the movement of catalytic motors we rely here on the dilution of a commercial 50% hydrogen peroxide that allows convenient preparation and evaluation of 90% (v/v) real samples, namely minimal sample dilution associated with the fuel addition (compared to early studies involving a 30% peroxide solution). In the following sections we will illustrate that the remarkably high power and speed of polymer-based microtube engines lead to effective propulsion in a wide range of fuel-enhanced untreated undiluted environmental, biological and beverage samples (with the exception of whole blood), and discuss the influence of such real-life matrices upon the observed movement. The new findings and discussion should guide the realization of practical micromotor applications in diverse real-life environments and indicate that the movement of different bubble-propelled microengines (with different geometries and compositions) may be affected differently by real-life samples.

3.3.2 Experimental section

The PEDOT/Pt microengines were prepared using the same electrodeposition protocol as Chapter 3.2.2.[22,68] The microtubes were electropolymerized at +0.80 V for a charge of 0.06 C from a plating solution containing 15 mM EDOT, 7.5 mM KNO_3 and 100 mM sodium dodecyl sulfate (SDS); subsequently, the inner Pt tube was deposited galvanostatically at -2 mA for 600 s from a commercial platinum plating solution (Platinum RTP; Technic Inc, Anaheim, CA).

Aqueous hydrogen peroxide solutions (Catalog No. 516813 and 216763, Sigma-Aldrich, St Louis, MO) with concentrations ranging were used as chemical fuels (1-5% (w/v)), containing 3% (w/v) sodium dodecyl sulfate (Sigma-Aldrich). Human serum (from human male AB plasma), human plasma, whole human blood, fresh red blood cells and human peripheral blood mononuclear cells (PBMC) were purchased from Sigma-Aldrich, Sigma-Aldrich, Bioreclamation, ZenBio and Precision Bioservices, respectively. Urine samples were collected from a healthy volunteer. Seawater samples were collected at Torrey Pines Beach (La Jolla, CA). River and lake water samples were collected from Merced River and Mirror Lake (CA) respectively. A 'Ocean Spray' 100% Apple Juice was used as the juice sample. Deionized water (18.2 MΩ·cm) and tap water were from the laboratory in UC San Diego.

3.3.3 Results and discussions

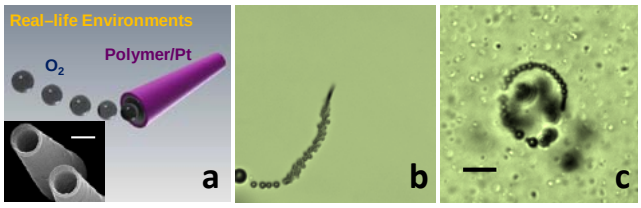

Figure 3.3.1 Polymer-based microengines in real-life environments. (a) Schematic of bubble-propelled polymer-based microengines. Inset: SEM image of the top view of the PEDOT/Pt microtubes. Scale bar, 1 µm. (b, c) Microscope images of the propulsion of polymer-based microengines in 90% (v/v) seawater (b) and 90% (v/v) human serum (c) containing 3% H_2O_2. Scale bar, 20 µm.

To evaluate and demonstrate the propulsion of polymer-based microengines in different environments, we investigated first their movement in fuel-enhanced raw undiluted human serum and seawater samples (with the exception of the fuel addition that resulted in 90% matrix). Figure 3.3.1 illustrates the highly efficient movement of the poly(3,4-ethylenedioxythiophene) (PEDOT)/Pt microtubes engines in both matrices (in the presence of 3% H_2O_2). The microengines are self-propelled at very high speeds of 360±83 µm/s (~50 body lengths/s) and 125±13.5 µm/s (~17 body lengths/s) in seawater and human serum, respectively. The trajectory

followed by the micromotors is not altered by the environment. These speeds are lower than that observed in deionized water (980 μm/s, *i.e.*, 140 body lengths/s). Yet, unlike Cu-Pt microengines that completely stopped their movement even in 50% of serum or 10% seawater samples,[66,67] the polymer-based microengines retain an attractive propulsion behavior in undiluted seawater and serum samples, indicating promise for diverse practical environmental and biomedical applications, such as oil remediation, toxicity assessment or target isolation. Note also from the SEM image of Figure 3.3.1a, the well defined geometry and large opening of the microtube engine are essential for efficient propulsion in diverse media.

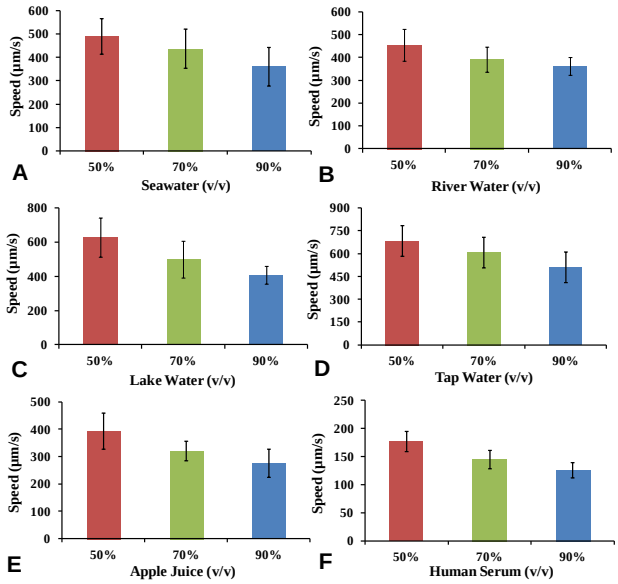

Figure 3.3.2 Propulsion of the polymer-based microengines in different real-life media: A) seawater; B) river water; C) lake water; D) tap water; E) apple juice; F) human serum, containing 3% H_2O_2. Error bars show standard deviations of the measured speed (n=50).

Figure 3.3.2 and Table 3.1 display the dependence of the speed of the polymer-based microengines upon the partial dilution of six different untreated real samples (sample content, 50-90%(v/v)), including seawater (A), river water (B), lake water (C), tap water (D), apple juice (E) and serum (F), along with 3% H_2O_2 fuel. In general, while the microengines display efficient movement in all these six samples, their speed decreases gradually (by 10~35 %) upon raising the sample content between 50 to 90%. As will be discussed later, the exact nature and complexity of

the sample, strongly affect the extent of these speed diminution. For example, the polymer-based microengines swim efficiently in untreated 90% seawater (*i.e.*, minimal dilution due to the fuel addition), at a fast speed of 360 μm/s despite the presence of ~0.5M NaCl; an even faster speed of 489 μm/s was observed when the sample is diluted 1:1 in deionized water. The favorable propulsion in saline environments holds considerable promise towards diverse potential applications of these microengines.[64] In contrast, analogous copper-based micromotors were reported recently to move at a speed of 63 μm/s in a 6% (v/v) seawater sample (4-fold slower compared to that in deionized water) and to completely stop their movement in a 10% seawater sample.[67] The data of Figure 3.3.1 and Figure 3.3.2 are in agreement with the high speed reported earlier for polyaniline/Pt microengines in highly saline environments, *i.e.* even in a 3 M NaCl solution in the presence of only 1.5% H_2O_2.[22] Increased viscosity account for the reduced speed of microengines in seawater (compared to deionized water).

Table 3.1 Speed of the micromotors in raw and diluted real-life environments (containing 3% hydrogen peroxide). Errors show standard deviations of the measured speed (n=50).

Real-life Media	Speed in 50% (v/v), μm/s	Speed in 70% (v/v), μm/s	Speed in 90% (v/v), μm/s
Deionized water	980±180		
Seawater	489±76	437±83	360±83
River Water	455±70	392±54	362±39
Lake Water	627±114	499±109	407±53
Tap Water	683±104	605±102	510±76
Apple Juice	394±66	321±36	276±51
Human Serum	177±17.5	144±16.3	125±13.5

Despite their microscale dimensions, the polymer-based microengines are moving effectively in a viscous fluid with a low Reynolds number. Such polymer-based microengines are reported to achieve a remarkable record-breaking speeds[54] which can be used to overcome viscosity limitations in real-life environments. Such ultrafast speed, and hence a remarkably high

propulsion force, are essential addressing the viscosity effect of real-life environments, reflecting that the Reynolds number is a measure of the ratio of inertial forces to viscous forces.

Assuming the microengine as a cylinder microrod, the drag force (equal to propulsion force) by using the Stokes' drag theory can be expressed as:[69]

$$F_d = \frac{2\pi\mu LU}{\ln(L/a) - 1/2}$$

where F_d is the drag force, U is the speed in the microengine, μ is the fluid dynamic viscosity, and L and a are the length and radius of the microtubes, respectively. Based on this equation (and assuming a constant drag force), it is clear that the speed of the microengines will decrease upon increasing the viscosity of the media. Yet, due to their remarkable intrinsic force and speed, such microengines still display a highly efficient propulsion behavior (e.g., a speed of 360 μm/s in 90% (v/v) seawater samples), despite of their diminished speed in raw and complex samples (vs. deionized water).

Envisioning practical environmental applications of the self-propelled micromotors, we examined their motion in untreated lake and river water samples. As illustrated in Figure 3.3.2B and Figure 3.3.2C, the PEDOT/Pt micromotors also display efficient propulsion in both natural water samples. For example, using 90% lake and river water matrices the micromotors move at speeds of 407±53 and 362±39, respectively; even higher speeds of 627±114 and 455±70 μm/s are observed in 50% of these natural water samples, respectively. While the speed of the micromotors decreases upon increasing the content of these water samples from 50 to 90% (reflecting the increased matrix complexity), the polymer/Pt microengines travel at very high speeds (exceeding 50 body-lengths/s) even in the fuel-enhanced 90% river and lake water samples.

To observe the effect of even more complex matrices and to expand the scope of polymer-based micromachines we subsequently investigated their movement in common tap water, beverage and biological samples (Figure 3.3.2D-F). For instance, the microengines

displayed high speeds of 510±76 and 683±104 μm/s in 90% and 50% (v/v) tap water, respectively. Apparently, the sample composition can affect the micromotor motion even when using tap water samples, where the higher ionic levels lead to a 25% decrease in the motors speed. A slightly higher matrix effect is observed using apple juice, with a 30% slower speed (276±51 vs. 394±66 μm/s) is observed upon raising the juice content from 50 to in 90 % (v/v). The speed observed in 90% apple juice sample is around 25% slower than that obtained in seawater at the same proportion (90%). This can be attributed primarily to the presence of complex juice constituents, including carbohydrates (~11% wt., such as sugars and ascorbic acid), inorganic ions and proteins, which results in higher viscosity and a slower micromotor speed. To further evaluate this effect, we tested the effect of a highly viscous human serum medium, containing elevated levels of dissolved proteins (without fibrinogen) and additional biomolecules (with a high viscosity of 3 cP).[70] As expected for such highly viscous medium, the speed of the micromotors decreased sharply down to 125 ± 13.5 μm/s in 90% human serum (i.e., to ~13% of the speed observed in deionized water); a slightly higher speed of 177 ± 17.5 (i.e., ~20% of the speed in deionized water) was observed upon lowering the serum content to 50% (v/v).

To better understand the performance of micromotors motion in various real-world media, their normalized speed and fraction of moving micromotors were examined upon increasing the content of different matrices (over the 50 to 90% range). Interestingly, the movement of the micromotors in all real-life samples followed a similar trend (Figure 3.3.3A). However, the normalized speeds in tap water and seawater are slightly different from those observed in apple juice and human serum. For example, the relative speed of the microengines in tap and sea water media was reduced by only ~20% upon raising the media content from 50 to 90%. Such lowered speed reflects the greatly higher ionic content of solutions with higher content of the matrix in the aqueous sample, *i.e.* 0.5 M NaCl in 90% sea water. A slightly larger speed diminution of 25% is observed upon increasing the content of the apple juice and human serum matrices between 50 to

90%, reflecting the higher complexity of these samples. For instance, serum plasma contains dissolved proteins, glucose, clotting factors, hormones and a high content on electrolytes, while the apple juice contains various carbohydrates, proteins and electrolytes. The number of active microengines, *i.e.* the microengines that move in the presence of these matrices, is consistent in seawater, lake water, river water, tap water, and apple juice (Figure 3.3.3B). For example, 100% of microengines are moving at a high speed of over 70 body lengths per second in 90% tap water, while over 96% of them navigate at fast speed in 90% seawater, lake water, river water and apple juice samples. In contrast, only a small fraction of Cu-Pt microjets reported recently to display movement in 70% (v/v) real-world environments (e.g., ~20% of the motors in 70% (v/v) tap water, rain water, or lake water and 0% in 10% (v/v) seawater).[67] However, the trend in human serum is greatly different, with 80% of the polymer-based micromotors being active in 50% human serum while only 30% of them display movement in the 90% serum sample. The significant reduction in the motors speed in serum samples reflects their high viscosity,[70] and is consistent with the behavior observed by previous studies.[9,10,63,65]

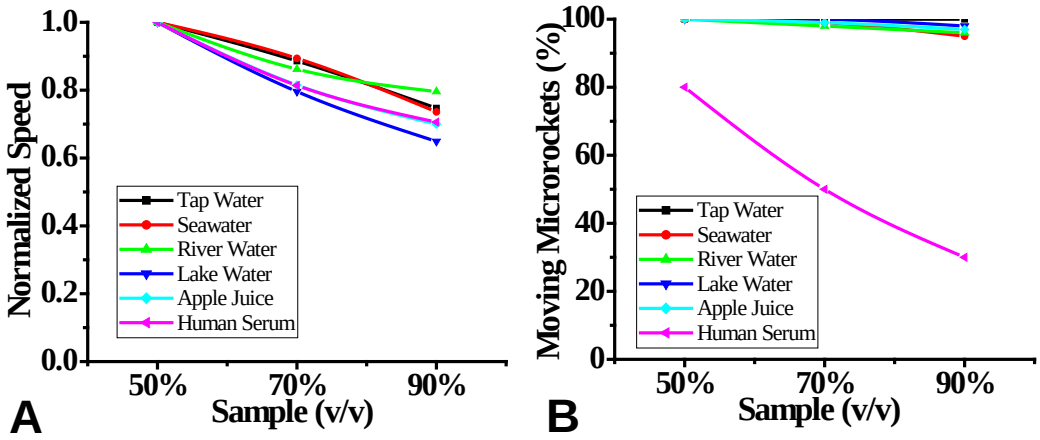

Figure 3.3.3 A) Normalized speed of the polymer-based microengines in different media (with sample v/v ranging from 50 to 90%). B) Ratio of the moving micromotors in different real-world environments.

Overall, these results clearly indicate that although the real samples matrix has a significant effect upon the microengine velocity (with higher speed diminutions upon increasing

the complexity of the matrix increase), polymer-based microtube engines can move efficiently at relatively high speeds in a broad spectrum of fluids. We attribute the favorable propulsion of polymer-based microtube engines in diverse raw real samples, compared to the greatly hindered motion reported recently for Cu-Pt microjets,[66,67] to their optimal geometry, well defined shape, large opening and lighter weight. Such polymer-based micromotors consist of a thin polymeric outer layer and a thin platinum inner layer (100 nm thick for each layer) and have relatively large openings in both sides (over 1.2 μm in the smaller opening), as clearly indicated in the inset SEM image of Figure 3.3.1a. As was illustrated earlier,[68] the openings of the microtubes have a profound effect upon their propulsion performance, with larger openings leading to a faster movement. As a result, polymer micromotors display a very large propulsion force and can swim well even in diverse fuel-enhanced raw real-world environments.

While displaying an attractive propulsion behavior in a variety of raw media, no directional movement was observed using the polymer-based microengines in whole blood samples (25-90% (v/v)). Due to the presence of the blood catalase, large oxygen bubbles were generated violently over the entire whole blood sample upon adding the hydrogen peroxide fuel, while no microbubbles are expelled from the inner catalytic layer of the microtubes. The peroxidase-like activity of hemoglobin and biofouling of the catalytic Pt surface may also contribute to the hindered movement in blood samples. The propulsion of the microengines was also tested in solutions of fresh red-blood cells (diluted 100-fold with 1X PBS buffer saline solution (pH 7.2)) and of 25% (v/v) human peripheral blood mononuclear cells (PBMC). We observed that the microengines displayed clear translational propulsion in these diluted samples. The microengine can be self-propelled in a 25% (v/v) diluted PBMC solution (containing 3% H_2O_2) at a speed of 47 μm/s. However, the human cells lyse (burst open) rapidly due to the surfactant addition (SDS, sodium cholate or Triton X-100), which represents a major challenge for practical applications for these microengines in human blood. A greatly hindered motion was

observed also in undiluted plasma samples, which reflects the high level of fibrinogen in plasma samples. The performance of the microengines in human saliva is similar as that observed in human serum.[10] Apparently, the intrinsic peroxidase (lactoperoxidase) activity of saliva samples has no major effect upon the locomotion in this medium. In addition, the propulsion of the polymer-based microengines is greatly hindered in undiluted human urine. Only a small fraction of the microengines displays net movement in 90% (v/v) human urine, reflecting the influence of the high organic and inorganic contents, including urea, uric acid, sugars and proteins. Such greatly inhibited propulsion can be attributed to increased viscosity, hindered catalytic activity (due to adsorption onto the Pt surface), and to the formation of peroxide-urea complex. However, the majority of the microengines can still move at a high speed in untreated urine samples that are diluted at least 4 fold (*i.e.*, below 25% (v/v)).

The movement in diverse untreated real media can be realized even in the presence of low peroxide concentrations. Figure 3.3.4 examines the dependence of the speed of polymer-based microengines upon the level of the hydrogen peroxide in 90% seawater (A) and apple juice (B) samples. Using the raw seawater sample, containing just 1% H_2O_2, the microengine moves readily at a speed of 143 μm/s (corresponding to a relative speed of around 20 body lengths/s). Increasing the fuel concentration in the 90% seawater medium rapidly increases the microengine speed. For example, an ultrafast speed of over 490 μm/s, *i.e.*, approaching 70 body lengths/s, is obtained in 90% seawater containing 5% H_2O_2. A similar behavior is observed in the 90% apple juice matrix, with speeds of 140 μm/s and 680 μm/s in 1% and 5% H_2O_2, respectively. The inset microscope images in Figure 3.3.4A and Figure 3.3.4B, illustrate the effective propulsion of the microengines in the 1% H_2O_2–enhanced 90% seawater and apple juice samples, respectively. A clear tail of microbubbles, ejected from the one side of the microtubes, is observed. A frequency of ~75 Hz has been estimated. Considering the average bubble radius (~1.8 μm), the propulsion speed of such microengines in raw samples corresponds closely to the product of the bubble

radius and frequency, which is consistent with earlier reports,[7,22] indicating that the drag forces on the microengines and bubbles are comparable. Such attractive propulsion behavior of polymer-based microengines in the raw real-world samples, containing very low hydrogen peroxide levels, holds considerable promise for practical applications.

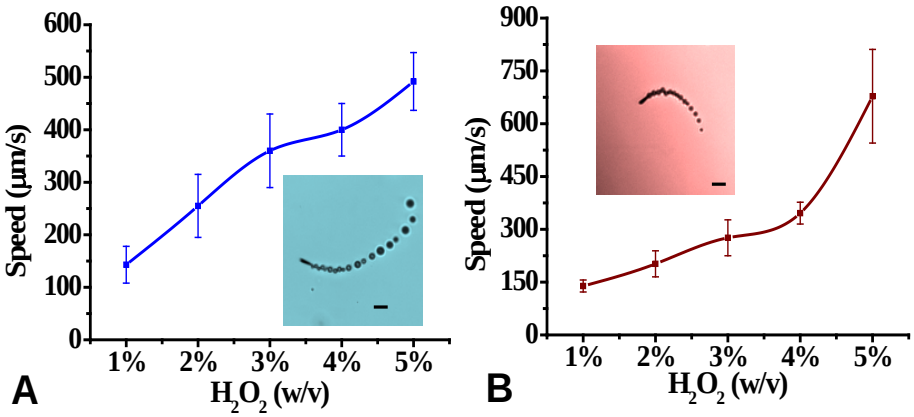

Figure 3.3.4 Dependence of the propulsion of the polymer-based microengines upon the fuel concentration (1~5% (w/v)) in 90% (v/v) seawater (A) and 90% (v/v) apple juice (B) samples. Insets, microscopic images illustrating the propulsion of the microengines in the 90% raw samples containing 1% H_2O_2. Scale bars, 10 μm.

3.3.4 Conclusions

In conclusion, we have demonstrated that template-prepared polymer-based catalytic microtube engines propel well in diverse real-life environments. Efficient bubble propulsion is thus illustrated even in 90% seawater, river and lake water, apple juice and serum samples. These finding confirm our preliminary data involving diluted real samples, and indicate that polymer-based microtube engines can readily operate in diverse real-life environments (with the exception of operation in whole blood) towards diverse new applications. Such movement reflects the large force of polymeric microengines, associated with their optimal geometry, openings, composition, and roughness of their inner Pt catalytic layer. Such favorable morphology and composition lead to a remarkably efficient propulsion behavior and hence to record-breaking speed.[21,22] Hence, such microengines can tolerate a diminished speed in raw viscous real-life media while still

display a highly efficient propulsion. Further improvements would require better understanding of the fundamental fluid flow physics that propel catalytic micro/nanomotors, and of the exact role of the motor design, composition and surface morphology, upon the propulsion efficiency in different media. The new findings, along with future developments, should open the door for new practical biomedical, environmental, biodefense and food applications of template-prepared polymer/Pt bilayer microengines in a wide range of diverse real-life matrices and should guide the successful realization of such applications. This study, along with recent literature reports,[66,67] indicate that real samples may exert different effects upon the propulsion of different bubble-propelled microtube engines, depending upon the specific design, composition and dimensions of such microengines, and yet such micromotors hold considerable promise for variety of real-life applications.

Chapter 3.1, in full, is a reprint of the material as it appears in Journal of the American Chemical Society, 2011, by Wei Gao, Sirilak Sattayasamitsathit, Jahir Orozco, Joseph Wang. Chapter 3.2, in full, is a reprint of the material as it appears in Nanoscale, 2012, by Wei Gao, Sirilak Sattayasamitsathit, Aysegul Uygun, Allen Pei, Adam Ponedal, Joseph Wang. Chapter 3.3, in full, is a reprint of the material as it appears in Nanoscale, 2013, by Wei Gao, Sirilak Sattayasamitsathit, Jahir Orozco, Joseph Wang. The dissertation author was the primary investigator and author of these papers.

3.4 References

1. Mirkovic, T.; Zacharia, N. S.; Scholes, G. D.; Ozin, G.A. *ACS Nano* **2010**, *4*, 1782-1789.

2. Wang, J. *ACS Nano* **2009**, *3*, 4-9.

3. Mallouk, T. E.; Sen, A. *Sci. Amer.* **2009**, *300*, 72-77.

4. Ebbens, S. J.; Howse, J. R. *Soft Matter* **2010**, *6*, 726–738.

5. Mei, Y. F.; Solovev, A. A.; Sanchez, S.; Schmidt, O. G. *Chem. Soc. Rev.*, **2011**, *40*, 2109.

6. Mei, Y. F.; Huang, G. S.; Solovev, A. A.; Urena, E. B.; Monch, I., Ding, F.; Reindl, T.; Fu, R. K. Y.; Chu, P. K.; Schmidt, O. G. *Adv. Mater.* **2008**, *20*, 4085–4090.

7. Solovev, A. A.; Mei, Y. F.; Urena, E. B.; Huang, G. S.; Schmidt, O. G. *Small* **2009**, *5*, 1688.

8. Sanchez, S.; Solovev, A. A.; Schulze, S.; Schmidt, O. G. *Chem. Commun.* **2011**, *47*, 698-700.

9. Balasubramanian, S.; Kagan, D.; Hu, C-M.; Campuzano, S.; Lobo-Castañon, M. J.; Lim, N.; Kang, D. Y.; Zimmerman, M.; Zhang, L.; Wang, J. *Angew. Chem. Int. Ed.* **2011**, *50*, 4161.

10. Kagan, D.; Campuzano, S.; Balasubramanian, S.; Kuralay, F.; Flechsig, G. U.; Wang, J. *Nano Lett.* **2011** *11*, 2083-2087.

11. Paxton, W. F.; Sundararajan, S.; Mallouk, T. E.; Sen, A. *Angew. Chem. Int. Ed.* **2006**, *45*, 5420-5429.

12. Manesh, K. M.; Yuan, R.; Clark, M.; Kagan, D.; Balasubramanian, S.; Wang, J. *ACS Nano*, **2010**, *4*, 1799-1804.

13. Hurst, S. J.; Payne, E. K.; Qin, L. D.; Mirkin, C. A. *Angew. Chem. Int. Ed.* **2006**, *45*, 2672-2692.

14. Parthasarathy, R. V.; Martin, C. R. *Chem. Mater.* **1994**, *6*, 1627-1632.

15. Lahav, M.; Weiss, E. A.; Xu, Q.; Whitesides, G. M. *Nano Lett.* **2006**, *6*, 2167-2171.

16. Guo, Y. G.; Hu, J. S.; Zhang, H. M.; Liang, H. P.; Wan, L. J.; Bai, C. L. *Adv. Mater.* **2005**, *17*, 746-750.

17. Chakarvarti, S. K.; Vetter, J. *Radiat. Meas.* **1998**, *29*, 149-159.

18. Li, N. C.; Yu, S. F.; Harrell, C. C.; Martin, C. R. *Anal. Chem.* **2004**, *76*, 2025-2030.

19. Sanchez, S.; Solovev, A. A.; Mei, Y. F.; Schmidt, O. G. *J. Am. Chem. Soc.*, **2010**, *132*, 13144-13145.

20. Solovev, A. A.; Sanchez, S.; Pumera, M.; Mei, Y. F.; Schmidt, O. G. *Adv. Funct. Mater.* **2010**, 20, 2430-2435.

21. Evans, S. A. G.; Elliott, J. M.; Andrews, L. M., Bartlett, P. N.; Doyle, P. J.; Denuault, G. *Anal. Chem.*, **2002**, *74*, 1322–1326.

22. Gao, W.; Sattayasamitsathit, S.; Orozco, J.; Wang, J. *J. Am. Chem. Soc.* **2011**, *133*, 11862.

23. Darmanin, T.; Guittard, F. *J. Am. Chem. Soc.* **2011**, *133*, 15627.

24. Long, Y. Z.; Li, M. M.; Gu, C.; Wan, M.; Duvail, J. L.; Liu, Z.; Fan, Z. *Prog. Polym. Sci.* **2011**, *36*, 1415.

25. Luo, S. C.; Ali, E. M.; Tansil, N. C.; Yu, H. H.; Gao, S.; Kantchev, E. A. B.; Ying, J. Y. *Langmuir* **2008**, *24*, 8071.

26. Guimard, N. K.; Gomez, N.; Schmidt, C. E. *Prog. Polym. Sci.* **2007**, *32*, 876.

27. Abidian, M. R.; Kim, D. H.; Martin, D. C. *Adv. Mater.* **2006**, *18*, 405.

28. Sekine, J.; Luo, S. C.; Wang, S.; Zhu, B.; Tseng, H. R.; Yu, H. H. *Adv. Mater.* **2011**, *23*, 4788.

29. Carpi, F.; Smela, E. *Biological Applications of Electroactive Polymer Actuators.* Wiley, 2009.

30. Pedrosa, V. A.; Luo, X.; Burdick, J.; Wang, J. *Small*, **2008**, *4*, 738.

31. Xia, L.; Wei, Z. X.; Wan, M. X. *J. Colloid Interface Sci.* **2010**, *341*, 1.

32. Pernaut, J. M.; Reynolds, J. R. *J. Phys. Chem. B* **2000**, *104*, 4080.

33. Cho, S. I.; Kwon, W. J.; Choi, S. J.; Kim, P.; Park, S. A.; Kim, J.; Son, S. J.; Xiao, R.; Kim, S. H.; Lee, S. B. *Adv. Mater.* **2005**, *17*, 171.

34. Cho, S. I.; Lee, S. B. *Acc. Chem. Res.*, **2008**, *41*, 699.

35. Cao, Y.; Andreatta, A.; Heeger, A. J.; Smith, P. *Polymer* **1989**, *30*, 2305.

36. Zhou, C.; Liu, Z.; Yan, Y.; Du, X.; Mai, Y. W.; Ringer, S. *Nanoscale Res. Lett.* **2011**, *6*, 364.

37. Bajpai, V.; He, P.; Dai, L. M. *Adv. Funct. Mater.* **2004**, *14*, 145.

38. Duic, L.; Mandic, Z. *J. Electroanal. Chem.* **1992**, *335*, 207.

39. Gospodinova, N.; Terlemezyan, L. *Prog. Polym. Sci.* **1998**, *23*, 1443.

40. Bazzaoui, E. A.; Aeiyach, S.; Lacaze, P. C. *Synth. Met.* **1996**, *83*, 159.

41. Sakmeche, N.; Aaron, J. J.; Fall, M.; Aeiyach, S.; Jouini, M.; Lacroix, J. C.; Lacaze, P. C. *Chem. Commun.* **1996**, 2723.

42. Liu, Z.; Zhang, X.; Poyraz, S.; Surwade, S. P.; Manohar, S. K. *J. Am. Chem. Soc.* **2010**, *132*, 13158.

43. Poverenov, E.; Li, M.; Bitler, A.; Bendikov, M. *Chem. Mater.* **2010**, *22*, 4019.

44. Jackowska, K.; Bieguński, A. T.; Tagowska, M. *J. Solid State Electrochem.* **2008**, *12*, 437.

45. Li, J. X.; Huang, G. S.; Ye, M. M.; Li, M. L.; Liu, R.; Mei, Y. F. *Nanoscale* **2011**, *3*, 5083.

46. Martin, C. R. *Science* **1994**, *266*, 1961.

47. Melato, A. I.; Viana, A. S.; Abrantes, L. M. *Electrochim. Acta* **2008**, *54*, 590.

48. Zhou, C. F.; Liu, Z. W.; Ringer, S.P. *Synth. Met.* **2010**, *160*, 1636.

49. Shimidzu, T.; Ohtani, A.; Iyoda, T.; Honda, K. *J. Electroanal. Chem.* **1987**, *224*, 123.

50. Zhang, Z.; Wei, Z.; Wan, M. *Macromolecules* **2002**, *35*, 5937.

51. Han, D.; Yang, G.; Song, J.; Niu, L.; Ivaska, A. *J. Electroanal. Chem.* **2007**, *602*, 24.

52. Balasubramanian, S.; Kagan, D.; Manesh, K. M.; Calvo-Marzal, P.; Flechsig, G. U.; Wang, J. *Small* **2009**, *5*, 11569.

53. Sanchez, S.; Ananth, A. N.; Fomin, V. M.; Viehrig, M.; Schmidt, O. G. *J. Am. Chem. Soc.* **2011**, *133*, 14860.

54. Gao, W.; Sattayasamitsathit, S.; Wang, J. *Chem. Rec.* **2012**, *12*, 224.

55. Laocharoensuk, R.; Burdick, J.; Wang, J. *ACS Nano* **2008**, *2*, 1069.

56. Harrison, J. A.; Khan, Z. A. *J. Electroanal. Chem.* **1970**, *28*, 131.

57. Gao, W.; Sattayasamitsathit, S.; Manesh, K. M.; Weihs, D.; Wang, J. *J. Am. Chem. Soc.* **2010**, *132*, 14403.

58. Ibele, M. E.; Liu, R.; Beiswenger, K.; Sen, A. *J. Mater. Chem.* **2011**, *21*, 14410.

59. Wang, Y.; Hernandez, R. M.; Bartlett, D. J.; Bingham, J. M.; Kline, T. R.; Sen, A.; Mallouk, T. E.; *Langmuir* **2006**, *22*, 10451.

60. Sanchez, S.; Solovev, A. A.; Mei, Y. F.; Schmidt, O. G. *J. Am. Chem. Soc.* **2010**, *132*, 13144.

61. Cui, C. H.; Li, H. H.; Yu, S. H. *Chem. Commun.* **2010**, *46*, 940.

62. Campuzano, S.; Orozco, J.; Kagan, D.; Guix, M.; Gao, W.; Sattayasamitsathit, S.; Claussen, J. C.; Merkoçi, A.; Wang, J. *Nano Lett.* **2012**, *12*, 396.

63. Orozco, J.; Cortés, A.; Cheng, G.; Sattayasamitsathit, S.; Gao, W.; Feng, X.; Shen, Y.; Wang, J. *J. Am. Chem. Soc.* **2013**, *135*, 5336.

64. Guix, M.; Orozco, J.; García, M.; Gao, W.; Sattayasamitsathit, S.; Merkoçi, A. A.; Escarpa, A.; Wang, J. *ACS Nano* **2012**, *6*, 4445.

65. Orozco, J.; Campuzano, S.; Kagan, D.; Zhou, M.; Gao, W.; Wang, J. *Anal. Chem.* **2011**, *83*, 7962.

66. Zhao, G.; Viehrig, M.; Pumera, M. *Lab Chip* **2013**, *13*, 1930.

67. Zhao, G.; Wang, H.; Khezri, B.; Webster, R. D.; Pumera, M. *Lab Chip* **2013**, *13*, 2937.

68. Gao, W.; Sattayasamitsathit, S.; Uygun, A.; Pei, A.; Ponedal, A.; Wang, J. *Nanoscale* **2012**, *4*, 2447.

69. Lauga, E.; Powers, T. R. *Rep. Prog. Phys.* **2009**, *72*, 096601.

70. Rosencranz, R.; Bogen, S. A. *Am. J. Clin. Pathol.* **2006**, *125*, S78.

Chapter 4 Catalytic Microengines for Biomedical Application

4.1 Lectin modified microengines for bacteria isolation

4.1.1 Introduction

Major threats to human health from *E. coli* infection have led to urgent demands to develop highly efficient new strategies for isolating and detecting this microorganism in connection to food safety, medical diagnostics, water quality, and counter terrorism.[1-3] *E. coli* and other pathogenic bacteria are commonly detected using traditional culture techniques, microscopy, luminescence, enzyme-linked immunosorbent assay (ELISA), biochemical tests and/or the polymerase chain reaction (PCR). These techniques, however, are time-consuming, labor-intensive and lack the ability to detect bacteria in real time.[4,5] There is therefore an urgent need for alternate platforms for rapid, sensitive, reliable yet simple isolation and detection of *E. coli*.

Here we present a new nanomotor strategy for isolating pathogenic bacteria from untreated clinical, environmental and food samples, involving the movement of lectin-functionalized microengines. The motion and power of self-propelled synthetic and natural nano/microscale motors have been exploited recently as an attractive route for transporting target biomaterials.[6-9] The limitations of biological motors for engineered microchip environments[6,10] have motivated the use of synthetic nanomotors for diverse biomedical and bioanalytical applications.[7,11,12] Particularly attractive for such applications are bubble-propelled microtube engines owing to their efficient movement in unprocessed biological fluids and their large towing forces.[13-16] Functionalizing photolitographically-prepared rolled-up microtube engines with

oligonucleotide or antibody receptors has been shown recently to be extremely effective for capturing and isolating target biomolecules and cells from biological samples.[15,17-19] Yet, the preparation of these rolled-up micrengines is complex, costly and requires clean-room facilities. Recently, we have developed smaller (8 μm) and highly efficient microtube engines (chapter 3), which can be mass-produced through a low-cost membrane template electrodeposition technique, and offer ultrafast speeds (i.e., large force) along with low fuel requirements.[20]

The efficient bacterial isolation platform, described in this section, relies on the attractive behavior of these new easily prepared microengines along with their functionalization with lectin receptors. Lectins are readily available glycoproteins that offer an attractive route for recognizing carbohydrate constituents of bacterial surface, via selective binding to cell-wall mono- and oligosaccharide components.[21] For example, ConA, the lectin extracted from *Canavalia ensiformis* and used in the present work, is a mannose- and glucose-binding protein able to recognize specific terminal carbohydrates of Gram-negative bacteria such as the *E. coli* surface polysaccharides.[22,23] Lectins have been recently used as the recognition elements of different biosensors for bacterial detection[24-30] but not in connection to nanomachines or nanoscale motion-based isolation.

4.1.2 Experimental section

Reagents and solutions

6-Mercaptohexanol (MCH), 11-mercaptoundecanoic acid (MUA), N-hydroxysuccinimide (NHS), 1-(3-dimethylaminopropyl)-N'-ethylcarbodiimide hydrochloride (EDC), polyaniline (PANI), lectin from *Canavalia ensiformes* (Concanavalin A, ConA), Ulex europaeus (UEA), acetic acid sodium salt, ethanolamine, 2-(*N*-morpholino) ethanesulfonic acid (MES), $CaCl_2$ and $MnCl_2$ were purchased from Sigma-Aldrich. The BB solution consisted of a 0.1 M acetate buffer, pH 5.0, containing 1 mM Mn^{2+} and 1 mM Ca^{2+}. These two divalent metals are necessary in order to get an active ConA conformation for its binding to carbohydrates.[1,2] A

0.1 M MES buffer solution pH 5.0 was used for the modification of the microengines. A 5% (w/v) Triton X-100 solution was prepared daily in this BB solution. 1 M ethanolamine solution pH 8.5 was used as a blocking agent for amine reactive-esters. Glycine, used to promote bacteria unloading was purchased from EM Science. Bacterial strains of *E. coli* NEB 5-α (New England Biolabs) were obtained from the Clinical Microbiology Laboratory, University of California Los Angeles (UCLA). The pellets were received in centrifuge tubes and were stored at -80 °C until use. Overnight bacterial cultures were freshly inoculated into Luria broth (LB) and grown to logarithmic phase as measured by the optical density at 600 nm. Concentrations in the logarithmic-phase specimens were determined by serial plating. *S. aureus* cells (10% wet w/v of essentially non-viable *S. aureus* Cowan strain cells in 0.04 M sodium phosphate buffer, pH 7.2, 0.15 M NaCl containing 0.05% NaN_3) were supplied by Sigma and *S. cerevisiae* were supplied by Science Stuff. Human urine samples were collected daily, drinking water and apple juice were purchased in a local supermarket and sea water (pH ~8) was from the shores of La Jolla, CA.

Microengine fabrication

Microtube engines were prepared by electrodepositing sequential layers into a cyclopore polycarbonate membrane, which contains numerous conical-shaped micropores with a maximum diameter of 2 μm (Catalog No 7060-2511; Whatman, Maidstone, U. K.). Standard electrodepostion of an outer PANI layer and inner Pt layer was conducted via a 3-electrode set-up, as was recently described by Gao et al.[3] In brief, PANI was electropolymerized for 5 s at +0.80 V (*vs* Ag/AgCl) from a plating solution containing 0.1 M H_2SO_4, 0.5 M Na_2SO_4 and 0.1 M PANI and Pt was galvanostatically deposited for 3600 s at a constant current of -2 mA using a commercial platinum plating solution (Platinum RTP; Technic Inc, Anaheim, CA). After electrodeposition the membrane was then dissolved and repeatedly washed in methylene chloride, ethanol and ultrapure water. The wires solution was then evaporated onto glass slides before the sequential deposition of 10 nm Ti (adhesion layer), 26 nm Ni (magnetic layer), and 12 nm of Au

(functionalization layer) over the microtubes using electron beam deposition. This additional steps provide the necessary magnetic directional control and surface modification capabilities for the appropriate guidance and pick-up of target bacterial cells.

Microengines modification

The external gold surface of the microengines was modified by an overnight immersion in a binary mixture of 0.25 mM of MUA and 0.75 mM of MCH in absolute ethanol. After washing with Milli-Q water, the resulting mixed monolayer-modified microengines were treated with a 20 mM NHS and 10 mM EDC in 0.1 M MES buffer solution pH 5.0 for 30 min, washed 1 min with BB solution and immersed 2 h in a BB solution containing 9 mg/ml of ConA (or UEA) receptor. The remaining amine reactive-esters from the activated monolayer were blocked with 1 M ethanolamine solution, pH 8.5, for 30 min and later resuspended in BB solution. Between each incubation and washing steps the microengines were isolated by centrifugation at 6,000 rpm during 4 min; all experiements were carried out at room temperature. 'Control' microengines (without the lectin receptor) were prepared using the same protocol (with the SAM assembly, activation and blocking steps) but omitting the addition of the Con A and carrying out the corresponding incubation in BB.

Preparation of bacterial suspension

E. coli stock suspension were prepared by resuspending the appropriate pellet containing ~ 10^7 colony forming units (cfu) bacteria in 100 μL of BB solution or in the undiluted sample matrix under study. This suspension was serially diluted in the same buffer (or sample matrix) to provide different concentrations of bacterial cells. *S. cerevisiae* and *S. aureus* stock solutions were prepared daily by resuspending the appropriate weight of the yeast or by diluting the required volume of the commercially-attenuated *S. aureus* cells suspension in the BB solution or in the sample under study.

Identification and isolation of target bacteria

For the detection and isolation of the target bacteria, 2 µl of modified-microengines suspension, 2 µl of 5% (w/v) Triton X-100 (prepared also in BB solution) and 2 µl of 30% (w/v) H_2O_2 solutions were mixed onto a freshly cleaned glass slide. Once the microrockets were deemed to possess the proper movement and magnetic guidance, 2 µl of the diluted bacterial cell suspension (prepared in the sample matrix or in the BB solution) were added to the mixture. The microengines were then magnetically guided towards the target cells and monitored using a Nikon Eclipse Ti-S/L100 optical microscope. Images were captured using Hamamatsu digital camera C11440, 40×objective (unless mentioned otherwise) and acquired at the frame rate of 20fps using the NIS-Elements AR 3.2 software. To test the performance of the lectin-based microengines in complex matrixes the undiluted sample under study was inoculated with the appropriate concentration of bacteria. It is worth to mention that according to the protocol described all the inoculated matrixes (originally undiluted) were finally diluted 4 times after mixing with equal volumes of the other 3 solutions required by the bioassay (microengines, 30% (w/v) H_2O_2 and 5% (w/v) Triton X-100). For unloading experiments, after capturing target bacteria following exactly the same protocol described in the previous section, 12 µL of the dissociation solution (10 mM glycine pH 2.5) were added to the glass slide. We monitored the navigation of the Con A-modified microengines in this solution during the required time to release the captured bacteria.

4.1.3 Results and discussions

As illustrated in Figure 4.1.1A (left), the new nanoscale bacteria isolation scheme utilizes the movement of ConA-functionalized microengines to scour, interact and isolate pathogenic bacteria from different environmentally, biomedically and food relevant complex samples. A second goal of the present work is to demonstrate a bacterial target unloading scheme through the controlled release of the captured bacteria from a moving synthetic microengine. Such triggered release has been accomplished using a low-pH glycine solution able to dissociate the lectin-

bacteria complex (Figure 4.1.1A, right). Finally, we present the ability of the new microengines to capture and transport simultaneously both the target bacteria as well as polymeric drug-carrier spheres (using the lectin and magnetic interactions, respectively), towards coupling of the *E. coli* isolation with 'on-the-spot' therapeutic action and adding a unique theranostics ('identify and eradicate') capability to nanomachine platforms. Overall, the new abilities of the template-prepared lectin-modified microengines hold considerable promise for diverse biomedical, food safety and biodefense applications.

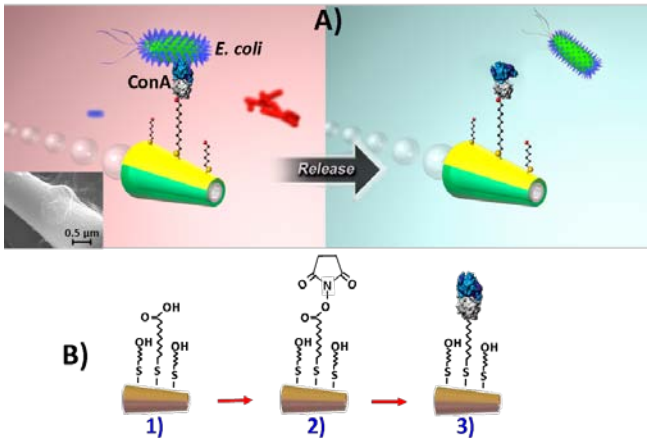

Figure 4.1.1 Lectin-modified microengines for bacteria isolation. Schemes depicting A) the selective pick-up, transport and release of the target bacteria by a ConA-modified microengine. Inset (in Scheme A, bottom left side), a SEM image of a portion of a ConA-modified microengine loaded with an *E. coli* cell. Scheme B, Steps involved in the microengines gold surface functionalization: 1) self-assembling of MUA/MCH binary monolayer; 2) activation of the carboxylic terminal groups of the MUA to amine-reactive esters by the EDC and NHS coupling agents; 3) reaction of NHS ester groups with the primary amines of the ConA to yield stable amide bonds.

The fabrication of this new microengine design involves a template-based electrodeposition of a polyaniline (PANI)/Pt bilayer microtube and e-beam vapor deposition of outer Ni/Au layers essential for the magnetic navigation and surface functionalization. As illustrated in Figure 4.1.1B, such functionalization involves the self assembly of alkanethiols and subsequent conjugation of the lectin receptor. The template fabrication process results in 8 µm-long microtube engines that are substantially smaller than common rolled-up tubular

microengines. The relative similar dimensions of the new microengine and of the target bacteria (~2 μm length ×0.5 μm width) permit convenient real-time optical visualization of the isolation process without the need for additional labeling. By varying the membrane pore size and deposition time, the microengine's aspect ratio can be tailored for meeting the needs of specific target bacteria detection paradigms. Similar to rolled-up microengines,[15,18,31-33] the template-prepared microengines are propelled efficiently in different media via the expulsion of oxygen bubbles generated from the catalytic oxidation of hydrogen peroxide fuel at the inner Pt layer.[20] The remarkably ultrafast speed of the template-prepared PANI/Pt bilayer microtube engines[20] is reduced by ca. 50% after the vapor deposition of the outer Ni/Au layers.

Next, the microengine functionalization protocol was optimized for efficient lectin-bacteria interaction and locomotion. As illustrated in Figure 4.1.1B, functionalization was accomplished by conjugating the lectin to the outer gold surface of the microengines via a self-assembled monolayer (SAM). A mixture of 11-mercatoundecanoic acid (MUA) and 6-mercaptohexanol (MCH) was used to create the binary SAM while 1-ethyl-3-(3-dimethylaminopropyl) carbodiimide (EDC)/N-hydroxysuccinimide (NHS) chemistry was used to activate the MUA carboxyl terminated groups for conjugation with ConA. To promote favorable target accessibility while minimizing non-specific adsorption the binary SAM was prepared using 0.25 mM MUA and 0.75 mM MCH as optimal alkanethiol concentrations.[34] The low concentrations of these thiols also ensure minimal poisoning of the inner catalytic platinum surface and hence a high catalytic activity.[35] Such surface modification of the Au/Ni/PANI/Pt microtubular engines resulted in an additional 50% speed reduction. After the SAM activation, the lectin receptor was immobilized via NHS/EDC coupling using a binding buffer (BB) solution containing 9 mg/ml of ConA. This step did not affect the microengine speed. Overall, the high speed of the modified microengines, localized fluid convection[18] and the strong lectin/bacteria interaction, ensure efficient bacteria pick-up and transport. The high speed of the new

microengines also reflects the high towing capacity, as will be illustrated below for the simultaneous transport of multiple bacteria or different cargoes.

The specific binding of the ConA-modified microengines to *E. coli* was examined first in inoculated human urine samples. These urine samples were inoculated with *E. coli* target bacteria along with a 5-fold excess *Saccharomyces cerevisiae* (*S. cerevisiae*), a species of yeast frequently responsible for yeast infections and UTIs. Figure 4.1.2 demonstrates the selective binding and transport of the rod-shaped (~2 μm length) gram-negative *E. coli* bacteria (delineated by green dotted circles). In contrast, the modified microengine does not capture the round-shaped *S. cerevisiae* cells (~5 μm in diameter) even when multiple contacts occur (delineated by red dotted circles) (Figure 4.1.2, a–c). The distinct size (~2 μm *vs* 5 μm) and shape (rod *vs* round) of the target *E. coli* and control *S. cerevisiae*, respectively, allow clear optical visualization and discrimination between the target and control cells during the motor navigation. Note again that the similar size scale of the microengine and bacteria facilitates such visualization in real time of the binding process (see Figure 4.1.2). This selective and rapid capture mechanism is attributed to the nearly instantaneous recognition of the sugar moieties on the bacterial cell wall by the lectin-modified microengine (Figures 4.1.2d-f). Indeed, the multivalent binding of ConA to the *E. coli* surface O-antigen favors strong adhesion of *E. coli* to the ConA-modified microengine surface[23,24] as illustrated clearly in the SEM image depicted in Figure 4.1.1A (bottom left side). To further corroborate the specificity of the ConA-modified microengines, we tested human urine samples inoculated with both *E. coli* and a 5-fold excess of another urinary pathogen *Staphylococcus aureus* (*S. aureus*), (i.e., a small, round, gram-positive UTI-related bacteria).[36] Both capture experiments results with *S. cerevisiae* and *S. aureus* controls in urine specimens demonstrate the high specificity of the ConA-modified microengines towards *E. coli* and their potential for the selective capture and transport of this microorganism from complex clinical samples.[37]

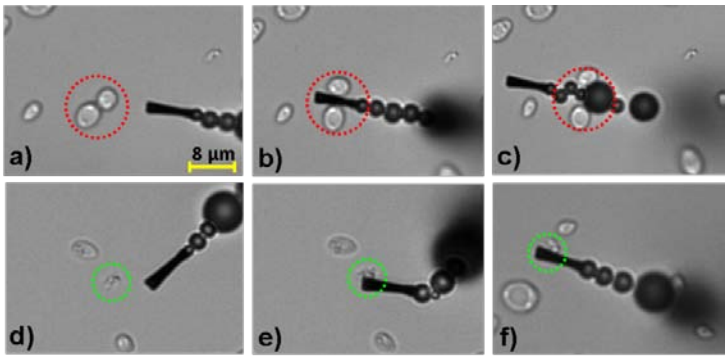

Figure 4.1.2 Selective interaction between the ConA-functionalized microengines and the *E. coli* target bacteria in an untreated and inoculated human urine sample. Time-lapse images showing before, during and after interaction of the ConA-modified microengines with *S. cerevisiae* negative control (a–c) and *E. coli* target (d-f) cells. Urine samples are inoculated with *E. coli* ($2.25x10^7$ colony forming units (cfu/ml) or $4.5x10^4$ cfu on the glass slide) and a 5-fold excess of *S. cerevisiae* and finally diluted 4 times in the glass slide to include the functionalized microengines and the fuel solutions. Fuel conditions: 7.5% (w/v) H_2O_2, 1.25% (w/v) Triton X-100.

Additional experiments were performed with "control" microengines (without the immobilized ConA) to demonstrate that the surface-confined lectin is solely responsible for the bacterial isolation. For example, these "control" microengines do not capture *E. coli* even after multiple contacts with the bacteria while navigating in the BB solution containing a 10-fold excess of *E. coli* (compared to solutions commonly used with the ConA-modified microengines). These results, along with mixture experiments involving large excess of a gram-positive bacteria or yeast clearly demonstrate that the capture of the *E. coli* occurs through the specific lectin-carbohydrate recognition and confirm the high specificity of surface-confined ConA towards lipopolysaccharide O-antigens characteristics of gram-negative bacteria.[23,24,26,29,38] The high selectivity, illustrated in Figure 4.1.2, is attributed not only to the high affinity of the lectin to the target bacteria but also to the effective minimization of non-specific binding associated with the highly dense hydrophilic SAM surface coating. These data also confirm that the peroxide fuel and Triton X-100 surfactant, essential for the microengine movement, do not compromise the specific lectin-bacterial cell wall interaction or the integrity of the assembled binary SAM.

The reproducibility of the new motion-based isolation was investigated by using 5 different batches of ConA-modified microengines following identical processing steps. The results (not shown) demonstrated very small (~5%) differences in the bacteria capture efficiency among different batches of modified microengines, demonstrating the reliability of their fabrication, modification and movement processes. While lectin-bacteria binding often requires long (30-60 min) incubation times,[30,39] the microengine-induced localized convection appears to dramatically accelerate the binding process. Short contact times with the target bacteria (few seconds) are thus sufficient for its effective capture. The new microengine platform thus presents a unique approach for meeting the need for the rapid, direct and real time isolation of biological agents.

The practical utility of the new microengine approach towards diverse practical applications was illustrated by the ability of the lectin-modified microengines to recognize the target bacteria in different untreated and inoculated real samples. These samples included common beverages (ranging from drinking water to apple juice) and environmental matrices (such as seawater). For example, Figure 4.1.3 clearly illustrates that the functionalized microengines display an immediate 'on the fly' *E. coli* capture upon contacting the target bacteria in each of these real samples. A successful pick-up rate (during the first engine-cell contact) of nearly 90% (n=50) has been observed in all the matrices tested. In rare occasions (less than 1% of the times) the cells were 'sucked up' into the front opening of the modified microrocket (i.e., captured non-specifically). Overall, the results of Figures 4.1.2 and 4.1.3 demonstrate the ability of the modified microengines to pick-up bacteria in the presence of diverse conditions, different environments and matrix effects, including low and high sugar concentrations (as in drinking water and apple juice, respectively) as well as high salt (seawater and urine) environments. Note also that the average speed of the functionalized microengines varies with the specific sample matrix. As expected, small changes (decrease) in the speed of around 10% are observed after

capturing the *E. coli* in the different matrices tested. Yet, efficient propulsion and transport of the captured bacteria are maintained.

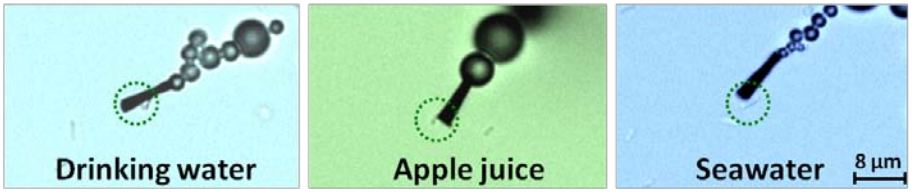

Figure 4.1.3 Isolation of the *E. coli* target bacteria from different real samples using ConA-functionalized microengines. Images demonstrating the *E. coli* pick-up and transport in untreated a) drinking water, b) apple juice and c) seawater samples inoculated with *E. coli* $1.8x10^7$ cfu/mL ($3.6x10^4$ cfu on the glass slide). Other conditions, as in Figure 4.1.2.

The ability to isolate and unload target bacteria is critical for identifying pathogenic bacteria serotypes using further analysis. To facilitate the release of the captured bacteria the loaded ConA-modified microengines were moved through a low-pH glycine-based dissociation solution that disrupts the sugar-lectin complex[40-42] (Figure 4.1.1A, right). Figure 4.1.4 illustrates images of the lectin-modified microengines before (a) and after (b) 20 min navigation in this dissociation solution. The multiple bacteria confined to the moving microengine are clearly released from its surface after movement in the low-pH glycine-based dissociation solution. The efficient removal of the captured bacteria is attributed to the unfolding of ConA in this low pH-solution, thereby dissociating the sugar-lectin complex and releasing the captured bacteria for subsequent re-use.[40-42] The unfolding of the immobilized bioreceptor in this low-pH solution is supported also by the inability of the ConA-modified microengines to capture target bacteria in this medium while contacting it multiple times. These mild dissociation conditions were shown not to affect the sugar binding capacity of the immobilized lectin[25,43,44] or the integrity of the assembled binary monolayer. Thus, a reversible refolding to the original active ConA conformation is expected after navigating in the BB solution, indicating great promise for reusing the same modified microengines in new isolation experiments.

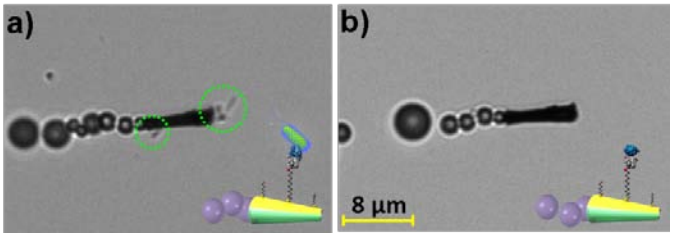

Figure 4.1.4 Release of the captured bacteria from the ConA-modified microengines. Images showing an *E. coli*-ConA-modified microengine before a) and after b) 20 min of incubation in a 10 mM glycine solution, pH 2.5. Other conditions, as in Figure 4.1.2.

4.1.4 Conclusions

In conclusion, we have demonstrated the use of new synthetic microengines, functionalized with lectin receptors, for the efficient isolation of target bacteria from diverse real samples. These novel modified-microengines offer very attractive capabilities for autonomous loading, directional transport and unloading of the captured bacteria towards subsequent reuse. The incorporation of the new microengine-based bacterial isolation protocol into microchannel networks could lead to microchip operations involving real-time isolation of specific bacteria, its lysis and unequivocally identification (by 16S rRNA gene analysis). The new capabilities of new lectin-modified microengines make them extremely attractive for a wide-range of fields including food and water safety, diagnosis of infectious diseases, biodefense, or clinical therapy treatments.

4.2 Micromotors based ‘lab-on-chip’ immunoassay

4.2.1 Introduction

The reliable identification, isolation and quantification of proteins holds an enormous potential to satisfy the growing demands in diverse fields, including medical diagnostics, food safety, forensic analysis, environmental monitoring and biodefense applications.[45] A wide variety of techniques are available for protein detection and purification. Particularly attention has been given to antibody-based standard ELISA protocols within multiple well plates,[46,47] although such assays often require long incubation times and multiple washing steps. Recent advances in the field of microanalytical systems have led to the development of lab-on-a-chip (LOC) immunoassays, coupling the power of microchip devices with the high specificity and sensitivity of antigen-antibody interactions.[48-52] Yet, new efficient microchip immunoassays offering direct, simple and rapid isolation of target proteins are desired.

Here we present a novel ‘on-the-fly’ microchip sandwich immunoassay based on self-propelled antibody-functionalized artificial microtransporters able to perform each of the immunoassay steps in different reservoirs and providing direct visualization of the protein binding event. Biological motors and related motion-driven processes have demonstrated the ability to capture and transport target proteins along microtubule tracks in microchip devices.[6,53-54] One attractive example is a kinesin-powered ‘smart dust’ sensing device, containing antibody-functionalized microtubules, where the antigen capture and transport allow the replacement of the common wash steps.[6] Microtubule-based molecular shuttles, coupled to kinesin-coated microchannel tracks, were also used for motion-based protein sorting.[53,54] However, practical utility of such kinesin-based microchip immunoassays is hindered by the limited operational stability and lifetime of biological motors in engineering environments (associated with the rapid

degradation of proteins outside biological environment) and by the necessity of preconfigured microlithographic tracks to guide their movement.[6,53]

The limitations of protein nanomotors have motivated the present study in which self-propelled antibody-functionalized artificial microtransporters have been incorporated for the first time into microchannel networks to create an advanced autonomous microchip device that integrates the protein capture, transport and detection operations within different separated zones. Synthetic catalytic nanomotors[7,9,16,55-58] are highly compatible with engineered microsystems and environments and can thus be readily adapted to different LOC formats.[59] Non-functionalized nanowire and microtube motors were used earlier for a guided movement and cargo-towing within complex microchannel networks of microchip devices.[60,61] Receptor-functionalized artificial nanomotors can offer the selective isolation of biological targets from raw physiological fluids by capturing and transporting them to a clean environment.[62] While several self-propelled microtransporters have thus recently been described for isolating different biological targets,[15,18,19] there are no reports on the use of artificial nanomotors for antibody-based protein immunoassays and related LOC protocols.

In this section we will demonstrate the first example of a LOC immunoassay based on the active transport of antibody-functionalized synthetic micromotors (Figure 4.2.1). As illustrated in Figure 4.2.1A, a simplified preparation of the functionalized microtransporters has been performed, relying on the presence of carboxy-terminated outermost polymeric layer of the template-deposited polymer/Ni/Pt microtubes. The resulting antibody-functionalized micromotors offer an ‘on-the-fly’ capture and transport of the target antigen and, in a second step, the pickup of a sphere-tagged secondary antibody, thus demonstrating the efficiency of the different conjugation events held in each microchip reservoirs (Figure 4.2.1II, left). Transport step thus replaces the washing steps common in traditional double-antibody sandwich assays (DASA), in a manner analogous to kinesin-based ‘smart dust’ immunoassays.[6] Tagging the secondary antibody

with the polymeric sphere offers a convenient direct visualization and detection of the immunoreactions. In a second approach, shown in Figure 4.2.1II (right), the functionalized microengine captures and transports the microsphere-tagged antigen through a microchannel network. Therefore, convenient optical visualization of the detection and transport events related to *Staphylococcus aureus* (*S. aureus*), used as target bacteria which contains protein A in its cell wall, is also achieved by using anti-Protein A antibody-functionalized microengines. Such marriage of immunoassays, self-propelled artificial microtransporters, motion-based direct detection and microchip devices holds considerable promise for diverse applications of lab-on-a-chip systems.

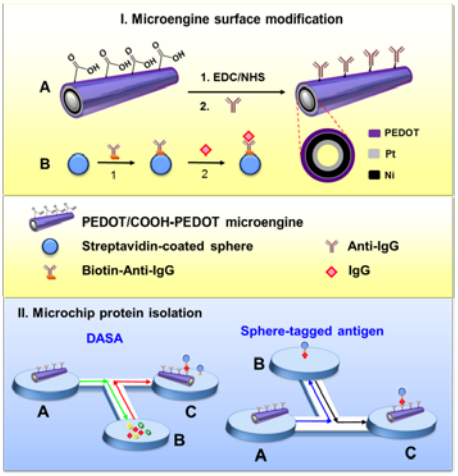

Figure 4.2.1 Schematic of the micromotor-based microchip immunoassay. Microengine surface modification (I): Immobilization of anti-IgG on the COOH-PEDOT:PEDOT microengine surface (A). Activation of the COOH groups through EDC/NHS chemistry (1) and immobilization of the anti-IgG antibody on the active moieties (2). Modification of streptavidin-coated PP (B) with the biotinylated-anti-IgG antibody (1) and IgG antigen (2). Micromotor-based microchip immunoassay (II): in a DASA format, the anti-IgG-modified microengines are introduced into reservoir A and guided towards reservoir B, where they navigate for 10 min in a solution containing the target protein in the presence 10-fold non-target proteins. The modified microengine with the target protein is conducted to a third reservoir containing the tagged-PP. In a sphere tagged-antigen format, the anti-IgG-modified microengines are introduced in reservoir A and guided towards a reservoir B to pick-up the anti-IgG-modified PP and guided to reservoir C.

4.2.2 Experimental section

Synthesis of multilayer microengines

The multilayer microtubes were prepared using the same electrodeposition protocol as Chapter 3.2.2. A cyclopore polycarbonate membrane, containing 2 μm maximum diameter conical-shaped micropores, was employed as a template. PEDOT/PEDOT-COOH microtubes were electropolymerized up to 0.5 C at +0.85 V from a plating solution containing 7.5 mM of each monomer (EDOT and EDOT-COOH), 100 mM SDS and 7.5 mM KNO_3. Then, the metallic layers were deposited from a Pt/Ni mixture solution. The first Pt layer was deposited galvanostatically at -2 mA for 500 s to provide a smooth and high conductive surface after the polymer deposition and also improve the deposition of the next metallic layers. Afterwards the intermediate Ni layer was deposited amperometrically at -1.3 V for 4.0 C to achieve the magnetic properties that allow the guidance by properly orienting the magnetic field created by a simple neodymium magnet. Finally the catalytic inner Pt layer was deposited galvanostatically at -2 mA for 450 s. The Pt/Ni mixture solution was prepared by mixing the same volume of a commercial platinum solution (Platinum RTP; Technic Inc, Anaheim, CA) and a Nickel solution containing a mixture of 20 gL^{-1} $NiCl_2 \cdot 6H_2O$, 515 gL^{-1} $Ni(H_2NSO_3)_2 \cdot 4H_2O$, and 20 g L^{-1} H_3BO_3.

Microengines functionalization

1-ethyl-3-(3-dimethylaminopropyl) carbodiimide (EDC)/N-hydroxysuccinimide (NHS) chemistry was used to activate the carboxyl-terminated groups from the polymer for conjugation with anti-Human IgG protein. For this purpose microengines were treated with 200 μl of a 0.1 M MES buffer solution pH 5.0 containing 20 mg EDC and 20 mg NHS for 15 min, washed with MES buffer 1 min and incubated with anti-Human IgG in PBS 1x pH 7.2 for 2h. The excess of antibody were washed in PBS buffer (1x) pH 7.2 containing 0.05% of tween 20. The remaining amine reactive-esters from the activated carboxylic groups were blocked with 1 M ethanolamine solution, pH 8.5, for 30 min and BSA 1% for 1 hour with a washing step in between in PBS 1x pH 7.2. In all the washing steps the microengines were centrifuged at 6000 rpm for 4 min.

Streptavidin polystyrene particles

20 µl of Streptavidin Polystirene Particles were washed twice with B&W buffer and then incubated in 50 µl of 400 µg/ml Biotin-anti-Human IgG antibody solution, for 15 min. The excess of reagents was washed with Milli-Q water and particles incubated with 50 µl IgG of 750 µg/ml IgG antigen solution, for 15 min. Finally the particles were washed with PBS buffer (1x) pH 7.2 containing 0.05% of tween 20 and then resuspended in 20 µl PBS buffer (1x) for analysis.

Experimental procedure

Catalytic microengines in the microchannel were operated by filling the reservoirs and microchannel with a navigating solution consisting of a 2% NaCh/1% H_2O_2 mixture in PBS buffer solution (pH 7.2). Subsequently, microengines and particles were added into the reservoirs and were equilibrated until quiescent conditions were obtained. Such addition ensures not only the autonomous navigation of the microengines over prolonged time periods but also the absence of solution flow during the experiments.

4.2.3 Results and discussion

The new immuno-microtransporters were prepared by a template-based electrodeposition of multilayer PEDOT:COOH-PEDOT/Ni/Pt microtubes. Figure 4.2.1I depicts the surface modification of the microengine (I) along with a schematic of the tubular microtransporter and its corresponding cross section. The outermost polymeric layer is synthesized by co-electropolymerization of PEDOT:PEDOT-COOH (from an electroplating solution containing the equimolar mixture of the monomers) followed by electrodeposition of the Ni and Pt metallic layers (from a Pt/Ni mixture electroplating solution). Whereas the inner Pt catalytic layer of the microtransporter is essential for generating the oxygen bubble thrust, the intermediate Ni layer is used for the magnetic guidance. The outermost PEDOT:COOH-PEDOT layer serves to anchor the antibody through the common carbodiimide (EDC)/N-hydroxysuccinimide (NHS) chemistry (Figure 4.2.1A). Initial efforts involving a single COOH-PEDOT external layer resulted with numerous COOH groups exposed on the microtransporter outermost surface for subsequent

functionalization step. However, the co-deposition of a COOH-PEDOT:PEDOT was proved necessary to avoid adherence of the PEDOT-based microtransporters to the surface of a glass slide after the antibody functionalization. Electrochemical deposition conditions, such as composition of the electroplating solutions, applied current, potential and deposition time, were optimized. Carboxy moieties from the electropolymerized PEDOT:COOH-PEDOT external layer allow a direct functionalization of the resulting microengines, thereby obviating the need for e-beam deposition process of an outer gold layer and related clean room facilities. Unlike other microtubular engines, whose speed is greatly reduced after the e-beam gold deposition and further surface functionalization, the fast original speed of the COOH-PEDOT:PEDOT/Ni/Pt microtransporters (~400 μm/s) is not affected by this direct functionalization process. Furthermore, eliminating the need for self-assembled monolayers of alkanethiols[25,26] obviates potential poisoning of the inner Pt surface, hence ensuring high catalytic activity and therefore the efficient microtransporters movement. It should be noted that unlike earlier gold-based microengine functionalization schemes, involving modification of half of the outer surface,[63,64] the present protocol allows the functionalization of the entire outer surface, as the carboxy moieties cover the entire outermost polymeric surface that will couple later to the antibody receptor.

The resulting polymer/Ni/Pt microtransporters propel efficiently via the expulsion of oxygen bubbles generated by the catalytic oxidation of hydrogen peroxide fuel at their inner Pt layer.[20,65] The template fabrication process results in 8 μm-long microtubes, similar to the scale of the particle-microsphere tag, which offers a convenient real-time optical visualization of the protein binding event. For example, the formation and movement of the immuno-sandwich complex can be readily visualized by tagging the secondary antibody with a microsphere tracer. Figure 4.2.II illustrates the micromotor-based microchip immunoassay protein isolation protocol. All the capture-transport-tag-transport steps involved in the immunoassay protocol are thus

carried out in the microfluidic device, hence replacing the capture-wash-tag-wash sequence common in conventional DASA protocols.

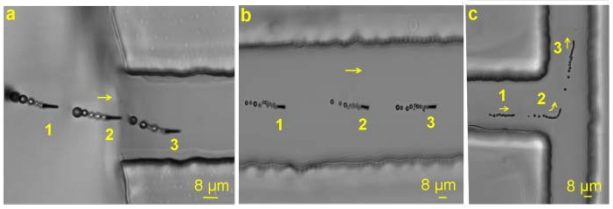

Figure 4.2.2 Navigation of an unmodified COOH-PEDOT:PEDOT microengine within a LOC device. Different overlaid time lapse images (labeled as 1, 2, 3) of the microengine leaving a reservoir (a), crossing the channel between two reservoirs (b) and entering the T-shape cross section (c). Arrows indicate the direction of the movement.

The ability of the micromotor to travel within a predetermined path along the microchip channels is crucial for the successful performance of the new LOC immunoassay protocol. Figure 4.2.2 shows the guided movement of the unmodified polymer/Ni/Pt microengine within different sections of the LOC microchannel network containing a PBS solution along with the H_2O_2 fuel and sodium cholate (NaCh) surfactant. These images demonstrate the self-propelled micromotor departing from the reservoir (a), crossing the channel interconnecting reservoirs (b) and entering the T-shape cross section while swimming within this junction (c). The generated oxygen bubbles are clearly noticeable during such autonomous movement inside the microchip, as previously reported for other microengines.[16,18] The microengine displays an efficient movement and advanced spatial motion control within the narrow channels and the different reservoirs in the microchip, reflecting the precise magnetic guidance associated with its intermediate Ni layer. Such advanced guided motion and efficient propulsion within the complex microchannel network meets the demands for the sandwich immunoassay and other complex microchip operations.

After demonstrating the precise microengine movement within the microchannel network, the microtransporters were functionalized with the corresponding antibody receptors to carry out the microchip immunoassays. In the first bioassay format, the recognition of the target proteins was performed by functionalizing the microtransporters with the antibody via EDC/NHS

chemistry (Figure 4.2.1, IA), followed by the detection of the target protein, which is conjugated to a secondary antibody functionalized with streptavidin-coated polystyrene particles (S-PP) (Figure 4.2.1, IB). Therefore, the target binding event can be easily visualized by optical microscopy, as the antibody-modified microtransporter is efficiently picking-up the protein target-conjugated secondary antibody-coated S-PP.

The microtransporter functionalization protocol was optimized for efficient protein-antibody interaction and locomotion. A highly reproducible loading protocol was accomplished by the systematic optimization of the experimental conditions involved in the recognition and labeling steps. The remaining amino moieties (after the modification) were blocked to minimize unspecific adsorption of the target proteins.[62]

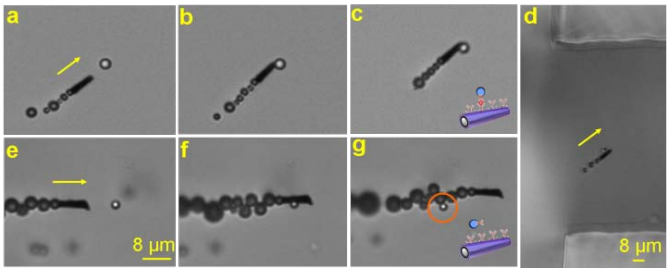

Figure 4.2.3 (a-d) Anti-IgG-modified microengines approaching, contacting and capturing the IgG-antibody-modified particle complex. (e-g) Anti-IgG-modified microengines approaching, contacting but not capturing the antibody-modified particle (no IgG present; S-PP highlighted by an orange circle). It must be pointed out that the anti-IgG-modified S-PP is not pre-incubated with the IgG. All negative "controls" were performed on the surface of a glass slide.

The specific capture of the target protein by the antibody-modified microtransporters was first examined by using the LOC device. Figure 4.2.3 (a-d) shows the pick-up and transport of a single antigen-conjugated microsphere by the anti-IgG-modified microtransporter. This figure illustrates the functionalized motor approaching (a), contacting (b) and capturing and transporting (c) the antigen-coated S-PP within the microchip reservoir, followed by its entrance into a microchannel (d). In contrast, no such pickup and transport are observed in the control experiment of Figure 4.2.3 (e-g) using the antibody-modified microtransporter and antibody-

modified particle (in absence of the IgG antigen), despite the multiple direct motor-particle contacts.

Other control experiments are carried out carefully. The modified microengine is shown first contacting but not capturing the unmodified PP (negative control 2; smaller size), while it is picking and transporting the IgG-B/anti-IgG-modified S-PP complex (acting as "positive control", bigger size). These results demonstrate that the antibody-modified microtransporters are able to specifically capture the target protein, indicating the great potential of these immuno-microengines for transporting and isolating proteins in a LOC device. The different size of these tagged and untagged particles (~2.0 μm *vs* 0.85 μm, respectively), allows a clear optical real-time visualization and discrimination between the "positive" and "negative controls" during the motor navigation in one single experiment. The similar size scale of the microengines and tags facilitates the clear visualization of the binding events in real time (see Figure 4.2.3). This selective and rapid capture mechanism is attributed to the nearly instantaneous recognition of the proteins by the antibody-modified microengine (Figures 4.2.3 a-c). The localized fluid convection associated with the microengine vortex effect leads to a fast protein binding event, as was demonstrated for other bioisolation strategies based on such machines.[59] Thus, unlike common immunoassays that require long incubation times (15-30 min)[46,52] the microengine-induced localized convection dramatically accelerates the binding process.

Additional control experiments were performed by using different assay formats to demonstrate that the surface-confined antibody is solely responsible for the selective protein isolation. For example, we find that an unmodified "control" microengine (without the immobilized antibody) do not capture the IgG-B/anti-IgG-modified S-PP complex, even after multiple direct contacts. Furthermore, no capture of the particle-protein complex was observed for microtransporters without COOH groups (on the outermost polymeric surface) that were incubated with the antibody.

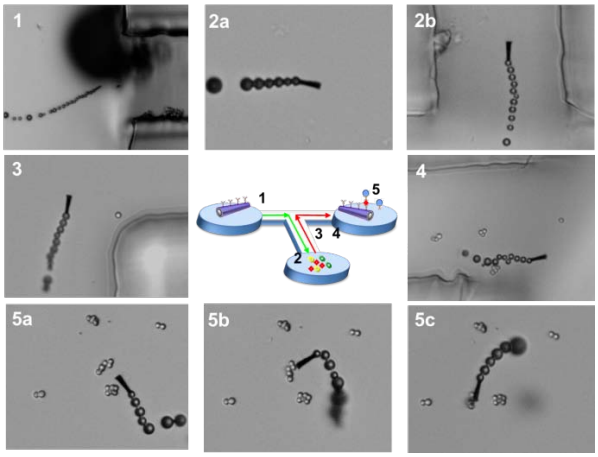

Figure 4.2.4 'On-the-fly' microchip sandwich immunoassay. Microtransporters are modifying with anti-IgG antibody and placed in a reservoir; S-PP are modified with the anti-IgG antibody and placed in another reservoir of the T-shaped LOC device; the free target IgG protein along with a 10-fold excess (µg/ml) of BSA and lysozyme are added into the third reservoir. A modified microtransporter moves from the modified-microengine reservoir (1) to the one containing the protein mixture (2a) and after a 10 min navigation is removed from the sample reservoir (2b and 2c) to the anti-IgG S-PP reservoir (4). In this last compartment the protein target, confined on the modified microtransporter, captures the modified particles (5a-c).

An 'on-the-fly' DASA assay of the protein mixture was also carried out to confirm the high specificity of the surface-confined antibody towards the target protein. In such microchip sandwich immunoassay the target protein is first captured from a mixture of proteins by the anti-IgG modified microtransporters and later tagged with the S-PP tracer conjugated to the anti-IgG secondary antibody. The antibody-functionalized motors and spheres were placed in two different reservoirs of the T-shaped LOC device, with the third reservoir containing the 750 µg/ml of free IgG protein target along with a 10-fold excess of two other proteins, *i.e.*, BSA and lysozyme (Figure 4.2.4). A modified microtransporter thus travels from the modified-microengine reservoir (Figure 4.2.4,1) to the sample reservoir containing the protein mixture (Figure 4.2.4, 2a); following a 10 min incubation while the microengine is continuously swimming, it departs from the sample reservoir (Figure 4.2.4, 2b and 3) towards to the anti-IgG antibody reservoir (Figure 4.2.4,4). In this last compartment, the captured target protein (on the microtransporter) binds to the secondary antibody-modified particle (Figure 4.2.4), hence completing the microchip

sandwich assay. These data clearly indicate the specific capture and transport of the target protein, reflecting the high affinity of the microtransporter surface antibody by the target protein and the effective minimization of non-specific binding due to the blocking of the remaining surface amino moieties after the antibody functionalization. In addition, the peroxide fuel and NaCh surfactant, essential for the microengine movement, do not compromise the specific protein-antibody interaction or the integrity of the bioreceptor coating.

The experimental reproducibility was investigated by using 8 different batches of the modified microtransporters following the identical processing steps. All the modified microtransporters were able to capture rapidly the S-PP-tagged-targets, most often immediately, upon few contacts. This indicates that different batches of modified transporters display a high protein capture efficiency and demonstrates the reliability of the fabrication, modification and movement steps involved in the entire process. The fast recognition and binding of the protein target indicates considerable promise for the rapid, direct and real time isolation of proteins.

Direct protein detection was tested by examining the ability of the antibody-modified microengines to recognize different quantities of the IgG target in the presence of a 10-fold excess of BSA and lysozyme. Capture and transport of the IgG was possible over the entire IgG concentration examined, i.e. from 20 to 750 µg/ml. The functionalized microengines display an immediate ‘on the fly’ protein capture upon contacting the tagged-antigen present at the 20 µg/ml level, in the presence of a 10-fold excess of BSA and lysozyme proteins.

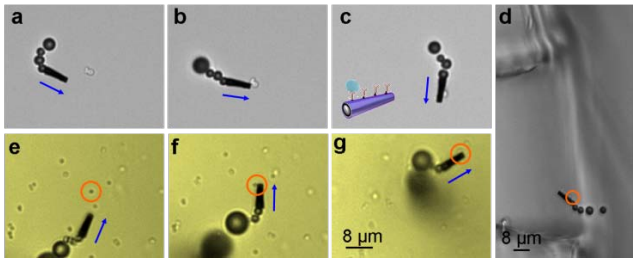

Figure 4.2.5 Anti-ProtA-modified microtransporter approaching, contacting and loading *S. aureus* cells within a LOC device containing PBS (a-d), and in a human urine media containing bacteria (e-g). The target bacteria are highlighted by orange circles.

The practical application of the new immunomicrotransporter microchip approach was demonstrated also by the label-free detection of *Staphylococcus aureus* target bacteria (containing protein A in its cell wall).[66] As illustrated in Figure 4.2.5 (a-d), an anti-proteinA antibody-modified microengine is able to recognize Protein A from the cell wall of *Staphylococcus aureus (S. aureus)* while moving within the microchip. The bacteria dimension (around 2 μm) offers convenient direct optical visualization of the binding event. The specific binding of the anti-proteinA-modified microengines to *S. aureus* was also examined in PBS containing *S. aureus* target bacteria along with a 5-fold excess *Saccharomyces cerevisiae* (*S. cerevisiae*), a yeast specie frequently responsible for yeast infections and UTIs. The selective binding and transport of the small rod-shaped (~2 μm length) *S. aureus* bacteria was clearly observed. In contrast, the modified microengine does not capture the larger round-shaped *S. cerevisiae* cells (~5 μm in diameter) even when multiple contacts occur. The distinctly different size of the target *S. aureus* and the *S. cerevisiae* control (~2 μm *vs* 5 μm, respectively), allows a clear optical visualization of the selective capture of the target cell and discrimination against non-target cells during the microengine movement. Note again that the similar size scale of the microengine and bacteria facilitates such real-time visualization of the binding event. Such selective and rapid capture event is attributed to the nearly instantaneous recognition of the Protein A molecules on the bacterial cell wall by the anti-proteinA-modified microengine. Finally, capture and transport of the bacteria in an inoculated human urine samples was also demonstrated in Figure 4.2.5(e-g).

4.3.4 Conclusions

In conclusion, we have demonstrated the first example of microchip immunoassay protocols based on the movement of antibody-functionalized synthetic microtransporters within microchannel networks. New PEDOT:PEDOT-COOH/Ni/Pt immuno-microengines have thus been used for an ‘on-the-fly’ microchip DASA involving antibody-functionalized microtransporters including their directed capture and transport of target proteins along

predetermined paths in the LOC system. Compared to common ELISA bioassays, the new motor-based immunoassay allows replacement of the common wash steps. Movement of the micrometer-size captured bacteria or sphere tag thus offer convenient direct real-time optical visualization of the protein binding event. Using different sizes of the microsphere tracers opens up the possibility of developing powerful chip-based multiplexed immunoassays involving different antibody-functionalized microtransporters. Such autonomous transport of antibody-functionalized nanomotors to 'on-the-fly' capture and isolate target proteins obviates the need for time-consuming and laborious multiple wash steps, hence greatly simplifying and accelerating the whole immunoassay protocol. Whenever needed, common regeneration procedures involving selected elution solutions,[67,68] can be used for releasing the captured antigen and re-using the microengine, These results demonstrate the great potential of the antibody-modified microengines for the selective recognition, loading and isolation of target proteins and cells in a microchip device. Self-propelled immuno-microengines are expected to lead to new LOC bioanalytical microsystems with attractive protein isolation and detection capabilities, thus offering numerous opportunities in diverse areas, ranging from medical diagnostics to food safety.

4.3 PAPBA based microengines for isolating sugar and cells

4.3.1 Introduction

As we demonstrated in Chapter 3, polymer/Pt microengines offer record breaking speed of over 1000 body lengths/s,[65] reflecting a large force and power essential to execute different tasks. The outer polymeric layer, commonly polyaniline (PANI) or poly(3,4-ethylenedioxythiophene) (PEDOT), has no active role besides supporting the metal catalyst deposition. In Chapter 4.1 and 4.2, functionalized microtube engines have been shown useful for the selective isolation of target biomolecules and cells from raw biological media by capturing and transporting them to a clean environment.[10,11,14-16] This attractive nanomachine-isolation strategy commonly requires additional fabrication and immobilization steps for functionalizing the microengines with the corresponding bioreceptor, through sputtering of the outer microtube surface with a gold layer, followed by the self assembly of a mixed alkanethiol monolayer and covalent coupling of the bioreceptor. Microengines functionalized with aptamers, antibody, lectin or oligonucleotide have thus shown extremely useful as self-propelled microtransporters for cancer cells,[15] nucleic acid,[18] proteins,[19] or bacteria,[63] respectively.

This section describes a new nanomachine-based 'capture and transport' strategy for isolating biological targets that does not require separate functionalization step with an additional receptor but exploits the 'built-in' recognition properties of the outer polymeric layer itself. The new microtransporter separation concept relies on a poly(3-aminophenylboronic acid) (PAPBA)/Ni/Pt microtube engine, coupling the recognition of monosaccharides by the boronic-acid-based outer polymeric layer with the catalytic function of the inner Pt layer for 'on-the-fly' binding and transport of target sugars. The complexation of monosaccharides with the boronic-acid ligand is well established.[69,70] Different monosaccharide sensors based on this boronic-acid complexation have been developed,[71-78] including electrochemical biosensors based on

electropolymerized PAPBA.[76] The ability of boronic acids to bind glucose has long been known[77,78] and has been widely used for the sensing glucose in connection to the management of diabetes.[79-82]

4.3.2 Experimental section

Fabrication of PAPBA/Ni/Pt microrockets

The PABPA/Ni/Pt microtubular rockets were prepared using a common template directed electrodeposition protocol in Chapter 3.2.2. PAPBA functionalized microrockets were then prepared by controlling electrochemical polymerization in an aqueous acidic solution containing 3-aminophenylboronic acid (APBA) (80 mM), sodium sulphate (0.3 M) and 0.125 M HCl. The electropolymerization was carried out at +0.9 V vs. Ag/AgCl and charge, 0.6 C. Subsequently, platinum-nickel alloy is plated at -0.5 V for 50 s (a thin Pt layer), -1 V for 300 s (Pt-Ni alloy, mostly Ni) and 0.5 V for 120 s (inner Pt layer) using a 1:1 (v:v) mixed solution of a commercial platinum solution and a nickel plating solution containing 20 g L^{-1} $NiCl_2 \cdot 6H_2O$, 515 g L^{-1} $Ni(H_2NSO_3)_2 \cdot 4H_2O$, and 20 g L^{-1} H_3BO_3. The resulting PAPBA/Pt/Pt-Ni Alloy/Pt microtubes are called as PAPBA/Ni/Pt in the text.

Incubation of PAPBA/Ni/Pt microrockets with glucose/disaccharide incubated PS

50 µL PS (2 µm diameter) dispersion and 50 µL glucose (2.5 mg/mL prepared in pH 8.5 phosphate buffer) were incubated overnight. Then the solution was washed with distilled water and kept into distilled water. PS/glucose solution was used to pick-up process of sugar by PABA/Ni/Pt microrockets.

50 µL PS (2 µm diameter) dispersion and 50 µL sucrose/lactose (25 mg/mL prepared in pH 8.5 phosphate buffer) were incubated overnight. Then the solution was washed with distilled water and kept into distilled water. PS/disaccharide solution was used as negative control to check any binding on PAPBA/Ni/Pt microrockets.

It should be also worthy to mention that there might be nonspecific binding of these microspheres if only they are suspended in H_2O. Phosphate buffered solutions (pH 8.5) involving slightly higher salt concentrations (including 150 mM NaCl) was used to prevent the interaction of PS with the microrockets.

UV-vis spectroscopy studies

Spectroscopic studies were carried out with Shimadzu UV-VIS Spectrophotometer UV-2450. Alizarin Red S was dissolved in phosphate buffer pH 8.2.

4.3.3 Results and discussions

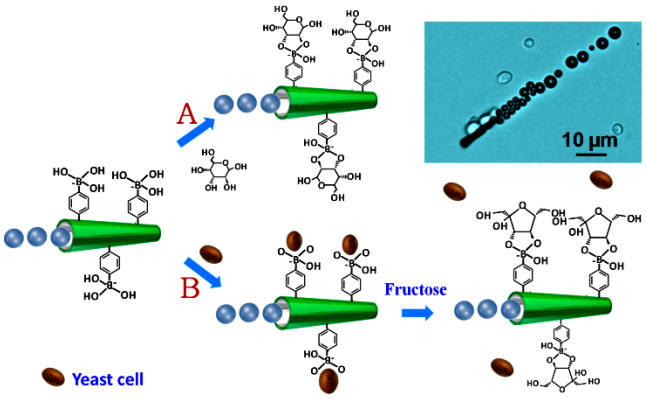

Figure 4.3.1 Microrocket with 'built-in' boronic-acid recognition of sugars and cells: Schematic representation of the poly(3-aminophenylboronic acid) (PAPBA)/Ni/Pt microrocket and its 'on-the-fly' interaction with (A) glucose and (B) yeast cell, along with triggered (fructose-induced) release of the cell. Inset image shows a carbohydrate-sensitive microrocket transporting multiple yeast cells (W303 strain).

Template electrodeposition of a PAPBA outer layer of the polymer/Ni/Pt microtube engine is used here for imparting the 'built-in' monosaccharide recognition onto the moving microengine (Figure 4.3.1). The resulting carbohydrate-sensitive microengines have been shown useful for capturing and transporting glucose (Figure 4.3.1A) and for binding and releasing yeast cells containing sugar residues on their wall (Figure 4.3.1B). For example, the inset of Figure 4.3.1 illustrates the ability of the new PAPBA/Ni/Pt microengine to transport multiple yeast cells. Efficient bubble-propulsion at a speed of 80 µm s^{-1}, along with directional transport of the 6 cells,

is observed. The similar size scale of the microrengine and cells facilitates real-time visualization of the binding process. Notice the strong adherence of the cells to the fast moving microengine despite of its sharp maneuvers and trajectory changes. Apparently, the outer PAPBA layer, containing the recognition moieties, does not hinder the efficient bubble propulsion and high speed inherent to polymer/Pt bilayer microtube engines.[65] These, and subsequent data, also indicate that the electropolymerization process does not compromise the inherent sugar recognition properties of the monomer, as expected from early biosensor efforts.[76]

The electrochemically-prepared PAPBA/Pt microrockets are ~10 μm long, have a front inner and outer opening diameters of ~0.8 and ~1.0 μm, respectively. Such shape is essential for generating the bubble thrust and reflects the micropores of the polycarbonate membrane template. Similar conical microtube engines have been reported using outer polymeric layers (e.g., PANI, PEDOT or polypyrrole)[65] that do not possess a recognition ability. The intermediate Ni layer allows convenient magnetic control of the microrocket motion.

Figure 4.3.2 illustrates the ability of the carbohydrate-sensitive microengine to approach (a), capture (b), transport (c) and release (d) a yeast cell. Such 'on-the-fly' capture process reflects the nearly instantaneous recognition of the cell-wall glucose residues by the boronic-acid based microengine. The microrocket speed is reduced from 40 to 20 μm s^{-1} after capturing the yeast cell (in the presence of the 3% H_2O_2 fuel and 1.5% NaCh). Such slower speed reflects the increased drag force associated with the larger and asymmetric motor/cell object.[83] Triggered unloading of the captured cell is also illustrated in Figure 4.3.2d in connection to addition of 20 mM fructose, which has a stronger binding affinity for the boronic-acid ligand.[84-86] Such competitive sugar binding thus leads to 'on-the-fly' detachment of the captured yeast cell towards subsequent reuse of the microengine, analogous to the release reported for single-cell electrode arrays.[84-86] Over the experimental time scale a large fraction of the cells is expected to maintain its viability in the peroxide fuel medium. In general, the new boronic-acid based nanomotor strategy allows for

isolation of different yeast-cell populations (independent of their viability). The ability to isolate dead cells is also attractive for tracing the source of an outbreak. A wide range of peroxide-free nanomotors (water-driven, magnetically or ultrasound actuated), could be combined with PAPBA polymer, and hence be used to ensure full viability of the yeast cell targets.[87-90]

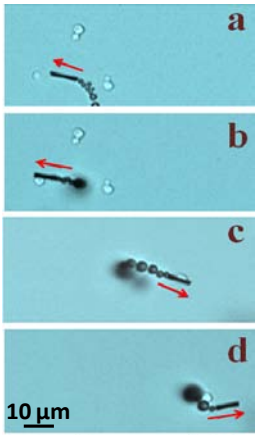

Figure 4.3.2 'Capture-Transport-Release' of yeast cells: a PAPBA/Ni/Pt microrocket approaching (a), capturing (b), transporting (c) and releasing (d) the yeast cell. Conditions: 50 mM phosphate buffer (pH 8.5) containing 150 mM NaCl, 3% H_2O_2 and 1.5% sodium cholate; 20 mM fructose used (in d) for triggering the release of the cell.

The specificity of the PAPBA/Ni/Pt microrocket to the yeast cell is illustrated in the control experiments of Figure 4.3.3. For example, no binding and transport are observed in Figure 4.3.3A in the presence of a 5-fold excess of the urinary pathogen *Staphylococcus aureus (S. aureus;* 1 µm diameter*)* containing mannose in its cell wall. The PAPBA used here is known to have a substantially higher affinity to glucose than mannose.[91,92] The PAPBA/Ni/Pt microrocket can contact but not capture or transport the round-shaped *S. aureus.* An additional control experiment involved yeast cells along with another polymer-based microrocket PEDOT/Ni/Pt,[65] that does not possess a carbohydrate-recognition ability (Figure 4.3.3B (a-c)). As expected, the direct deliberate contact of the yeast cell with the PEDOT/Ni/Pt microrocket does not lead to the capture and transport processes observed with the carbohydrate-sensitive PAPBA-based microengine.

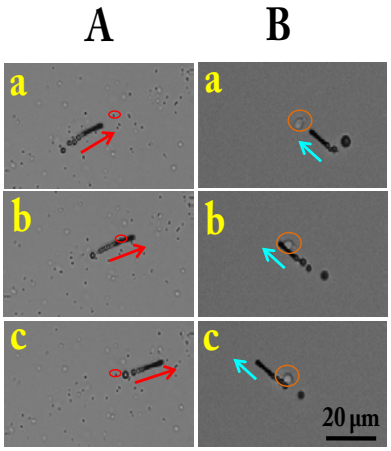

Figure 4.3. 3 Selectivity of the PAPBA/Ni/Pt microrockets: (A) a PAPBA/Ni/Pt microrocket approaching (a), contacting (b) and moving without capturing (c) a *S. aureus* cell. (B) a PEDOT/Ni/Pt microrocket approaching (a), contacting (b) and continually moving without carrying (c) the yeast cell. Conditions, as in Figure 4.3.2.

The selectivity and scope of the new microengine-target isolation protocol have been examined also by incubating different saccharides with 2 µm microspheres tags for the direct visualization of the motor-saccharide interaction. As expected, and clearly illustrated in Figure 4.3.4, the moving PAPBA-based microengine selectively interacts with the glucose monosaccharide (7 mM) (a), but not with a 10-fold excess of sucrose (c) or lactose (d) disaccharides. Similarly, no capture and transport processes are observed using the PAPBA/Ni/Pt microrocket in the presence of a large excess of unmodified microspheres (b) or using the glucose-loaded sphere along with a 'control' PANI/Ni/Pt microrocket (e).

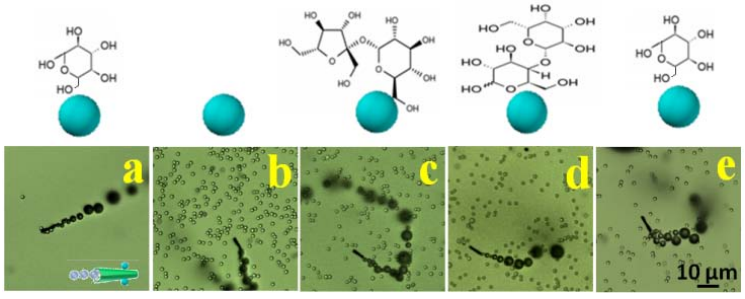

Figure 4.3.4 Selectivity and scope of the motor isolation protocol. Interactions of the PABPA/Ni/Pt microrocket with 7 mM glucose incubated PS (a), bare PS (b), 70 mM sucrose-incubated PS (c), 70 mM lactose-incubated PS (d) and PANI/Ni/Pt microrocket with 7 mM glucose-incubated PS (e). Conditions, as in Figure 4.3.2.

UV-vis spectroscopy, based on a dye-boronic acid affinity reaction, was also used for monitoring and verifying the chemical interaction between the PAPBA/Ni/Pt microrockets and glucose molecules (Figure 4.3.5). Alizarin Red S (ARS), which is commonly used for probing the binding of boronic acid with carbohydrates,[93-96] displays a distinct changes in the absorbance intensity and maximum wavelength in response to binding with boronic acid and subsequent displacement of the dye from the complex. As expected and illustrated in Figure 4.3.5, the absorption peak of ARS (a) shifted to shorter wavelength after adding the boronic-acid functionalized microrockets into the dye solution (b). Additions of 5 and 10 mM glucose into the dye/boronic-acid complex solution resulted in successive diminutions of the complex peak (c and d, respectively), indicating the displacement of ARS by glucose.[93-96]

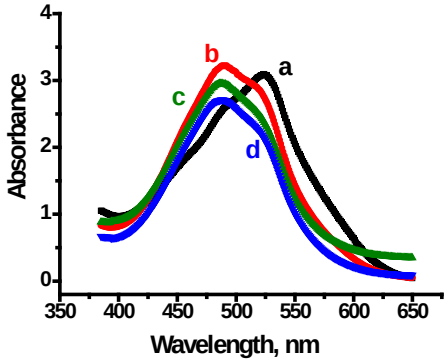

Figure 4.3.5 Absorption spectra of a) ARS; b) ARS+PABPA/Ni/Pt microrockets; c) ARS+PABPA/Ni/Pt microrockets+5 mM glucose; d) ARS+PABPA/Ni/Pt microrockets+10 mM glucose (phosphate buffer pH 8.2).

4.3.4 Conclusions

In conclusion, we have described a new nanomachine-based capture and transport strategy exploiting the 'built-in' recognition properties of the outer polymeric layer itself for isolating target sugars and cells. The new concept has been illustrated in connection to PAPBA-based nanomachines whose outer polymeric layer provides the specific monosaccharide recognition. The polymer layer thus acts as the receptor recognizing the target biomolecule, eliminating the need for additional receptor functionalization steps. These template-prepared

carbohydrate-sensitive microengines offer very attractive capabilities for autonomous loading, directional transport and triggered unloading (‘catch and release’) of monosaccharides and yeast cells. Controlled release of the captured cells towards subsequent reuse has been accomplished by the addition of fructose. This new carbohydrate-sensitive nanomachine concept can be expanded further towards a glucose-responsive controlled insulin delivery.[97] While the concept of nanomachines with a ‘built-in’ recognition has been illustrated here for isolating monosaccharides and cells it could be readily extended to the capture and transport of other important target molecules in connection to outer polymeric layers with different recognition capabilities.

4.4 MIP based microengines for protein transport

4.4.1 Introduction

Recent progress in the field of man-made nanomachines has opened the door to new and important applications.[6,9,16,56-58] For example, active transport by receptor-functionalized artificial nanomotors propelling in complex samples offers an attractive strategy for isolating target analytes,[15-19] in a manner analogous to transport processes by protein motors.[6,98] In particular, autonomously moving chemically-powered tubular microengines, functionalized with different bioreceptors (e.g., oligoncleotides, antibodies), have been shown extremely useful for 'on-the-fly' recognition and transport of a wide range of biological targets, ranging from nucleic acids to proteins and cancer cells.[15-20] Such nanomachines-driven target isolation and transport capability of receptor-modified microtransporters holds considerable promise for diverse biomedical and environmental applications.

Here we present a new nanomachine-based separation concept that relies on molecularly imprinted artificial recognition cavities. Molecularly imprinted polymers (MIPs), containing selective recognition sites,[99-101] have attracted considerable interest in a variety of sensor and separation applications owing to their high specificity, ease of preparation, and thermal and chemical stability.[102-106] Such specific artificial recognition cavities are introduced within the polymeric matrix via polymerization around the analyte (template) molecule followed by removal of the print template to leave behind complementary binding sites. The resulting matrices offer selective binding and can exert antibody-like affinities toward the target substances.[106] In the following sections we will illustrate that molecular imprinting allows cost-effective preparation of tailor-made self-propelled microtransporters with predetermined specificity for selective 'on-the-fly' isolation of target substances. Unlike bioreceptor-functionalized motors, the recognition properties of the imprinted synthetic polymers can withstand harsh conditions, such as high

temperature, pressure, extreme pH, and organic solvents (compared to their natural counterparts),[101] making the new MIP-based nanomachines attractive for diverse practical applications. Similarly, the presence of the hydrogen peroxide fuel, that may affect the bioreceptor stability and biorecognition event, has no effect upon the operation of the MIP micromotors.

4.4.2 Experimental section

Reagents and apparatus

3,4-ethylenedioxythiophene (EDOT), poly(sodium-4-styrenesulfonate) (NaPSS, MW ~70 000), sodium dodecyl sulfate (SDS, MW 288.38 g/mol), avidin-FITC from egg white were purchased from Sigma. Proteins were dissolved in 0.05 M phosphate buffer pH 7.0, prepared from analytical grade KH_2PO_4 and K_2HPO_4. The washing solution (PBST-20X) consisted of 0.05 M phosphate buffer pH 7.0 containing 0.15 M potassium chloride and 0.05% Tween-20.

Preparation of the MIP-based micromotor.

The polycarbonate membrane was sonicated for 3 min to remove the air that can be present in the micropores and then was incubated in solution containing 0.5 mg/mL of Av-FITC target protein (template) in a humid chamber for 30 min and in air for additional 20 min. After rinsing with water, PBST-20X and water, the membrane (with the pre-adsorbed protein template) was sputtered with Au on one of its sides to provide the conductivity and use as working electrode. Tubular microengines were prepared using the same electrodeposition protocol in Chapter 3.2.2.[65] Poly(3,4-ethylenedioxythiophene) (PEDOT) microtubes were prepared via electropolymerization at +0.80 V using a charge of 4 C from a plating solution containing 10 mM EDOT and 125 mM NaPSS. Subsequently, an initial Pt layer was deposited galvanostatically at -2 mA for 200 s from a commercial platinum plating solution (Platinum RTP; Technic Inc, Anaheim, CA) to improve the mechanical properties of the polymeric layer. Then, an additional Pt layer was deposited at -2 mA for 300 s from a Pt–Ni mixture solution to provide a smooth and

high conductive surface after the polymer deposition and improve the deposition of subsequent metallic layers. An intermediate Ni layer (essential for magnetic guidance) was then deposited potentiostatically at -1.3 V for 2.0 C. Finally, the inner catalytic Pt layer was deposited galvanostatically at -2 mA for 450 s. The Pt–Ni mixture solution was prepared by mixing equal volumes of the commercial platinum plating solution and of a nickel plating solution (a mixture of 20 g/l $NiCl_2.6H_2O$, 515 g/l $Ni(H_2NSO_3)_2.4H_2O$, and 20 g/l H_3BO_3). All microengines were stored in ultrapure water at room temperature until use after dissolution of membrane template. Preliminary incubation experiments were carried out by removing the supernatant (at 6000 rpm for 3 min) of 50 µl of template-imprinted microtubes solution and incubating them in solutions containing increasing Av-FITC concentrations (0-1) mg/ml in 0.05 M phosphate buffer pH 7.0, at quiescent conditions, for 30 min. To remove non-specifically bound proteins, the micromotors were washed with 100 µl stirred PBST-20X for 10 min and resuspended in 50 µl of phosphate buffer (0.05M, pH 7.0). “On the fly” capture and transport experiments were performed by placing a total of 8 µl of a solution mixture on a glass slide. The mixture consisted of four different solutions (2 µl each), including the template-imprinted microtubes, 5% NaCh, 3% H_2O_2 and protein solution (in the desired concentration).

Fluorescence microscopy

Images were captured using CoolSNAP HQ2 camera, 40X objective (unless mentioned otherwise) and acquired at a frame rate of 10 frames/s using the Metamorph 7.1 software (Molecular Devices, Sunnyvale, CA). A Nikon Eclipse 80i upright microscope with B2-A FITC filter was used to capture fluorescence images. The protein coverage on the micromotors was estimated by analyzing the corresponding time-lapse images using the ImageJ software (where 100% means complete fluorescent coverage of the exposed surface). The obtained mean fluorescence-intensity values (n=3) were corrected with the cameras’s gain control and plotted as arbitrary units in all the graphs depicting fluorescence.

4.4.3 Results and discussions

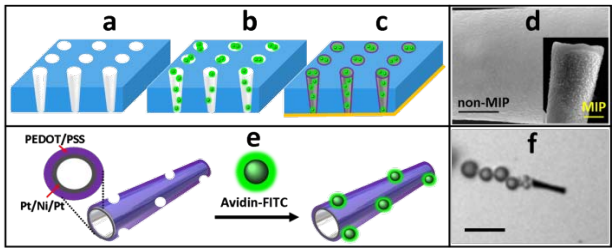

Figure 4.4.1 Scheme illustrating the preparation and characterization of the MIP-based micromotor along with the strategy for capture and transport the target protein. To fabricate the template-imprinted microtubes a dry hydrophobic sacrificial polycarbonate membrane (a) adsorbs the positively charged protein template by electrostatic interaction (b); after sputtering a conductive Au layer, sequential deposition is used to deposit the PEDOT, Pt, Ni and Pt layers (c). The resulting PEDOT-Pt-Ni-Pt multilayer microtubes are released from the membrane by immersion in an organic solvent that also removes the template protein, leaving imprinted nanocavities on their micromotor outermost surface. (d) SEM images of the surface of the resulting MIP-based micromotor (inset) and of a non-MIP micromotor (control); scale bar, 500 nm. (e) Scheme illustrating the capture of the fluorescent-tagged target protein by the self-propelled MIP microengines. (f) Image illustrating the bubble propelled MIP micromotor in a PBS solution containing 0.75% H_2O_2. Scale bar, 20 μm.

To illustrate the new nanomachine-MIP 'capture–and–transport' concept, we designed tubular microtransporters with cavity binding sites for avidin-FITC (Av-FITC) within their outer polymeric layer. The imprinted recognition sites for the target protein template have been introduced onto the nanomachine surface during the electropolymerization of the outer PEDOT layer. Electropolymerization has been widely used for preparing molecularly-imprinted recognition cavities for a variety of optical or electrochemical biosensors.[103,107] Gyurcsanyi and colleagues have reported recently on the preparation of avidin-imprinted PEDOT nanorods and films, doped with poly(styrenesulfonate) (PSS), for label-free surface plasmon resonance (SPR) sensing of proteins.[108,109] The PEDOT/PSS complex is ideally suitable for imprinting protein targets owing to its ability to generate the necessary hydrogen bonds, and electrostatic and p–p interactions.[108] (Figure 4.4.1b). The outer tubular PEDOT layer of our microengine has been grown into the inner walls of the micropores of a polycarbonate (PC) membrane that contained the pre-adsorbed Av-FITC template. The electropolymerization of the outer layer has been

followed by electrodeposition of the inner Ni and Pt metallic layers for magnetic guidance and generating the oxygen-bubble propulsion thrust, respectively, and dissolution of the membrane and concomitant removal of the protein template. A SEM image of the MIP-based micromotor (Figure 4.4.1d, inset) indicates a highly rough outermost polymeric surface, reflecting the large number of exposed complementary imprinted cavities. In contrast, a greatly smoother surface is observed (in Figure 4.4.1d) for the non-MIP micromotor. The essential conical shape of the microtube is retained following the imprinting process.

As will be demonstrated below, the micromachine-based MIP-isolation concept relies on the selective and efficient 'on-the-fly' binding of the fluorescent-tagged protein to the cavity recognition sites (Figure 4.4.1e). The outer polymeric layer thus possesses 'built-in' recognition properties, eliminating the need for additional receptor functionalization steps. Autonomous movement of the template-imprinted microtransporter in the sample mixture results in selective loading of the target protein, along with effective discrimination against non-target proteins. Direct extraction and isolation of Av-FITC from raw serum and saliva samples can thus be accomplished following short navigation times. Figure 4.4.1f illustrates that the template-imprinted microengine moves rapidly at 247 ± 10.5 μm/s in the presence of a low fuel level (0.75% H_2O_2, containing 1.25 % sodium cholate), similar to its non-MIP counterpart that moves at 241 ± 11.9 μm/s under the same conditions. Apparently, introduction of the MIP-recognition cavities has no effect upon the efficient propulsion behavior characteristic of polymer/Pt microtube engines. The MIP microengine moves straight while releasing, from its wider opening, a distinct oxygen bubble trail generated from the catalytic oxidation of its hydrogen peroxide fuel at the inner Pt layer. Greatly slower speeds of 34.8 ± 4.2 and 29.6 ± 0.3 μm/s, have been observed for the magnetically-guided MIP and non-MIP micromotors (containing an intermediate Ni layer), respectively. Such slower speeds are expected for Ni-containing polymer-based microtubular engines.[18]

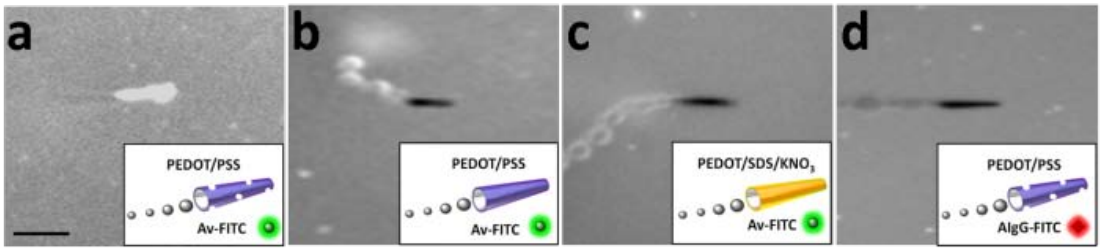

Figure 4.4.2 Specificity of the 'Capture-Transport' process by the template-imprinted microengines: (a) Time-lapse images taken after the MIP-based micromotor has navigated for 14 min in the 0.25 mg/ml Av-FITC target protein solution. (b-d) Control experiments involving a 20 min navigation: non-MIP micromotors (with PSS (b) and SDS (c) as counter ions, respectively) in a 0.5 mg/ml Av-FITC target protein solution; (d) MIP-based micromotor (with PSS counterion) moving in a solution containing 0.5 mg/ml of the non-target AIgG-FITC. Conditions, as in Figure 4.4.1. Scale bar, 20 μm.

The resulting template-imprinted microengines offer a direct target recognition, capture and transport, with the fluorescent (FITC) tag of the target protein providing real-time optical visualization of the MIP-avidin binding event based on changes in the fluorescent intensity. For example, the optical image of Figure 4.4.2a indicates that a short navigation time (of 14 min) in the 0.25 mg/ml target protein solution yields a complete fluorescent coverage of the microengine surface. These data, along with the subsequent control experiments (discussed below), confirm the presence of the complementary surface recognition sites, (in accordance with early work on non-motor nanorods),[108] and indicate again that the template imprinting does not compromise the efficient bubble propulsion. In agreement with early work,[19] the protein solution leads to a slower (16.6 ± 1.3 μm/s) speed. As will be illustrated below, the target recognition is coupled with effective discrimination against co-existing compounds.

Different negative controls have been used to evaluate the binding specificity of the protein-imprinted microtubes toward the target avidin protein (Figure 4.4.2b and c). For example, a non-MIP micromotor was prepared using similar conditions as the MIP-based motor, but without the pre-adsorbed Av-FITC protein template. The optical microscope image of Figure 2b, obtained with the non-MIP PEDOT/PSS micromotor, illustrates no apparent binding of the protein (despite of its higher concentration and the longer navigation time). Similarly, no capture

of the target protein is observed using conventional microengines,[65] based on the anionic SDS surfactant (instead of PSS polyanion) (Figure 4.4.2c), which is attributed partially to SDS-induced denaturation of the protein that affects the 3D MIP-protein structure. Specific binding is a key requirement for the new MIP-based nanomotor isolation platform. The avidin-imprinted PEDOT/PSS microtransporters were shown to discriminate against functional homologues of avidin, *e.g.* anti-immunoglobulin-FITC (AIgG-FITC) protein.[108] No binding and transport are observed in Figure 4.4.2d following a 20 min movement of the MIP-based PEDOT/PSS micromotor in a phosphate buffer solution containing 0.5 mg/ml of the non-target protein AIgG-FITC (Figure 4.4.2d). Such results clearly illustrate the specificity of the MIP-PEDOT/PSS microtransporter, the negligible nonspecific adsorption onto the PEDOT/PSS outer polymer, and the crucial role of the MIP recognition sites in attaining such efficient and selective uptake of the target protein onto the moving machine.

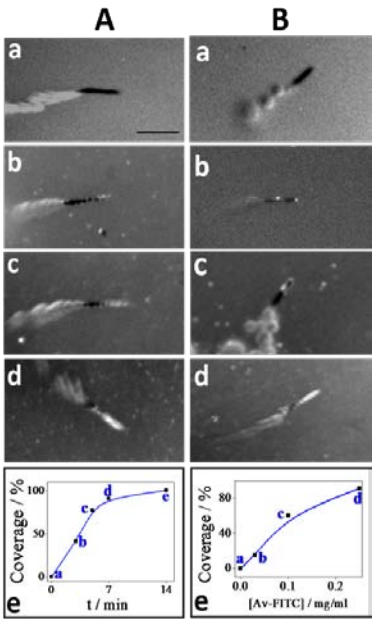

Figure 4.4.3 Dependence of the protein uptake by the MIP-based micromotor upon the locomotion time (A) and upon the target concentration (B). (A) Time-lapse images taken over a 3 s period, after the MIP-based micromotor has navigated in a solution containing 0.25 mg/ml Av-FITC target protein for: a) 0, b) 3, c) 5 and d) 7 min. (B) Time-lapse images taken after the template-imprinted microtubes have navigated for 7 min in a solution containing increasing concentrations of Av-FITC target protein: a) 0, b) 0.03, c) 0.1 and d) 0.25 mg/ml.

The imprinted polymeric layer selectively concentrates the fluorescent-tagged target protein onto the moving microengine. Such enrichment is illustrated in Figure 4.4.3A which shows the influence of the navigation time (in a 0.25 mg/ml target solution) upon the preconcentration efficiency (estimated from the fluorescent coverage). These time-lapse images illustrate that the surface coverage increases rapidly and linearly with the time up to 5 min (a-c), and then more slowly (d-e). The corresponding coverage vs. time profile (e) indicates that a complete fluorescent coverage is approached within 14 min (e), which is in agreement with Figure 4.4.2a. Overall, Figure 4.4.3A indicates that short navigation times (~5-10 min) offer convenient isolation of the target protein. The practical utility of the new microtransporter approach was achieved by the ability of the self-propelled protein-imprinted microengine to recognize the target Av-FITC in a complex unprocessed biological media, such as human serum and saliva samples (not shown).

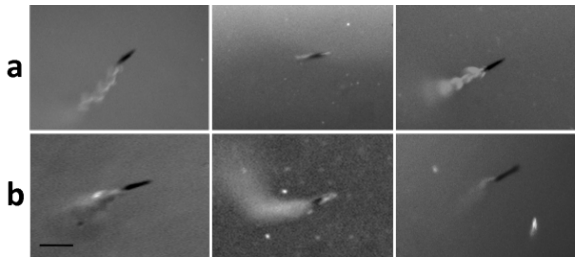

Figure 4.4.4 Capture and transport of target protein in biological fluids with 0.25 mg/ml Av-FITC: serum (a) and saliva (b) samples. Time-lapse images show the MIP-based micromotor after moving for 0 and 7 min in the samples (left and middle images, respectively). The right images represent the negative controls using a non-MIP micromotor after its 7 min navigation in the spiked human serum (a) and saliva (b) samples. Conditions, as in Figure 4.4.2. Untreated samples were diluted 1:4 in phosphate buffer. Scale bar, 20 μm.

4.4.4 Conclusions

In conclusion, we have demonstrated that MIPs represent an attractive route for creating specific artificial recognition sites in synthetic self-propelled nanomachines. Tailor-made recognition sites have thus been introduced into catalytic tubular microengine transporters through nanocavities in the outer polymer layer. The resulting template-imprinted microengines

offer attractive capabilities for autonomous binding, directional transport and enrichment of the target protein template, including ‘on-the-fly’ isolation from complex matrices. While the MIP microtransporter concept has been illustrated using the Av-FITC model protein, it could be readily extended for the selective isolation of variety of target analytes, along with the construction of self-propelled microscopic and macroscopic objects,[110] offering considerable promise for diverse potential biomedical and environmental applications.

Chapter 4.1, is based, on the material as it appears in Nano Letters, 2012, by Susana Campuzano, Jahir Orozco, Daniel Kagan, Maria Guix, Wei Gao, Sirilak Sattayasamitsathit, Jonathan C. Claussen, Arben Merkoçi and Joseph Wang. Chapter 4.2, is based, on the material as it appears in Nanoscale, 2013, by Miguel García, Jahir Orozco, Maria Guix, Wei Gao, Sirilak Sattayasamitsathit, Alberto Escarpa, Arben Merkoci and Joseph Wang. Chapter 4.3, is based on, the material as it appears in Journal of the American Chemical Society, 2012, by Filiz Kuralay, Sirilak Sattayasamitsathit, Wei Gao, Aysegul Uygun, Adlai Katzenberg, Joseph Wang. Chapter 4.4, is based on, the material as it appears in Journal of the American Chemical Society, 2013, by Jahir Orozco, Allan Cortés, Guanzhi Cheng, Sirilak Sattayasamitsathit, Wei Gao, Xiaomiao Feng, Yufeng Shen and Joseph Wang. The dissertation author was the primary investigator and author of these papers.

4.6 References

1. Laurino, P.; Kikkeri, R. *Nano Lett.* **2011**, *11*, 73.

2. Liao, J. C.; Mastali, M.; Gau, V.; Suchard, M. A.; Møller, A. K.; Bruckner, D. A.; Babbitt, J. T.; Li, Y.; Gornbein, J.; Landaw, E. M.; McCabe, E. R. B.; Churchill, B. M.; Haake, D. A. *J. Clin Microbiol.* **2006**, *44*, 561.

3. Guven, B.; Basaran-Akgul, N.; Temur, E.; Tamer, U.; Boyacı, I. H. *Analyst* **2011**, *136*, 740.

4. Wang, R.; Ruan, C.; Kanayeva, D.; Lassiter, K.; Li, Y. *Nano Lett.* **2008**, *8*, 2625.

5. Arya, S. K.; Singh, A.; Naidoo, R.; Wu, P.; McDermott, M. T.; Evoy, S. *Analyst* **2011**, *136*, 486.

6. Fischer, T.; Agarwal, A.; Hess, H. *Nat. Nanotechnol.* **2009**, *4*, 162.

7. Wang, J. *ACS Nano* **2009**, *3*, 4.

8. Schmidt, C.; Vogel, V. *Lab Chip* **2010**, *10*, 2195.

9. Pumera, M. *Nanoscale* **2010**, *2*, 1643.

10. Hiyama, S.; Inoue, T.; Shima, T.; Moritani, Y.; Suda, T.; Sutoh, K. *Small* **2008**, *4*, 410.

11. Wu, J.; Balasubramanian, S.; Kagan, D.; Manesh, K. M.; Campuzano, S.; Wang, J. *Nat. Commun.* **2010**, *1*, 36.

12. Kagan, D.; Laocharoensuk, R.; Zimmerman, M.; Clawson, C.; Balasubramanian, S.; Kang, D.; Bishop, D.; Sattayasamitsathit,S.; Zhang, L.; Wang, J. *Small* **2010**, *6*, 2741.

13. Manesh, K. M.; Cardona, M.; Yuan, R.; Clark, M.; Kagan, D.; Balasubramanian, S.; Wang, J. *ACS Nano* **2010**, *4*, 1799.

14. Solovev, A. A.; Sánchez, S.; Pumera, M.; Mei, Y. F.; Schmidt, O. G. *Adv. Funct. Mat.* **201**0, *20*, 2430.

15. Balasubramanian, S.; Kagan, D.; Hu, C. J.; Campuzano, S.; M. Jesus Lobo-Castañon, Lim, N.; Kang, D. Y.; Zimmerman, M.; Zhang, L.; Wang, J. *Angew. Chem. Int. Ed*. **2011**, *50*, 4161.

16. Mei, Y. F.; Solovev, A. A.; Sanchez, S.; Schmidt, O. G. *Chem. Soc. Rev.* **2011**, *40*, 2109.

17. Sánchez, S.; Solovev, A. A.; Schulze S.; Schmidt, O. G. *Chem. Commun.* **2011**, *47*, 698.

18. Kagan, D.; Campuzano, S.; Balasubramanian, S.; Kuralay, F.; Flechsig, G.-U.; Wang J. *Nano Lett.* **2011**, *11*, 2083.

19. Orozco, J.; Campuzano, S.; Kagan, D.; Ming, Z.; Gao, W.; Wang, J. *Anal. Chem.* **2011**, *83*, 7962.

20. Gao, W.; Sattayasamitsathit, S.; Orozco, J.; Wang, J. *J. Am. Chem. Soc.* **2011**, *133,* 11862.

21. Haseley, S. R. *Anal. Chim. Acta* **2002**, *457*, 39.

22. Loaiza, O. A.; Lamas-Ardisana, P. J.; Jubete, E.; Ochoteco, E.; Loinaz, I.; Cabañero, G.; García, I.; Penadés, S. *Anal. Chem.* **2011**, *83*, 2987.

23. He, X.; Zhou, L.; He, D.; Wang, K.; Cao, J. *Analyst* **2011**, *136*, 4183.

24. Shen, Z.; Huang, M.; Xiao, C.; Zhang, Y.; Zeng, X.; Wang, P. G. *Anal. Chem.* **2007**, *79*, 2312.

25. Safina, G.; van Lier, M.; Danielsson, B. *Talanta* **2008**, *77*, 468.

26. Lu, Q.; Lin, H.; Ge, S.; Luo, S.; Cai, Q.: Grimes, C. A. *Anal. Chem.* **2009**, *81*, 5846.

27. Gamella, M.; Campuzano, S.; Parrado, C.; Reviejo, A. J.; Pingarrón, J. M.. *Talanta* **2009**, *78*, 1303.

28. Wan, Y.; Zhang, D.; Hou, B. *Talanta* **2009**, *80*, 218.

29. Gao, J.; Liu, D.; Wang, Z. *Anal. Chem.* **2010**, *82*, 9240.

30. Grünstein, D.; Maglinao, M.; Kikkeri, R.; Collot, M.; Barylyuk, K.; Lepenies, B.; Kamena, F.; Zenobi, R.; Seeberger, P. H. *J. Am. Chem. Soc.* **2011**, *133*, 13957.

31. Mei, Y.; Huang, G.; Solovev, A. A.; Bermúdez Ureña, E.; Mönch, I.; Ding, F.; Reindl, T.; Fu, R. K. Y.; Chu, P. K.; Schmidt, O. G. *Adv. Mater.* **2008**, *20*, 4085.

32. Solovev, A. A.; Mei, Y. ; Bermúdez Ureña, E.; Huang, G.; Schmidt, O. G. *Small* **2009**, *5*, 1688.

33. Li J. X.; Huang, G. S.; Ye, M. M.; Li, M. L.; Liu, R.; Mei, Y. F. *Nanoscale* **2011**, 3, 5083.

34. Briand, E.; Salmain, M.; Herry, J. M.; Perrot, H.; Compère, C.; Pradier, C.-M. *Biosens. & Bioelectron.* **2006**, *22*, 440.

35. Bartholomew, C. H.; Agrawal, P. K.; Katzer J. R. in Advances in Catalysis, Vol. 31, Academic Press, 1982, pp. 135.

36. Muder, R. R.; Brennen, C.; Rihs, J. D.; Wagener, M. M.; Obman, A.; Stout, J. E.; Yu, V. L. *Clin. Infect. Dis.* **2006**, *42*, 46.

37. Pistole, T. G. *Ann. Rev. Microbiol.* **1981**, *35*, 85.

38. Gao, J.; Liu, C.; Liu, D.; Wang, Z.; Dong, S. *Talanta* **2010**, *81*, 1816.

39. Serra, B.; Gamella, M.; Reviejo, A. J.; Pingarrón, J. M.. *Anal. Bioanal. Chem.* **2008**, *391*, 1853.

40. Švitel, J.; Dzgoev, A.; Ramanathan, K.; Danielsson, B. *Biosens. & Bioelectron.* **2000**, *15*, 411.

41. Duverger, E.; Frison, N.; Roche, A. C.; Monsigny, M. *Biochimie* **2003**, *85*, 167.

42. Witten, K.G.; Rech, C.; Eckert, T.; Charrak, S.; Richtering, W.; Elling, L.; Simon, U. *Small* **2011**, *7*, 1954.

43. Murthy, B.N.; Sinha, S.; Surolia, A.; Indi, S.S.; Jayaraman, N. *Glycoconj. J.* **2008**, *25*, 313.

44. Yakovleva, M. E.; Safina, G. R.; Danielsson, B. *Anal. Chim. Acta* **2010**, *668*, 80.

45. Weinberger, S. R.; Morris, T. S.; Pawlak, M. *Pharmacogenomics* **2000**, 1, 395.

46. Vandermeeren, M.; Mercken, M.; Vanmechelen, E.; Six, J.; Van de Voorde, A.; Martin, J.; Cras, P. *J. Neurochem.* **1993**, 61, 1828.

47. Lequin, R. M. *Clin. Chem.* **2005**, *51*, 2415.

48. Chiem, N. H.; Harrison, D. J. *Clin. Chem.* **1998**, *44*, 591.

49. Wang, J.; Ibáñez, A.; Chatrathi, M. P.; Escarpa, A. *Anal. Chem.* **2001**, 73, 5323.

50. Crevillen, A. G.; Hervás, M.; López, M. A.; González, M. C.; Escarpa, A. *Talanta* 2007, 74, 342.

51. Herr, A. E.; Hatch, A. V.; Throckmorton, D. J.; Tran, H. M.; Brennan, J. S.; Giannobile, W. V.; Singh, A. K. *Proc. Natl. Acad. Sci. USA*, **2007**, *104*, 5268.

52. Nam, J. M.; Thaxton, C. S.; Mirkin, C. A. *Science* **2003**, *301*, 1884.

53. Bachand, G. D.; Hess, H.; Ratna, B.; Satird, P.; Vogel, V. *Lab Chip* **2009**, *9*, 1661.

54. Lin, C. T.; Kao, M. T.; Kurabayashi, K.; Meyhofer, E. *Nano Lett.* **2008**, *8*, 1041.

55. J. Wang, *Nanomachines: Fundamentals and Applications*, Wiley-VCH, Weinheim, Germany, 2013.

56. Mallouk, T. E.; Sen, A. *Sci. Amer.* **2009**, *300*, 72.

57. Ozin, G. A.; Manners, I. Fournier-Bidoz, S.; Arsenault, A. *Adv. Mater.* **2005**, *17*, 3011.

58. Paxton, W. F.; Kistler, K. C.; Olmeda, C. C.; Sen, A.; St. Angelo, S. K.; Cao, Y.; Mallouk, T. E.; Lammert, P. E.; Crespi, V. H. *J. Am. Chem. Soc.* **2004**, *126*, 13424.

59. Wang, J. *Lab Chip* **2012**, *12*, 1944.

60. Burdick, J.; Laocharoensuk, R.; Wheat, P. M.; Posner, J. D.; Wang, J. *J. Am. Chem. Soc.* **2008**, *130*, 8164.

61. Sanchez, S.; Solovev, A. A.; Harazim, S. M.; Schmidt, O. G. *J. Am. Chem. Soc.* **2011**, 133, 701.

62. Campuzano, S.; Kagan, D.; Orozco, J.; Wang, J. *Analyst* **2011**, *136*, 4621.

63. Campuzano, S.; Orozco, J.; Kagan, D.; Guix, M.; Gao, W.; Sattayasamitsathit, S.; Claussen, J. C.; Merkoçi, A.; Wang, J. *Nano Lett.* **2012**, *12*, 396.

64. Guix, M.; Orozco, J.; García, M.; Gao, W.; Sattayasamitsathit, S.; Merkoçi, A. A.; Escarpa, A.; Wang, J. *ACS Nano* **2012**, *6*, 4445.

65. Gao, W.; Sattayasamitsathit, S.; Uygun, A.; Pei, A.; Ponedal, A.; Wang, J. *Nanoscale* **2012**, *4*, 2447.

66. Esteban-Fernández de Ávila, B.; Pedrero, M.; Campuzano, S.; Escamilla-Gómez, V.; Pingarrón, J. M. *Anal. Bioanal. Chem.* **2012**, *403*, 917.

67. Pei, R.; Cui, X.; Yang, X.; Wang, E. *Talanta* **2000**, 53, 481.

68. Gilligen, J. J.; Schuck, P.; Yergey, A.L. *Anal. Chem.* **2002**, 74, 2041.

69. James, T. D.; Phillips, M. D.; Shinkai, S. *Boronic Acids in Saccharide Recognition*, RSC Publishing: Dorchester, UK, 2006.

70. Wang, W.; Gao, X. M.; Wang, B. H. *Current Organic Chem.* **2002**, *14*, 1285.

71. James, T. D.; Sandanayake, K. R.A.S.; Shinkai, S. *Angew. Chem. Int. Ed.* **1996**, *35*, 1910.

72. Kikuchi, A.; Suzuki, K.; Okabayashi, O.; Hoshino, H.; Kataoka, K.; Sakurai, Y.; Okano, T. *Anal. Chem.* **1996**, *68*, 823.

73. Pickup, J. C.; Hussain, F.; Evans, N. D.; Rolinski, O. J.; Birch, D. J. S. *Biosens. Bioelectron.* **2005**, *20*, 2555.

74. Takahashi, D.; Hirono, S.; Hayashi, C.; Igarashi, M.; Nishimura, Y.; Toshima, K. *Angew. Chem. Int. Ed.* **2010**, *49*, 10096.

75. Abad, J. M.; Velez, M.; Santamaria, C.; Guisan, J. M.; Matheus, P. R.; Vazguez, L.; Gazaryan, I.; Gorton, L.; Gibson, T.; Fernandez, V. M. *J. Am. Chem. Soc.* **2002**, *124*, 12845.

76. Aytac, S.; Kuralay, F.; Boyacı, I. H.; Unaleroglu, C. *Sens. Actuat. B: Chem.* **2011**, *160*, 405.

77. Lorand, J. P.; Edwards, J. O. *J. Org. Chem.* **1959**, *24*, 769.

78. Tsukagoshi, K.; Shinkai, S. *J. Org. Chem.* **1991**, *56*, 4089.

79. Francesconi, K. A.; Pannier, F. *Clin. Chem.* **2004**, *50*, 2353.

80. Fang, H.; Kaur, G.; Wang, B. *J. Fluorescence* **2004**, *14*, 481.

81. Park, S.; Boo, H.; Dong Chung, T. *Anal. Chim. Acta*, **2006**, *556*, 46.

82. Kabilan, S.; Marshall, A. J.; Sartain, F. K.; Lee, M. –C. Hussain, A.; Yang, X.; Blyth, J.; Karangu, N.; James, K.; Zeng, J.; Smith, D.; Domschke, A.; Lowe, C. R. *Biosens. Biolectron.* **2005**, *20*, 1602.

83. Zhao, G.; Pumera, M. *Phys. Chem. Chem. Phys.* **2012**, *14*, 6456-6458.

84. Polsky, R.; Harper, J. C.; Wheeler, D. R.; Arango, D. C.; Brozik, S. M. *Angew. Chem. Int. Ed.* **2008**, *47*, 2631.

85. Ma, Y.; Yang, X. *J. Electroanal. Chem.* **2005**, *580*, 348.

86. Torun, Ö.; Dudak, F. C.; Baş, D.; Tamer, U.; Boyacı, İ. H. *Sens. Actuat. B: Chem.* **2009**, *140*, *597*.

87. Kagan, D.; Benchimol, M. J.; Claussen, J. C.; Chuluun-Erdene, E.; Esener, S.; Wang, J. *Angew. Chem. Int. Ed.* **2012**, *51*, 7637.

88. Gao, W.; Pei, A.; Wang, J. *ACS Nano* **2012**, *6*, 8432.

89. Gao, W.; Sattayasamitsathit, S.; Manesh, K. M.; Weihs, D.; Wang, J. *J. Am. Chem. Soc.* **2010**, *132*, 14403.

90. Wang, J.; Gao, W. *ACS Nano*, **2012**, *6*, 5745.

91. Sun, X. –Y.; Liu, B.; Jiang, Y. –B. *Anal. Chim. Acta* **2004**, *515*, 285.

92. Li, S.; Davis, E. N.; Anderson, J.; Lin, Q.; Wang, Q. *Biomacromolecules* **2009**, *10*, 113.

93. Springsteen, G.; Wang, B. *Chem. Commun.* **2001**, *17*, 1608.

94. Cannizzo, C.; Amigoni-Gerbier, S.; Larpent, C. *Polymer* **2005**, *46*, 1269.

95. Springsteen, G.; Wang, B. *Tetrahedron* **2002**, *58*, 5291.

96. Lee, K.; Asher, S.A. *J. Am. Chem. Soc.* **2000**, *122*, 9534.

97. Zhao, Y.; Trewyn, B.G.; Slowing, I.I.; Lin, V.S.Y. *J. Am. Chem. Soc.* **2009**, *131*, 8398.

98. van den Heuvel, M.G.L. Dekker, C. *Science*, **2007**, *317*, 333.

99. Wulff, G. *Angew. Chem., Int. Ed.* **1995**, *34*, 1812.

100. Mosbach, K.; Ramström, O. *Nat. Biotechnol.* **1996,** *14*, 163.

101. Chen, L.; Xu, S.; Li, J. *Chem. Soc. Rev.* **2011**, *40*, 2922.

102. Blanco-López, M. C.; Lobo-Castañón, M. J.; Miranda-Ordieres, A. J.; Tuñón-Blanco, P. *Trends Anal. Chem*. **2004**, *23*, 36.

103. Merkoci, A.; Alegret, S. *Trends Anal. Chem*. **2002**, *21*, 717.

104. Piletsky, S. A.; Turner, A. P. F. *Electroanalysis* **2002**, *14*, 317.

105. Kriz, D.; Ramstroem, O.; Svensson, A.; Mosbach, K. *Anal. Chem*. **1995**, *67*, 2142.

106. Ansell, R.J.; Ramström, O.; Mosbach, K. *Clin. Chem.* **1996**, *42*, 1506.

107. Malitesta, C.; Losito, I.; Zambonin, P.G. *Anal. Chem.* **1999**, *71*, 1366.

108. Menaker, A.; Syritski, V.; Reut, J.; Opik, A.; Horvath, V.; Gyurcsanyi, R. E. *Adv. Mater*. **2009**, *21*, 2271.

109. Lautner, G.; Kaev, J.; Reut, J.; Öpik, A.; Rappich, J.; Syritski, V.; Gyurcsányi, R. E. *Adv. Funct. Mater*. **2011**, *21*, 591.

110. Zhao, G. and Pumera, M. *Chem. Asian J*. **2012**, 7, 1994.

Chapter 5 Catalytic Microengines for Environmental Monitoring and Remediation

5.1 The environmental impact of micro/nanomotors

5.1.1 Introduction

The propulsion of nanoscale objects represents a major challenge and opportunity, and has thus stimulated considerable research efforts.[1-12] Tremendous progress has been made recently towards the fabrication of micro/nano motors that can be propelled by different mechanisms, such as self-electrophoresis,[13-15] bubble propulsion,[16-21] diffusiophoresis,[22-25] and by using external stimuli such as light,[26,27] magnetic[28-32] or ultrasound[33,34] fields. Inspired by the 'Fantastic Voyage' movie, early efforts in synthetic nanomachines have focused on diverse biomedical applications.[35-38] These include targeted drug delivery,[39-41] the manipulation and isolation of cells,[42-44] bioimaging,[45] nanosurgery and nanodrilling,[46] and very recently intracellular propulsion.[47] However, we will demonstrate that micro/nanomachines could also have a profound impact upon the environmental field.

Environmental sustainability represents a major challenge that our planet is currently facing. Human activity during the era of industrialization has resulted in excessive emissions of hazardous pollutants into our water and air resources. Aquatic ecosystems, which are crucial for sustainable development and for human well-being, have thus been severely threatened throughout the globe. The continued environmental degradation, along with the rapid population growth and increasing demands for clean water, place urgent needs for new technologies and

innovative solutions aimed at protecting our water and air resources and ensuring widespread access to clean and affordable water.[48,49]

Nanotechnology presents significant opportunities for a wide range of environmental applications, and has already made a profound impact in the environmental field. For example, advanced nanosensors and reactive nanomaterials have been developed to facilitate the detection of major pollutants[50] or the remediation of contaminated sites,[48,51,52] respectively. These environmental applications have relied on the attractive properties of nanomaterials, including high surface area, catalytic and antimicrobial activity, size-dependent tunable optical behavior and surface chemistry.[49]

While nanotechnology has been shown extremely useful for addressing environmental problems for nearly two decades, related applications of nanomachines have realized only over the past three years. These recent proof-of concept efforts have demonstrated that synthetic nanomachines can open the door to diverse environmental applications.[53-56] The objective of this section is to show how the movement of polymer based microengines adds a new and powerful dimension to environmental monitoring and remediation. Such applications benefit also from the ability of these tiny machines to penetrate otherwise inaccessible locations.

5.1.2 Environmental monitoring

Environmental monitoring describes activities aimed at characterizing the quality of water and air resources by measurements of chemical, biological or physical variables. The major goals of environmental monitoring are to establish the current status of an environment, to warn about sudden changes and incoming threats, to monitor remediation processes, and to establish trends and baselines in environmental parameters. Major challenges for such effective environmental monitoring activities are high sensitivity towards extremely low concentrations of toxic micropollutants, enhanced specificity and stability in complex natural water media (with little or no sample preparation steps), and fast response times.[49] On-site and real-time analytical

measurements have been introduced in recent years to address the limitations of discrete sample collection and subsequent laboratory analysis.[57] Nanomachines could offer innovative concepts for effective environmental monitoring. For example, the large cargo-towing force of modern micromachines, along with their ease of surface functionalization, can enable new target isolation (*'Capture-Transport'*) strategies.[58] Mimicking biological behavior, nanomachines could use chemotactic search strategies to trace chemical plumes to their source. Catalytic micromotors have been shown to display a chemotactic behavior in the presence of a gradient of the fuel concentration, with a directed movement and increased speed toward higher peroxide concentrations.[59,60] Changes in the swimming behavior in the presence of hazardous chemicals can offer direct and timely visualization of chemical stress. Finally, autonomous mobile nanomachines hold considerable promise for monitoring inaccessible locations or hostile environments.

5.1.3 Environmental remediation

The removal and destruction of pollutants from contaminated media is an important focus of environmental sustainability.[61] The field of water purification and wastewater treatment has grown rapidly during the 1980s and 1990s due to the urgent demands for sustainable water resources and new stringent water quality regulations. Environmental remediation uses a wide variety of methods for cleaning up wastewater, contaminated groundwater, surface water, or sediments. Nanotechnology-based remediation methods (nanoremediation) entail the application of reactive nanomaterials for transformation and detoxification of pollutants toward purifying our water and air resources.[49] In particular, reactive nanomaterials have attractive properties that enable the efficient transformation of toxic pollutants.[51,52]

Nanomachines offer distinct advantages over conventional nanoremediation agents. Such tiny machines add a new dimension based on motion to decontamination processes, lead to new *in situ* and *ex situ* nanoremediation protocols, and have the potential to reduce the cleanup time

and overall cleanup costs. In particular, the continuous movement of such nanoscale objects can be used for transporting reactive (water-purification) nanomaterials throughout contaminated samples, for releasing remediation agents over long distances, and for imparting significant mixing during detoxification processes. Eventually, one would expect autonomous multi-functional ‘remisense’ nanomachines, coupling the remediation and sensing of pollutants into the same platform, analogous to theranostic particles used for biomedical applications. As will be illustrated below, these capabilities open up the door for efficient cost-effective routes for environmental remediation.

5.2 Artificial microfish for water quality monitoring

5.2.1 Introduction

Pollution by aquatic contaminants is among the most challenging issues to our ecosystems and living environment. One of the oldest and most widely used approaches for testing the quality of our water resources relies on changes in the swimming behavior and lifetime expectancy of live fish in the presence of toxic substances.[62-64] Such monitoring of fish survival and performance provides qualitative and quantitative information about the quality of the water system. The main technical drawbacks associated with fish-toxicity assays are standardization problems of the organisms, lack of reproducibility and the requirement for skilled operators.[65,66] In addition, there are growing ethical concerns and related regulations and costs that hinder live-fish lethal bioassays.

Here we demonstrate a novel nanotechnological alternative for assessing the water quality and indicating the presence of aquatic pollutants based on the use of enzyme-powered artificial 'microfish'. The motion of synthetic micromotors has received a considerable fundamental and practical interest over the past decade.[1-10] Bubble-propelled catalytic and biocatalytic tubular microengines have been particularly useful for various practical applications due to their efficient propulsion in various real-life media.[15-17,42] Biocatalytic layers, based on immobilized catalase, have been shown to be attractive alternative to catalytic Pt metal layers for propelling such hydrogen-peroxide powered microengines.[18,67]

The new microengine-based water toxicity testing relies on changes in the propulsion behavior associated with the inhibition of the catalase biocatalytic layer by common pollutants such as heavy metals, pesticides and herbicides (Figure 5.2.1). Enzyme-based inhibition assays have been widely used for measuring toxins in diverse matrices based on the decreased biocatalytic activity that leads to lower optical or electrical signals.[68-72] The antioxidant activity of

catalase has been suggested as a vital biomarker of fish intoxication when exposed to chemical pollutants.[73] In the following sections we will illustrate that well defined changes in the swimming performance and lifetime expectancy (survival) of self-propelled biocatalytic microengines are observed in the presence of a wide variety of organic and inorganic contaminants known to inhibit the catalase activity.[68,74,75] Optical tracking of the movement of the artificial microfish thus offers a simple and direct visualization of these toxin-induced changes in the swimming performance. Such real-time tracking of changes in the swimming behavior of the artificial microfish has been illustrated upon exposure to model aquatic pollutants, including the heavy metals mercury and copper, the sodium-azide (NaN_3) pesticide and the aminotriazole herbicide, with the peroxide fuel acting also as the substrate of such motor-based inhibition assays. Copper and mercury are of special concern among metal pollutants, owing to their considerable toxicity to aquatic animals at relevant concentrations.[62] Quantitative assessment of the toxin-microswimmer effect is obtained by estimating ecotoxicological parameters, such as 50% exposure concentration effect (EC_{50}) and survival time (T_{50}), commonly used in live-fish water testing.[62] The observed trends in the EC_{50} and T_{50} values thus reflect the adverse effects of toxins upon the propulsion behavior and correlate well with their known inhibitory action.[62,75]

The new nanoswimmer water-toxicity assay strategy offers direct monitoring of aquatic contaminants down to the micromolar levels and addresses standardization and reproducibility problems and major ethical concerns associated with live-fish toxicity bioassays. Unlike live fish, artificial micromotors are not subject to differences in metabolic and excretion rates, or stress level, and can be mass-produced and functionalized in a highly reproduced fashion. This novel nanomachine-based toxicity assay approach thus represents an attractive environmentally-friendly nanotechnological alternative to the common use of aquatic organisms for testing the quality of our water resources.

5.2.2 Experimental section

Preparation of the artificial microfish

Tubular microengines were prepared using the same electrodeposition protocol in Chapter 3.2.2.[67] Poly(3,4-ethylenedioxythiophene) (PEDOT) microtubes were electropolymerized at +0.80 V using a charge of 0.06 C from a plating solution containing 15 mM EDOT, 7.5 mM KNO_3 and 100 mM sodium dodecyl sulfate (SDS); subsequently, gold was plated at -0.9 V for 1 C from a commercial gold plating solution (Orotemp 24 RTU RACK; Technic Inc.).

Immobilization of Catalase

The inner Au layer of the bilayer microtubes was functionalized first with a mixed MUA/MCH alkanethiol monolayer. A solution mixture of 2.5 mM MUA and 7.5 mM MCH was prepared in ethanol. The microtubes were incubated in the MUA/MCH solution overnight. After rinsing the tubes with ethanol for 5 min, they were transferred to an eppendorf vial containing a 200 µl PBS buffer (pH 5.5) solution with the coupling agents 1-Ethyl-3-[3-dimethylaminopropyl] carbodiimide hydrochloride (EDC), N-hydroxylsulfosuccinimide (Sulfo-NHS) at 0.4 M and 0.1 M respectively, and the catalase enzyme (2 mg/mL). This incubation was carried out for 7 h at 37 ºC, followed by two 15 min rinsing steps with PBS solution (pH 5.5), containing 0.05 wt % SDS. Finally, the microengines were washed repeatedly by centrifugation at 6000 rpm for 3 min with water for three times to remove the excess of catalase from the solution, and were suspended in 5.5 pH buffer and stored at 4º C until use.

Experimental setup

Experiments were performed by casting equal volumes (~2.0 µl) of solutions containing microfish, sodium cholate (NaCh) and hydrogen peroxide solutions on a glass slide to obtain final concentrations of 5% NaCh and 2.0% H_2O_2. Once the movement of the artificial microfish was established, a dose of the target pollutant (containing also the same peroxide and NaCh levels) was added to obtain the desired concentration of pollutant. Movement of the microfish was

recorded first in the unpolluted solution and subsequently after adding the contaminant for at least 10 min, in one minute intervals.

5.2.3 Results and discussion

The artificial microfish were fabricated by a template-based electrodeposition of PEDOT/Au bilayer microtubes.[67] Such microfish have a defined conical microtube configuration, with a length of ~8 μm, outer diameters of 2.0 and 1.2 μm, along with inner openings of 1.6 and 0.8 μm.[67] Figure 5.2.1 depicts a layout of this synthetic nanoswimmer, illustrating the chemistry used for linking catalase to its inner gold surface along with a cross section of the microengine and the corresponding surface layers. The outermost polymeric tubular layer was prepared by electropolymerization of the EDOT monomer on the walls of the membrane micropores, followed by electrodeposition of the gold metallic layer. The enzyme was anchored to the gold layer *via* a common carbodiimide (EDC)/N-hydroxysuccinimide (NHS) chemistry through a mixed self-assembled binary monolayer of 11-mercaptoundecanoic acid (MUA)/6-mercaptohexanol (MCH) alkanethiols. The biocatalytic decomposition of the hydrogen peroxide fuel at the inner enzymatic layer of the microtube thus generates the oxygen bubble thrust and leads to an efficient swimming motion of the microfish. In the presence of chemical stress (*e.g.*, heavy metals, pesticides and herbicides), such biocatalytic activity of catalase is inhibited, resulting in a lower bubble frequency and an impaired locomotion of the artificial microfish (Figure 5.2.1, bottom). Time-dependent optical tracking of changes in the microfish speed and of its lifetime (survival), thus provide useful information on the inhibitory activity and toxicity of the corresponding pollutants. Unlike earlier motion-based biosensing applications involving the attachment of bioreceptors,[35,42] no additional surface functionalization is required for realizing the microfish-based water-quality testing.

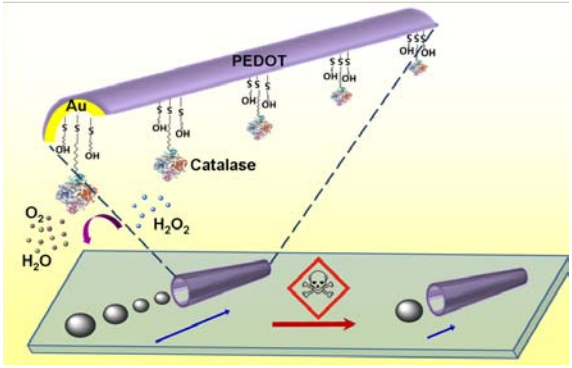

Figure 5.2.1 Scheme illustrating the pollutant effect on the microfish locomotion speed through inhibition of the catalase biocatalytic layer along with the protocol used for immobilizing the enzyme at the inner gold surface of the tubular microengine through a mixed MUA/MCH self-assembled monolayer.

The propulsion efficiency of artificial biocatalytic microswimmers depends on the influence of the toxin upon the activity of the enzyme powering the motor. The locomotion and survival of the artificial microfish are impaired by exposure to a broad range of contaminants *via* inhibition of the catalase activity. Such changes in the movement of the microfish can be readily visualized and tracked in real time using optical microscopy images. The 8-μm length of our biocatalytic microengines thus offers a convenient visualization of these swimmers and direct tracking of the toxin-induced changes in the propulsion behavior. Such changes in the swimming performance and lifetime expectancy of microfish were evaluated by using model pollutants, representative of heavy metals, pesticides and herbicides contaminants.

The attenuated motion of the artificial microfish in the presence of these pollutants is clearly indicated by observing changes in the ejection of oxygen bubbles (from the tail end of the microfish) that are responsible for its efficient propulsion. For instance, Figure 5.2.2 displays time-lapse images illustrating changes in the microfish locomotion in the presence of three common contaminants. These images were recorded over a 3 s period following 0 (a), 2 (b) and 4 (c) min exposures to 0.2 mM Cu (A), 25 μM NaN_3 (B) and 625 mM aminotriazole (C). For example, navigation in the 0.2 mM copper solution resulted in a sharp decrease in the number of

oxygen bubbles (observed during this 3 s period) from ~20 to 7 and 2 following 2 and 4 min exposures, respectively (A). Similar changes in the bubble frequency and propulsion efficiency are observed following 2 and 4 min movement in the 25 μM NaN_3 (B) and 625 mM aminotriazole (C) solutions. The time-lapse images clearly illustrate the reliable real-time tracking of the changes in the swimming performance, including the diminished bubble ejection and greatly reduced speed in the presence of these chemicals. A dramatic change in the swimming behavior is thus observed after the 2 min exposure, with a nearly complete attenuation of the movement indicated following the 4 min exposure. However, no apparent change in the trajectory of the microswimmers accompanies these changes in the enzymatic activity.

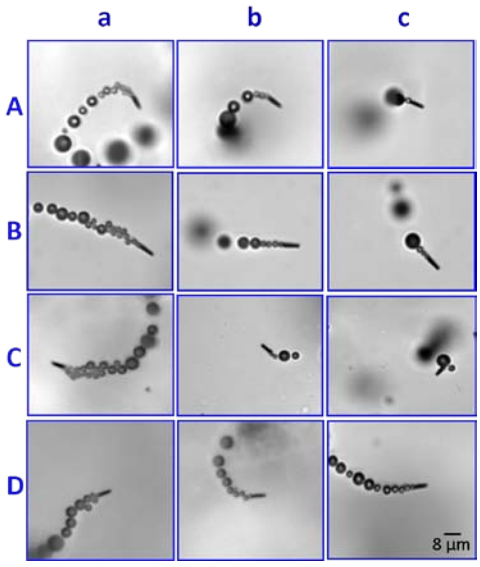

Figure 5.2.2 Toxin-induced changes in the swimming behavior. Time-lapse images over a 3 s period following a) 0, b) 2 and c) 4 min exposures of the microengines to different water pollutants: A) 0.2 mM Cu, B) 25 μM NaN_3 and C) 625 mM aminoriazole; (D) Control (blank solution). Substrate/fuel concentration, 2% hydrogen peroxide.

Figure 5.2.3 displays a comparative study of the changes in the propulsion behavior of the catalase-based microengine over a 10 min period in the presence of 4 common contaminants: mercury (black), sodium azide (Red), aminotriazole (Blue), and copper (purple). To account for the broad range of the toxicity of these contaminants and monitoring significant changes within the same short time scale, the level of these pollutants was adjusted to 100 μM Hg, 0.6 mM Cu,

25 µM sodium azide, and 625 mM aminotriazole. These toxin levels lead to a rapidly diminished propulsion efficiency with speed diminutions of about 70-75%, 80-85% and 90-95% within 1, 2, and 6 min exposures to these contaminants, respectively. For example, the presence of 0.6 mM Cu leads to a 95% diminution of the microfish speed within 4 min. A nearly complete loss of the swimming ability is thus observed in the presence of the 4 chemicals within the experimental time scale. In contrast, no apparent change in the propulsion behavior is observed during the same period in the absence of toxins (Green; control experiment). Also shown in Figure 5.2.3 (inset), are time-lapse images of the microfish locomotion before and after a 4 min navigation in the mercury solution. These images illustrate a substantially fewer ejected oxygen bubbles following such exposure to mercury.

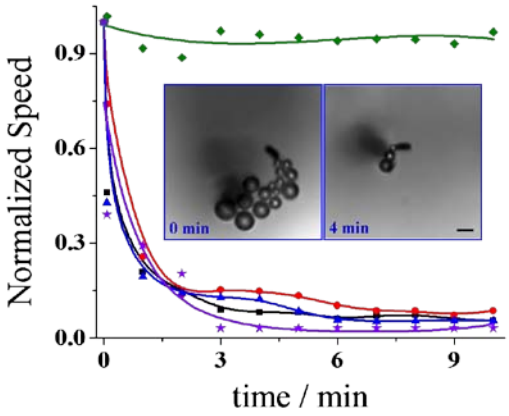

Figure 5.2.3 Changes in the swimming behavior of the artificial microfish as a function of time upon exposure to 100 µM Hg (black square), 0.6 mM Cu (purple stars), 25 µM sodium azide (red circle), 625 mM aminotriazole (blue triangle), and a control experiment without the toxins (green diamond). Curves were plotted by tracking the normalized microfish speed after exposure to the pollutants. Inset: time-lapse images of the microfish recorded after 0 and 4 min swimming in a 100 µM Hg solution. Scale bar, 6.0 µm.

Major drawbacks associated with live-fish toxicity assays are standardization problems of the organisms, lack of reproducibility, and the requirement for skilled operators.[65,66] To ensure reproducible results, the live fish used should be from the same source and of the same age. In contrast, the membrane template preparation of our artificial microtube swimmers leads to highly reproducible microengines and propulsion behavior.[67] The reproducibility and stability of the new

microfish-based water-quality testing approach were investigated by tracking the movement of multiple swimmers from the same batches and from different batches, following identical motor fabrication and surface-modification procedures. The results demonstrated highly reproducible propulsion behavior among different microfish in both unpolluted and polluted water samples. For example, a series of measurements involving 10 different batches of swimmers (and 5 swimmers from each batch) displayed a reproducible initial speed of 54.0 ± 3.5 μm/s. Such speed decreased to 32.6 ± 4.1μm/s after a 10 s exposure to a 5 μM Hg solution. The initial speed of the catalase-powered microengines remained constant for up to one week from their preparation (with variations lower than 10%), thus demonstrating their stability and potential use as reliable long-term pollution indicator.

Analogous to the common use of LD_{50} in live fish toxicity testing,[63] IC_{50} is used in enzyme-inhibition assays to estimate the inhibitor concentration leading to a 50% enzymatic inhibition, while EC_{50} is used as the ecotoxicological parameter assessing the behavioral response.[62] Herein we define EC_{50} and EC_{90} as the contaminant concentrations leading to 50% and 90% attenuation of the nanomotor locomotion within 2 and 10 min, respectively. Table 5.1 summarizes the experimental EC_{50} and EC_{90} values obtained for the catalase-powered microengine. Sodium azide displayed the lower EC_{50} value (2.5 μM), followed by Hg, Cu and aminotriazole with 50% speed decays at 50 μM, 0.2 mM and 375 mM, respectively. The EC_{90} values are 25 μM, 100 μM, 0.6 mM and 625 mM for NaN_3, Hg, Cu and aminotriazole, respectively. Furthermore, we define T_{50} as the time taken for the microfish speed to decrease by 50% (from the initial one) in the presence of the inhibitor at EC_{90}. T_{50} values of 12, 15, 24 and 33s have thus been estimated for aminotriazole, Hg, Cu and NaN_3, respectively. The extremely short analysis times of the artificial microfish approach (from few seconds to 10 min), compared to 24 - 92 hours for conventional live-fish toxicity assays,[62] make the new nanomotor strategy extremely attractive for rapid screening for water pollution and hazards.

Table 5.1 Summary of the microfish toxicity indicators data for the individual pollutants tested.

Pollutant	**Range tested**	**EC_{50}**	**EC_{90}**	**T_{50}, s**	**T_{90}, s**
Hg	5.0-200 µM	50 µM	100 µM	15	180
Cu	0.2-1.0 mM	0.2 mM	0.6 mM	24	135
NaN_3	2.5-25 µM	2.5 µM	25 µM	33	375
Aminotriazole	375-750 mM	375 mM	625 mM	12	276

Figure 5.2.4 presents the behavior response of the artificial microfish after a 2 min exposure to different concentrations of heavy metals (a) and pesticides and herbicides (b). Both mercury and copper display a dramatic effect upon the microfish swimming behavior, with a substantial and rapid speed diminution of nearly 80% at 50 µM Hg and 300 µM Cu, followed by a leveling off up to 140 µM Hg and 600 µM Cu, and a nearly complete (~95%) attenuation of the movement around 210 µM Hg and 1000 µM Cu (Figure 5.2.4a). These results indicate that Hg is producing a similar effect on the microfish swimming performance as Cu does at 4-6 fold higher concentrations. This is in agreement with live-fish bioassays that display a higher effect of Hg on the lethargic and erratic swimming behavior of live fish, compared to Cu, starting within 48 h exposure to 100 µg/L Hg and 800 µg/L Cu, respectively.[62] The most widely reported ecologically sensitive parameter has been the swimming distance in the presence of the EC_{50} levels of 1.2 and 12.3 µg/L for Hg and Cu, respectively.[62] Figure 5.2.4b illustrates the effect of NaN_3 pesticide and aminotriazole herbicide by varying their levels from 2.5 to 25 µM (NaN_3) and from 375 to 750 mM (aminotriazole). A similar behavioral response is observed for these pollutants with a gradual decrease of the original speed by up to 15% at around 25 µM NaN_3 and 625 mM aminotriazole, respectively. Yet, NaN_3 displays the stronger effect upon the swimming behavior of the microfish, considering its greatly lower concentration range.

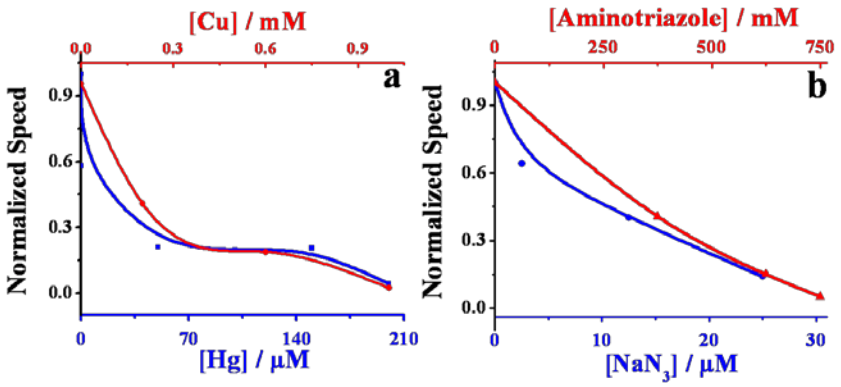

Figure 5.2.4 Effect of the pollutant concentration upon the swimming performance of the microfish, as indicated from changes in the locomotion speed after a 2 min exposure. (a) Influence of the metals Hg (blue) and Cu (red) over the 0.05-0.20 mM and 0.2-1.0 mM ranges, respectively. (b) Influence of NaN_3 (blue) and aminotriazole (red) over the 2.5 - 25 µM and 375 - 750 mM ranges, respectively.

Measurements of the life expectancy of the artificial microfish were further used to evaluate its behavior response in the presence of common contaminants. To assess the life expectancy of the artificial swimmer, we defined the survival time as the time period, from the initial exposure to a given toxin concentration, taken for the microfish to lose its directional movement and reach its minimal speed**.** Figure 5.2.5 displays the dependence of the survival time of the microfish upon the concentration of the different pollutants. As expected, the survival time is strongly dependent upon the level of these contaminants, *e.g.*, decreasing rapidly from 6 min to 30 s upon raising the mercury concentration from 50 to 200 µM. Different concentration ranges were used for the different pollutants, reflecting their broad range of toxicities. In all cases, the microfish survival time is lower than 10 min, with the shortest time of 10 s observed for 750 µM aminotriazole and 200 µM Hg. Overall, the data of Figure 5.2.5 indicate that NaN_3 displays the strongest effect upon the survival time of the artificial microfish (with short survival times at lowest concentrations), followed by Hg, Cu, and aminotriazole.

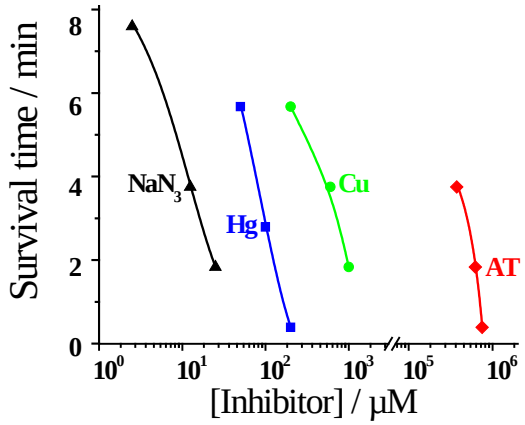

Figure 5.2.5 Dependence of the survival time of the artificial microfish upon the pollutant concentration (2.5-25 µM NaN_3, black; 50-200 µM Hg, blue s; 0.2-1.0 mM Cu, green; and 375-750 mM aminotriazole (AT), red). Survival time is defined as the time takes for the fish to lose its directional movement (and reaches its minimal speed).

5.2.4 Conclusions

We have presented a new simple and cost-effective nanotechnology strategy for water-quality testing based on changes in the propulsion behavior and lifetime of artificial biocatalytic microswimmers in the presence of aquatic pollutants, in a manner analogous to changes in the swimming behavior and survival of natural fish used for toxicity testing. Various model organic and inorganic pollutants have displayed a significant concentration-dependent effect upon the swimming behavior of the microfish swimmer. Such use of self-propelled artificial swimmers allows direct visualization (optical tracking) of the changes in the swimming behavior in response to the presence of chemical stress. Such changes in the swimming behavior reflect the inhibition of the biocatalytic layer responsible for the bubble-propulsion thrust, and hence the toxin-induced hindered movement and life expectancy of these tubular microengines. Similar to the common use of live fish, the microfish water-quality testing involves changes in the propulsion behavior and lifetime of biocatalytic microengines. While various toxins display different effects upon the propulsion behavior (as common also in live-fish testing), the new microfish method does not offer a selective response, as expected for enzyme inhibition processes.[68] Other non-toxic compounds or salts are not expected to influence the movement of bubble-propelled microtubular

engines.[17,76] The minimal salt effect[76] indicates suitability of the microfish for monitoring a variety of natural water systems with different ionic strengths. Self-driven millimeter-sized motors (based on changes in the surface tension), in contrast, display different speeds in the presence of organic solvents such as acetonitrile or *N*,*N*′-dimethylformamide.[77] The composition of our enzyme-powered polymer-based microengines[67] makes these microfish highly compatible and environmentally friendly. By addressing major drawbacks and ethical concerns associated with live-fish toxicity assays the new man-made nanomachine strategy offers an attractive alternative to the common use of aquatic organisms for water-quality testing.

5.3 Hydrophobic alkanethiol-coated microsubmarines for oil remediation

5.3.1 Introduction

In this section, we demonstrate the first example of using functionalized nanomachines towards environmental remediation of contaminated water. In particular, we illustrate how the deliberate modification of the rough outer surface of microengines with highly hydrophobic long-chain self assembled alkanethiol monolayers offers considerable promise for the capture, transport and removal of oil droplets from water samples. Oil is a major source of ocean pollution and ground water contamination. The presence of oils in wastewaters as a product of various manufacturing processes is common in different industries. Furthermore, episodes of major water pollution, caused by oil spillage, result in the release of millions of tons each year. For example, the 1989 *Exxon Valdez* and 2010 *Deepwater Horizon* incidents spilled millons of gallons of crude oil.[78,79] The removal of oils and organic solvents from contaminated water is thus of considerable importance for minimizing the environmental impact of these pollutants.

Substantial efforts have thus been devoted to develop effective tools towards the remediation and clean-up of oil spills. Although oils in wastewater plants are mostly removed by a mechanical separation, other methods have been proposed to address related pollution episodes.[80,81] However, most of these methods lack the desired selectivity and efficiency and are not cost-effective or environmental friendly. Accordingly, the development of new highly effective oil-water separation methods is highly desired.

Different synthetic and natural materials have been proposed as possible sorbents for oil removal. Surfaces with superhydrophobic properties have recently attracted particular interest for oil-water separation owing to their high efficiency and selectivity,[80-84] although their high cost, complex preparation processes, and scalability issues, have hindered their practical

applications.[78] These hydrophobic surfaces tend to repel water while strongly interact with nonpolar or oily liquids, which firmly adhere to textured interfaces.[83] Both the micro-nano-hierarchical texture and the chemical composition are essential for promoting the superhydrophobic character necessary for effective oil removal. The surface polarity and roughness are thus expected to influence the extent of the oil-surface interaction.[85,86] Self-assembled monolayers (SAMs), formed by the spontaneous and strong chemisorption of alkanethiols at gold or silver surfaces, have been particularly useful for transforming these surfaces into superhydrophobic interfaces.[86] Guo et al.[87] reported that ZnO hydrophilic surfaces become superhydrophobic after exposure to an octadecanethiol solution. Tailoring the length of the alkanethiol chain has allowed the control of the surface polarity and hence tuning the partition of hydrophobic drugs.[88] The choice of the ending functional group is also vital for tailoring the polarity of the SAMs. For example, water contact angle studies reveal that methyl-terminated SAMs lead to hydrophobic surfaces, while hydroxyl terminated ones provide wettable surfaces.[89] However, there are no reports of integrating these oil-sorption properties into self-propelled microengines and using such superhydrophobic nanomotors to facilitate the capture, transport and separation of oil droplets. Autonomously moving synthetic nanomotors have recently been employed for the pick-up and transport of diverse payloads, ranging from cancer cells to drug-loaded polymeric spheres,[39,42] but not in connection to the isolation of oily contaminants.

The method herein presented is based on the creation of a SAM-modified microtubular engine able to strongly interact with oily liquids *via* adhesion and permeation onto its long alkanethiol coating. As illustrated in Figure 5.3.1, the new catalytic microsubmarine is template-prepared by electroplating poly(3,4-ethylenedioxythiophene) (PEDOT)/Pt bilayer followed by e-beam deposition of Ni/Au and subsequent functionalization with the SAM. In particular, dodecanethiol-coated Au/Ni/PEDOT/Pt microsubmarines are shown in the following sections to offer an effective capture and transport of oil droplets from aqueous media. The influence of the

alkanethiol chain length upon the oil-nanomotor interaction and the collection efficiency has been examined using SAMs of different chain lengths, i.e. hexanethiol (C-6), dodecanethiol (C-12) and octadecanethiol (C-18). The optimal C-12 superhydrophobic SAM-coated microsubmarine has shown a strong prolonged interaction with large oil droplets (attached to the glass-slide surface) along with the effective pickup and transport of multiple small oil droplets present in an oil-contaminated water sample. Unmodified microengines did not show such affinity to oil droplets. These results demonstrate that SAM-functionalized microsubmarines can be useful for facile, rapid and high efficient collection of oils in water samples. This high oil-absorption ability indicates considerable potential for environmental remediation of oil-contaminated water samples, and other contaminated water systems.

5.3.2 Experimental section

Synthesis of multilayer microsubmarines

The multilayer microtubes were prepared using the same electrodeposition protocol as Chapter 3.2.2.[67] Briefly, PEDOT microtubes were electropolymerized up to 0.1 C at +0.80 V from a plating solution containing 15 mM EDOT monomer, 50 mM SDS and 7.5 mM KNO_3. The inner Pt tube was deposited galvanostatically at -2 mA for 600 s from a commercial platinum plating solution (Platinum RTP; Technic Inc, Anaheim, CA). After dissolution and washing steps, the microtubes suspension was evaporated onto glass slides before the sequential deposition of 10 nm Ti (adhesion layer), 15 nm Ni (magnetic layer), and 15 nm of Au (functionalization layer) over the microtubes by using electron beam deposition. These additional steps provide the necessary magnetic directional control and the appropriate gold surface for the later modification with self-assembled monolayers.

Microsubmarines modification

The external gold surface of the microsubmarines was modified by immersion in a 0.5 mM dodecanethiol in absolute ethanol (from Sigma-Aldrich), after which the resulting

monolayer-modified microsubmarines were washed with Milli-Q water and isolated by centrifugation at 6,000 rpm during 4 min. All experiments were carried out at room temperature. Study of the chemical structure effect, e.g. length chain and terminal groups, on the speed was performed with different thiols, including hexanethiol, mercaptohexanol, dodecanethiol and octadecanethiol, all received from Sigma-Aldrich and were dissolved in ethanol. Bare microsubmarines without the monolayer were also used as control experiments.

5.3.3 Results and discussions

The fabrication of the oil-sorption hydrophobic microsubmarines, depicted in Figure 5.3.1, involves a template-based electrodeposition of a PEDOT/Pt bilayer microtube and e-beam vapor deposition of the Ni and Au outer layers, essential for the magnetic navigation control and surface functionalization, respectively. As illustrated in Figure 5.3.1A(d), such functionalization involves the formation of a superhydrophobic layer by self-assembly of long alkanethiols chains on the rough outer gold surface. A SEM image of the unmodified microengine (Figure 5.3.1B) indicates a rough surface, characteristic of nitrate-doped PEDOT films. The template fabrication process results in 8 μm-long microtubes that are substantially smaller than common rolled-up tubular microengines.[43] The relative similar dimensions of microsubmarine and oil droplets (which range from ~1 to ~100 μm, depending on the emulsion composition) permit convenient real-time optical visualization of the oil-microengine interaction. Similar to recently developed PANI/Pt microengines,[17] the new template-prepared PEDOT/Pt microtubes propelled efficiently in different media *via* the expulsion of oxygen bubbles generated from the catalytic oxidation of hydrogen peroxide fuel at their inner Pt layer.[17] Several factors, such as additional Ni and Au layers influence the microengine speed. For example, and as expected for polymer/Pt microengines,[67] the fast speed of the PEDOT/Pt microengines (~420 μm/s average) is reduced by up to 50% after the e-beam deposition of the outer Ni/Au layers.

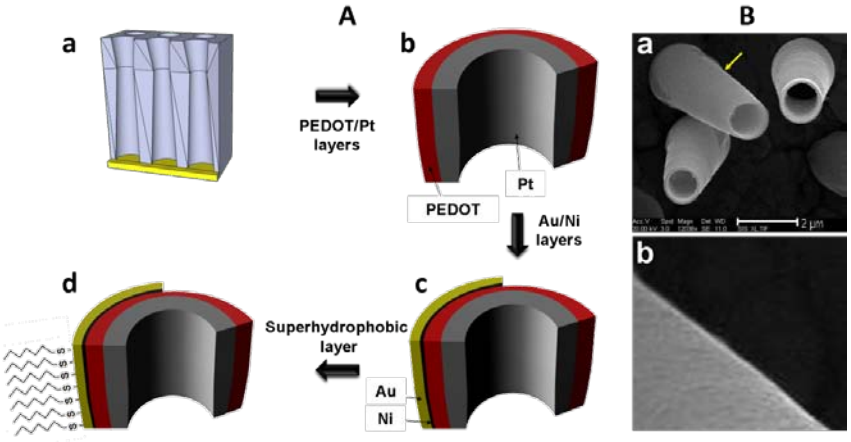

Figure 5.3.1 Fabrication and modification of the SAM-Au/Ni/PEDOT/Pt micromotors for environmental remediation. (A) A Cyclopore polycarbonate membrane is used as a template (a), PEDOT and Pt layers are electroplated into the template (b), Au and Ni layers are sputtered by E-beam (c) and a superhydrophobic layer is formed on the microsubmarine surface by incubation in a 0.5 mM n-dodecanethiol ethanolic solution (d). (B) SEM image of the resulting PEDOT/Pt microsubmarine (a) with a zoom in of the zone highlighted with a yellow arrow (b).

The resulting Au/Ni/PEDOT/Pt microsubmarines were then immersed in a 0.5 mM dodecanethiol ethanolic solution for 30 min to form the hydrophobic monolayers on the outer gold surface. Such surface modification of the Au/Ni/PEDOT/Pt microsubmarine resulted in an additional ~50% speed reduction, reflecting the partial blocking of the inner Pt catalytic layer.[90] However, the reduced speed is sufficient for transporting large cargoes in a manner analogous to our previously reported Au/Ni/PANI/Pt microengines.[91]

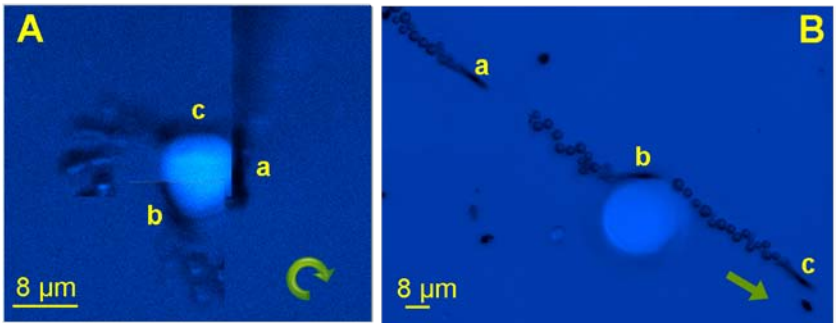

Figure 5.3.2 SAM-modified (A) and unmodified (B) microsubmarines in the presence of a stained olive oil droplet (attached to a glass slide). Images show (in a single overlaid image) the following sequential steps: approaching, contacting and spinning around (A, a-c) the droplet and approaching, contacting and leaving (B, a-c) the oil droplet, respectively. Fuel conditions (final concentration): 0.4 % NaCh and 10 % H_2O_2. Arrows indicate the microsubmarine trajectory.

Figure 5.3.2A shows the Au/Ni/PEDOT/Pt micromotor approaching, contacting and spinning around a stained olive oil drop firmly attached to a glass slide. The strong interaction between the SAM-modified microsubmarine and an oil droplet results in a continuous spinning of the modified engine around the droplet with an accelerated speed ranging up to 200 μm/s. It should be pointed out that such continuous high-speed spinning is observed even after a prolonged 20 min period. These data also confirm that the hydrogen peroxide fuel and the sodium cholate (NaCh) surfactant, essential for the microsubmarine movement, do not compromise its interaction with the oil droplet or the integrity of the SAM. In contrast, no such interaction is observed using an unmodified microsubmarine (Figure 5.3.2B). This bare Au/Ni/PEDOT/Pt micromotor moves rapidly, while approaching, contacting and bypassing the droplet.

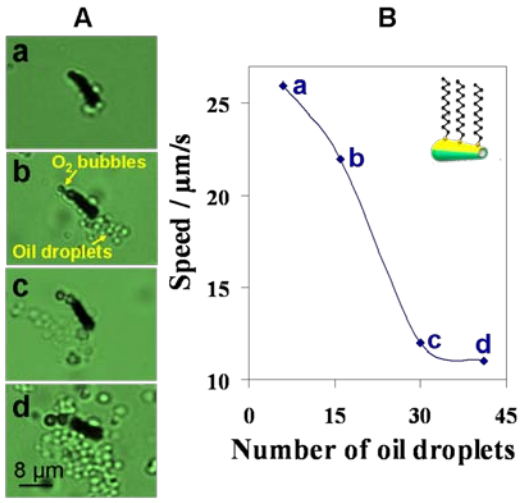

Figure 5.3.3 Dodecanethiol (C12-SAM)-modified microsubmarine carrying floating olive oil droplets. (A) Images a-d were taken after navigating in the water-oil (10% fuel) solution for 5, 12, 66 and 80 s, respectively (conditions, as in Figure 5.3.2). (B) The dependence of the microsubmarine speed upon the number of cargos (olive oil droplets). Inset, cartoon of the dodecanethiol-modified microsubmarine.

Efficient capture and transport of oil droplets has been observed when the modified microsubmarine navigates in contaminated water samples containing small ‘free-floating’ oil droplets. Figure 5.3.3 illustrates the capture and transport of multiple small olive oil droplets by the SAM-modified microsubmarine. The longer the navigation time the more oil droplets are

collected and confined onto the surface of the self-propelled micromotor. While around 5 droplets (1.7 ± 0.4 μm size) are captured and transported in Figure 5.3.3A after a 12 s navigation, around 40 droplets are attached to the motor surface following 80 s (Figure 5.3.3A(d). These observations demonstrate that these SAM-modified microengines provide high towing force for transporting efficiently approximately 10-fold their volume, and indicate considerable potential for oil removal applications. As expected from the increased drag force (Stokes's law),[92] the speed of the micromachine decreases upon increasing the cargo size (i.e., number of captured droplets). This is illustrated in Figure 5.3.3B that displays the dependence of the microsubmarine speed upon the number of transported oil droplets. The speed rapidly decreases from 26 to 12 μm/s upon increasing the number of droplets from 7 to 30 and then more slowly to 11 μm/s for 43 droplets. As common for nanomotor-based cargo pickup, the optimal motor speed will provide a trade-off between sufficient contact time and large contact rate.[93,94]

Particularly attractive is the ability to tailor the polarity of the microsubmarine surface *via* a judicious choice of the chain length of the n-alkanethiol coating and hence their capture and transport properties. Chain length, head groups, preparation time and other conditions (e.g. temperature) give rise to different SAM packing densities, configurations, and polarity.[33] The influence of the alkanethiol chain length upon the oil-nanomotor interaction was thus examined by modifying the microengine with SAMs of different alkanethiol lengths (C6, C12 and C18). A considerable difference in the microsubmarine-oil droplet interaction was observed using C6 and C12 SAM-coated microsubmarines. Notice, for example, the strong microsubmarine-oil interaction of the C12-modified microengine spinning around a large olive oil droplet (Figure 5.3.2B) compared to the weaker interaction experienced by the C6-modified motor, where no spinning around the droplet is observed. Similarly, we observe higher number of captured oil droplets using the C12 SAM modification (C) compared to the lower number of droplets attached to the C6-modified motor (B) and to the absence of captured droplets using the unmodified

microsubmarine (A). These results are consistent with the different surface wettability properties observed in contact angle studies of n-alkanethiols of different lengths.[95,96] Based on the higher hydrophobic character of long chain thiols, C18 SAM-coated microsubmarines expect to offer higher oil-adsorption capabilities. However, such C18-SAM modified microsubmarines hardly move owing to greater blocking of the inner Pt catalytic layer expected in the presence of longer alkanethiols.[91] Selective modification using alkane isonitriles[97] may be used to minimize the Pt blocking by the alkanethiol SAM thus retaining microengine speed.

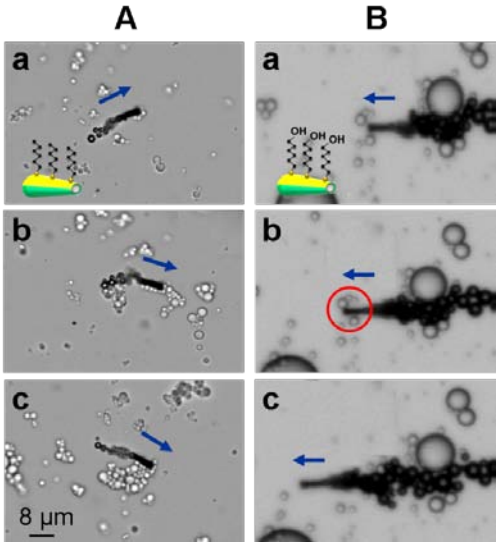

Figure 5.3.4 C6-SAM-modified microsubmarines with different head functional groups interacting with small olive oil droplets. Hexanethiol-modified microsubmarines are able to confine a payload of multiple oil droplets (A) (a, b and c, time-lapse images at different navigation times: 11, 50, and 73 seconds (for A) and 6.57, 6.66, and 6.71 seconds (for B). The corresponding mercaptohexanol-modified counterparts (B) are not able to pick such droplets (a, b and c images corresponds to approaching, contacting and leaving the droplets).

The influence of the SAM head group and hence surface polarity on the microsubmarines-oil interaction was examined by comparing the behavior of microengines coated with C6 SAM containing methyl and hydroxyl terminal groups using different time scales. Figure 5.3.4A (a-c) illustrates small droplets attached to the hexanethiol-modified microsubmarine upon navigating in the sample. In contrast, and as expected from wettability measurements using hydroxyl-terminated SAM,[89] the mercaptohexanol-modified

microsubmarines do not interact with the large or small olive oil droplets upon rapidly contacting them. It is remarkable that even prolonged navigation of the mercaptohexanol-modified microsubmarines does not lead to any capture of the oil droplets. Clearly, and as expected,[89] the polarity of the head functional group strongly influences the interaction between the modified microsubmarines and the oil droplets, and represents another key consideration (besides the chain length) when modifying the outer microengine surface.

5.3.4 Conclusions

We have presented the first example of using artificial nano/microscale machines for environmental remediation applications and specifically the tailoring of the surface of such self-propelled machines to interact strongly with oily liquids. The new SAM-Au/Ni/PEDOT/Pt micromotors thus offer a facile, rapid and highly efficient collection and transport of oil droplets in aqueous environments through the interaction with the hydrophobic alkanethiol monolayer coating. Comparison of different alkanethiol modifiers indicates that the dodecanethiol (C12-SAM)-modified microsubmarines offer the most favorable performance in terms of oil recovery and propulsion. Such high oil-absorption ability indicates considerable promise for the cleanup of contaminated water samples. The extent of the micromotor-oil interaction and the collection efficiency can be tuned by controlling the surface hydrophobicity through the use of different chain lengths and head functional groups. The new microsubmarine capability was demonstrated either by a strong interaction between the modified nanomotor and large oil droplets (attached to a glass slide), or by the collection and transport of multiple free-floating small olive and droplets of motor oil present in a contaminated water sample. These micromotor-oil interactions can be exploited in the suitable final disposition of oily wastes (or other organic solvents) by collecting them in a controlled fashion within a certain spatially separated zone. Simultaneous parallel movement of multiple SAM-modified microsubmarines holds promise for improving the efficiency of oil-removal processes. The new superhydrophobic microswimmers offer also

considerable promise for the isolation of hydrophobic molecules, *e.g.*, drugs, or for transferring target analytes between liquid-liquid immiscible interfaces, and hence great potential for diverse analytical microsystems. Multifunctional coatings of mixed (or multi) layers, coupling the preferential partition of hydrophobic compounds into the SAMs with additional functions (*e.g.*, biocatalysis), could lead to additional advantages towards on-the-fly 'capture and destroy' operation.

Chapter 5.1, is based, on the material as it appears in ACS Nano, 2014, by Wei Gao, Joseph Wang. Chapter 5.2, is based, on the material as it appears in ACS Nano, 2013, by Jahir Orozco, Victor García-Gradilla, Mattia D'Agostino, Wei Gao, Allan Cortés and Joseph Wang. Chapter 5.3, is based on, the material as it appears in ACS Nano, 2012, by Maria Guix, Jahir Orozco, Miguel Garcia, Wei Gao, Sirilak Sattayasamitsathit, Arben Merkoci, Alberto Escarpa, Joseph Wang. The dissertation author was the primary investigator and author of these papers.

5.4 References

1. Wang, J. *Nanomachines: Fundamentals and Applications*, Wiley-VCH, Weinheim, 2013.
2. Mallouk, T. E.; Sen, A. *Sci. Amer.* **2009**, *300*, 72–77.
3. Mirkovic, T.; Zacharia, N. S.; Scholes, G. D.; Ozin, G. A. *ACS Nano* **2010**, *4*, 1782–1789.
4. Wang, J. *ACS Nano* **2009**, *3*, 4–9.
5. Ozin, G. A. *Adv. Mater.* **2005**, *17*, 3011–3018.
6. Sanchez, S.; Pumera, M. *Chem.–Asian J.* **2009**, *4*, 1402–1410.
7. Mei, Y.; Solovev, A. A.; Sanchez, S.; Schmidt, O. G. *Chem. Soc. Rev.* **2011**, *40*, 2109–2119.
8. Ebbens, S. J.; Howse, J. R. *Soft Matter* **2010**, *6*, 726–738.
9. Wang, W.; Duan, W.; Ahmed, S.; Mallouk, T. E.; Sen, A. *Nano Today* **2013**, *8*, 531–554.
10. Sengupta, S.; Ibele, M. E.; Sen, A. *Angew. Chem. Int. Ed.* **2012**, *51*, 8434–8445.
11. Pumera, M. *Chem. Commun.* **2011**, *47*, 5671–5680.
12. Ghosh, A.; Fischer, P. *Nanoscale* **2011**, *3*, 557–563.
13. Paxton, W. F.; Kistler, K. C.; Olmeda, C. C.; Sen, A.; St. Angelo, S. K.; Cao, Y.; Mallouk, T. E.; Lammert, P. E.; Crespi, V. H. *J. Am. Chem. Soc.* **2004**, *126*, 13424–13431.
14. Fournier-Bidoz, S.; Arsenault, A. C.; Manners, I.; Ozin, G. A. *Chem. Commun.* **2005**, 441–443.
15. Burdick, J; Laocharoensuk, R; Wheat, P. M.; Posner, J. D.; Wang J. *J. Am. Chem. Soc.* **2008**, *130*, 8164–8165.
16. Mei, Y. F.; Huang, G. S.; Solovev, A. A.; Urena, E. B.; Monch, I.; Ding, F.; Reindl, T.; Fu, R. K. Y.; Chu, P. K.; Schmidt, O. G. *Adv. Mater.* **2008**, *20*, 4085–4090.
17. Gao, W.; Sattayasamitsathit, S.; Orozco, J.; Wang, J. *J. Am. Chem. Soc.* **2011**, *133*, 11862–11864.
18. Sanchez, S.; Solovev, A. A.; Mei, Y. F.; Schmidt, O. G. *J. Am. Chem. Soc.* **2010**, *132*, 13144–13145.
19. Wilson, D. A.; Nolte, R. J. M.; van Hest, J. C. M. *Nat. Chem.* **2012**, *4*, 268–274.
20. Zhao, G.; Pumera, M. *RSC Adv.* **2013**, *3*, 3963–3966.

21. Dong, B.; Zhou, T.; Zhang, H.; Li, C. Y. *ACS Nano* **2013**, *7*, 5192–5198.

22. Howse, J. R.; Jones, R. A.; Ryan, A. J.; Gough, T.; Vafabakhsh, R.; Golestanian, R. *Phys. Rev. Lett.* **2007**, *99*, 048102.

23. Gibbs, J. G.; Zhao, Y.-P. *Appl. Phys. Lett.* **2009**, *94*, 163104.

24. Baraban, L.; Makarov, D.; Streubel, R.; Monch, I.; Grimm, D.; Sanchez, S.; Schmidt, O. G. *ACS Nano* **2012**, *6*, 3383–3889.

25. Gao, W.; Pei, A.; Feng, X.; Hennessy, C.; Wang, J. *J. Am. Chem. Soc.* **2013**, *135*, 998–1001.

26. Ibele, M.; Mallouk, T. E.; Sen, A. *Angew. Chem. Int. Ed.* **2009**, *48*, 3308–3312.

27. Palacci, J.; Sacanna, S.; Vatchinsky, A.; Chaikin, P. M.; Pine, D. J. *J. Am. Chem. Soc.* **2013**, *135*, 15978–15981.

28. Zhang, L.; Abbott, J. J.; Dong, L.; Peyer, K. E.; Kratochvil, B. E.; Zhang, H.; Bergeles, C.; Nelson, B. J. *Nano Lett.* **2009**, *9*, 3663–3667.

29. Ghosh, A.; Fischer, P. *Nano Lett.* **2009**, *9*, 2243–2245.

30. Gao, W.; Sattayasamitsathit, S.; Manesh, K. M.; Weihs, D.; Wang, J. *J. Am. Chem. Soc.* **2010**, *132*, 14403–14405.

31. Tottori, S.; Zhang, L.; Qiu, F.; Krawczyk, K. K.; Franco-Obregón, A.; Nelson, B. J. *Adv. Mater.* **2012**, *24*, 811–816.

32. Gao, W.; Feng, X.; Pei, A.; Kane, C. R.; Tam, R.; Hennessy, C.; Wang, J. *Nano Lett.* **2014**, *14*, 305–310.

33. Kagan, D.; Benchimol, M. J.; Claussen, J. C.; Chuluun-Erdene, E.; Esener, S.; Wang, J. *Angew. Chem. Int. Ed.* **2012**, *51*, 7510–7522.

34. Wang, W.; Castro, L. A.; Hoyos, M.; Mallouk, T. E. *ACS Nano* **2012**, *6*, 6122–6132.

35. Wang, J.; Gao, W. *ACS Nano* **2012**, *6*, 5745–5751.

36. Nelson, B. J.; Kaliakatsos, I. K.; Abbott J. J. *Annu. Rev. Biomed. Eng.* **2010**, *12*, 55–85.

37. Abdelmohsen, L. K. E. A.; Peng, F.; Tu, Y.; Wilson, D. A. *J. Mater. Chem. B* **2014**, *2*, 2395–2408.

38. Patra, D.; Sengupta, S.; Duan, W.; Zhang, H.; Pavlick, R.; Sen, A. *Nanoscale* **2013**, *5*, 1273–1283.

39. Kagan, D.; Laocharoensuk, R.; Zimmerman, M.; Clawson, C.; Balasubramanian, S.; Kang, D.; Bishop, D.; Sattayasamitsathit, S.; Zhang, L.; Wang, J. *Small* **2010**, *6*, 2741–2747.

40. Gao, W.; Kagan, D.; Pak, O. S.; Clawson, C.; Campuzano, S.; Chuluun-Erdene, E.; Shipton, E.; Fullerton, E. E.; Zhang, L.; Lauga, E.; Wang, J. *Small* **2012**, *8*, 460–467.

41. Wu, Z.; Wu, Y.; He, W.; Lin, X.; Sun, J.; He, Q. *Angew. Chem. Int. Ed.* **2013**, *52*, 7000–7003.

42. Balasubramanian, S.; Kagan, D.; Hu, C. J.; Campuzano, S.; Lobo-Castaño, M. J.; Lim, N.; Kang, D. Y.; Zimmerman, M.; Zhang, L.; Wang, J. *Angew. Chem. Int. Ed.***2011**, *50*, 4161–4164.

43. Sanchez, S.; Solovev, A. A.; Schulze, S.; Schmidt, O. G. *Chem. Commun.* **2011**, *47*, 698–700.

44. Petit, T.; Zhang, L.; Peyer, K. E.; Kratochvil B. E.; Nelson, B. J. *Nano Lett.***2012**, *12*, 156–160.

45. Olson, E. S.; Orozco, J.; Wu, Z.; Malone, C. D.; Yi, B.; Gao, W.; Eghtedari, M.; Wang, J.; Mattrey, R. F. *Biomaterials* **2013**, *34*, 8918–8924.

46. Solovev, A. A., Xi, W.; Gracias, D. H.; Harazim, S. M.; Deneke, C.; Sanchez, S.; Schmidt, O. G. *ACS Nano* **2012**, *6*, 1751–1756.

47. Wang, W.; Li, S.; Mair, L.; Ahmed, S.; Huang, T. J.; Mallouk, T. E. *Angew. Chem. Int. Ed.* **2014**, *53*, 3201–3204.

48. Karn, B.; Kuiken, T.; Otto, M. *Environ. Health Perspect.* **2009**, *117*, 1813–1831.

49. Qu, X.; Brame, J.; Li, Q.; Alvarez, P. J. J. *Acc. Chem. Res.* **2012**, *46*, 834–843.

50. Andreescu, S.; Njagi, J.; Ispas, C.; Ravalli, M. *J. Environ. Monit.* **2009**, *11*, 27–40.

51. Zhang, W. *J. Nanopart. Res.* **2003**, *5*, 323–332.

52. Ariga, K.; Ishihara, S.; Abe, H.; Li, M.; Hill, J. P. *J. Mater. Chem.* **2012**, *22*, 2369–2377.

53. Orozco, J.; Cheng, G.; Vilela, D.; Sattayasamitsathit, S.; Vazquez-Duhalt, R.; Valdes-Ramirez, G.; Pak, O. S.; Escarpa, A.; Kan, C.; Wang, J. *Angew. Chem. Int. Ed.* **2013**, *52*, 13276–13279.

54. Soler, L.; Magdanz, V.; Fomin, V. M.; Sanchez, S.; Schmidt, O. G. *ACS Nano* **2013**, *7*, 9611–9620.

55. Orozco, J.; García-Gradilla, V.; D'Agostino, M.; Gao, W.; Cortés, A.; Wang, J. *ACS Nano* **2013**, *7*, 818–824.

56. Guix, M.; Orozco, J.; Garcia, M.; Gao, W.; Sattayasamitsathit, S.; Merkoci, A.; Escarpa, A.; Wang, J. *ACS Nano* **2012**, *6*, 4445–4451.

57. Hanrahan, G.; Patil, D. G.; Wang, J. *J. Environ. Monit.* **2004**, *6*, 657–664.

58. Campuzano, S.; Kagan, D.; Orozco, J.; Wang, J. *Analyst* **2011**, *136*, 4621–4630.

59. Sen, A.; Ibele, M.; Hong, Y.; Velegol, D. *Faraday Discuss.* **2009**, *143*, 15–27.

60. Solovev, A. A.; Sanchez, S.; Schmidt, O. G. *Nanoscale* **2013**, *5*, 1284–1293.

61. Whicker, F. W.; Hinton, T. G.; MacDonell, M. M.; Pinder III, J. E.; Habegger, L. J. *Science* **2004**, *303*, 1615–1616.

62. Vieira, L.R.; Gravato C.; Soares, A. M. V. M.; Morgado, F.; Guilhermino, L. *Chemosph.* **2009**, *76*, 1416–1427.

63. Buikema, A. L. Jr.; Niederlehner, B. R.; Cairns, J. K. Jr. *Water Res.* **1982**, *16*, 239–262**.**

64. Sprague, J. B. *Water Res.* **1969**, *3*, 793−821.

65. Farré, M.; Barceló, D. *Trends Anal. Chem.* **2003**, *22*, 299−310.

66. Parvez, S.; Venkataraman, C.; Mukherji, S. *Environ. Int.* **2006**, *32*, 265-268.

67. Gao, W.; Sattayasamitsathit, S.; Uygun, A.; Pei, A.; Ponedal, A.; Wang, J. *Nanoscale* **2012**, *4*, 2447−2453.

68. Sole, S. Merkoci, A.; Alegret, S. *Crit. Rev. Anal. Chem.* **2003**, *33*, 89–126.

69. Trojanowicz, M. *Electroanal.* **2002**, *14*, 1311–1328.

70. Amine, A.; Mohammadi, H.; Bourais, I.; Palleschi, G. *Biosens. Bioelectron.* **2006**, *21*, 1405–1423.

71. Wang, J.; Nascimento, V.G.; Kane, S.A.; Rogers, K.; Smyth, M.R.; Agnes, L. *Talanta* **1996**, *43*, 1903–1907.

72. Sezgintürk, M.K.; Göktuğ, T.; Dinçkaya, E. *Biosens. Bioelectron.* **2005**, *21*, 684–688.

73. Vasylkiv, O.Y; Kubrak, O.I.; Storey, K.B.; Lushchak, V.I. *Pestic. Biochem. Physiol.* **2011**, *101*, 1–5.

74. Singh, S. M.; Sivalingam, P. M. *J. Fish Biol.* **1982**, *20*, 683–688.

75. Margoliash, E.; Novogrodsky A. and Schejter, A. *Biochem. J.* 1960, *74*, 339–348.

76. Manesh, K.M.; Cardona, M.; Yuan, R.; Kagan, D.; Balasubramanian, S.; Wang, J. *ACS Nano* **2010**, 4, 1799–1804.

77. Zhao, G.; Seah T. H.; Pumera, M. *Chem. Eur. J.* **2011**, *17*, 12020-12026.

78. Biswas, S.; Chaudhari, S. K.; Mukherji, S. *J. Chem. Technol. Biotechnol.* **2005**, *80*, 587-593.

79. Machlis, G. E.; McNutt, M. K. *Science* **2010**, *329*, 1018-1019.

80. Zhu, Q.; Pan, Q.; Liu, F. *J. Phys. Chem. C* **2011**, *115*, 17464-17470.

81. Cheng, M.; Gao, Y.; Guo, X.; Shi, Z.; Chen, J. F.; Shi, F. *Langmuir* **2011**, *27*, 7371-7375.

82. Yao, X.; Song, Y.; Jiang, L. *Adv. Mater.* **2011**, 23, 719-734.

83. McHale, G.; Shirtcliffe, N. J.; Aqil, S.; Perry, C. C.; Newton, M. I. *Phys. Rev. Lett*. **2004**, *93*, 036102.

84. Zhang, J.; Pu, G.; Severtson, S. J. *ACS Appl. Mater. Interfaces* **2010**, *2*, 2880-2883.

85. Shirtciffe, N.; McHale, G.; Newton, M. I.; Chabrol, G.; Perry, C. C. *Adv. Mater.* **2004**, *16*, 1929-1932.

86. Fragoso, A.; Laboria, N.; Latta, D.; Sullivan, C. K. O. *Anal. Chem.* **2008**, *80*, 2556-2563.

87. Guo, M.; Diao, P.; Cai, S. *Thin Solid Films* **2007**, *515*, 7162-7166.

88. Wang, J.; Wu, H.; Angnes, L. *Anal. Chem.* **1993**, *65*, 1893-1896.

89. Faucheux, N.; Schweiss, R.; Lutzow, K.; Werner, C.; Groth, T. *Biomaterials* **2004**, *25*, 2721-2730.

90. Floridia, M.A.; Rubert, A.A.; Benítez, G.A.; Fonticelli, M.H.; Carrasco, J.; Carro P. and Salvarezza, R. C. *J. Phys. Chem. C* **2011**, *115*, 17788–17798.

91. Campuzano, S.; Orozco, J.; Kagan, D.; Guix, M.; Gao, W.; Sattayasamitsathit, S.; Claussen, J. C.; Merkoci, A.; Wang, J. *Nano Lett.* **2012**, *12*, 396−401.

92. Wang, J. *Lab Chip* **2012**, 12, 1944–1950.

93. Katira, P.; Hess, H. *Nano Lett.* **2010**, *10*, 567–572.

94. Agarwal, A.; Katira, P.; Hess, H. *Nano Lett.* **2009**, *9*, 1170–1175.

95. Mendoza, S. M.; Arfaoui, I.; Zanarini, S.; Paolucci, F.; Rudolf, P. *Langmuir* **2007**, *23*, 582-588.

96. Offord D. A.; John C. M.; Linford M. R.; Griffin J. H. *Langmuir* **1994**, *10*, 883-889.

97. Lee, T. R.; Laibinis, P. E.; Folkers, J. P.; Whitesides, G. M. *Pure & Appl. Chem*. **1991**, *63*, 821-828.

Chapter 6 Towards the In Situ Fuels: Alternative Fuels Powered Autonomous Micromotors

6.1 Polymer-zinc microrockets in strongly acidic media

6.1.1 Introduction

Designing and powering new synthetic nano/micro scale motors represent a major challenge and opportunity. Considerable efforts have thus been devoted to the preparation of efficient nanomotors propelled by different mechanisms.[1-12] Particular attention has been given to chemically-powered catalytic micro/nanomotors, based on different compositions and structures, that are capable of moving autonomously in the presence of hydrogen peroxide fuel.[13-18] Among these catalytic motors, self-propelled tubular microbots are particularly attractive for practical biomedical applications.[18-22] The oxygen-bubble propulsion mechanism of such tubular microbots leads to efficient propulsion in relevant biological fluids and high ionic-strength media, as desired for diverse practical applications ranging from directed cargo transport in microchips[23,24] to isolation of target biomaterials from body fluids.[25-28] A simplified template electrosynthesis of highly efficient, ultrafast and small PANI/Pt bilayer microtube engines was reported recently.[29] However, the requirement of high concentration of the hydrogen peroxide fuel has greatly hindered practical applications of these and other catalytically propelled micro/nanomotors. Sen's group developed recently a bisegment Pt/Cu nanowire motor that uses bromine or iodine fuels, instead of hydrogen peroxide.[30] Yet, owing to its self-electrophoresis propulsion mechanism, such nanowire motor cannot be operate in high ionic strength environments.[31]

This Communication reports on a new PANI/Zn microrocket that propels autonomously and efficiently in extreme acidic environments without additional fuels. Such acid-driven microtubular rocket relies on a bubble propulsion mechanism associated with the continuous thrust of hydrogen bubbles generated at the inner zinc layer (Figure 7.1.1a), analogous to that of oxygen-bubble propelled catalytic microengines.[18-22] When the new PANI/Zn bilayer microrockets are immersed in a strongly acidic medium, a spontaneous redox reaction - involving the Zn oxidation along with generation of hydrogen bubbles - occurs on their inner Zn surface:

$$Zn(s) + 2\ H^{+}(aq) \rightarrow Zn^{2+}(aq) + H_2(g) \quad E^{o} = 0.76\ V \qquad (6.1.1)$$

leading to an ultrafast propulsion that can exceed 100 body lengths/s. Zinc has a more negative redox potential than hydrogen and thus promotes hydrogen gas evolution,[32,33] and hence has been widely used for producing hydrogen energy.[34, 35] Other metals (e.g., Fe, Co, Sn, Pb) with a more negative redox potential than hydrogen were tested but displayed a much weaker bubble thrust. Alkali metals (e.g. Li, K), that can also lead to efficient hydrogen evolution, cannot be electrodeposited and are too reactive for a safe operation. Zn, in contrast, is an attractive candidate for the microrocket inner layer as it is biocompatible 'green' nutrient trace element, vital for many body functions and metabolic and enzymatic processes,[36] that can be readily electrodeposited and offers an efficient and safe acid-driven propulsion.

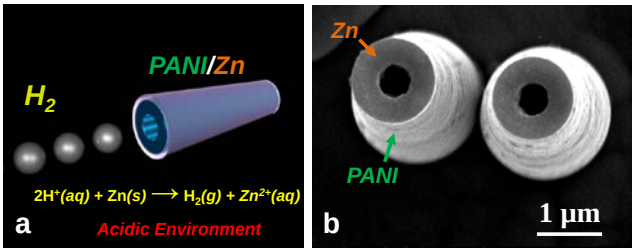

Figure 6.1.1 Acid-driven PANI-Zn microrocket: a) Schematic of motion in an acidic environment; b) SEM images of the top view of two PANI-Zn microtubes (prepared using a membrane with 2 µm diameter pores).

Strongly acidic environments can be found everywhere in our life, from diverse industrial processes to our own human stomach. Autonomous microrocket movement in such acidic media

can thus lead to diverse biomedical or industrial applications, and hence greatly expand the scope of applications of nano/microscale motors compared to common peroxide-driven catalytic micro/nanomotors. As will be illustrated below, the new acid-driven PANI/Zn microrockets can also serve as an attractive platform for sensitive pH measurements in these extreme environments.

6.1.2 Experimental section

Synthesis of Zinc based Microrockets

The PANI/Zn microtubes were prepared using a common template directed electrodeposition protocol. The Cyclopore polycarbonate membranes, containing 2 μm diameter (Catalog No 7060-2511; Whatman, Maidstone, U. K.) and 5 μm diameter (Catalog No 7060-2513; Whatman, Maidstone, U. K.) conical-shaped micropores, were employed as the templates. A 75 nm gold film was first sputtered on one side of the porous membrane to serve as working electrode using the Denton Discovery 18. A Pt wire and an Ag/AgCl with 3 M KCl were used as counter and reference electrodes, respectively. The membrane was then assembled in a plating cell with an aluminum foil serving as a contact. Polyaniline microtubes were prepared by modifying the previously described method.[29] Briefly, aniline (Sigma-Aldrich, St Louis, MO) was distilled before use at a vapor temperature of 100 °C and a pressure of 13 mm Hg. Polyaniline (PANI) microtubes were electropolymerized at +0.80 V for 0.02 C (0.1 C for membrane with 5 μm pore size) from a plating solution containing 0.1 M H_2SO_4, 0.5 M Na_2SO_4 and 0.1 M aniline; subsequently, the inner zinc tube was deposited galvanostatically at -6 mA for 1800 s (2400 s for membrane with 5 μm pore size) from a commercial zinc plating solution containing 80 g l^{-1} $ZnSO_4$, and 20 g l^{-1} H_3BO_3 solutions (buffered to pH = 2.5 with sulfuric acid). The sputtered gold layer was completely removed by hand polishing with 3-4 μm alumina slurry. The membrane was then dissolved in methylene chloride for 10 min to completely release the microtubes. The latter were collected by centrifugation at 6000 rpm for 3 min and washed repeatedly with methylene chloride, followed by ethanol, three times of each. All microtubes were stored in ethanol at room

temperature since zinc is an active metal and slowly react with water. Before usage, the microtubes were washed twice with ultrapure water (18.2 MΩ cm) at 6000 rpm for 3 min. To achieve the magnetic directional control, the microrocket solution (ethanol) was evaporated onto glass slides before the sequential E-beam deposition of 10 nm Ti (adhesion layer), 20 nm Ni (magnetic layer), over the microtubes. Experiments in human serum samples, from human male AB plasma (Sigma-Aldrich, St. Louis, MO), were carried out by mixing sequentially 5 µL of the microrocket solution with 5 µL 5% Triton X-100, 5 µL biological media and 5 µL 2 M HCl, leading to a final solution corresponding to 25% of the raw samples.

Equipments

Template electrochemical deposition of microtubes was carried out with a CHI 661D potentiostat (CH Instruments, Austin, TX). SEM images were obtained with a Phillips XL30 ESEM instrument, using an acceleration potential of 20 kV. The SEM images were taken shortly after the microtube samples in ethanol suspension freshly dried up. Mapping analysis was investigated by Oxford EDX attached to SEM instrument and operated by Inca software. Images are captured by an inverted optical microscope (Nikon Instrument Inc. Ti-S/L100), coupled with a 10x objective, a Hamamatsu digital camera C11440 using the NIS-Elements AR 3.2 software.

6.1.3 Results and discussions

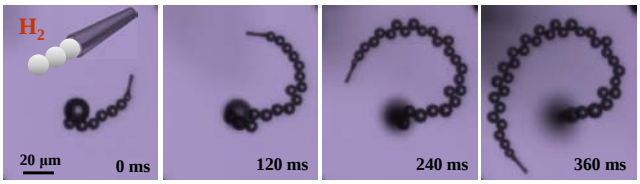

Figure 6.1.2 Acid-powered microengine: time lapse images of the propulsion of a PANI/Zn microrocket (2 µm diameter) at 0, 120, 240, 360 ms, respectively. Medium, 1 M HCl solution containing 1.67 % Triton X-100.

To take the advantage of the Zn-induced hydrogen generation for the new bubble propelled motors, PANI/Zn bilayer microtubes have been fabricated within a Cyclopore polycarbonate template containing microconical pores. The outer PANI tube was prepared in a

manner analogous to that reported recently for preparing oxygen-bubble propelled PANI/Pt microrockets.[29] Subsequently, a zinc layer has been deposited galvanostatically within the PANI layer using an 80 g l^{-1} $ZnSO_4$/20 g l^{-1} H_3BO_3 solution (buffered to pH = 2.5 with sulfuric acid). Figure 6.1.1b displays SEM images of the PANI/Zn bilayer microtube rockets prepared electrochemically using the 2 μm membrane. (2 μm refers to the diameter of the bigger opening of the conical pore.) The resulting microrockets are around 10 μm long, have a front inner opening diameter of around 350 nm, a front outer diameter of around 1.2 μm, and include a ~150 nm thick PANI outer layer and a ~300 nm Zn inner layer. The presence of carbon and zinc in the resulting bilayer microtubes was confirmed b EDX mapping analysis (not shown).

Figure 6.1.2 displays time-lapse images, for the movement of the PANI/Zn microrocket over a 360 ms period at 120 ms intervals in a strongly acidic environment (1.0 M HCl, pH=0). These images illustrate a tail of hydrogen microbubbles (~4-5 μm in diameter) generated on the inner Zn surface and released from the rear large-opening-side of the microtube at a rate of 75 bubbles/s. The microrocket is self-propelled at an ultrafast speed over 500 μm/s, which corresponds to a relative speed of nearly 50 body lengths/s. Such speed is stable during the motor lifetime, except for an initial (~1 s) acceleration after immersion in the acid solution that reflects the increased inner diameter.

The speed of the acid-driven PANI/Zn microrocket is strongly dependent on the acid concentration. Figure 6.1.3 illustrates the influence of the pH and HCl concentration upon the speed of microrockets with 2 and 5 μm diameters (black and red curves, respectively). As expected, both microrockets display their highest speed using the highest (1.6 M) acid concentration tested (corresponding to pH -0.2). For the 2 μm rocket, the speed decreases gradually from 650 μm/s (at pH -0.2) to 550 μm/s (at pH 0.0), then more rapidly to 300 μm/s (at pH 0.2), and subsequently slowly to 8 μm/s (at pH 1.0). The 5 μm diameter microrocket displays a similar trend, along with a higher initial speed, and slightly wider pH range. This microrocket

achieves an ultrafast speed of 1050 μm/s (~100 body-lengths/s) at pH -0.2, that decays gradually to 140 μm/s at pH 0.4 and then more slowly to 10 μm/s at pH 1.3. Note that such wider operational pH range makes these rockets useful for movement in the extreme stomach environment of pH 0.8-2.0. The lifetime of the corresponding microrockets is influenced by the rate of the Zn dissolution and may range from 10 sec to 2 min. This depends upon the surrounding pH (that influences the rate of the Zn dissolution) and upon the amount of Zn present. For example, a prolonged movement of the 5 μm microrocket over 1 min in a 60 mM HCl solution (pH=1.2) at a speed of 20 μm/s can be obtained. Another key factor affecting the lifetime is the thickness of the inner Zn layer. This can be used for predicting theoretically the motor lifetime using simple kinetic calculations and assuming a cylindrical microtube motor.[22] The motor's lifetime, t, is given by ρh/v, where ρ, h are the density, thickness of the Zn layer, respectively, and v is the mass reaction rate. The latter (v) depends upon the acid concentration and corresponds to around 4.87×10^{-5} g/(cm^2·s) using 0.25 M H_2SO_4.[37] A lifetime of ~30 s can thus be estimated for a 5 μm diameter microrocket with a Zn-layer thickness of around 2 μm, that propels in 0.25 M H_2SO_4. Such theoretical value is in close agreement with the experimental lifetime observed under these conditions.

The defined speed-pH profiles of Figure 6.1.3 can form the basis for sensitive motion-based pH measurements in extremely acidic environments where common glass pH electrodes lead to a large 'acid error'.[38,39] Microrocket-based pH sensing could involve measurements of the speed and/or distance travelled by the microrocket, analogous to a recent motion-based DNA sensing protocol.[27,40] Such motion-based pH sensing could find important applications ranging from detecting changes in the stomach acidity to remote monitoring of etching baths in semiconductor processing. Changing movement in an acid gradient (i.e., chemotaxis) can also be envisioned based on the data of Figure 6.1.3.

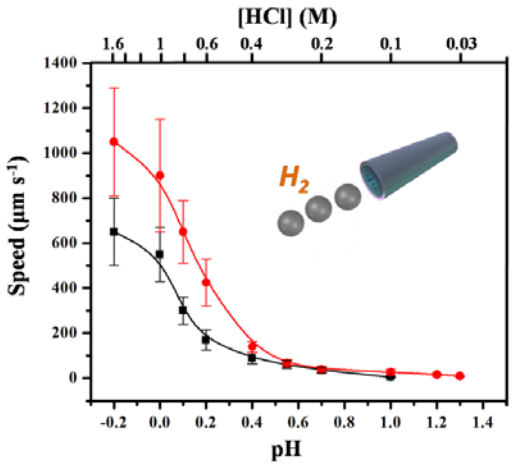

Figure 6.1.3 pH dependence of the speed of PANI/Zn microrockets in solutions of different HCl concentrations over the 0-1.6 M range. 1.67 % Triton X-100 was added as the surfactant. Error bars show standard deviations of the measured speeds (n=30). Red and black curves, microrockets with 5 and 2 μm diameter, respectively.

Table 6.1 Comparison of the speed of PANI/Zn microrockets in the presence of different acids.[a]

Acid Type	Speed (μm/s)
HCl	140
H_2SO_4	80
H_3PO_4	20

a. 0.5 M HCl, 0.25 M H_2SO_4 and 0.167 M H_3PO_4 were used along with 1.67% Triton X-100 surfactant.

The propulsion of the PANI/Zn microrocket in different acidic environments has also been investigated. Table 6.1 shows the speed of the Zn-based microrockets in different common strong acids (HCl, H_2SO_4 and H_3PO_4). While a fast speed of 140 μm/s is observed in 0.5 M HCl, significantly slower speeds of 80 and 20 μm/s are obtained in H_2SO_4 and H_3PO_4, respectively, reflecting their decreasing acid dissociation constants.[41] Such speed variations are consistent with the pH dependence of the PANI/Zn microrocket observed in Figure 6.1.3. In contrast, no efficient propulsion was observed in a 0.5 M HNO_3 solution, although the zinc layer was dissolved. The lack of movement in nitric acid reflects the generation of N_2O (instead of H_2), which is much more soluble in water, in according to:

$$4\ Zn + 10\ HNO_3\ (dilute) \rightarrow 4\ Zn(NO_3)_2 + N_2O + 5\ H_2O \qquad (6.1.2)$$

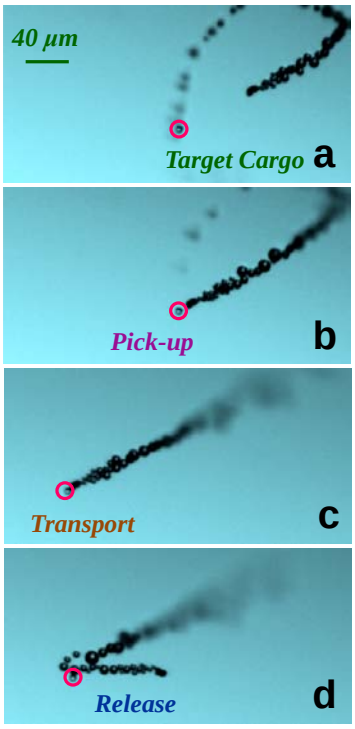

Figure 6.1.4 Cargo manipulations: time-lapse images of a PANI/Zn microrocket (5 μm diameter) approaching (a), capturing (b), transporting (c) and releasing (d) the 5 μm target sphere. Medium, 400 mM HCl solution containing 1.67 % Triton X-100.

A magnetic layer can be incorporated into the PANI/Pt microrockets by E-beam deposition of Ti-Ni layers on the outer PANI surface, to allow magnetic control of their directionality and cargo pick up, as desired for practical applications of nano/microscale machines. The magnetically-guided PANI/Zn microrocket (5 μm in diameter) can move in a 0.4 M hydrochloric acid at a speed of near 100 μm/s. Such speed is slower than that of the PANI/Zn microrocket under the same conditions (140 μm/s), reflecting the influence of the additional Ti/Ni layers. Directed transport of cargo is important in diverse applications of micro/nanomotors.[23,42-44] The optical images of Figure 6.1.4 illustrate an entire cargo "load, drag, and drop" operation by the magnetically-guided Ni/Ti/PANI/Zn microrocket (b, c, d, respectively) in a strong acidic environment (400 mM HCl, pH=0.4). The microrocket thus approaches the 5 μm diameter magnetic polystyrene microsphere (a), captures it magnetically (b), transports it over a

predetermined path (c), and finally releasing it by rapidly changing the direction the magnetic field direction (d). The speed of the microrocket decreases from 110 μm/s to 90 μm/s after capturing the polystyrene cargo, reflecting the increase fluid drag force exerted by the larger largo. A drag force of ~5 pN can be estimated considering the microrocket as a cylindrical nanorod.[22,29] Direct locomotion in untreated biological environments has also been illustrated. We observe the efficient movement of the H_2-bubble propelled PANI/Zn microrocket in acidified human serum. Despite the raw biological medium, the PANI/Zn microrocket moves rapidly, yet at a slower speed of 92 μm/s compared to 170 μm/s in the aqueous acid solution. The higher viscosity of the human serum leads to a larger size and lower frequency of the hydrogen bubbles, and hence to a slower speed.[29]

6.1.4 Conclusions

In conclusion, we demonstrated here the first example of microtube rockets that propel efficiently by the thrust of hydrogen bubbles in extreme acidic environments. Unlike common oxygen-bubble propelled microengines, these mass-produced low cost PANI/Zn microrockets are fueled by their own acid environment, without additional hydrogen peroxide. The new self-propelled microrockets display an ultrafast propulsion (as high as 100 body lengths/s) along with attractive capabilities ranging from guided cargo transport to propulsion in raw biological media. Such acid-powered microrockets could greatly expand the scope of applications of nano/microscale motors towards new extreme environments (e.g. the human stomach or silicon wet-etching baths) and could thus lead to diverse new biomedical or industrial applications ranging from targeted drug delivery or nanoimaging to the monitoring of industrial processes. In addition, such self-propelled microrockets offer considerable promise for motion-based pH sensing in extreme conditions.

6.2 Fully-loaded micromotors for combinatorial delivery

6.2.1 Introduction

Operating on locally supplied fuels such as hydrogen peroxide or acid, the artificial motors can perform considerably complex tasks.[13-15] For instance, hydrogen-peroxide powered micromotors have shown a remarkable ability to isolate circulating tumor cells, protein and bacteria from raw biological fluids.[25,45,46] Previous studies have also demonstrated that by attaching drug-loaded nanoparticles onto the outer surface of micromotors, the motors can deliver their therapeutic payloads to a target destination through pre-defined paths with a speed over three orders of magnitude higher than regular Brownian motion, reflecting the large propelling and towing forces of the motors.[44] Along with remarkable control over the movement directionality, these man-made microscale devices are currently a subject of intense fundamental and practical research activities.[1] While still in an early stage, attempts to explore biomedical applications of micromotors are extremely active and encouraging.[1-4,13-15]

Delivering cargoes in a defined and fast manner represents a major application of synthetic micromotors.[44-46] The key challenge, however, is how to design, fabricate, and optimize new motors with appropriate functions for effective delivery and efficient release of their payloads. A reliable delivery vehicle is expected to have the capability for carrying a large amount of cargoes for enhanced effectiveness (e.g., therapeutic efficacy in drug delivery), delivering simultaneously different types of cargoes for multitasking (e.g., theranostics or combination therapy to overcome drug resistance), releasing payloads in a responsive manner (e.g., controlled drug release), and destroying itself when no longer needed. To meet these critical multifunctionality requirements, we successfully constructed in the present study a novel chemically-powered zinc-based micromotor that displays impressive cargo loading, delivery, and release capabilities.

6.2.2 Experimental Methods

Cyclopore polycarbonate membranes, containing 2 μm diameter micropores (Catalog No 7060-2511; Whatman, Maidstone, U. K.), were used as templates. A 75 nm gold film was first sputtered on one side of the porous polycarbonate membrane to serve as the working electrode using the Denton Discovery 18 Sputter System. Solutions of 500 nm SiO_2 particles (Bangs Laboratories, IN), diluted 60 or 15 fold, were passed through membrane pores by vacuum infiltration.[47,48] A polycarbonate membrane with pore sizes of 200 nm was placed below the 2 μm diameter polycarbonate membrane (with the sputtered Au side down) to retain the SiO_2 particles within the upper 2 μm membrane pores. The membrane was then assembled in a plating cell with aluminum foil serving as a contact. A Pt wire and an Ag/AgCl (3 M KCl) served as counter and reference electrodes, respectively. Zinc was electrodeposited using a potential of -1.2 V for a total charge of 8 C, from a plating solution consisting of 68 g/L $ZnCl_2$, and 20 g/L H_3BO_3 (pH 2.5, adjusted with sulfuric acid). After the Zn deposition, the sputtered gold layer was removed by mechanical polishing of the surface with 3-4 μm alumina slurry. The membrane was then dissolved in methylene chloride for 3 min to completely release the micromotors. The micromotors were collected by centrifugation at 3000 rpm for 3 min and washed repeatedly with methylene chloride, ethanol and water (two times of each). The SiO_2 loaded micromotors were then ready to be used. For longer storage times, the micromotors were kept in ethanol. Mixtures of 20 nm Au nanoparticles (Ted Pella, Inc., Redding, CA) and SiO_2 particles and a combination of 2 different sizes of SiO_2 particles (500 and 250 nm) were used for fabricating the multi-cargo loaded micromotors. For the binary Au-SiO_2 cargo mixture, the Au nanoparticles (from the 2 mL commercial solution) were preconcentrated by centrifugation. The top layer of the supernatant was removed to a final volume of 200 μL. The Au nanoparticles were then redispersed in a 10X diluted 500 nm SiO_2 particle solution. For the binary SiO_2 loading, 500 nm and 250 nm SiO_2 particles were mixed at a volume ratio of 1:2, followed by a 10 fold dilution. Zinc was

electroplated after infiltrating these particles using the deposition conditions described earlier. The propulsion of micromotors was examined in HCl solutions containing 1.6% Triton X-100.

6.2.3 Results and discussions

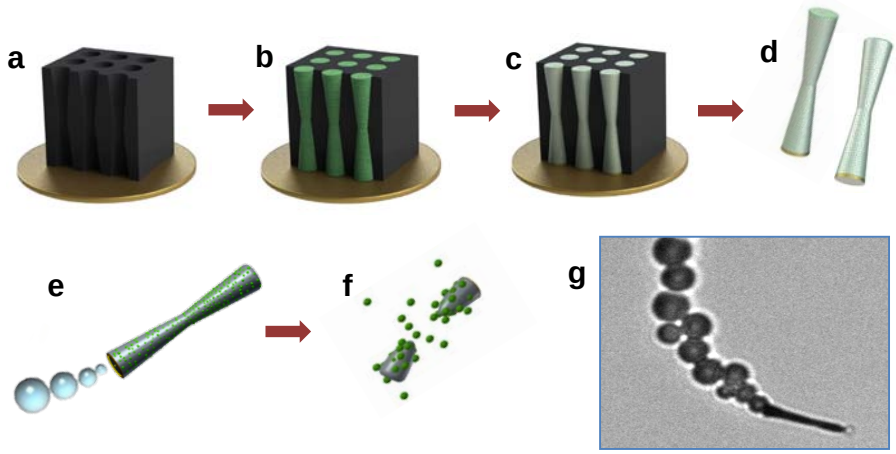

Figure 6.2.1 Dual-template fabrication of the fully-loaded zinc-based micromotors. (a) sputtering membrane template with a gold conducting layer; (b) packing nanoparticle cargoes into the membrane pores; (c) electrodeposition of zinc into the biconical pores; (d) dissolution of the membrane template to release individual micromotors; (e-f) hydrogen-bubble propulsion in acid and autonomous release of the cargoes while the motors are dissolved and destroyed; (g) microscopic image of a bubble-propelled cargo-loaded micromotor in HCl.

The fully-loaded double-conical zinc micromotors are fabricated by coupling template-electrodeposition with particle-infiltration techniques using silica and gold nanoparticles as model cargo analogues. As illustrated in Figure 6.2.1, the motor fabrication route involves the electrodeposition of zinc within the conical micropores of a polycarbonate membrane which are tightly packed with the cargo particles. Dissolution of the membrane template results in the release of the freestanding double-conical shaped micromotors, characterized with a remarkably high cargo packing fraction of up to 74% of the entire motor body (for mono-sized spherical cargos according to Kepler conjecture).[49] This loading fraction can be further increased by combining different sized spherical particles or using particles with different shapes. When the micromotors are placed in acidic fuel media, hydrogen bubbles are spontaneously ejected from one end, leading to a bubble thrust and a fast movement (Figure 6.2.1e). Such directional

locomotion is enabled by the formation of a galvanic cell between the zinc and the sputtered gold contact.[50] The dissolution of the zinc body leads to an autonomous release of the encapsulated cargoes and eventual splitting apart of the motors (Figure 6.2.1f), while the motors are moving till they are almost fully dissolved.

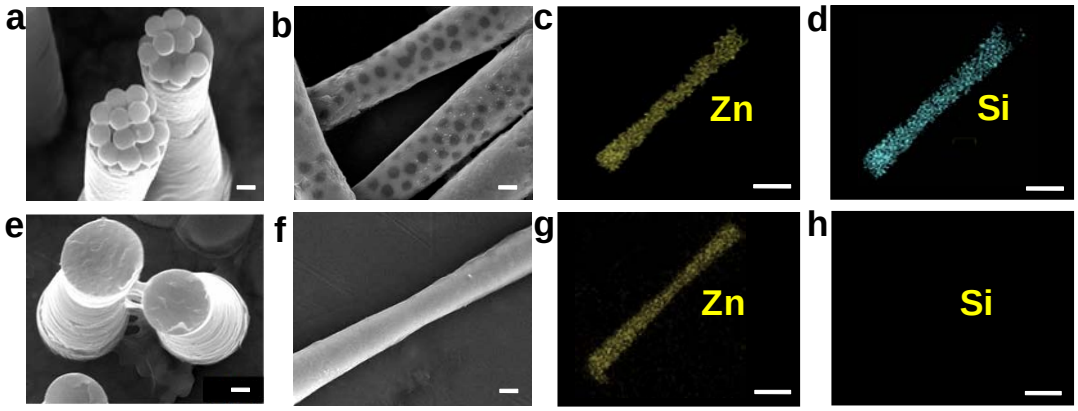

Figure 6.2.2 SEM images (a,b,e,f) and EDX analysis (c,d,g,h) of Zn micromotors. (a-d), Zn micromotors encapsulated with 500 nm SiO_2 particles: top view (a), side view (b), and EDX analysis (c, d). (e-h), control Zn micromotors without the SiO_2 particles. Top view (e), side view, (f) and EDX analysis (g, h). Scale bar, 0.5 μm (b,f), 1 μm (a,e), and 2 μm (c,d,g,h).

The scanning electron microscopy (SEM) images demonstrate the morphology of the template-prepared Zn micromotors loaded with monodisperse SiO_2 nanoparticles (diameter ~500 nm) (Figure 6.2.2a,b). Infiltrating the cargo spheres within the micropores of the membrane template allows for convenient and efficient cargo encapsulation within the electrodeposited zinc without any chemical linking steps. The resulting cargo-loaded micromotors are 20 μm long and have a double-cone structure (with 2 μm diameter at both ends and 1 μm diameter in their center), reflecting the shape of the micropores of the polycarbonate membrane template. These SEM images illustrate that the SiO_2 particles are tightly packed (with minimal gaps) and fully-loaded within the body of the zinc micromotors. As expected, only a small portion of the particles is visible on the outside of the fully-loaded Zn body (Figure 6.2.2b). The corresponding energy-dispersive X-ray spectroscopy (EDX) data indicates that the SiO_2 particles are dispersed uniformly and densely throughout the entire micromotor body, with zinc deposited in the voids

between these cargo particles (Figure 6.2.2c,d). Control experiments were carried out using zinc micromotors without the SiO_2 particles. SEM images (Figure 6.2.2e,f) and EDX examination (Figure 6.2.2g,h) confirm that only elemental zinc is present in these control micromotors.

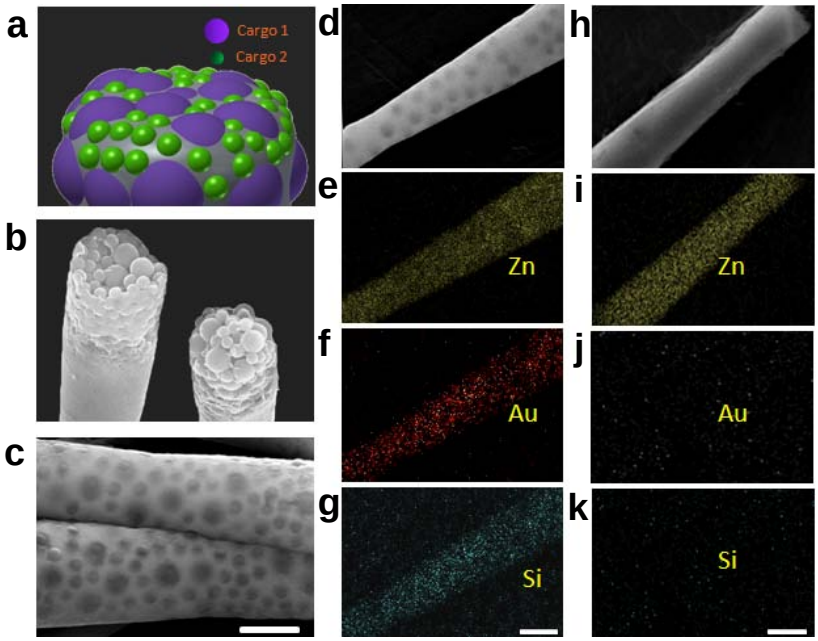

Figure 6.2.3 Multi-cargo loaded micromotors. (a) Model depicts the encapsulation of different types of cargos, (b-c), SEM images display the top view (b) and side view (c) of the micromotors fully loaded with two differently sized SiO_2 particles (500 and 250 nm in diameter). (d-g), SEM image (d) and EDX analysis (e-g) of the micromotors fully loaded with both SiO_2 nanoparticles (500 nm) and Au nanoparticles (25 nm). (h-k), SEM image (h) and EDX analysis (i-k) of a control zinc micromotor without any particle loading. All scale bars, 1 μm.

Next, we demonstrated the capabilities of the zinc micromotors for combinational cargo delivery and multifunctional operation. For this purpose, the micromotors were successfully loaded with a binary cargo mixture of different sizes and types of nanoparticles. As illustrated in Figure 6.2.3a, such simultaneous encapsulation of different cargo populations was tested using SiO_2 nanoparticles of different sizes (500 nm and 250 nm in diameter), as well as co-encapsulation of Au nanoparticles (diameter ~20 nm) and SiO_2 nanoparticles (diameter ~500 nm). As shown in Figure 6.2.3b and c, the top and side-view SEM images of the micromotors clearly indicate a homogeneous full loading of 500 nm and 250 nm SiO_2 particles within the motors. The

SEM image (Figure 6.2.3d) and EDX mapping (Figure 6.2.3e-g) further confirm that the zinc micromotors can be fully loaded with 20 nm Au nanoparticles together with 500 nm SiO_2 particles. Furthermore, the EDX mapping analysis shows the uniform distribution of elemental Au and Si over the entire body of the micromotor. Note that the Au nanoparticles cannot be observed in the SEM image owing to their small size. The SEM image (Figure 6.2.3h) and EDX mapping (Figure 6.2.3i-k) of the control zinc micromotors (without particle loading) confirm the absence of Au and Si within the zinc body of the micromotors. Collectively, these results demonstrate that the micromotor preparation route allows convenient packing of multicomponent cargoes at predetermined sizes, compositions and proportions.

Since the maximum packing capacity for mono-sized spheres is 74% of the total container volume according to Kepler conjecture,[49] the maximum packing capacity of 250 and 20 nm diameter cargo spheres within the 36.7 μm^3 volume of the double-cone micromotor is estimated to be slightly over 3,000 and 6,000,000 particles per micromotor, respectively. However, as the particle size increases, the container wall has a greater influence on the packing arrangement of the particles and increases the void volume within the micromotor. By packing the micromotors with two populations of nanoparticles of greatly different sizes (e.g., 20 and 500 nm, as the case in Fig. 3d), it is likely to have a packing fraction higher than 74%, because smaller cargoes can fill the voids between larger cargoes. Moreover, changing to non-spherical nanoparticle shapes, such as hexagons, may further increase the packing capacity.

Such high particle loading capacity and new functionalities do not compromise the locomotion behavior of the motors. For example, the time-lapse images in Figure 6.2.4a show the effective movement of several zinc micromotors fully-loaded with SiO_2 nanoparticles (500 nm in diameter) in a strongly acidic environment and the concomitant cargo release from the motors. The cargo-loaded micromotors are self-propelled with an average initial speed of 110 $\mu m\ s^{-1}$ in a 0.7 M HCl solution. A hydrogen bubble tail generated from one side of the micromotor is clearly

observed (Figure 6.2.4a, 0 s). As their zinc body is oxidized and dissolved by the acid fuel, the cargoes are released autonomously. Such gradual zinc dissolution leads to the breaking apart of the motors at their narrow center region, and eventually to a complete release of the encapsulated cargoes (Figure 6.2.4a, 6-9 s). Within less than 15 s, the micromotors stop their motion and nearly disappear (Figure 6.2.4a, 12 s). To better illustrate the cargo release process, we intentionally stopped the motion of the motors by reducing the fuel (acid) concentration and then focused on a single stationary micromotor with higher magnification. It was shown that the motor started to break apart 3 s after adding the acid, leading to the release of a large amount of cargo particles, and to complete dissolution of the motors (Figure 6.2.4b).

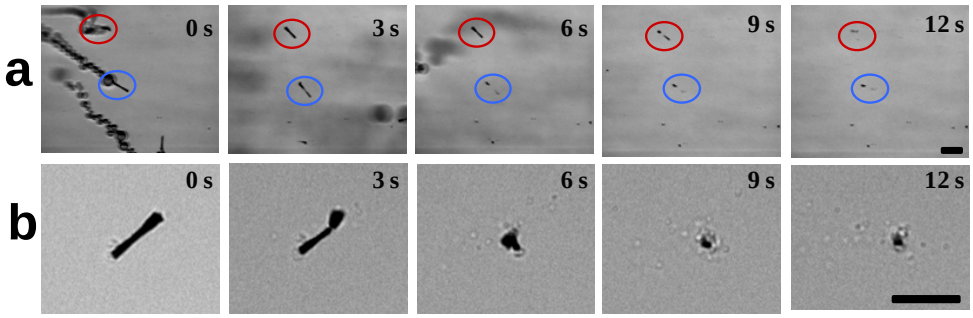

Figure 6.2.4 Time-lapse images of the SiO_2–loaded micromotors. (a) Self-propulsion of multiple micromotors and autonomous cargo release in a 0.7 M HCl fuel solution. (b) Close-up images of the cargo release from a fully-loaded stationary micromotor in a 0.3 M HCl solution. Images (a) and (b) were taken at 3 s intervals. Scale bars, 20 μm.

The speed and life time of the acid-powered micromotors are strongly dependent on the concentration of the surrounding acid and upon their payload loading fraction. The zinc micromotors without SiO_2 particle loading are self-propelled in the 0.7 M HCl solution at a speed of 160 μm s^{-1}, which corresponds to a relative speed of 8 body lengths s^{-1}. In contrast, the SiO_2-loaded micromotors are moving at a slower speed of 110 μm s^{-1} (5.5 body lengths s^{-1}). In addition, the cargo-loaded motors are fully destroyed in this solution within 15 s, as compared to the 20 s lifetime of the control motors which have higher zinc content.

6.2.4 Conclusions

An attractive self-propelled microscale motor has been developed that concurrently possesses multiple functions for potential biomedical applications, including a remarkably high loading capacity, combinatorial delivery of different cargoes and autonomous ‘on-the-fly’ release of payloads. Moreover, unlike most existing micromotors that are designed to withstand deterioration, these new micromotors destroy themselves upon completing their delivery mission. While the concept was illustrated through the loading of model SiO_2 and Au nanoparticle cargoes, it could be readily expanded to simultaneous encapsulation of a wide variety of payloads possessing different biomedical functions such as therapy, diagnostics, and imaging. This development is thus expected to advance significantly the emerging field of cargo- towing nano/micromotors and to further expand the opportunities for biomedical applications of nano/microvehicles.

6.3 Multi-fuel driven Al-based Janus micromotors

6.3.1 Introduction

As we discussed in previous sections, the requirement of high concentration of hydrogen peroxide fuel has greatly hindered practical applications of catalytically propelled micro/nanomotors.[51] Accordingly, there has been a considerable recent interest in identifying new compositions of micromotors that can harvest energy from different chemical reactions of their surrounding environment. Sen's team described a bisegment Pt/Cu nanowire motor that uses bromine or iodine fuels, instead of hydrogen peroxide,[52] while Wang's group illustrated acid-driven microtubular engines propelled by hydrogen bubbles formed by oxidation of their zinc layer in the acidic media.[53] Gao et al. demonstrated the first example of a hybrid nanomotor which can be powered both catalytically and magnetically.[54] However, there are no reports about multi-fuel based locomotion of the same chemically-powered micromotor. Many future practical applications would require micro/nanomotors that can propel in different environments, with or without hydrogen peroxide. These include the use of microrobots in harsh industrial processes, involving both extreme alkaline and acidic conditions.

Here I demonstrate the first example of a chemically-driven hybrid nanomotor that can be powered by reactions of three different fuels: base, acid or hydrogen peroxide, and illustrate that its autonomous fuel switching process (in response to a change in the surrounding environment) has a negligible effect upon the propulsion efficiency. In the following sections we will characterize the design and operation of such *multi-fuel* micromotor, address fundamental issues associated with the use of each fuel, and discuss the advantages of such hybrid operation. Relying on multiple types of fuels to power the same micromotor represents a major challenge in view of the fundamentally different chemical and operational requirements associated with each fuel.

6.3.2 Experimental section

The micromotors were prepared using aluminum microspheres with different diameters (5~30 μm, Alpha Chemicals, Missouri, MO) as the base particles. Aluminum particles were dispersed into isopropanol and filtered through the filter membranes with different pore sizes. Subsequently, the particles were spread onto a glass slide and were coated with a 50 nm thick titanium layer and a 300 nm thick Pd layer using Temescal BJD 1800 E-beam Evaporator under a pressure of 1×10^{-7} Torr. After a brief sonication of the slides in water, the micromotors were released from the glass slide and dispersed into water.

Surfactants were used in the experiments to reduce the surface tension, including 1.25% and 5% Triton X-100 for motion in acid and peroxide, respectively, and 1.25% sodium cholate for the movement in base. 1.25% of Triton X-100 was added for the adaptive fuel-switching operation. Experiments under physiological temperature were carried out using a peltier - thermoelectric cooler module (CH-109-1.4-1.5) coupled with a K type thermocouple and a dual digital display PID temperature controller SSR.

6.3.3 Results and discussions

To address this challenge and realize the multi-fuel operation, the new hybrid micromotors are based on the aluminum microparticles (5 to 30 μm in diameter). These microparticle are coated on one side with a catalytic palladium layer to form the Janus particles. As illustrated in Figure 6.3.1, the resulting Al/Pd Janus microparticle motors are self-propelled in different media, by hydrogen bubbles generated from the different reactions of their Al constituent with either strongly acidic or basic solutions:

$$2\ Al(s) + 6\ H^{+}(aq) \rightarrow 2\ Al^{3+}(aq) + 3\ H_2(g) \qquad (6.3.1)$$

$$2\ Al(s) + 2\ OH^{-}(aq) + 2\ H_2O(l) \rightarrow 2\ AlO_2^{-}(aq) + 3\ H_2(g) \qquad (6.3.2)$$

reflecting the amphoteric properties of the aluminum and aluminum oxide.[55] While aluminum is commonly protected by a dense oxide layer, some strongly acidic and alkaline media (such as

HCl and NaOH solutions) can remove this coating, and react with aluminum to generate the hydrogen bubble thrust. In addition, such Janus micromotors can also be propelled in the opposite direction by an oxygen bubble thrust associated with the hydrogen peroxide catalytic decomposition at the asymmetric Pd coating in intermediate media (pH 4-11):

$$2\ H_2O_2(aq) \rightarrow 2\ H_2O(l) + O_2\ (g) \qquad (6.3.3)$$

As will be illustrated below, the new hybrid chemically-powered micromotors hold considerable promise for designing self-regulated nanovehicles that adapt their operation according to the surrounding fuel towards various important practical applications.

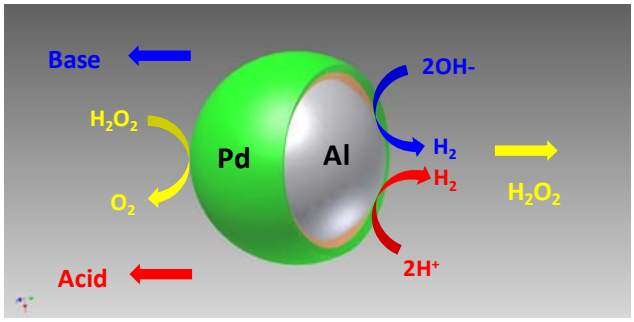

Figure 6.3.1 Schematic of bubble-propelled Pd/Al spherical hybrid micromotors which can operate using three different fuels: acid, base and hydrogen peroxide solutions. Also shown are the corresponding reactions and motion direction.

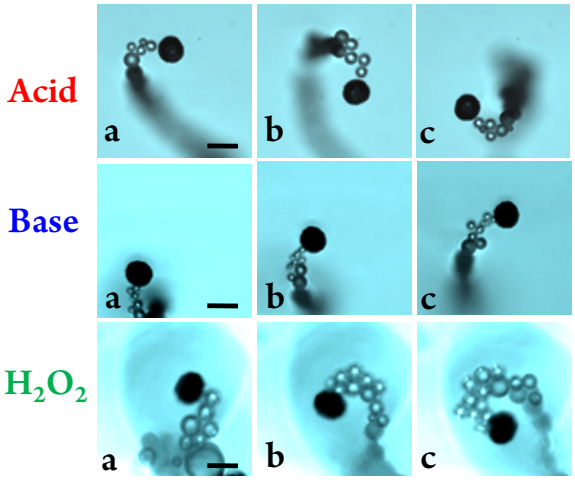

Figure 6.3.2 Multi-fuel operation mode: motion of spherical hybrid micromotors in various environments: acid, base and hydrogen peroxide. Time-lapse images showing the movement of micromotor in acid (0.1 M HCl, pH 1; Top), in alkaline media (0.1 M NaOH, pH 13, Center), and in hydrogen peroxide (10% H_2O_2, Bottom) at a) 0, b) 1, c) 2 s, respectively. Scale bar, 20 µm.

Figure 6.3.2 displays time-lapse images, for the movement of the hybrid micromotor (20 μm diameter) in three different media: strong acid (HCl, 100 mM), strong base (NaOH, 100 mM) and hydrogen peroxide solution (10% w/w). These images illustrate the efficient propulsion in the different surrounding environments, with speeds of 36 μm s^{-1}, 25 μm s^{-1} and 35 μm s^{-1} in the acid, base and hydrogen peroxide solutions, respectively, i.e., a higher speed in acid (vs. base of same concentration). Distinct tails of bubbles, ejecting out continuously from one side of the microparticles, are observed in these three different media, allowing convenient visualization of their well-defined trajectories. To our knowledge, this represents the first example of clear observation of bubble tails propelling spherical Janus micromotors. These reflect the detachment of hydrogen bubbles (from the exposed Al side) in acidic and basic media or of oxygen bubbles from the catalytic Pd surface in the hydrogen peroxide solution. Such bubble detachments in these three different chemical environments lead to a net momentum, i.e., propulsion thrust, and hence to directional continuous motion, analogous to the oxygen-bubble propelled hydrogen-peroxide driven platinum-based micromotors.[18-20] In contrast, no direct motion was observed for bare Al microparticles in alkaline, acid and hydrogen peroxide media. While Brownian motion has influence on the motor movement at the nanoscale,[56] such effect is negligible (compared to the powerful bubble thrust) for 'larger' motors, such as the 20 μm particle used here. Notice that the new hybrid motor is expected to move in different directions (in the peroxide vs acid/base solutions) due to the generation of the oxygen and hydrogen bubble thrusts on the opposite sides of the microsphere. The diameters of the oxygen bubbles in the hydrogen peroxide fuel are usually larger than the hydrogen bubbles generated in acidic or basic environments. This may be attributed to the oxygen generation over the entire Pd surface, compared to the localized Al dissolution and hydrogen-evolution reactions (as will be discussed below). For the bubble-propelled Janus motor system, the driving force F due to the bubble thrust is balanced by the viscous drag force F_{drag} to reach a stable velocity.[16]

The influence of the particle size upon the speed and lifetime of the motor in alkaline media is illustrated in Figure 6.3.3 using spheres ranging from 5 to 20 μm. Well-defined propulsion is observed using the different particle sizes, with larger particles displaying higher speeds and longer lifetimes. For example, the 5 μm particles achieve a speed of 20 μm s^{-1} in 0.3 M NaOH, with the bubble propulsion lasting around 3 min. Increasing the particle diameter to 10 μm and 20 μm raises the speed to 25 μm s^{-1} and 40 μm s^{-1}, respectively, while extending the life time to 5 min and 8 min. As expected, the larger the particle size the longer it takes for the aluminum to be dissolved. The greatly extended lifetime of these hydrogen propelled micromotors makes them attractive for diverse practical applications. It can also be clearly observed that the bubble frequency of the micromotor increases with the particle size, reflecting the greater hydrogen gas evolution on the larger surface aluminum area. Larger particles thus result in a faster absolute speed; yet, due to increased fluid drag force, such particles have a lower relative speed.

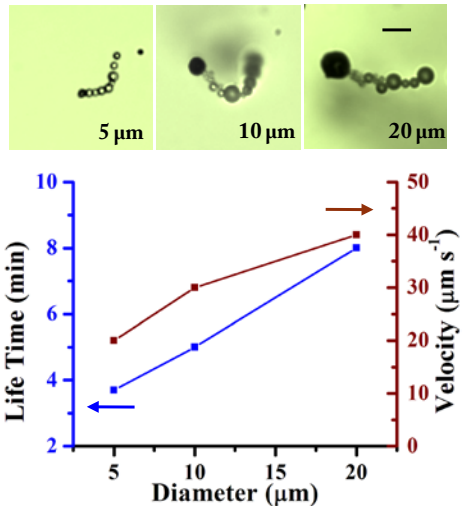

Figure 6.3.3 Dependence of the speed and lifetime upon the size (diameter) of the base-driven motor in 0.3 M (pH 13.5) NaOH. Scale bar, 20 μm.

The speed of the hybrid micromotor is strongly dependent on the base concentration (Figure 6.3.4). As expected, the micromotors (average 20 μm diameter) display their fastest speed (220 and 80 μm s^{-1} at 37 and 23 ºC, respectively) using the highest base concentration tested (1M,

corresponding to pH 14 and 13.6 at 23 ºC and 37 ºC). At room temperature (23 °C), the speed increases gradually between pH 12.5 to 13.0 to 25 μm s^{-1} and then it levels off till pH 14. However, at physiological temperature (37 °C), the hybrid micromotor displays a wider operational pH range (with movement observed above pH 11), along with higher speed, expected from the temperature effect upon the hydrogen evolution reaction.[57,58] This micromotor speed thus gradually increases from 0 to 50 μm s^{-1} over the 11-13 pH range, then it rapidly accelerates to achieve the fastest speed of 220 μm s^{-1} at 1 M NaOH. Such wider operational pH range makes these micromotors useful for movement in strongly alkaline environments.

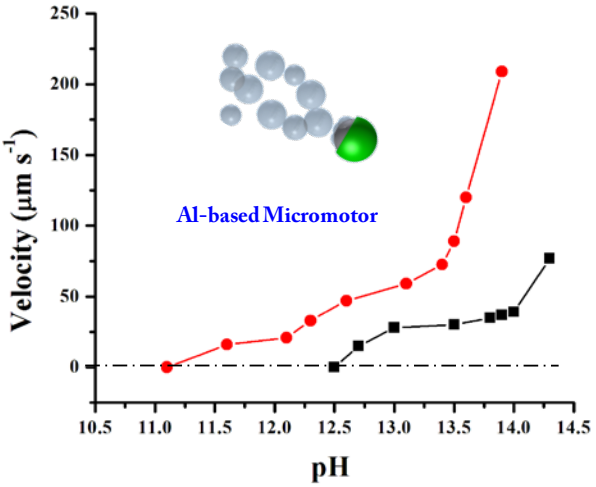

Figure 6.3.4 Dependence of the speed of the hybrid nanomotor upon the pH of the alkaline media. Black squares and red circles curves represent the speed at room temperature (23 °C) and physiological temperature (37 °C), respectively.

Similarly, the speed of the hybrid micromotor in acidic media depends also on the surrounding pH and temperature (Figure 6.3.5, Left). At room temperature, the micromotor moves very rapidly at over 200 μm s^{-1} in 1 M HCl solution (pH 0). The speed decreases rapidly to 35 and 20 μm s^{-1} upon raising the pH to 1 and 2, respectively. Faster acid-driven movement is observed at 37 °C with the speed decreasing rapidly from 240 to 15 μm s^{-1} between pH 0 to 3, respectively. This represents a wider acidic operational range compared to formerly reported zinc-based acid-driven microrockets which cannot move in environments with pH values higher

than 2.[53] The upper acidic pH range can be raised to 3.6 using a physiological temperature of 37 °C. The wider acidic operational range is of practical significance for the future applications (e.g. drug delivery or nanosurgery in human stomach). The Janus micromotor also displays longer lifetimes in acidic media (e.g., ~ 8 min in pH 1). Over the intermediate pH range (pH 4-11) the micromotor can rely on the catalytic decomposition of hydrogen peroxide (15% w/w) at its partial Pd coating (Figure 6.3.5, Center). High propulsion efficiency, with a speed of 75 μm s^{-1}, can thus be observed. Apparently, the environmental pH has a negligible effect upon the catalytic peroxide decomposition process and locomotion over such wide pH range (4-11).

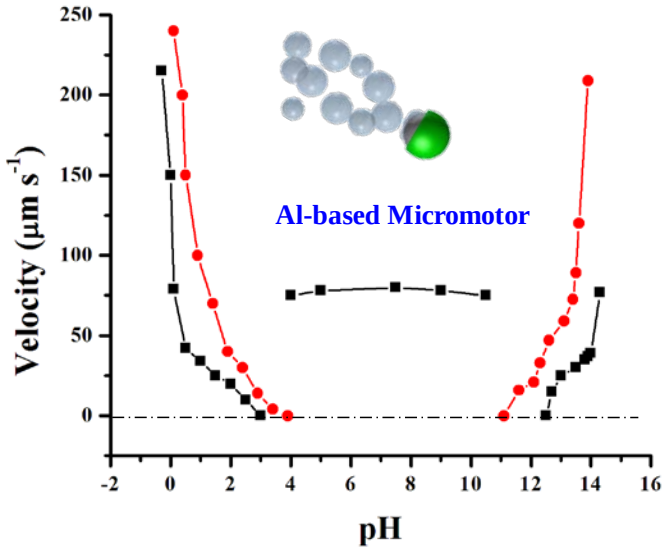

Figure 6.3.5 Dependence of the speed of the hybrid micromotor (~20 μm diameter) upon the pH of the different media. Black squares and red circles curves represent the speed at room temperature (23 °C) and physiological temperature (37 °C), respectively.

The nature of the anion has a profound effect upon the propulsion in acidic media. For example, while no bubble generation and movement are observed in 1M sulfuric acid, adding increasing levels of sodium chloride into this medium leads to a gradual increase of the bubble generation and to movement at speeds of 10 and 30 μm s^{-1} for 0.05 and 1M NaCl, respectively. Such behavior reflects the pitting corrosion processes of Al by chloride ions[59,60] that lead to localized 'blisters' that are filled with hydrogen and water as they rupture.

Many future practical applications would require micro/nanomotors that can propel in different environments, with or without hydrogen peroxide. These include the use of microrobots in harsh industrial processes, involving both extreme alkaline and acidic conditions. Quite often the environment is changing dynamically and these would require an adapted motor operation for meeting the new condition or preferably a motor capable of swimming in both environments. The present hybrid nanomotor can reconfigure its operation autonomously in response to such change of the surrounding environment (i.e., local fuel). Figure 6.3.6a illustrates that an Al-based micromotor (with a 24 μm diameter) moves in the alkaline media (pH 13.5) at a speed of 35 μm s^{-1} based on the Al reaction with the base (eqn 6.3.2). Such efficient propulsion is maintained upon switching the surrounding pH from 13.5 to 0.5, i.e., adding excess of acid (Figure 6.3.6b), with a high speed of 40 μm s^{-1} in the presence of the acid fuel (eqn 6.3.1). Apparently, the micromotor can reconfigure its fuel requirement according to the surrounding environment. Such adaptive fuel switching process of hybrid nanomotor holds great promise for diverse practical applications. Notice also the distinct three bubble tails, ejecting out continuously from the Al side, that are observed in both media. However, a mixture of acid or base with hydrogen peroxide is expected to lead to bubbles from both sides.

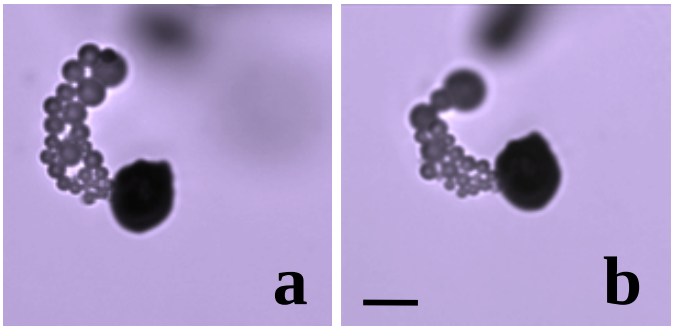

Figure 6.3.6 Adaptive operation of the hybrid micromotors: continuous movement upon switching the environment (local fuel) from (a) alkaline (pH 13.5) to (b) acidic (pH 0.5) media. Scale bar, 20 μm.

6.3.4 Conclusions

In conclusion, we demonstrated here the first example of a hybrid micromotor which can be powered by multiple (three different) fuels: acid, base and hydrogen peroxide solutions. The Janus micromotors – prepared by coating one side of Al microspheres with catalytic Pd coating - are propelled efficiently by the thrust of hydrogen bubbles in extreme acidic/alkaline environments and by oxygen bubbles in hydrogen peroxide solutions. The new multi-fuel motor moves in different directions (in the peroxide vs acid/base solutions) due to the generation of oxygen and hydrogen bubble thrusts on the opposite sides of the microsphere. Unlike the common oxygen-bubble propelled microengines or acid-driven microrockets, these low cost aluminum-based microsphere motors are fueled by triple environments. Such multi-fuel motor technology should be attractive in situations where one of the fuels is not available. The Janus Al microspheres lead also to the first example of a chemically-powered micromotor that can operate in a strong alkaline medium, and to the first observation of bubble tails propelling such Janus micromotors. This also represents the first example of self-propelled spherical Janus micromotor with clear bubble observation. The multi-fuel powered hybrid nanomotor can autonomously switch its fuel in response to changes in the surrounding environment. Such multi-fuel motor operation capability offers a broader scope of operation and considerable promise for diverse and adaptive operations in different chemical environments.

6.4 Water-driven Al-Ga micromotors

6.4.1 Introduction

Extending the scope of chemically-powered nanomotors to diverse biomedical operations and different biological fluids would require the identification of new *in situ* fuels in connection with new catalytic materials and reactions. Ultimately, it would be beneficial to explore the sample matrix itself as the fuel source, thus obviating the need for adding external fuels and not compromising the viability of the biological target. Particularly attractive would be new micro/nanomotors that can harvest energy from their own surrounding environment, *i.e.*, use the sample matrix itself as their fuel source, thus obviating the need for adding external fuels such as hydrogen peroxide.[53,61] Although in previous sections I have demonstrated the use of acid or base instead of hydrogen peroxide as the fuel to power micromotors, for majority applications, water will be the ideal fuel to power the micromotors.

This section describes the first example of a water-driven microscale motor. To accomplish the goal of generating the bubble-thrust essential for an efficient autonomous movement, we have focused here on the water-splitting reaction generating hydrogen bubbles. One of the promising approaches to produce hydrogen involves the use of aluminum to reduce water to hydrogen:[62-65]

$$2Al(s) + 6H_2O(aq) \rightarrow 2Al(OH)_3(s) + 3H_2(g) \quad (1)$$

However, the utility of this reaction process is strongly hindered by a rapidly-formed oxide passivation layer on the Al surface.[65] This problem can be addressed by using aluminum alloys, particularly with gallium, indium, or tin.[66-68] In particular, using the Al-Ga system, liquid Ga rapidly penetrates into the solid Al along its grain boundaries in a process known as liquid metal embrittlement (LME).[68] The surface diffusion of Ga is responsible for the removal of the reaction-hindering Al oxide film, thus dramatically promoting the aluminum-water reaction. The

presence of such liquid phase in the alloy microstructure thus leads to a continuous generation of hydrogen, making Al-Ga alloys attractive candidates for designing water-driven micromotors. Unlike violently hydrogen-generating alkali metals, such as sodium and potassium, aluminum alloys offer greater stability and much lower costs.

6.4.2 Experimental Section

The micromotors were prepared using aluminum microparticles (average 20 μm size, Alpha Chemicals, Missouri, MO) as the base particles. Aluminum particles were spread onto a glass slide while gallium (Catalog # 263265, Sigma-Aldrich, St Louis, MO) was melted at 80°C and spread onto another glass slide, at a level corresponding to a mass ratio of 1:1 (Al:Ga). The two slides were pressed together and mixed until the particles were evenly distributed and well-coated. Then, the particles were kept for 1 hour at 80°C. The alloy particles were coated with a titanium layer at 2.5 Å/s for 200 nm using Temescal BJD 1800 E-beam Evaporator under a pressure of 1×10^{-7} Torr. After sonicating the slides briefly in isopropanol, the micromotors were released from the glass slide and dispersed into isopropanol. The motors were stored in the pure isopropanol solution until use. This process leads to a relatively high yield, with more than 75% of particles displaying efficient bubbling in water. Aluminum-Gallium-Indium alloy particles were prepared using a similar protocol but using Gallium-Indium eutectic (Catalog # 495425, Sigma-Aldrich).

6.4.3 Results and discussions

In order to use the hydrogen-releasing reaction between aluminum alloys and water, we have designed spherical bubble-propelled Janus micromotors based on coating one side of an Al-Ga microparticle with a titanium layer (Figure 6.4.1). The new micromotors have an average diameter of 20 μm and can be propelled at very high speed of 3 mm s^{-1}, corresponding to 150 body length s^{-1}. Such fast movement reflects the net momentum associated with the detachment of hydrogen bubbles (from the exposed Al-Ga side), that leads to a directional propulsion thrust,

analogous to the oxygen-bubble propelled-peroxide driven Pt-based Janus micromotors.[16] In the following sections we will describe the preparation of such water-propelled Al-Ga/Ti Janus microparticles and discuss their locomotion behavior (speed, lifetime, directionality, *etc.*) under different experimental conditions (media, pH, and ionic strength).

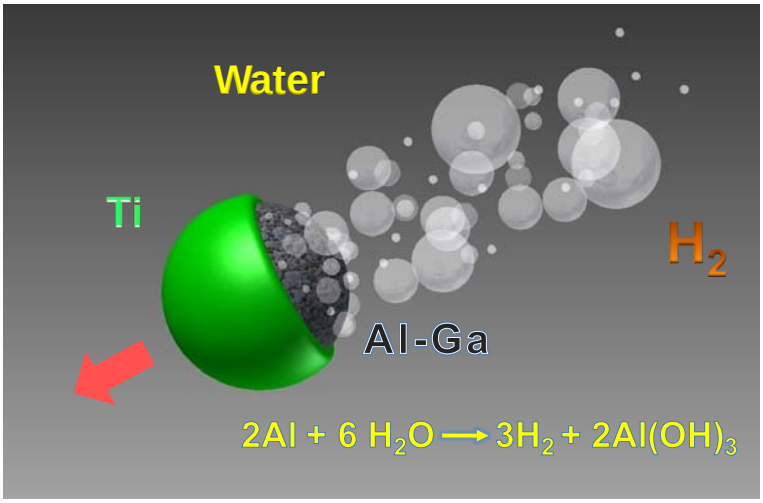

Figure 6.4.1 Schematic image of a water-driven hydrogen-propelled Al-Ga/Ti micromotor. The dark hemisphere (right) represents the Al-Ga alloy while the green area (left) corresponds to the asymmetric Ti coating on one side of the sphere.

The spherical Al-Ga/Ti micromotors were fabricated through the simple sequential process illustrated in Figure 6.4.2. Aluminum particles (average size, 20 μm) and liquid gallium (at 80 °C) are spread onto separate glass slides at a 1:1 mass ratio (a). The two slides were then pressed and kept together for 1 hour at 80 °C, allowing formation of the Al-Ga alloy *via* microcontact mixing (b). During this period, gallium penetrated into the aluminum particles to form the outer alloy layer. The slides were then separated with the Al-Ga microparticles remaining on one of the surfaces (c). Subsequently, one side of the particles was coated with a titanium layer *via* E-beam evaporation to form the asymmetric Janus microstructure (d). After brief sonication in isopropanol, the micromotors were released from the glass slide and dispersed into isopropanol (e) for storage until use.

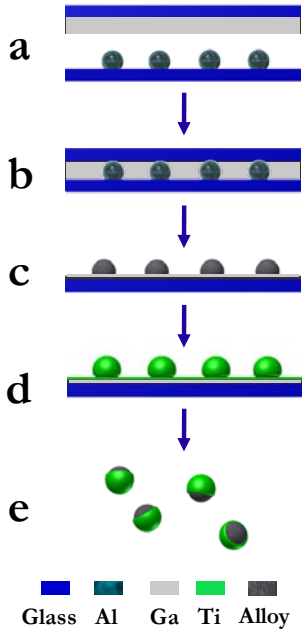

Figure 6.4.2 Fabrication of water-driven Al-Ga/Ti micromotors: coating the liquid gallium and aluminum particles on separate slides (a), alloy formation by microcontact mixing of the aluminum particles and 'liquid' gallium (b), detachment of the slides (c), coating one side of the Al-Ga particles with a Ti layer by E-beam evaporation (d), and separation of the individual micromotors by sonication in isopropanol (e).

The resulting Janus micromotors were characterized by scanning electron microscope (SEM) and energy-dispersive X-ray spectroscopy (EDX) analysis. The EDX data of Figure 6.4.3 illustrate the distribution of gallium, aluminum and titanium within the Janus spherical micromotor. It indicate that gallium has penetrated into the grain boundaries of the aluminum particle (*via* liquid metal embrittlement) while aluminum has dissolved into the liquid gallium coating, forming an Al-Ga alloy layer over the entire surface. The EDX and SEM data also show that the outer titanium layer covers slightly more than half of the particle, as desired for facilitating the bubble ejection from the opposite (exposed Al-Ga) side and creating a directional propulsion thrust.

X-ray Fluorescence (XRF) analysis was used for estimating the Ga/Al composition ratio of the micromotor. The spectrum indicates mass and atomic Ga/Al ratios of ~3:7, and 14:86%, respectively (not shown). These ratios correspond to a lower fraction of gallium in the particles

than originally used during their preparation, reflecting the gallium portion remaining on the glass slide after the microparticle removal (Figure 6.4.2; step d).

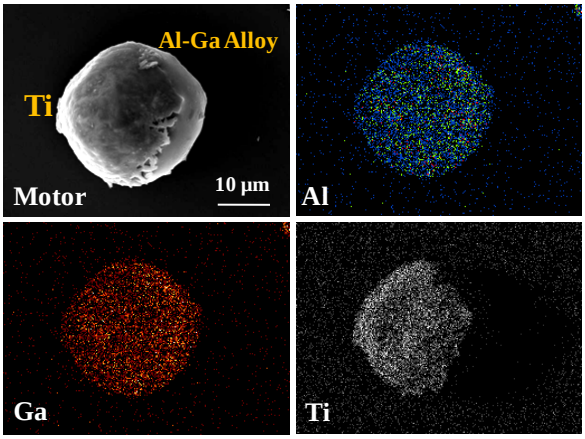

Figure 6.4.3 Scanning electron microscope (SEM) image and Energy-dispersive X-ray (EDX) spectroscopy results showing the distribution of Ga, Al and Ti in the Janus Al-Ga/Ti micromotor.

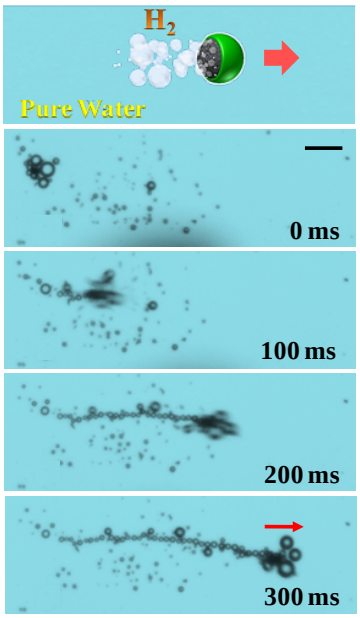

Figure 6.4.4 Water-driven Al-Ga/Ti micromotor: time-lapse images, illustrating the motor propulsion at 0, 100, 200 and 300 ms intervals. Scale bar, 100 µm. Medium: ultrapure water containing 0.05% Triton X-100.

Figure 6.4.4 illustrates the ultrafast propulsion of an Al-Ga/Ti micromotor in ultrapure water. It shows time-lapse images, over a 300 ms period. A long tail of hydrogen bubbles, generated on one side of the micromotor, is clearly observed, reflecting the rapid spontaneous

reaction of aluminum with the surrounding water. The average diameter of these ejected hydrogen bubbles is around 10 μm. The fast production of small bubbles and the steady motor propulsion are also clearly illustrated in the images. Such bubble generation imparts the strong momentum that propels the micromotor forward in a relatively straight path. This leads to a remarkable speed of 3 mm s^{-1}, which corresponds to 150 body length s^{-1}. This represents a very large drive force of over 500 pN, based on the drag force for a spherical colloid (equals to the drive force), $F=6\pi\mu a v$, where a is the radius of the sphere, v is the speed of the micromotor and μ is the viscosity of water.[16] Such speed and force are significantly higher than those reported for common (peroxide-driven) catalytic Janus particles.[16,69,70]

Various control experiments, illustrated in Figure 6.4.5, were used to demonstrate the crucial roles of the 'liquid' phase of the Al-Ga microparticles and of the sputtered Ti layer in the observed directional propulsion. For example, no bubble generation is observed in Figure 6.4.5a for the plain Al microparticle, as the presence of an oxide passivation layer (expected in the absence of Ga) hinders the Al reaction with water.[66,67] Similarly, no directional movement is observed in Figure 6.4.5b for an Al-Ga alloy particle, without the partial Ti coating, owing to the symmetric generation of numerous hydrogen bubbles from the entire surface. In contrast, a clear directed movement is observed in Figure 6.4.5c for the partially covered microparticle, reflecting the asymmetric bubble generation associated with the effectiveness of the Ti layer in blocking the aluminum-water reaction.

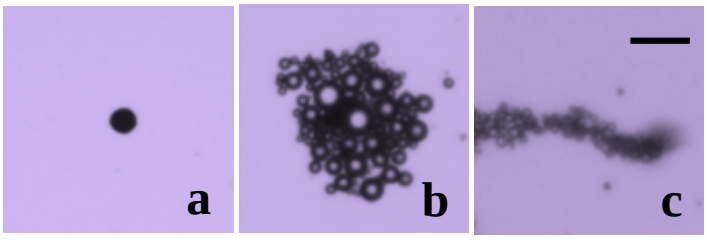

Figure 6.4.5 Control experiments using an Al microparticle (a), and an uncoated Al-Ga alloy microparticle (b), compared to an Al-Ga/Ti micromotor (c). Media, pure water with 0.1% Triton X-100. Scale bar, 50 μm.

The liquid phase of the Al-Ga particles – essential for the aluminum-water reaction[68,71] – is readily obtained by heating the particles during the preparation process (described previously), as the melting point of the resulting alloy is lower than room temperature.[71] This liquid phase of the Al-Ga alloy is developed when small amounts of solid Al dissolve into the liquid Ga occupying the outer particle layer. It is this solvated Al, present in the liquid phase, that reacts readily with water[68] at the motor-solution interface, generating hydrogen bubbles. As this localized Al is dissolved and depleted during the reaction, additional Al from the interior of the solid particle dissolves into the outer Ga layer to restore the liquid-phase equilibrium. Eventually, this process depletes the solid Al at the center of the particle. The generation and ejection of the hydrogen bubbles leads to the removal of the passivating $Al(OH)_3$ layer formed at the surface of the liquid phase. The melting point of the Al-Ga alloy depends on the specific Al/Ga ratio in the particle; for the Al/Ga ratio in this study, the alloy remains in the liquid phase at room temperature,[71] which is essential for aluminum-water reaction and continuous motor operation.

The micromotors maintain a similar propulsion behavior (with a speed of around 3 mm/s) in weak acid or base solutions of pH values ranging from pH 4 to pH 10, reflecting the fact that these media have limited effect upon the efficiency of the aluminum-water reaction.[72] However, in strongly acidic or alkaline media ($pH<2$ or $pH>12$, respectively), different hydrogen generation reactions take place, reflecting the amphoteric properties of the aluminum and aluminum oxide.[73] It is well-established that strong acids and bases are able to destroy the protective oxide layer on the aluminum surface to facilitate different hydrogen generation pathways.[73] This is also supported by additional experiments illustrating significantly longer motor lifetimes (of over 5 minutes) in pH 0 or pH 14 compared to the limited lifetime and hydrogen yield observed under mild environments.

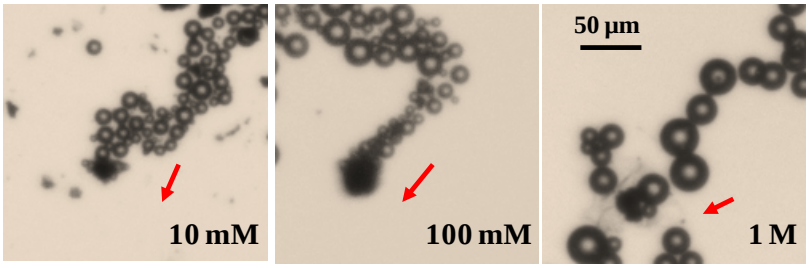

Figure 6.4.6 Influence of the salt (sodium chloride) concentration upon the propulsion of the Al-Ga/Ti micromotor. Conditions, as in Figure 6.3.5c.

The influence of the salt (chloride ion) concentration upon the water-driven movement was also examined. Figure 6.4.6 illustrates the motion of the Al-Ga/Ti micromotor in sodium chloride solutions of different concentrations (10-1000 mM). These images clearly indicate that the efficiency of the micromotors decreases as the salt concentration increases. Accordingly, the speed of the micromotor is reduced from 3000 µm s^{-1} without the salt to 1300 and 100 µm s^{-1} in 10 mM and 1M NaCl solutions, respectively. The increased salt concentration leads to a lower bubble frequency and a larger bubble size, reflecting the lower reaction rate (*i.e.*, slower Al dissolution) in the salt-rich media. As expected,[29] such larger bubble size and lower frequency lead to a slower propulsion speed. The slower hydrogen evolution at higher NaCl concentrations leads also to longer motor lifetimes of up to 5 min. It has been shown that chloride ions readily penetrate the oxide layer formed on the Al surface upon contact with water, resulting in local Al dissolution (under the oxide film) through a pitting corrosion process.[74,75] The pitting corrosion of Al leads to 'blisters' that fill with hydrogen gas and water as they rupture. As illustrated in Figure 6.4.7b, the Al-Ga/Ti micromotor can move even in a 3 M sodium chloride solution at a speed of 45 µm s^{-1} without adding any surfactant. In contrast, no obvious bubble generation and movement are observed upon exposing Janus Al/Ti microparticles (without Ga) to 3M sodium chloride (Figure 6.4.7a). In addition, no obvious movement was observed using the Al-Ga/Ti microparticle in sodium sulfate solutions (containing more than 0.5 M salt), reflecting the inhibited aluminum-water reaction by sulfate ions (compared to the chloride ions).[76]

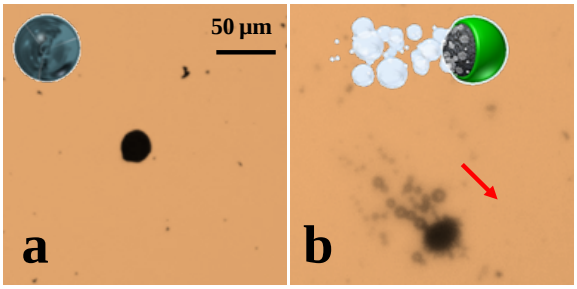

Figure 6.4.7 Al/Ti particles (a) and Al-Ga/Ti (b) micromotors in 3 M sodium cholride.

The lifetime of the Al-Ga micromotor can range from a few minutes down to a few seconds, depending on the size of the Al particle, surrounding solution, temperature, and preparation process that influence the aluminum-water reactivity and Al mass. For example, the longer life time of 5 min was observed in 3 M sodium chloride solutions using 20 µm diameter Al-Ga/Ti microparticles prepared by alloying the Al for one week (for increasing the amount of Al involved in the hydrogen generation[68]). Additional parameters, such as the temperature, Al grain size, strain rate, stress and exposure time to the liquid metal prior to testing, could also influence the reaction efficiency and lifetime of Al-Ga/Ti micromotors.

The new Al-Ga alloy micromotor can operate in different environments such as pure water, PBS buffer, human serum and cell culture media. The speed decreased from 3 mm s^{-1} in pure water to 1200, 600 and 500 µm s^{-1} in the cell culture media, PBS and human serum, respectively. Such slower speeds reflect the increased environmental viscosity in these media. Protein fouling of the motor surface may also contribute to the substantially slower speed observed in human serum. Yet, even the slowest speed (observed in serum) corresponds to a very high relative speed of 15 body-length s^{-1}. This efficient locomotion in various biological media holds great promise for future practical applications.

Further improvements in the propulsion of Al-based alloy motors are expected by replacing the current binary Al-Ga alloy with ternary Al-Ga-In or quaternary Al-Ga-In-Sn alloys. The total percent hydrogen-gas yield of increases sharply from 3-8% (for the Al-Ga alloy) to

around 80% (using Al-Ga-In-Sn), reflecting a higher Al fraction involved in the reaction.[68] Such efficient gas generation would allow the water-driven motor to sustain movement over extended periods. The lower hydrogen yield of the binary alloy is consistent with the observations of short motor lifetimes (of less than a minute) in pure water, as only a very small portion of the motor is involved in the reaction with water. Additional experiments have thus been performed towards micromotors based on the ternary Al-Ga-In alloy. Yet, because of the high reactivity and low stability of the Al-Ga-In alloy, the microparticles reacted with the water vapor in the air immediately after their preparation. Such fast reaction could be clearly observed by a gradual color change of the particles and from the growth of oxide microstructures on the particle surfaces. The reaction of these water-vapor exposed Al-Ga-In/Ti particles in aqueous medium lasted over two minutes, compared to Al-Ga/Ti particles, reflecting the overall higher hydrogen yield of the ternary alloy. Preparing and storing ternary or quaternary alloy micromotors in an inert environment should lead to more sustained motor lifetimes.

6.4.4 Conclusions

We have presented the first example of chemically-powered micromotors propelled autonomously using water as the sole fuel source. While the water splitting reaction was used before to drive bipolar-electrochemical macroscale motors under an external electrical field,[10] it has not been used for the locomotion of self-propelled chemically-powered micromotors. The water-splitting reaction, involving Al-Ga alloys, has been used for realizing such water-driven microscale motion, with the reaction and propulsion efficiencies improving *via* the liquid metal embrittlement in the Al-Ga system. The presence of such liquid phase in the alloy microstructure facilitates the continuous hydrogen-generating reaction between aluminum and water. We have demonstrated that the resulting water-driven Al-Ga/Ti micromotors can swim in water at 150 body lengths per second, as well as in biological media such as human serum. Further improvements in the propulsion behavior are expected by enhancing the alloy reactivity *via* a

judicious control of its microstructure and composition. New water-splitting catalytic reactions and materials, offering extended motor lifetimes and/or higher efficiency, are also highly desired for future water-driven nanomotor operations. The new water-driven motion capability should greatly expand the scope of applications and environments of chemically-powered nanomachines. In particular, these water-driven micromotors could have a profound impact on diverse biomedical or industrial applications of micromotors, ranging from targeted drug delivery to microchip diagnostics, where the use of the common peroxide fuel is not desirable or possible.

6.5 Seawater-driven magnesium based Janus micromotors for environmental remediation

6.5.1 Introduction

New micro/nanomotors that can harvest energy from their own surrounding environment, *i.e.*, use the sample matrix itself as their fuel source, are highly desired for eliminating the need for adding toxic external fuels. Water is the obvious ideal choice of fuel for the majority practical nanomachine applications. In section 6.4, I described the first example of a water-driven micromotor, based on Al/Ga microparticles, which displayed efficient propulsion in aqueous solutions.[78] However, due to the toxicity of aluminum and gallium, more biocompatible and environmentally friendly materials are highly desired for different applications of water-driven micromotors.

Here we demonstrate a new hydrogen-bubble-propelled Janus micromotor, based on the magnesium/water reaction, which can be self-propelled in seawater without an external fuel. Common active metals (*e.g.*, Li, Na, K, Ca), can lead to efficient hydrogen evolution from the water/metal reaction, but are too reactive for a safe operation and are not stable in air. Magnesium, in contrast, is an attractive candidate material for the design of water-driven micromotors as it is a biocompatible 'green' nutrient trace element, vital for many body functions and enzymatic processes. In addition, Mg is a low cost metal and Mg^{2+} is present in different natural environments (*e.g.*, seawater). The Mg-water reaction is commonly hindered in ambient atmospheres due to the formation of a compact hydroxide passivation surface layer. Accordingly, Mg cannot continuously reduce water to generate hydrogen bubbles.[79,80] However, we demonstrate in the following sections that the micromotor can display efficient and prolonged propulsion in chloride-rich environments (such as seawater) owing to the combination of macrogalvanic corrosion and chloride pitting corrosion processes (discussed below). The new

seawater-driven micromotors can be guided magnetically (through the incorporation of a magnetic Ni layer) and be functionalized to perform various important tasks. For example, modification of the outer gold patch with long-chain alkanethiols leads to a super-hydrophobic surface that can be used for environmental oil remediation.

6.5.2 Experimental sections

Synthesis of Mg-Ti-Ni-Au Janus Micromotors

The micromotors were prepared using magnesium microparticles (Catalog # 465666, Sigma-Aldrich, St Louis, MO, powder, -325 mesh, 99.5% trace metals basis) as the base particles. The Mg particles were placed onto glass slides and coated with a 20 nm titanium layer at 1 Å/s, a 80 nm nickel layer at 2 Å/s, and a 10 nm gold layer at 1 Å/s using Temescal BJD 1800 E-beam Evaporator. After a brief sonication in ethanol, the micromotors were released from the glass slide and dispersed into ethanol. The motors were stored in the pure ethanol solution until use. For the control experiments, Mg particles were similarly coated with 100 nm Ti (for Mg-Ti particles), 100 nm Ti and 10 nm Ag (for Mg-Ti-Ag particles), and 100 nm Ti and 10 nm Au (for Mg-Ti-Au particles).

Micromotor Modification

The external gold surface of the micromotors was modified by immersion in 1 mM octadecanethiol (Sigma-Aldrich) in absolute ethanol (Sigma-Aldrich) for 1 hour, after which the resulting monolayer-modified micromotors were washed with ethanol and isolated by centrifugation at 6000 rpm for 2 min. All experiments were carried out at room temperature.

Equipment and Experimental Procedure

Seawater used as propulsion media in the experiments was collected at Torrey Pines Beach, La Jolla, CA. All the solutions (seawater, NaCl, $NaNO_3$ and Na_2SO_4) used in the work contained 0.5% Triton X-100 (Fisher Scientific, Fair Lawn, NJ). For the oil remediation experiments, an emulsion of seawater/motor oil sample (20:1), with 0.5% Triton, was first

prepared. Images were captured by an inverted optical microscope (Nikon Instrument Inc. Ti-S/L100), coupled with 10x and 4x objectives, a Hamamatsu digital camera C11440 using the NIS-Elements AR 3.2 software.

6.5.3 Results and discussions

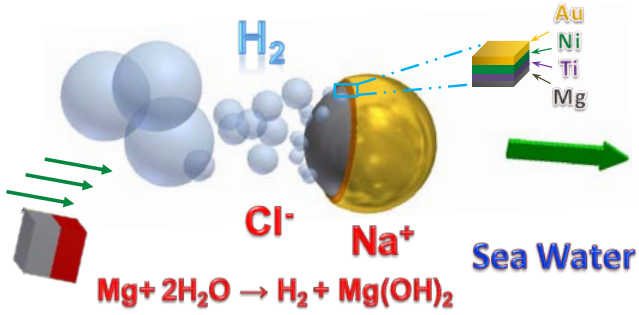

Figure 6.5.1 Schematic of the Mg-based seawater-driven Janus micromotors.

Figure 6.5.1 displays the schematic of the hydrogen-bubble-propelled seawater-driven Janus Mg-based micromotors. The Mg particles have an average size of ~30 μm and are asymmetrically coated by e-beam evaporation with Ti, Ni and Au layers to form the Janus micromotors (with the Ti layer providing a good contact between the Ni-Au layers and the Mg surface). Upon immersing into seawater, a spontaneous redox reaction occurs, involving the oxidation of the Mg surface to reduce water to hydrogen bubbles:

$$Mg(s) + 2H_2O(aq) \rightarrow Mg(OH)_2(s) + H_2(g) \qquad (6.5.1)$$

While the rapidly-formed oxide passivation layer on the Mg surface can hinder the process,[79,80] we found that the presence of the gold layer and chloride ions allows the reaction to proceed (by combination of macrogalvanic corrosion and pitting corrosion processes, respectively), hence leading to continuous formation of hydrogen bubbles to propel the microparticles.

Figure 6.5.2 displays time-lapse images of the movement of the Janus Mg micromotor in seawater over a 4 s period at 1 s intervals. These images illustrate the continuous stream of hydrogen microbubbles released from the exposed Mg surface. The micromotor is self-propelled

at a high speed of over 90 μm/s, which corresponds to a relative speed of nearly 3 body lengths/s. The Mg Janus micromotor follows predetermined trajectories under the magnetic guidance. As illustrated in Figure 6.5.2 (b-e), such magnetic guidance steers the micromotor along different trajectories to offer high spatial and temporal resolution essential for a variety of applications. The micromotor thus executes sharp and rapid turns and travels in a square pattern.

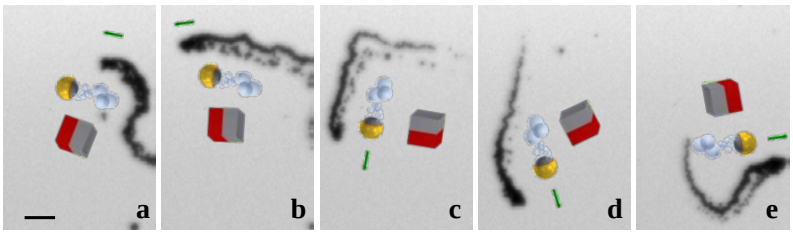

Figure 6.5.2 Seawater-driven magnetically-guided Mg-based micromotor: time-lapse images showing the propulsion of micromotor in seawater in one second intervals with spatial magnetic motion control. Scale bar, 40 μm.

The presence of the gold layer plays a crucial role in the self-propulsion of the Mg-based micromotor, as was demonstrated by various control experiments. Figure 6.5.3A clearly indicates that the bare Mg particles and Mg/Ti Janus particles display no bubble generation and net displacement in seawater. Some bubble formation, with no directional propulsion, is observed using the Mg-Ti-Ag microparticle in the seawater. In contrast, replacing the Ag layer with a Au layer leads to efficient motion in seawater, reflecting the enhanced Mg-water reaction. The important role of the gold in the increased reaction rate and propulsion efficiency is associated with the macrogalvanic corrosion mechanism, which is an electrochemical process in which one metal corrodes preferentially to another one when both metals are in electrical contact and immersed in an electrolyte.[81] When the Janus micromotor is immersed into seawater, a short-circuited galvanic cell is formed. The anodic indexes for gold and silver are -0.0 V and -0.15 V, respectively, while magnesium has a very low potential of -1.75 V.[82] The Au-Mg system thus has a larger electrochemical potential difference, compared to the Ag-Mg couple, resulting in a considerably faster and preferential dissolution of magnesium in the presence of gold.

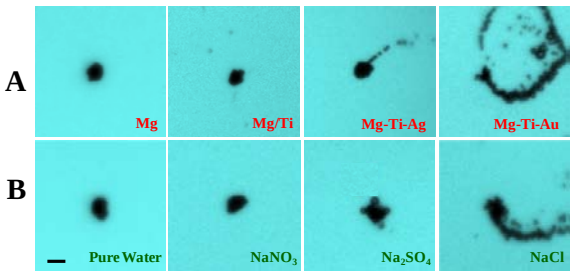

Figure 6.5.3 (A) Control experiments using Mg, Mg/Ti, Mg/Ti/Ag and Mg/Ti/Au microparticles in seawater over a 5 second period. (B) Anion effect upon the movement of Mg/Ti/Au micromotors using pure water, 0.5 M $NaNO_3$, 0.5 M Na_2SO_4 and 0.5 M NaCl solutions (over a 6 second period). Scale bar, 30 μm.

Additionally, we observed that such macrogalvanic corrosion of Mg (and the corresponding propulsion) is strongly influenced by co-existing anions. For example, Figure 6.5.3B compares the bubble generation and motion of Mg/Ti/Au Janus micromotors in the presence of different electrolytes ($NaNO_3$, Na_2SO_4, and NaCl). No bubble generation is observed on the micromotors in pure water and sodium nitrate solutions, while very slow bubble generation is observed in the sodium sulfate medium; in contrast, a fast and strong bubble generation is observed in the sodium chloride solution. Overall, Figure 6.5.3B clearly indicates that the chloride-induced pitting corrosion on the Mg surface plays a critical role in the observed bubble generation and propulsion (in addition to the galvanic corrosion). Pitting corrosion commonly occurs in metals that are protected by a passivation layer (*e.g.*, Mg with a $Mg(OH)_2$ layer).[83-86] It is well known that chloride ions promote the corrosion of Mg in aqueous solutions.[85] Aggressive anionic species, such as chloride, are able to penetrate the passivation layer and are further electrostatically transported into the pit, where they serve to balance the charge within the corrosion pits as the Mg^+ cation concentration builds up.[81,83] As the Mg corrosion continues, the OH^- is depleted within the pit, preventing the passivation of the pit surfaces.[84] The pit environment becomes weakly acidic due to the build-up of Mg^+ and Cl^- levels, further promoting the Mg dissolution in the pit. The intermediate Mg^+ near the surface of the pit then reacts to form H_2 gas:[83]

$$2\ Mg^{+}(aq) + 2\ H_2O(aq) \rightarrow 2\ Mg^{2+}(s) + 2\ OH^{-} + H_2(g) \quad (6.5.2)$$

This process is autocatalytic, and proceeds as long as there is consistent electrolytic migration of Cl^- into the pit.[84] The high level of Cl^- in seawater (54.6 mmol/kg) thus strongly promotes this reaction mechanism. Sulfate ions can still facilitate the reaction but display a much weaker effect (compared to the chloride ions),[85,86] which is consistent with the experimental results shown in Figure 6.5.3B; nitrate ions, in contrast, have no apparent effects on the reaction rate,[31,32] and hence no bubbles are observed in $NaNO_3$.

It appears that the macrogalvanic corrosion and pitting corrosion effects - when coupled together as in these Mg motors - work synergistically to enhance the overall rate of Mg dissolution and reaction. The galvanic coupling of the Mg particle with the Au layer leads to an enhanced preferential corrosion and anodic dissolution of Mg at the exposed regions, along with the cathodic evolution of H_2 gas at the Au surface. However, the control experiments clearly illustrate that the H_2 bubbles, generated at the Mg surface in the presence of chloride ions due to the pitting corrosion mechanism, have a dominating effect upon the observed propulsion. In fact, the intrinsic galvanic cell (macrogalvanic and microgalvanic effects from the gold coating and impurities of the Mg particles, respectively) serves to further increase the anodic dissolution of Mg, assisting in the pitting corrosion.[81] Thus, the rapidly evolving hydrogen bubbles at the Mg surface, provide the thrust essential for the directional propulsion of the Janus micromotors.

The autonomous motion performance of the new Mg-based Janus micromotors depends strongly upon the chloride ion concentrations in the aqueous media (Figure 6.5.4). As was discussed earlier, the presence of chloride ions increases the amount of dissolved intermediate Mg^+ that can react to form hydrogen. The reaction of the Mg/Ti/Ni/Au particles can be observed from the evolution of a clear bubble tail even in the 0.001 M sodium chloride media, reflecting the strong pitting corrosion effect of the chloride ions. As expected,[85] higher chloride concentrations induce faster reaction rates. For example, the micromotors display an efficient

speed of 90 μm/s in 0.3 M sodium chloride (b), and an even higher speed of 300 μm/s in 3 M sodium chloride (c). This increased rate of bubble generation in chloride solution further confirms the presence of the pitting corrosion mechanism. Despite the continuous dissolution of the Mg microparticle, the Janus Au/Ti/Ni/Mg micromotors display a lifetime of over one min in seawater. Various factors, including the particle size and shape and the exact fuel composition are currently being examined towards extending the motor lifetime.

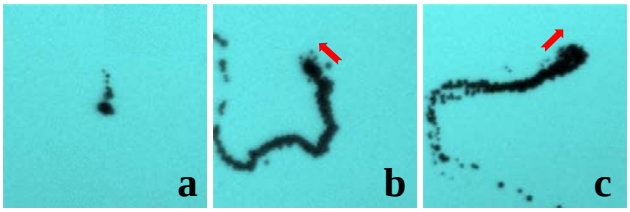

Figure 6.5.4 Motion of the Mg/Ti/Ni/Au micromotors in the presence of different levels of chloride ions: 0.001 M (a), 0.5 M (b) and 3 M NaCl (c) solutions.

We also examined the influence of the solution pH and the presence of a metal complexing agent (EDTA) upon the speed of the micromotors. The micromotors displayed a comparable propulsion behavior in weak acidic or alkaline seawater of pH values ranging from pH 4 to pH 10, reflecting the limited effect of these media upon the efficiency of the Mg–water reaction. Even faster Mg dissolutions and propulsions were observed in strongly acidic environments (pH<2), while strongly alkaline media (pH>12) resulted in nearly complete hindrance of the Mg-water reaction.[81] Adding EDTA to the natural seawater resulted in a decreased speed, indicating the influence of possible chelation on the rate of hydrogen evolution (eqn 6.5.2).

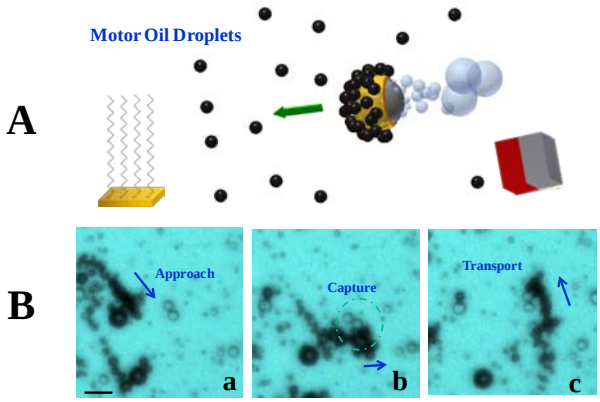

Figure 6.5.5 (A) Schematic hydrophobic seawater driven alkanethiol-modified Mg micromotor for environmental oil remediation. (B) Time lapse images of a Mg Janus micromotor approach (a), capture (b) and transport (c) oil droplets in seawater. Scale bar, 50 µm.

The practical utility of the new Mg-based seawater-driven Janus micromotors has been illustrated in the present study towards the capture and transport of oil droplets from contaminated seawater. The removal of oil spills from contaminated seawater is of considerable importance for minimizing environmental hazards. Most of the common cleaning methods lack the desired efficiency and are neither cost-effective nor environmentally-friendly. Accordingly, the development of effective oil–water separation methods is highly desired. Guix *et al.* reported recently a motion-based oil cleaning strategy involving hydrophobic surface/oil interaction.[87] However, the micromotors used were powered by the hydrogen peroxide fuel which is not compatible with large-scale environmental cleanup. The seawater-driven Mg based Janus micromotor can serve as an attractive platform for environmental remediation of oil contaminants. As demonstrated in the schematic in Figure 6.4.5A, the Mg-based micromotors were modified with self-assembled monolayers (SAMs) of long-chain alkanethiols for imparting the desired strong surface hydrophobicity essential for 'on-the-fly' collection of oil droplets. Figure 6.5.5B demonstrates a SAM-modified Mg Janus micromotor being guided (by the external magnetic field) to approach (a), capture (b) and transport (c) the motor oil droplets in seawater. The modified micromotor moves initially at a speed of 90 µm/s (similar to that of bare

micromotors in seawater), indicating that the SAM layer does not affect the galvanic role of the gold layer. Upon contacting the pair of oil droplets (of 20 μm diameter each), the micromotor instantaneously captures them. As expected, the speed of the motor greatly decreases to around 44 μm/s while carrying the droplets, reflecting the larger drag force. In contrast, control experiments involving unmodified micromotors (*i.e.*, without the alkanethiols) displayed no affinity to such droplets after direct contact.

6.5.4 Conclusions

In conclusion, we have presented a new chemically-powered magnesium-based Janus micromotor that propels autonomously using seawater as the sole fuel source and a hydrogen bubble thrust generated from the Mg-water reaction. The hydrogen-bubble propulsion mechanism has been attributed to the combination of galvanic corrosion and pitting corrosion effects, and the important related roles of the gold coating and the ionic (particularly chloride- rich) environments have been discussed. Accordingly, the Mg-based micromotors are expected to move efficiently in other biological media which contain high chloride concentrations. The new water-driven motion capability should greatly expand the scope of applications and environments of chemically-powered nanomachines. The composition of the motor and the fuel makes these micromotors highly biocompatible and environmentally-friendly. We also demonstrated the first example of a surface-functionalized water-driven micromotor towards practical applications in realistic environments. SAM-modified hydrophobic Mg micromotors were thus applied successfully for oil cleaning in seawater and show considerable potential for environmental remediation. Depending on the specific application, smaller Mg-based motors can be prepared using smaller Mg particles. Additional efforts should be devoted to extending the lifetime of Mg-based motors for addressing the requirements of many practical applications. We expect that the Mg-based Janus micromotor will have a profound impact upon diverse applications in various aqueous environments.

Chapter 6.1, is based, on the material as it appears in Journal of the American Chemical Society, 2012, by Wei Gao, Aysegul Uygun, Joseph Wang. Chapter 6.2, is based on, the material as it appears in Small, 2014, by Sirilak Sattayasamitsathit, Huanhuan Kou, Wei Gao, Walter Thavarajah, Kevin Kaufmann, Liangfang Zhang and Joseph Wang. Chapter 6.3, is based, on the material as it appears in Small, 2013, by Wei Gao, Mattia D'Agostin, Victor Garcia Gradilla, Jahir Orozco, Joseph Wang. Chapter 6.4, is based on, the material as it appears in ACS Nano, 2012, by Wei Gao, Allen Pei, Joseph Wang. Chapter 6.5, is based on, the material as it appears in Nanoscale, 2013, by Wei Gao, Xiaomiao Feng, Allen Pei, Yonge Gu, Jinxing Li, Joseph Wang. The dissertation author was the primary investigator and author of these papers.

6.6 References

1. Wang, J. *Nanomachines: Fundamentals and Applications*, Wiley-VCH, Weinheim, Germany, 2013.

2. Paxton, W. F.; Kistler, K. C.; Olmeda, C. C.; Sen, A.; St. Angelo, S. K.; Cao, Y.; Mallouk, T. E.; Lammert, P. E.; Crespi, V. H. *J. Am. Chem. Soc.* **2004**, *126*, 13424–13431.

3. Fournier-Bidoz, S.; Arsenault, A. C.; Manners, I.; Ozin, G. A. *Chem. Commun.* **2005**, *4*, 441-443.

4. Mallouk, T. E.; Sen, A. *Sci. Amer.* **2009**, *300*, 72-77.

5. Dreyfus, R.; Baudry, J.; Roper, M. L.; Ferminger, M.; Stone, H. A.; Bibette, J. *Nature* **2005**, *437*, 862-865.

6. Zhang, L.; Abbott, J. J.; Dong, L. X.; Kratochvil, B. E.; Bell, D.; Nelson, B. J. *Appl. Phys. Lett.* **2009**, *94*, 64107.

7. Gao, W.; Sattayasamitsathit, S.; Manesh, K. M.; Weihs, D.; Wang, J. *J. Am. Chem. Soc.* **2010,** *132*, 14403-14405.

8. Loget, G.; Kuhn, A. *J. Am. Chem. Soc.* **2010**, *132*, 15918-15919.

9. Calvo-Marzal, P.; Sattayasamitsathit, S.; Balasubramanian, S.; Windmiller, J. R.; Dao, C.; Wang, J. *Chem. Commun.* **2010**, *46*, 1623-1624.

10. Pavlick, R. A.; Sengupta, S.; McFadden, T.; Zhang, H.; Sen, A. *Angew. Chem. Int. Ed.* **2011**, *50*, 9374-9377.

11. Hong, Y. Y.; Diaz, M.; Cordova-Figueroa, U. M.; Sen, A., *Adv. Funct. Mater.* **2009**, *20*, 1568-1576.

12. Zhao, G. J.; Seah, T. H.; Pumera, M. *Chem. Eur. J.* **2011**, *17*, 12020-12026.

13. Wang, J. *ACS Nano* **2009**, *3*, 4-9.

14. Ozin, G. A.; Manners, I.; Fournier, S. B.; Arsenault, A. *Adv. Mater.* **2005**, *17*, 3011-3018.

15. Sanchez, S.; Pumera, M. *Chem.—Asian J.* **2009**, *4*, 1402– 1410.

16. Gibbs, J.; Zhao, Y. -P. *Appl. Phys. Lett.* **2009**, *94*, 163104.

17. Gao, W.; Sattayasamitsathit, S.; Wang, J. *Chem. Rec.* **2012**, *12*, 224.

18. Mei, Y. F.; Solovev, A. A.; Sanchez, S.; Schmidt, O. G. *Chem. Soc. Rev.*, **2011**, *40*, 2109-2119.

19. Mei, Y. F.; Huang, G. S.; Solovev, A. A.; Urena, E. B.; Monch, I., Ding, F.; Reindl, T.; Fu, R. K. Y.; Chu, P. K.; Schmidt, O. G. *Adv. Mater.* **2008**, *20*, 4085–4090.

20. Solovev, A. A.; Mei, Y. F.; Urena, E. B.; Huang, G. S.; Schmidt, O. G. *Small* **2009**, *5*, 1688-1692.

21. Manesh, K. M.; Yuan, R.; Clark, M.; Kagan, D.; Balasubramanian, S.; Wang, J. *ACS Nano*, **2010**, *4*, 1799-1804.

22. Li , J. X.; Huang, G. S.; Ye, M. M.; Li, M. L.; Liu, R.; Mei, Y. F. *Nanoscale* **2011**, *3*, 5083.

23. Solovev, A. A.; Sanchez, S.; Pumera, M.; Mei, Y. F.; Schmidt, O. G. *Adv. Funct. Mater.* **2010**, *20*, 2430-2435.

24. Sanchez, S.; Solovev, A. A.; Harazim, S. M.; Schmidt, O. G. *J. Am. Chem. Soc.* **2011**, *133*,701.

25. Balasubramanian, S.; Kagan, D.; Hu, C. J.; Campuzano, S.; M. Jesus Lobo-Castañon, Lim, N.; Kang, D. Y.; Zimmerman, M.; Zhang, L.; Wang, J. *Angew. Chem. Int. Ed.* **2011**, *50*, 4161-4164.

26. Kagan, D.; Campuzano, S.; Salasubramanian, S.; Kuralay, F.; Flechsig, G. U.; Wang, J. *Nano Lett.* **2011**, *11*, 2083-2087.

27. Orozco, J.; Campuzano, S.; Kagan, D.; Zhou, M.; Gao, W.; Wang, J. *Anal. Chem.*, **2011**, *83*, 7962-7969.

28. Campuzano, S.; Kagan, D.; Orozco, J.; Wang, J. *Analyst* **2011**, *136*, 4621-4630.

29. Gao, W.; Sattayasamitsathit, S.; Orozo, J.; Wang, J. *J. Am. Chem. Soc.* **2011**, *133*, 11862-11864.

30. Liu R.; Sen, A. *J. Am. Chem. Soc.* **2011**, *133*, 20064-20067.

31. Paxton, W. F.; Baker, P. T.; Kline, T. R.; Wang, Y.; Mallouk, T. E.; Sen, A. *J. Am. Chem. Soc.* **2006**, *128*, 14881-14888.

32. Belay, N.; Daniels, L. *Antonie van Leeuwenhoek* **1990**, *57*, 1-7.

33. Yano, M.; Fujitani, S.; Nishio, K.; Akai, Y.; Kurimura, M. *J. Power Source*, **1998**, *74*, 129-134.

34. Funke, H.; Diaz, H.; Liang, X.; Carney, C. S.; Weimer, A. W.; Li, P. *Int. J. Hydrogen Energy* **2008**, *33*, 1127–1134.

35. Sato, Y.; Takahashi, M.; Asakura, H.; Yoshida, T.; Tada, K.; Kobayakawa, K.; Chiba, N.; Yoshida, K. *J. Power Source*, **1992**, *38*, 317-325.

36. Chiplonkar, S.A.; Kawade, R. Nutrition, 2011, DOI:10.1016/j.nut.2011.08.019.

37. Agrawal, Y. K.; Talati, J. D.; Shah, M.D.; Desai, M.N.; Shah, N. K. Corros. Sci., 2004, *46*, 633-651.

38. Kurz, J. L.; Farrar, J. M. *J. Am. Chem. Soc.* **1969**, *91*, 6057–6062.

39. Wang, J. *Analytical Electrochemistry*, 3rd ed.; John Wiley & Sons, Inc: Hoboken, NJ, **2006**.

40. Wu, J.; Balasubramanian, S.; Kagan, D.; Manesh, K. M.; Campuzano, S.; Wang, J. *Nat. Commun*. **2010**, *1*, DOI: 10.1038/ ncomms1035.

41. Perrin, D. D. Ionisation Constants of Inorganic Acids and Bases in Aqueous Solution, 2nd ed.; Pergamon: Oxford, UK, **1982**.

42. Burdick, J.; Laocharoensuk, R.; Wheat, P. M.; Posner, J. D.; Wang, J. *J. Am. Chem. Soc.* **2008**, *130*, 8164-8165.

43. Sundararajan, S.; Lammert, P. E.; Zudans, A. W.; Crespi, V. H.; Sen, A. *Nano Lett.* **2008**, *8*, 1271-1276.

44. Kagan, D.; Laocharoensuk, R.; Zimmerman, M.; Clawson, C.; Balasubramanian, S.; Kang, D.; Bishop, D.; Sattayasamitsathit, S.; Zhang, L.; Wang, J. *Small* **2010**, *6*, 2741-2747.

45. Orozco, J.; Cortes, A.; Cheng, G.; Sattayasamitsathit, S.; Gao, W.; Feng, X.; Shen, Y.; Wang, J. *J. Am. Chem. Soc.* **2013**, *135*, 5336–5339.

46. Campuzano, S.; Orozco, J.; Kagan, D.; Guix, M.; Gao, W.; Sattayasamitsathit, S.; Claussen, J. C.; Merkoçi, A.; Wang, J. *Nano Lett.* **2012**, *12*, 396.

47. Li, F.; He, J.; Zhou, W. L.; Wiley, J. B. *J. Am. Chem. Soc*. **2003**, *125*, 16166.

48. Li, F.; Badel, X.; Linnros, J.; Wiley, J. B. *J. Am. Chem. Soc*. **2005**, *127*, 3268.

49. Hales, T. C. A proof of the Kepler conjecture. *Ann. Math.* **162**, 1065–1185 (2005).

50. Roberge, P. R. *Handbook of Corrosion Engineering*, McGraw-Hill Professional, New York, 2000.

51. Wang, J.; Gao, W. *ACS Nano* **2012**, *6*, 5745-5751.

52. Liu, R.; Sen, A. *J. Am. Chem. Soc.* **2011**, *133*, 20064.

53. Gao, W.; Uygun, A.; Wang, J. *J. Am. Chem. Soc.* **2012**, *134*, 897.

54. Gao, W.; Manesh, K. M.; Hua, J.; Sattayasamitsathit, S.; Wang, J. *Small* **2011**, *7*, 2047.

55. Birnbaum, H. K.; Buckley, C.; Zeides, F.; Sirois, E.; Rozenak, P.; Spooner, S.; Lin, J. S. *J. Alloys Comp.* **1997**, *253-254*, 260.

56. Dunderdale, G.; Ebbens, S.; Fairclough, P.; Howse, J. *Langmuir* **2012**, *28*, 10997.

57. Balasubramanian, S.; Kagan, D.; Manesh, K. M.; Calvo-Marzal, P.; Flechsig, G. U.; Wang, J. *Small* **2009**, *5*, 1569.

58. Sanchez, S.; Ananth, A. N.; Fomin, V. M.; Viehrig, M.; Schmidt, O. G. *J. Am. Chem. Soc.* **2011**, *133*, 14860.

59. McCafferty, E. *Corro. Sci.* **2003**, *45*, 1421.

60. Pyun, S. I.; Moon, S. M. *J. Solid State Electrochem.* **1999**, *3*, 331.

61. Gao, W.; D'Agostino, M.; Garcia-Gradilla, V.; Orozco, J.; Wang, J. *Small* **2013**, *9*, 467.

62. Soler, L.; Macanás, J.; Muñoz, M.; Casado, J. *J. Power Sources* **2007**, *169*, 144–149.

63. Wang, H. Z.; Leung, D. Y. C.; Leung, M. K. H.; Ni, M. *Renew. Sustain. Energy Rev.* **2009**, *13*, 845–853.

64. Roach, P. J.; Woodward, W.; Castleman Jr., A. W.; Reber, A. C.; Khanna, S. N. *Science* **2009**, *323*, 492–495.

65. Szklarska-Smialowska, Z. *Corro. Sci.* **1999**, *41*, 1743–1767.

66. Flamini, D. O.; Saidman, S. B.; Bessone, J. B. *Corro. Sci.* **2006**, *48*, 1413–1425.

67. Kravchenko, O.V.; Semenenko, K. N.; Bulychev, B.M.; Kalmykov, K. B. *J. Alloys Comp.* **2005**, *397*, 58–62.

68. Ziebarth, J. T.; Woodall, J. M.; Kramer, R. A.; Choi, G. *Int. J. Hydrogen Energy* **2011**, *36*, 5271–5279.

69. Howse, J. R.; Jones, R. A.; Ryan, A. J.; Gough, T.; Vafabakhsh, R.; Golestanian, R. *Phys. Rev. Lett.* **2007**, *99*, 048102.

70. Baraban, L.; Makarov, D.; Streubel, R.; Monch, I.; Grimm, D.; Sanchez, S.; Schmidt, O. G. *ACS Nano* **2012**, *6*, 3383– 3389.

71. Baker, H. *ASM_Handbook, Alloy Phase Diagrams*. Materials Park, OH: ASM International, *3*, 1992.

72. Kolics, A.; Besing, A. S.; Baradlai, P.; Haasch, R.; Wieckowski, A. *J. Electrochem. Soc.* **2001**, *148*, B251–B259.

73. Birnbaum, H. K.; Buckley, C.; Zeides, F.; Sirois, E.; Rozenak, P.; Spooner, S.; Lin, J. S. *J. Alloys Comp.* **1997**, *253-254*, 260–264.

74. Czech, E.; Troczynski, T. Hydrogen Generation through Massive Corrosion of Deformed Aluminum in Water. *Int. J. Hydrogen Energy* **2010**, *35*, 1029–1037.

75. McCafferty, E. Sequence of Steps in the Pitting of Aluminum by Chloride Ions. *Corro. Sci.* **2003**, *45*, 1421–1438.

76. Pyun, S. I.; Moon, S. M. *J. Solid State Electrochem.* **1999**, *3*, 331–336.

77. Loget, G.; Kuhn, A. *Nat. Commun.* **2011**, 2, 10.1038/ncomms1550.

78. Gao, W.; Pei, A.; Wang, J. *ACS Nano* **2012**, *6*, 8432.

79. Lee, G.; Park, J. *Geochim. Cosmochim. Acta* **2013**, *102*, 162.

80. Makar, G. L.; Kruger, J. *Int. Mater. Rev.* **1993**, *38*, 138.

81. Song, G.; Atrens, A. *Adv. Eng. Mater.* **2003**, *5*, 837.

82. Roberge, P. R. *Handbook of Corrosion Engineering*, McGraw-Hill Professional, New York, 2000.

83. Song, G.; Atrens, A.; St John, D.; Wu, X.; Nairn, J. *Corr. Sci.* **1997**, *39*, 1981.

84. Frankel, G. S. *J. Electrochem. Soc.* **1998**, *145*, 2186.

85. Tunold, R.; Holtan, H.; Berge, M. B. H.; Lasson, A.; Steen-Hansen, R. *Corr. Sci.* **1977**, *17*, 353.

86. Xin, Y.; Huo, K.; Tao, H.; Tang, G.; Chu, P. K. *Acta Biomater.* **2008**, *4*, 2008.

87. Guix, M.; Orozco, J.; García, M.; Gao, W.; Sattayasamitsathit, S.; Merkoçi, A. A.; Escarpa, A.; Wang, J. *ACS Nano* **2012**, *6*, 4445.

Chapter 7 Bioinspired Magnetic Nanoswimmers and Their Applications

7.1 Magnetically-powered flexible metal nanowire motors

7.1.1 Introduction

As we discussed in Chapter 1, micro/nano-scale propulsion in fluids is challenging due to low Reynolds number fluids. The difficulties are summarized by Purcell's famous "scallop theorem",[1] which states that a reciprocal motion cannot lead to any net propulsion at low Reynolds numbers. Natural microorganisms inhabit a world where Re ~ 10^{-5} (flagellated bacteria) to 10^{-2} (spermatozoa),[2,3] and they achieve their propulsion by propagating traveling waves along their flagella (or rotating them) to break the time-reversibility requirement, and hence escape the constraints of the scallop theorem.[2,4] Such nanoscale propulsion requires breaking of the system symmetry by deforming the motor shape.[4] For example, *E. Coli* bacterial uses rotating helical flagella to propel in viscous media.[5] Because of the potential of nano-sized machines in future biomedical applications, such as targeted drug delivery and microsurgery, interdisciplinary efforts by scientists and engineers have recently resulted in major advances in the design and fabrication of artificial micro/nano-scale locomotive systems.[6-12]

Broadly speaking, these micro/nano-swimmers can be classified into two categories, namely chemically-powered nanomotors[6–8] and externally-powered swimmers.[9,10] Chemically-powered nanomotors generally deliver higher propulsion speeds, but due to the requirements for chemical fuels and reactions, their applications in real biological environments face a number of challenges. In the previous sections, we demonstrated such catalytic micro/nanomotors can be

potentially used for diverse biomedical and environmental applications.[11,12] However, numerous potential applications of future nanomachines - particularly biomedical ones - would require elimination of the fuel requirements. Externally-powered swimmers are often actuated by external magnetic fields. Magnetically-controlled motion, inspired by the motility of prokaryotic and eukaryotic microorganisms,[4,5] represents one attractive route for addressing the challenge of nanoscale propulsion and accomplishing a fuel-free locomotion. Magnetic force has been widely used to provide the mechanical deformation essential for breaking the symmetry. Note that these externally-powered locomotive systems are often referred to as micro- or nano-swimmers in the literature, but strictly speaking, they do not represent true self-propulsion because of the presence of non-zero external torques.

According to their propulsion mechanisms, magnetically powered swimmers can be further categorized into three groups.[13-19] The first group includes helical swimmers,[13,14] as inspired by helical bacterial flagella,[5] which propel upon rotation imposed by external magnetic fields. Nelson[18] and Fischer[19] reported recently the fabrication and magnetically-controlled motion of efficient artificial flagella consisting of helical tails. These cork-screw swimmers offer attractive propulsion but require specialized ‘top down’ self-scroll or shadow-growth preparation routes along with advanced microfabrication facilities. The second group of swimmers relies on a surface to break the spatial symmetry and provide one additional degree of freedom to escape the constraints from the scallop theorem, and hence are termed surface walkers.[15–18] Finally, the third type of swimmers, referred to as flexible swimmers, exploits the deformation of flexible filaments for propulsion.[19,20] The new nanomotor presented in this section falls into this category.

In this section, we demonstrate a simple new approach for addressing the fuel requirement and for creating magnetically-driven propulsion based on easily prepared flexible metal nanowire swimmers. The new 3-segment nanowire motors (~6 μm long, 200 nm in diameter) are readily prepared using a template electrodeposition approach. Such preparation

involves the sequential deposition of the Au, Ag, and Ni segments into the alumina membrane micropores. Subsequent dissolution of the template and release of the nanowires is followed by partial dissolution of the central silver segment in hydrogen peroxide to create the flexible thinner joint (linking the Au 'head' and Ni 'tail') essential for the controlled mechanical deformation. The flexibility of thin Ag nanowires has been discussed earlier.[21,22] Flexible nanorods based on a polyelectrolyte bridge were also described by Ozin's team but not in connection to directed motion.[23] The new template electrochemical synthesis of flexible metal nanowires greatly simplifies the preparation of magnetic swimmers compared to the fabrication of cork-screw or helical magnetic swimmers,[13,14] and offer reproducible preparation that reflects the precise charge control. The resulting fuel-free flexible nanowire swimmers offer great promise for diverse biomedical applications as indicated below from their efficient propulsion in urine medium.

7.1.2 Experimental methods

Synthesis of the flexible gold/silver/nickel magnetic nanowires

The gold/silver/nickel magnetic nanowires were prepared using common template-directed electrodeposition protocols. A silver film was first sputtered on one side of the porous alumina membrane template containing 200 nm diameter cylindrical pores and 25 mm diameter (Catalog No 6809-6022; Whatman, Maidstone, U. K.) to serve as a working electrode. The membrane was then assembled in a plating cell with an aluminum foil serving as a contact for the sputtered silver. Copper was electrodeposited in the branch area from a 1 M $CuSO_4 \cdot 5H_2O$ solution, using a charge of 8 C and a potential of -0.9 V (vs. Ag/AgCl reference), along with a Pt-wire counter electrode; subsequently, gold was plated from the commercial gold-plating solution (Orotemp 24 RTU RACK; Technic Inc.) at -1.0 V (vs. Ag/AgCl), using a charge of 4 C or 3C (for 'forward' or 'backward' motions, respectively), silver was plated at -0.9 V (vs. Ag/AgCl) for a total charge of 3 C (for forward) or 3.5 C (for backward) using a commercial silver plating solution (1025 RTU @ 4.5 Troy/gallon; Technic Inc., Anaheim, CA); finally, Ni was plated from

a nickel plating solution containing 20 g L^{-1} $NiCl_2 \cdot 6H_2O$, 515 g L^{-1} $Ni(H_2NSO_3)_2 \cdot 4H_2O$, and 20 g L^{-1} H_3BO_3 at -1.0 V (vs. Ag/AgCl) for 2 C (for 'forward') or 3 C (for 'backward'). The sputtered silver layer was mechanically removed from the membrane by polishing with 3-4 μm alumina particles; and the copper sacrificial layer was dissolved using 20% HCl and 0.5 M $CuCl_2$. The membrane was then dissolved in a 3 M NaOH solution for 30 min to completely release the nanowires. The nanowires were collected by centrifugation at 6000 rpm for 5 min and were washed repeatedly with nanopure water (18.2 MΩ·cm) until a neutral pH was achieved. All nanowire solutions were stored in nanopure water at room temperature. The flexible thinner joint of central silver segment is prepared by its partial dissolution accomplished by mixing 10 μl of diluted Au-Ag-Ni nanowire solution with 10 μl of a 16% hydrogen peroxide solution for 1 min. The nanowires were then washed under optical microscope using nanopure water (18.2 MΩ·cm) until a neutral pH was achieved. The preparation yield of backward moving wires is higher compared to the forward moving ones. Most work thus employed backward moving motors. The nanowire sample for imaging of the partially dissolved Ag segment was dissolved on the glass slide for 1 min, then washed with nanopure water on the glass slide, then dried.

Magnetic driven movement

Movement studies were performed by using alternating magnetic field with 5 Gauss Magnetic Induction) was provided by a rotating magnet (Cole-Parmer magnetic stirrer EW-84000-00) and a static magnet. The static magnet stabilizes the nanowire swimmer by eliminating the whole body rotation (in the perpendicular direction). The locomotion of nanoswimmers in high salt and urine samples (collected from a healthy volunteer) were carried out by mixing directly with the nanomotor solution (1:1 mixing).

7.1.3 Results and discussions

The rapid and yet incomplete dissolution of the central Ag segment and formation of a flexible joint can be observed within 10-15 s in the peroxide solution. A SEM image of the

resulting flexible Ag section (Figure 7.1.1) indicates a rough porous segment of a slightly smaller diameter compared to its non-porous metal neighbors. The dissolution of silver in hydrogen peroxide:

$$2Ag\ (s) + H_2O_2 \rightarrow 2Ag^+\ (aq) + 2OH^-$$

leads to hydroxyl products that chemisorb on the Ag surface and results in AgOH and Ag_2O surface products.[24-26] Such formation of surface byproducts in the presence of hydrogen peroxide has been shown to hinder further silver dissolution.[24-26]

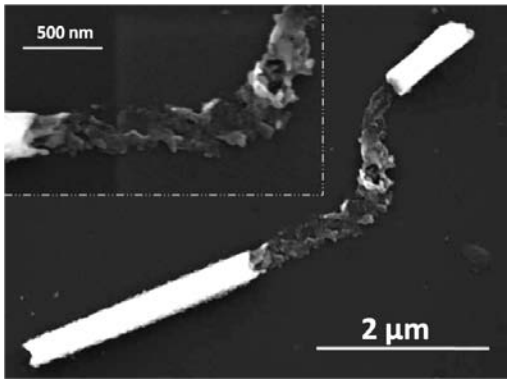

Figure 7.1.1 The SEM image of a partially dissolved flexible silver segment.

To illustrate the critical role of the nanowire flexibility in achieving the magnetic propulsion we compared the motion of Au/Ag/Ni nanowires before and after the partial silver dissolution. Figure 7.1.2A displays the motion trajectories of conventional Au/Ag/Ni nanowires (a) and flexible $Au/Ag_{flex}/Ni$ (b) over a 15 s period under the rotating magnetic field. The flexible nanowire exhibits defined locomotion over a dramatically long path, parallel to the magnetic field axis (b), with a cone-shaped rotation of the Ni 'tail'. The speed of this nanomotor is ~3 µm s^{-1}, i.e., approximately 0.5 body-length s^{-1}. In contrast, no directed motion is observed for the control experiment involving the rigid Au/Ag/Ni nanowires over the same time period (a).

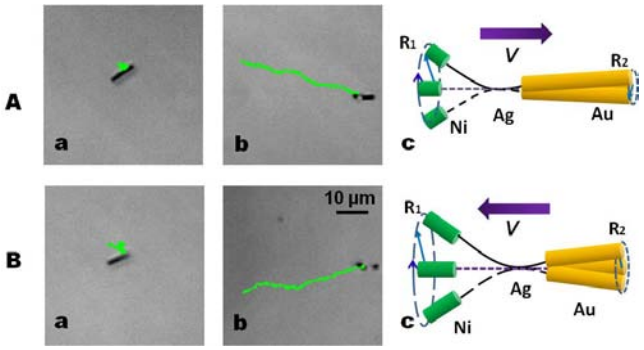

Figure 7.1.2 Comparison of the 'forward' (A) and 'backward' (B) movement of rigid Au/Ag/Ni (a) and flexible Au/Ag_{flex}/Ni (b) nanowires under a rotating magnetic field (5 Gauss, f=15(A); 10 (B) Hz) over a 15 s period. The lengths of the Au, Ag and Ni segments are: A) 3, 3 and 0.5 µm; B) 2, 3.5 and 1 µm, respectively.

To actuate the locomotion in a nonreciprocal fashion at low Reynolds number, artificial swimming devices deform their shape. The observed locomotion of the nanowire swimmer is attributed to the transfer of the magnetic energy into cyclic mechanical deformations. The flexible Ag bridge is essential for generating such cyclic mechanical deformations under an external rotating magnetic field. The rotation of the Ni 'tail' resembles the rotation mechanism of microorganisms. Similar to natural microorganisms, our artificial nanowire swimmers consist of a body and a propulsive appendage, deforming in a continuous fashion. The rotating magnetic field creates a cone shaped rotation of the Ni segment which causes rotation of the Au segment on the opposite end. Such rotation of Au and Ni segments with different amplitudes and phase difference, due to bending of the Ag joint, breaks the system symmetry to induce the movement (Figure 7.1.2c). Propulsion is achieved when the flexibility of the connecting thin Ag wire allows for bending, so that the shorter Ni segment - which has larger amplitude - is tilted backwards relative to the cone surface. Thus, when rotated, this section produces a force away from centroid of the swimmer. The flexibility of the central Ag bridge facilitates generation of rotation of the Ni segment around the nanowire axis under the rotating magnetic field. The magnetic field generates torques which leads to the rotation of the entire nanowire along its axis, resulting in breaking of the symmetry which induces the movement.

Tailoring the length of the Au ‘head’ and Ni ‘tail’ changes the asymmetry geometry and allows reversal of the motion direction. Different rotation amplitudes can thus be generated on both sides (Figure 7.1.2(c)), leading to the forward (‘pusher’) or backward (‘puller’) locomotion.[4] For example, flexible nanowires - with longer Au segment (3 μm) and a shorter Ni one (0.5 μm) - will move ‘forward’ in the rotating magnetic field (Figure 7.1.2A(b)). Under this condition, the rotation amplitude of the Ni segment (R_1) is much larger than the rotational amplitude of the Au segment (R_2), i.e. $R_1 >> R_2$ (Figure 7.1.3A(c)), resembling a ‘pusher’.[4] Here, the rotation of the Ni segment induces a flow field directed away from the nanowire along its swimming direction. The shorter the tail, the larger conical angle of the nickel segment (compared to the gold one), and hence the larger the average force in the direction of the head (as the force and speed are directly proportional to the projection of the area in the direction of motion). Another factor that affects the motion is the fluid flow, which is moving at higher speed relative to the swimmer on the lagging section. On the other hand, a ‘backward’ movement (with the Ni tail upfront) is observed with a shorter Au segment (2 μm) and a longer Ni one (1 μm). Such directed ‘backward’ (pulling) movement at a speed of 4 μm s^{-1} is illustrated in Figure 7.1.2B(b). Analogous experiments without dissolving the Ag segment display no directed movement (Figure 7.1.2B(a)). Additional data indicate that the ‘backward’ (‘puller’) motion is more efficient and offers higher reproducibility along with improved motion control compared to the ‘forward’ one. This is in agreement with an early report comparing ‘pullers’ and ‘pushers’.[27] It is also not surprising, as a pulling motion of slender bodies in a resistant medium is more stable than a pushing one (analogous to pushing a string on a frictional surface, as opposed to pulling it). Accordingly, such ‘backward’ motion was used in most subsequent work. Certain lengths of the ‘Tail’ and ‘Head’ (around 0.7 and 2.5 μm, respectively) represent the cross-over values where both ‘forward’ and ‘backward’ motions can be observed randomly.

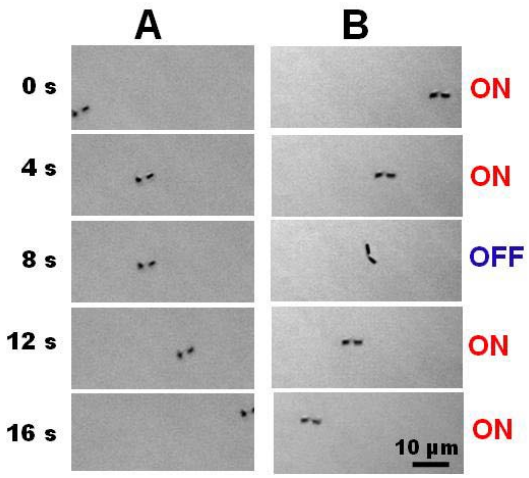

Figure 7.1.3 Time-lapse images illustrating the On/Off 'forward' (A) and 'backward' (B) motions of Au/Ag_{flex}/Ni nanomotors under the rotating magnetic field. Conditions, as in Figure 7.1.2.

Modulating the magnetic field allows precise On/Off motion control of the flexible nanowire motors. The magnetic nanowire motor stops and resumes its motion reversibly upon turning the magnetic field Off and On, respectively. For example, Figure 7.1.3 demonstrates an On/Off/On cycle in connection to a modulated magnetic field, along with 'forward' (A) and 'backward' (B) movements. These data clearly illustrate that the directional movement of these nanomotors is stopped in the absence of the magnetic field and renewed upon switching the field 'On'. Such precise motion control, along with other capabilities (described below), holds great promise for designing functional devices that perform multiple tasks. The flexible silver joint is highly rigid and does not break apart even under continuous prolonged operation in a rotating magnetic field with higher frequency and induction.

Common catalytic nanowire motors operate only in low ionic-strength aqueous solutions,[28] and hence cannot be applied in realistic biological environments. The magnetic nanowire swimmer addresses this ionic-strength limitation and can expand the scope of artificial nanomotors to salt-rich environments. We examined the movement of the flexible nanowire in the absence of salt and in 30 µM and 30 mM KCl solutions. These experimental data indicate that the

high ionic-strength medium has a minimal effect upon the movement of the magnetic swimmers, with no obvious speed change in the different salt environments. The favorable locomotion in salt-rich environments has important implications upon future applications of artificial nanomotors. For example, Figure 7.1.4 displays time-lapse images of the movement of magnetic nanowire swimmer in undiluted urine sample. As indicated from the images, the motor displays an efficient locomotion over a defined path in this biological medium.

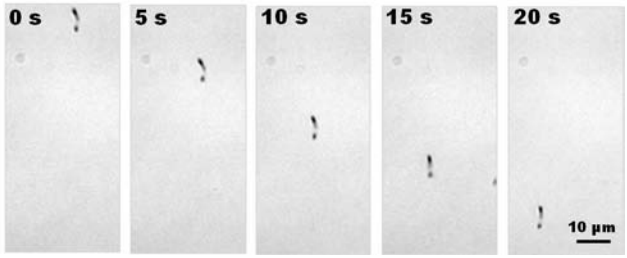

Figure 7.1.4 Time-lapse images of the 'backward' motion of Au/Ag_{flex}/Ni nanomotors in a urine sample under the rotating magnetic field. Conditions, as in Figure 7.1.2B.

7.1.4 Conclusion

In conclusion, we have demonstrated for the first time the propulsion of readily prepared flexible magnetic nanowire swimmers under an external magnetic field. Such magnetically-driven nanowire locomotion obviates the fuel requirement of catalytic nanowire motors and resembles microorganisms that use rotation mechanism for their motion. The simple design obviates also the requirement for helical (cork-screw) microstructures of recently described magnetic swimmers.[13,14] Critical to the realization of such magnetic propulsion of nanowires is the flexibility of the Ag joint created by partial dissolution in hydrogen peroxide. The new magnetic nanomotors are mass produced using the template electrodeposition strategy and could be functionalized (by modification of their Au segment) towards the creation of nanomachines performing practical tasks and diverse applications. In particular, the fuel-free operation could facilitate different biomedical applications such as targeted drug delivery.

7.2 High-speed propulsion of flexible nanoswimmers: theory and experiments

7.2.1 Introduction

In chapter 7.1, I proposed a flexible metallic nanowire motor (with three segments of Au, Ag and Ni) readily prepared using a template electrodeposition approach, and able to swim at speeds of up to 6 μm s^{-1} for a size of 6.5 μm. In contrast to the propeller proposed by Dreyfus *et al.*,[19] the actuation in the device of our flexible nanoswimmer[20] acted only on the magnetic Ni portion of the filament (the head), while the rest of nanomotor was passive. To perform different task, the high cargo towing abilities and high speed of the flexible nanowire swimmers is desired. Thus understanding the fundamental microfluidic dynamics to further improve the performances of such magnetic nanoswimmers are of great interest.

In the following section, I will present both a new design and a theoretical modelling approach for a flexible nanowire motor which offers an improved propulsion performance (up to $U \approx 21$ μm s^{-1} at an actuation frequency (f) of 35 Hz), approaching thus the speed of natural microscopic swimmers, such as *Escherichia coli* ($U \approx 30$ μm s^{-1} at $f = 100$ Hz)[5] while using a lower frequency. The effect of size and frequency can be scaled off by nondimensionalizing the propulsion speed by the intrinsic velocity scale (the product of body length and frequency, Lf) to obtain a dimensionless propulsion speed, U/Lf, which can be interpreted as the number of body lengths travelled per revolution of actuation (or also referred to as the stride length in terms of body length in the biomechanics literature). The nanomotor put forward in this section displays remarkable dimensionless propulsion speeds compared with natural microorganisms and other artificial locomotive systems.[13-20]

After presenting the experimental method and its performance, I study the propulsion characteristics of this new high-speed flexible nanomotor theoretically *via* an analytical model.

The critical role of flexibility in this mode of propulsion is established first using simple physical arguments, followed by an asymptotic analysis which predicts the filament shape and propulsion speed in different physical regimes. The theoretical predictions are compared with experimental measurements and we obtain good agreement. The improved propulsion performance of the new fuel-free nanowire motor makes it attractive for future biomedical applications, which we further illustrate by demonstrating the performance of the propulsion mechanism in an untreated human serum sample.

7.2.2 Experimental section

Synthesis of the flexible Ni-Ag nanowires

The nanowire motors were prepared using the same electrodeposition protocol as 7.1.2. Copper was electrodeposited in the branch area of the membrane from a 1M $CuSO_4 \cdot 5H_2O$ solution, using a charge of 8C and a potential of -0.9V (vs. Ag/AgCl reference electrode, along with a Pt-wire counter electrode); subsequently, gold was plated next from the commercial gold plating solution (Orotemp 24 RTU RACK; Technic Inc.) at -0.9V (vs. Ag/AgCl), using a charge of 0.5C, which was used for protecting the Ni while dissolving the membrane later; nickel was deposited from a nickel plating solution containing $20gL^{-1}$ $NiCl_2 \cdot 6H_2O$, $515gL^{-1}$ $Ni(H_2NSO_3)_2 \cdot 4H_2O$, and $20gL^{-1}$ H_3BO_3 at -1.0V (vs. Ag/AgCl) for 6C, finally, silver was plated subsequently at -0.9V (vs. Ag/AgCl) for a total charge of 4.5C using a commercial silver plating solution (1025 RTU @ 4.5 Troy/gallon; Technic Inc., Anaheim, CA). All nanowires were stored in nanopure water at room temperature. Flexibility of the silver segment was achieved by its partial dissolution accomplished by mixing 10 µl of the diluted Ni/Ag nanowire solution with 10 µl of the 10% hydrogen peroxide solution for 1 minute. The nanowires were then washed on the glass slide using nanopure water (18.2 MΩ·cm) until a neutral pH was achieved.

Magnetic driven movement

The magnetic field was achieved by a triaxial Helmholtz coil, consisting of one homogeneous rotating magnetic field a constant magnetic field which is perpendicular to the axis of the rotating one. The magnetic induction was measured using a Gaussmeter (Model 475 DSP Gaussmeter, Lake Shore Cryotronics, Inc, Westerville, OH). The locomotion of nanoswimmer in human serum samples were carried out by mixing directly with the nanomotor solution (1:1 ratio).

7.2.3 Design and efficient propulsion of the nanoswimmers

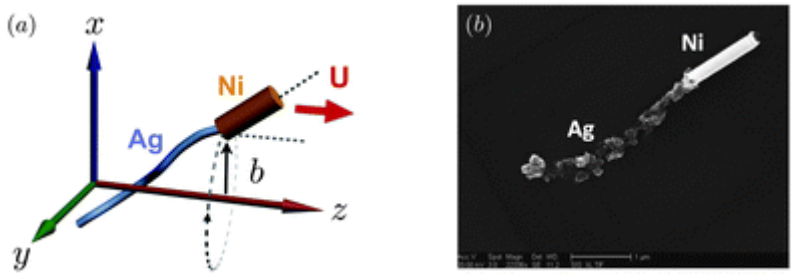

Figure 7.2.1 (a) Schematic representation of a Ni–Ag nanowire motor, and notation for the model. (b) SEM image showing the topography of Ni–Ag nanowire which was partially dissolved in 5% H_2O_2 for 1 min.

In contrast to the previous three-segment (Ni–Ag–Au) design by shown in chapter 7.1, the new design relies primarily on a 1.5 μm-long Ni head and a 4 μm-long flexible Ag tail (see a SEM image in Figure 7.2.1b). A 0.3 μm-long Au segment was also included (adjacent to the Ni segment) to protect the Ni segment from acid etching during the dissolution of the Cu sacrificial layer, and to allow functionalizing the motor with different types of biomolecules and cargos. Both the Ni and Au segments have a diameter of 200 nm. While the Ni segment has a length of 1.5 μm useful to generate sufficient magnetic torques, only a very short segment of Au (0.3 μm) was used to minimize the overall fluid drag of the nanomotor. Flexibility of the silver segment (Figure 7.2.1b) was achieved by its partial dissolution in hydrogen peroxide solution.[20] The dissolution step leads also to hydroxyl products that chemisorb on the Ag surface and result in AgOH and Ag_2O surface products. The dissolved Ag filament had a reduced diameter of approximately 100 nm. For the hydrodynamic model considered in this work, the

rigid short Au segment is hydrodynamically indistinguishable from the rigid Ni segment, and hence the Ni and Au segments are considered in the model as a single rigid 1.8 μm-long segment (1.5 μm Ni + 0.3 μm Au), *i.e.* the nanomotor has a total length of 5.8 μm.

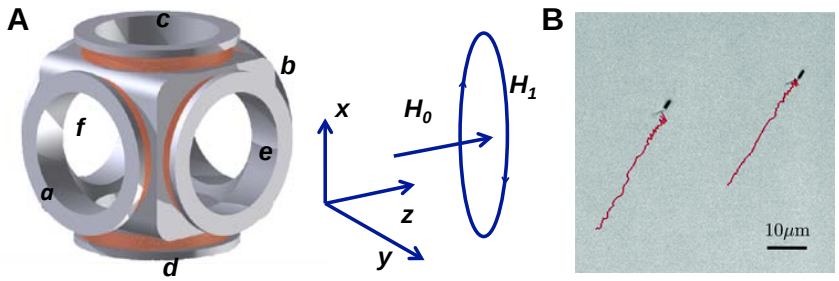

Figure 7.2.2 A) The magnetic field setup in the experiments. H_0 is a longitudinal constant component of the magnetic field generated by a Helmholtz pair: coils *a* & *b*, carrying an constant electrical current *I*; H_1 is a transverse rotating magnetic field generated by two Helmholtz pairs: coils *c* & *d and* coils *e* & *f*, carrying the sinusoidal currents I_1 and I_2, respectively. I_1 and I_2 have a 90 degree phase shift). B) Two identical nanomotors swimming under the same magnetic field at a frequency f = 20 Hz. The red lines display the superimposed location of the nanomotors over a 2-second interval.

The flexible nanomotors were driven by a magnetic field with an unsteady component of amplitude H_1, rotating sinusoidally in a plane perpendicular to a constant component, H_0. See Figure 7.2.2A for magnetic field setup in the experiments The magnetic field precessed about the direction of the constant magnetic field at an angular frequency $\Omega = 2\pi f$. The nanomotor was observed to propel unidirectionally (straight trajectories) in the direction of the constant magnetic field. In Figure 7.2.2 we show two nearby identical nanomotors under the actuation of the external magnetic field at $f =$ 20 Hz. These two nanowires propel at essentially the same swimming speed along the same direction (the red lines are their trajectories in a period of 2 s), illustrating the stability of this mode of propulsion. For helical swimmers,[13,14] swimming is due to the rotation of rigid chiral objects and hence the swimming kinematics scales linearly with the applied field: a reversal of the direction of rotation of the magnetic field leads to propulsion in the opposite direction for these rigid chiral objects. In contrast, the flexible nanowire motors here exhibit uni-directional swimming, independent of the rotational direction of the external magnetic field. This is due to the nonlinear swimming kinematics arising from the flexibility of

the nanowire. This simple test illustrates the fundamental difference between the propulsion of rigid chiral objects and flexible swimmers. In our case, the direction of swimming can be controlled by altering the orientation of the axial constant component of the magnetic field, H_0.

We further show in Figure 7.2.5(a) the trajectories of the same nanomotor at different frequencies (see captions for details) over a 3 second period. Upon the settings H_1 = 10 G, H_0 = 9.5 G, and f = 15 Hz, we are able to achieve a propulsion speed of $U = 14.3 \pm 2.46$ μm s^{-1}. The speed of 20 different nanomotors were measured, with all other experimental conditions kept fixed; the values of the swimming speeds, U, reported in this paper are averaged quantities over these different nanomotors. One meaningful method of comparing the propulsion speed between various swimmer designs consists in scaling the speed with the only intrinsic characteristic velocity scale of the swimmer Lf, where L is a characteristic body length, and f is a characteristic frequency. This allows to quantify the distance travelled by the swimmer in terms of body lengths per revolution of rotation. *Escherichia coli* bacteria[5] typically propel with $U/Lf \approx 0.03$ body lengths per revolution, while the flexible nanomotor reported here was able to travel 0.164 body lengths per revolution at f = 15 Hz. The maximum dimensional speed achieved was $U = 20.8 \pm 3.07$ μm s^{-1} with f = 35 Hz, corresponding in that case to≈0.1 body lengths per revolution. We then experimentally measured the speed-frequency characteristics of these flexible nanowire motors (results shown as symbols in Figure 7.2.5(b)). In the next section we present a simple physical model for the locomotion of flexible nanomotors, and compare our theoretical predictions with these experimental measurements.

7.2.4 A minimal model for flexible nanomotors

7.2.4.1 Chiral propulsion

In this section, we illustrate the working principles of the flexible nanowire motors. First, we establish that it is essential for the nanowire to deform in a chiral fashion in order to achieve propulsion.

For low Reynolds number incompressible flows, the governing equations are the Stokes equation $\nabla p = \mu \nabla^2 \mathbf{u}$, and the continuity equation $\nabla \cdot \mathbf{u} = 0$, where μ is the shear viscosity, and p and $\mathbf{u}$ are the fluid pressure and the velocity field respectively. Two properties of the Stokes equation can be used to deduce the necessity of the nanowire being chiral in order to achieve net swimming, as shown by Childress.[3] First, it can be shown that the mirror image of a Stokes flow is also a Stokes flow. Therefore, suppose a nanowire swims with a velocity **U** along its rotation axis, then its mirror image will also swim at the same velocity **U** (see Figure 7.2.3). Second, since time does not appear in Stokes equation, it only enters the problem as a parameter through the boundary conditions. This leads to the time reversibility of the Stokes equation, meaning that the velocity field $\mathbf{u}$ reverses its sign upon a $t \rightarrow -t$ time reversal. In the context of our nanowire motors, suppose the nanowire propels at a velocity **U**, then when time is reversed, the nanowire will propel at a velocity $-\mathbf{U}$ (Figure 7.2.3). If the deformation of the nanowire is not chiral, the mirror image of the nanowire can be superimposed with the original nanowire, and the only thing reversed in the mirror image is the rotational kinematics (*i.e.* if the original nanowire rotates clock-wisely, its mirror image will have exactly the same shape but rotates counter-wisely; note that the translational velocity is unchanged in the mirror image). In this case, one can also notice that the kinematics in the mirror image is the same as a time reversal of the original kinematics, except that the translational velocity is also reversed for the case of time-reversal ($-\mathbf{U}$, due to the time-reversibility of Stokes flows). In other words, we have now two nanowires (a mirror-imaged nanowire and a time-reversed nanowire) having exactly the same deformation kinematics but with opposite translational velocity ($-\mathbf{U} = \mathbf{U}$), and therefore we conclude that this can happen only if the translational velocity is identically zero ($\mathbf{U} = \mathbf{0}$). Therefore non-chiral deformation cannot lead to net propulsion. This simple physical argument shows that a combination of rotational actuation and nanowire flexibility is critical for this mode of propulsion. Recently, the dynamics of tethered elastic filaments actuated by precessing

magnetic fields has been studied[29–36] and chiral deformation along the filament has been found to produce propulsive force and fluid pumping. The swimming behaviours of an untethered flexible magnetic filament displaying chiral deformation was also addressed computationally.[37]

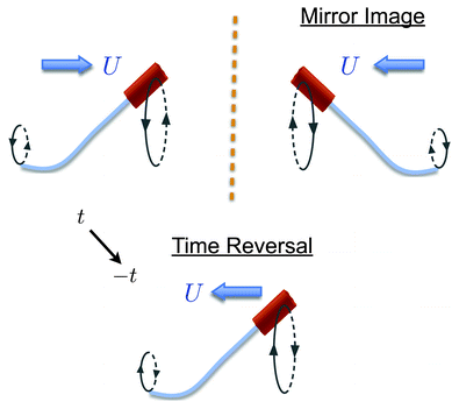

Figure 7.2.3 Physical explanation of the necessity of chiral deformation in achieving propulsion. If the deformation is not chiral, the kinematics of the mirror image of the nanowire is identical to the time-reversed kinematics, leading to **U** = **0**.

7.2.4.2 Model setup

Next we show that a simple model taking into account the elasticity of the nanowire and its hydrodynamic interaction with the fluid medium captures the essential physics and provides quantitative agreement with experimental measurements. We first solve for the detailed shape of the silver filament, we then predict the propulsion speed, and finally we compare our results with the experimental measurements. Theoretical modelling of this type belongs to the general class of elastohydrodynamical problems, which has recently received a lot of attention in the literature.[32,38–44]

Under our theoretical framework, we model the magnetic Ni segment as a rigid slender rod (radius a_m = 100 nm, length L_m = 1.8 μm) (the short Au segment is considered to be part of the rigid rod in this model, as discussed above, see Fig. 1), and the flexible Ag nanowire (radius a = 50 nm, length L = 4 μm) as a classical Euler–Bernoulli beam.[45] We then employ a local fluid drag model, known as resistive force theory,[4] to describe the fluid–body interaction. The use of a local and linear theory significantly simplifies the analysis and is

expected to provide quantitative agreement because geometric nonlinearities and nonlocal hydrodynamic effects were proven to be subdominant for gentle distortions of a slender body in previous work.[39,42,43]

Notation for the model is shown in Figure 7.2.1(a). The external magnetic field precesses about the z-axis in the clock-wise direction, and can be described as $\mathbf{H} = (H_1\cos\Omega t, -H_1\sin\Omega t, H_0) = H_0(h\cos\Omega t, -h\sin\Omega t, 1)$, where $h = H_1/H_0$ is the dimensionless relative strength of the rotating (H_1) and constant (H_0) components of the magnetic field. We study the regime where thenanowire follows synchronously the precessing magnetic field, rotating at the same angular frequency (Ω) as the magnetic field about the z-axis. In addition, we can move in a rotating frame in which the magnetic field is fixed and the shape of the flexible nanowire does not change with time. In this frame, the precessing magnetic field is given by $\mathbf{H} = H_0(h, 0, 1)$, and thenanowire has a non-changing shape $\mathbf{r}(s) = (\mathbf{r}_\perp(s), z(s)) = (x(s), y(s), z(s))$ in a background flow, $\mathbf{v}_b$, rotating counter-clockwise about the z-axis: $\mathbf{v}_b = \Omega\mathbf{e}_z \times \mathbf{r}_\perp = \Omega(-y, x, 0)$, where $\mathbf{e}_z$ is the unit vector in the z-direction and s is the arclength parameter along the filament.

7.2.4.3 Elastohydrodynamics at low Reynolds number

We describe the fluid-body interaction by resistive force theory, which states that the local fluid drag depends only on the local velocity of the filament relative to the background fluid (although in a non-isotropic fashion). This is thus a local drag model which ignores hydrodynamic interactions between distinct parts of the filament, but was shown to be quantitatively correct for gentle distortions of the filament shape.[39,42,43] The viscous force acting on the filament is thus expressed as

$$\mathbf{f}_{vis} = -[\xi_\parallel \mathbf{tt} + \xi_\perp(1 - \mathbf{tt})]\cdot\mathbf{u}, \tag{7.2.1}$$

where $\mathbf{t}(s)$ is the local tangent vector, $\mathbf{u}(s) = \mathbf{U} - \mathbf{v}_b$ is the local velocity of the filament relative to the background flow $\mathbf{v}_b$, and $\mathbf{U}$ is the swimming velocity of the nanomotor. Here, $\xi_\parallel$ and $\xi_\perp$are the

tangential and normal drag coefficients of a slender filament ($L \gg a$) and are given approximately by

$$\xi_{\parallel} = \frac{2\pi\mu}{\log(L/a) - 1/2}, \; \xi_{\perp} = \frac{4\pi\mu}{\log(L/a) + 1/2}, \tag{7.2.2}$$

where μ is the viscosity of the fluid (water, $\mu = 10^{-3}$ N s m^{-2}). Since the Ni and Ag segments have different aspect ratios (L_m/a_m for the Ni segment), a different set of drag coefficients ($\xi_{m\parallel}$, $\xi_{m\perp}$) is used for the rigid segment.

When the flexible Ag filament of the nanomotor is deformed, elastic bending forces arise trying to minimize the bending energy. This elastic bending force can be obtained by taking a variational derivative of the energy functional $\mathscr{E} = \frac{1}{2}\int_0^L A\left(\partial^2 \mathbf{r}/\partial s^2\right)^2 \mathrm{d}s$, where A is the bending stiffness of the material. The elastic bending force is then given by

$$\mathbf{f}_{\text{elastic}} = -A\frac{\partial^4 \mathbf{r}}{\partial s^4}. \tag{7.2.3}$$

Since we are in the low Reynolds number regime, inertial forces are negligible, and the local viscous fluid forces balance the elastic bending forces, $\mathbf{f}_{\text{vis}} + \mathbf{f}_{\text{elastic}} = \mathbf{0}$, which yields the equation governing the filament elastohydrodynamics

$$[\xi_{\parallel}\mathbf{tt} + \xi_{\perp}(\mathbf{1} - \mathbf{tt})] \cdot \mathbf{u} = -A\frac{\partial^4 \mathbf{r}}{\partial s^4}. \tag{7.2.4}$$

The flexible Ag filament is clamped to the magnetic Ni segment, which is assumed to be rigid and straight. Hence, its position vector is given by $\mathbf{r}_m(s) = \mathbf{r}|_{s=L} + \mathbf{t}|_{s=L}(s - L)$, where $s \in [L, L + L_m]$.

7.2.4.4 Nondimensionalization

We now nondimensionalize the variables and equations and identify the relevant dimensionless parameters governing the physics of this problem. Specifically, we scale lengths

by L, rotation rates by $\Omega = 2\pi f$, times by Ω^{-1}, velocities by $L\Omega$, fluid forces by $\xi_\perp L^2\Omega$, fluid torques by $\xi_\perp L^3\Omega$, elastic forces by A/L^2, and elastic torques by A/L. Using the same symbols for simplicity, the dimensionless elastohydrodynamic equation now reads

$$\left[\gamma^{-1}\mathbf{tt} + (\mathbf{1} - \mathbf{tt})\right] \cdot \mathbf{u} = -\mathrm{Sp}^{-4} \frac{\partial^4 \mathbf{r}}{\partial s^4}, \tag{7.2.5}$$

where we have defined $\gamma = \xi_\perp/\xi_\parallel$, and $\mathrm{Sp} = L(\xi_\perp\Omega/A)^{1/4}$ is termed the sperm number, which characterizes the relative influence of the fluid and bending forces.

7.2.4.5 Asymptotic analysis

The geometrical nonlinearity of eqn (7.2.5) renders the elastohydrodynamic equation only solvable *via* numerical simulation in most situations. Here we are able to illustrate the essential physics of flexible nanomotor propulsion analytically *via* an asymptotic analysis for the case where $h = H_1/H_0$ is small. Such an approximation drops the geometrical nonlinearities and, as will be shown below, separates the task of determining the filament shape and swimming velocities of the nanomotor, as the axial velocities are one order of magnitude smaller than the transverse velocities, the axial swimming kinematics being thus slaved to the transverse kinematics.[44] Even with this simple model, we find that the theoretical predictions agree well with the experimental measurements. In the experiments, we do not observe very significant distortion of the flexible Ag filament, which might explain the success of this simple model.

As the nanomotor was observed to propel unidirectionally in the z-direction in the experiments (*i.e.* the direction about which the actuating magnetic field precesses), we write the swimming speed as $\mathbf{U} = (0, 0, U)$ and aim at predicting the leading order swimming speed in h. We do not expect any $O(h^0)$ deformation nor swimming velocities, and hence the appropriate expansions for the deformation of the nanowire and the swimming speed are given by

$$\mathbf{r}_\perp(z) = h\mathbf{r}_\perp(z) + h^2\mathbf{r}_\perp(z) + O(h^3), \tag{7.2.6}$$

$$U = hU_1 + h^2U_2 + O(h^3), \tag{7.2.7}$$

where we have $s \approx z + O(h^2)$.

The elastoydrodynamic equation is a fourth-order partial differential equation in space, and needs thus to be supplied with four boundary conditions. We prescribe dynamic boundary conditions at the free end $z = 0$, requiring it to be force-free and torque-free, which is $\partial^3\mathbf{r}/\partial z^3(z = 0) = \mathbf{0}$ and $\partial^2\mathbf{r}/\partial z^2(z = 0) = \mathbf{0}$ respectively. Since the deformed shape rotates about the z-direction, without loss of generality, we assume the Ni head lies on the $x - z$ plane. We then prescribe kinematic boundary conditions at the other end $z = 1$: $\mathbf{r}_\perp(z = 1) = (b,0)$ and $\partial\mathbf{r}_\perp/\partial z(z = 1) = (h,0)$. From experimental observations, the value of b is seen to be negligibly small ($b \approx 0$) and is difficult to measure accurately. Here, for simplicity, we thus take $b = 0$ in our calculations below. In this geometric model, we assume that the slope of the magnetic Ni head, $\partial x(z)/\partial z(z = 1)$, follows the slope of the external field ($h = H_1/H_0$), which is a good approximation when the magnetic field strength is strong or when the frequency of actuation is low, such that the Ni head can align closely with the external magnetic field. The magnitude of the magnetic torque can be compared with the viscous torque acting on the Ni head, and their ratio is given by the so-called Mason number, Ma. The ratio varies from 0.018–0.12, for frequency varying form 5 Hz to 35 Hz. One can also compare the magnetic torque to the characteristic viscous torque acting on the Ag filament, and it varies from 0.13–0.93, for the same range of frequency. In both cases, Ma is thus typically small and is at most $O(1)$ at high frequencies. Therefore, within the range of frequency explored in the experiment, our geometrical model is considered to be a valid approximation. At higher frequencies, we would get $\mathrm{Ma} \gg 1$, which would play a role in the boundary condition at $z = 1$. In that regime, the viscous torque would dominate the typical actuation torque by the magnetic field, and the Ni segment would therefore not be able to align with the magnetic field closely. We expect that the slope of the Ni rod might then be smaller than that of the magnetic field, and the phase lag between the motion of the Ni segment and the magnetic field could be

substantial. As a result, a degradation in the propulsion performance would be expected to occur in this regime.

Determining the flexible filament shape: *O*(*h*) calculations. At order $O(h)$, the local viscous force is given by $\mathbf{f}_{\text{vis}} = h(-y_1(z), x_1(z), -\gamma^{-1}U_1) + O(h^2)$. From here, we can integrate the $O(h)$ local viscous force in the z-direction over the entire nanomotor and since this total force needs to vanish because of the absence of external forces, we find $U_1 = 0$: swimming occurs therefore at order $O(h^2)$. The elastic force is given by $\mathbf{f}_{\text{elastic}} = -h\,\text{Sp}^{-4}(\partial^4 x_1/\partial z^4, \partial^4 y_1/\partial z^4, 0) + O(h^2)$. Balancing the local viscous and elastic forces in the transverse directions yield the hyper-diffusion equations[42]

$$-y_1 = \text{Sp}^{-4}\frac{\partial^4 x_1}{\partial z^4}, \tag{7.2.8}$$

$$x_1 = \text{Sp}^{-4}\frac{\partial^4 y_1}{\partial z^4}, \tag{7.2.9}$$

which govern the first order filament shape. The general solution to this system of partial differential equations is given by

$$x_1(z) = \sum_{n=1}^{8} A_n \exp(\text{Sp}\, r_n z), \tag{7.2.10}$$

$$y_1(z) = \sum_{n=1}^{8} -A_n r_n^4 \exp(\text{Sp}\, r_n z), \tag{7.2.11}$$

where r_n is the n-th eight roots of -1, and A_n are complex constants to be determined by the boundary conditions. The boundary conditions to this order at $z = 0$ are given by $\partial^3 x_1/\partial z^3(z = 0) = \partial^3 y_1/\partial z^3(z = 0) = \partial^2 x_1/\partial z^2(z = 0) = \partial^2 y_1/\partial z^2(z = 0) = 0$. The appropriate boundary conditions at $z = 1$ are given by $x_1(z = 1) = y_1(z = 1) = 0, \partial x_1/\partial z(z = 1) = 1$, and $\partial y_1/\partial z(z = 1) = 0$. The $O(h)$ filament shape is now completely determined.

Determining the swimming speed: O(h^2) calculations. At order $O(h^2)$, the local viscous fluid force acting on the flexible filament in the z-direction is given by

$$\mathbf{e}_z \cdot \mathbf{f}_{\mathrm{vis}_2} = \begin{cases} -\left(\gamma^{-1}-1\right)\Lambda(z) - \gamma^{-1}U_2, & 0 \le z < 1, \\ \dfrac{\xi_{\mathrm{m}\perp}}{\xi_\perp}\left[-\left(\gamma_{\mathrm{m}}^{-1}-1\right)\Lambda(z) - \gamma_{\mathrm{m}}^{-1}U_2\right], & 1 < z \le 1 + l_{\mathrm{m}}, \end{cases}$$

where $l_{\mathrm{m}} = L_{\mathrm{m}}/L$, and we have introduced the function $\Lambda(z) = y_1(z)\partial x_1/\partial z(z) - x_1(z)\partial y_1/\partial z(z)$. Since the nanomotor is overall force-free, the second order swimming speed U_2 can be determined by integrating the local viscous fluid in the z-direction over the entire nanomotor and requiring this total force to vanish, *i.e.*

$$\int_0^{1+l_{\mathrm{m}}} \mathbf{e}_z \cdot \mathbf{f}_{\mathrm{vis}_2}\,\mathrm{d}z = 0, \tag{7.2.12}$$

and we see that the swimming speed is slaved to the first order filament shape ($x_1(z)$, $y_1(z)$) *via* the function $\Lambda(z)$. Upon simplification with eqn (7.2.8) and (7.2.9) and the boundary conditions at z = 0, we obtain

$$U_2 = \frac{1-\gamma}{\mathrm{Sp}^4\left(1+\alpha l_{\mathrm{m}}\right)} \times \left[\frac{\partial x_1}{\partial z}\frac{\partial^3 x_1}{\partial z^3} - \frac{1}{2}\left(\frac{\partial^2 x_1}{\partial z^2}\right)^2 + \frac{\partial y_1}{\partial z}\frac{\partial^3 y_1}{\partial z^3} - \frac{1}{2}\left(\frac{\partial^2 y_1}{\partial z^2}\right)^2\right]_{z=1}, \tag{7.2.13}$$

where $\alpha = \xi_{\mathrm{m}\parallel}/\xi_\parallel$. In dimensional form, the leading order swimming speed, is given by

$$U = h^2 \frac{A\left(\xi_\parallel - \xi_\perp\right)}{\xi_\perp\left(L\xi_\parallel + L_m\xi_{m\parallel}\right)} \times \left[\frac{\partial x_1}{\partial z}\frac{\partial^3 x_1}{\partial z^3} - \frac{1}{2}\left(\frac{\partial^2 x_1}{\partial z^2}\right)^2 + \frac{\partial y_1}{\partial z}\frac{\partial^3 y_1}{\partial z^3} - \frac{1}{2}\left(\frac{\partial^2 y_1}{\partial z^2}\right)^2\right]_{z=1} + O\left(h^3\right). \tag{7.2.14}$$

As in previous work,[32,33,43,44,46,47] we observe that this mode of propulsion relies on the drag anisotropy of slender filaments, $\gamma = \xi_\perp/\xi_\parallel \neq 1$. Indeed, when $\gamma = 1$, the swimming speed vanishes. Note that for very slender filaments, we have $\gamma \approx 2$ (see eqn (7.2.2)).

We also see that the swimming speed scales quadratically with the relative strength of the rotating and constant components of the magnetic field, $U \sim h^2$, for $h \ll 1$. This scaling is confirmed by a complementary asymptotic calculation valid for low sperm numbers.

Next, we plot our predicted dimensionless second order swimming speed as a function of the sperm number Sp (Figure 7.2.4a) together with the predicted filament shapes (Figure 7.2.4b), and observe three different characteristic regimes. The sperm number Sp is the most important dimensionless group governing the propulsion performance. For Sp $\ll$ 1, bending forces dominate and the filament is effectively straight (Figure 7.2.4b-i). Hence, the filament motion is almost kinematically reversible, and it produces small propulsion. Quantitatively, a small Sp asymptotic analysis reveals that the dimensionless swimming speed grows with the fourth power of the sperm number, $U_2 \sim \mathrm{Sp}^4$, for Sp $\ll$ 1. On the other hand, from eqn (7.2.10) and (7.2.11), we see that most deflection is concentrated around a small region $0 \leq z < 1/\mathrm{Sp}$, when Sp $\gg$ 1, due to the exponential decay of the solution amplitude. In this regime (Sp $\gg$ 1), the viscous forces dominate, and propulsion is inefficient because a large portion of the filament has small deflection and thus experiences drag but contributes to no thrust (Figure 7.2.4b-iii & iv). As a result, we expect optimal swimming to occur when Sp is of order one, where the total drag of the nanomotor is kept low while the drag-induced bending is fully exploited to produce propulsion. This is confirmed in our calculation, and we observe the optimal sperm number to occur at $\mathrm{Sp} \approx 2$, which gives a maximum propulsion speed of $U_2 \approx 0.042$ (Figure 7.2.4a). The filament shape close to optimal swimming (Sp = 2) is shown in Figure 7.2.4b-ii.

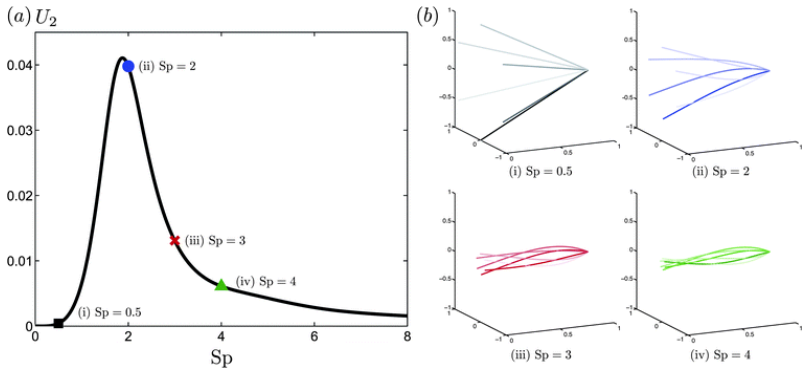

Figure 7.2.4 (a) Variation of the dimensionless propulsion speed at second order, U_2, with the sperm number, Sp. (b) Superimposed snapshots of predicted three-dimensional shape of the Ag nanowire at equal time intervals (t = [T/6,2T/6,…,5T/6,T] from dark to bright color, where T is the period of the rotating magnetic field), for four different sperm numbers. The Ni head is not shown here for simplicity.

7.2.4.6 Comparison with experimental measurements

Under fixed magnitude of the rotating and constant components of the magnetic field, the swimming speed of a nanomotor was measured with the frequency of the magnetic field varying between 0 to 35 Hz. The experiment was repeated on the same nanomotor for three different settings of magnetic field strengths (shown using three different symbols with error bars in Figure 7.2.5b; a total of 20 different nanowires were sampled). The rotating magnetic field strength H_1 was kept constant at H_1 = 10 G, and the constant magnetic field strength was set to be H_0 = 14.3 G (blue squares), H_0 = 11.8 G (red circles), and H_0 = 9.5 G (green diamonds).

We then compare in Figure 7.2.5b our theoretical predictions (solid lines) with experimental measurements, plotted as swimming velocity *vs.* frequency (main figure) or sperm number (inset). In our theoretical model, the value of the bending stiffness A of the flexible filament is unknown. Standard bending stiffness of pure silver is inapplicable here since the dissolution of silver inhydrogen peroxide rendered the filament a porous structure with significantly reduced strength and a different chemical composition (Ag_2O, AgOH). A value of $A = 3.6 \times 10^{-24}$ N m^{-2} fits, with the least total squared errors, the experimental data with H_1 = 10 G, H_0 = 14.3 G (blue squares), which is the case where our model is expected to work best as

the ratio $h = H_1/H_0$ is the smallest. This bending stiffness is then used to predict the propulsion speed under different magnetic field settings (green and red solid lines in Figure 7.2.5b, see captions for details).

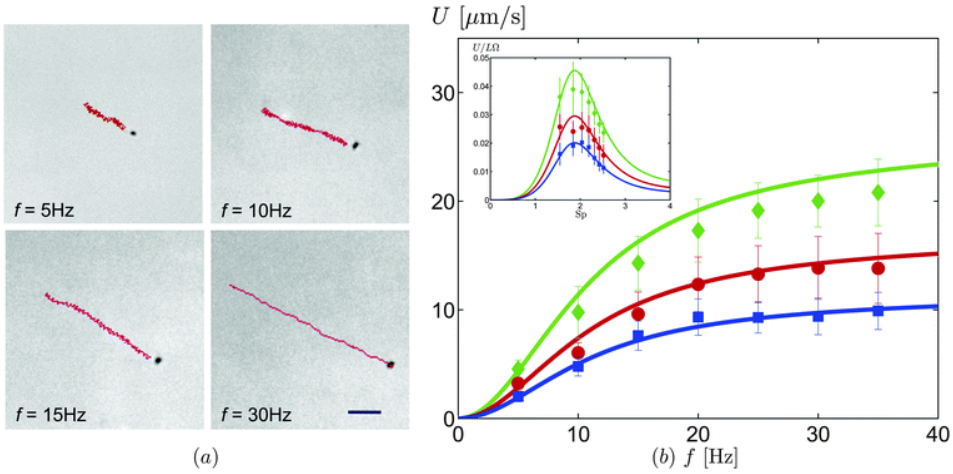

Figure 7.2.5 Dependence of the nanomotor swimming speed on the actuation frequency. (a) Superimposed trajectories of the same Ni–Ag nanomotor at different frequencies f = 5, 10, 15, 30 Hz (as indicated) over a 3-second period (red lines), with H_1 = 10 G and H_0 = 9.5 G. The scale bar is 10 μm. (b) Speed-frequency characteristics of flexible nanowire motors. Symbols represent experimental data for different setups of the magnetic field: blue squares (H_1 = 10 G, H_0 = 9.5 G); red circles (H_1 = 10 G, H_0 = 11.8 G); green diamonds (H_1 = 10 G,H_0 = 14.3 G). Error bars show standard deviations of the measured speeds. The solids lines show the theoretical predictions (eqn (7.2.14)) with $A = 3.6 \times 10^{-24}$ N m^2. The inset in (b) displays the dependence of the swimming speed on the sperm number, Sp.

The theoretical model is seen to capture both qualitatively and quantitatively the speed-frequency characteristics of these flexible nanomotors. Qualitatively, the rate of change of the swimming speed with respect to the frequency increases at low frequencies ($U \sim f^2$ for small f), but then gradually decreases as the frequency continues to increase, and eventually levels off at high frequencies. Physically, increasing the actuation frequency is equivalent to increasing the sperm number. When the frequency is varied from 0 to 35 Hz, it corresponds to a variation of the sperm number Sp from 0 to 2.6, experiencing a degradation in swimming performance beyond the optimal sperm number Sp≈ 2, which corresponds to a frequency of around 15 Hz in our experiment. This degradation manifests as a less-than linear speed-frequency variation (since the dimensional swimming speed scales as $L\Omega$, linearly in Ω) beyond the frequency 15 Hz, resulting

in the level-off at higher frequencies. As noted above, at very high frequencies, the magnetic Ni head will be unable to follow synchronously the rapid rotating magnetic field. The dynamics of propulsion will be more complicated in that regime, and the simple model presented here will likely be inapplicable.

The agreement between our theoretical model and our experimental results is very satisfactory. The discrepancies are larger for the setup H_1 = 10 G, H_0 = 9.5 G (green lines and squares), which is expected because $h \approx 1.1$ in this case and the asymptotic assumption of small h is less valid. Note that our measurements did not sample the low Sp regime as in our experiments, swimming at low frequencies appear to be significantly influenced by Brownian motion.

Our model has only one fitting parameter, the bending stiffness A, which—as explained above—we fit to the bottom data set in Figure 7.2.5b, and use to predict the other two data sets. The estimated value we obtain from the fitting is equivalent to a pure silver nanowire of diameter ≈6 nm (with elastic modulus, E = 80 G Pa), which is much smaller than the diameter of flexible segment observed. This is expected because the chemical composition of silver is altered after the dissolution, and a large portion of the flexible nanowire is indeed a thick layer of surface byproducts formed after the chemical reaction, which contributes little, if any, to the bending strength. The diameter of the actual structural filament that bears the bending loads is difficult to measure experimentally (see details of the structure in Figure 7.2.1b). In addition, non-uniform chemical reactions lead to strong local defects or points of weakness along the nanowire, which might significantly reduce the bending strength. We can compare our estimated bending stiffness, $A = 3.6\times10^{-24}$ N m^2, with the bending stiffness of typical flagella of natural microscopic swimmers, such as eukaryotic spermatozoa, which also rely on the flexibility of flagella for propulsion. These biological filaments have their bending stiffnesses ranging from[48] 10^{-24} N m^2 to[49] 10^{-22} N m^2, which is the range in which our estimated value lies.

7.2.5 Conclusions

In this work, we designed and fabricated a high-speed fuel-free nanomotor utilizing the flexibility of nanowires for propulsion. These flexible nanomotors demonstrate a number of advantages: first, the fabrication process is relatively simple and involves a common template-directed electrodeposition protocol of nanowires; second, these nanowire motors are able to propel at high speeds, both dimensional (up to≈21 μm s^{-1}) and dimensionless (up to 0.164 body lengths per revolution), and their performance compares very well with natural microorganisms and other synthetic locomotive systems; third, they are actuated by external magnetic field and do not require specific chemical environments (fuels) for propulsion, which is preferable for biomedical applications. Indeed, the performance of the nanomotors reported here is not affected by the presence of ions or other chemical species, and they are able to propel equally well in real biological settings. As an illustration, we have placed these flexible nanomotors in human serum, and observed similar propulsion behaviors (Figure 7.2.6). This demonstrates an exciting potential of these flexible nanomotors for future biomedical applications such as targeted drug delivery systems, or cell manipulation.

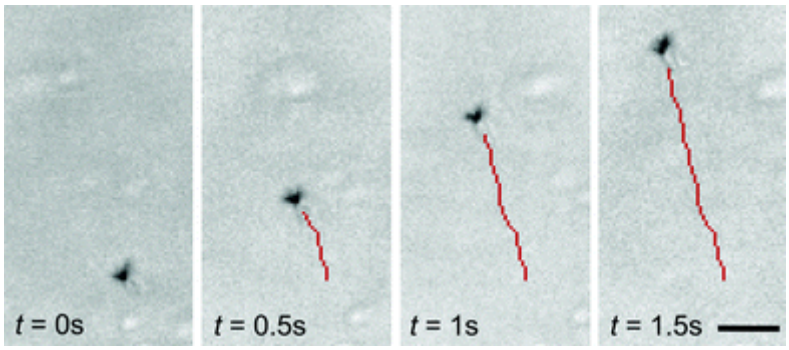

Figure 7.2.6 Time lapse images (time as indicated) of the motion of nanowire motor (velocity, U = 15 μm s^{-1}) in human serum at f = 15 Hz, with H_1 = 10 G and H_0 = 9.5 G. Scale bar is 5 μm.

The fundamental physics of the flexible nanomotors has been illustrated by a simple analytical elastohydrodynamic model. The propulsion characteristics were experimentally studied

and compared with the theoretical model, with good agreement. Strictly speaking, the results of the asymptotic model presented in this wrok are valid only for $h \ll 1$. However, as shown in other previous studies which compared asymptotic results with numerical and experimental studies,[39,42,43] these asymptotic models often remain valid even up to $h \sim 1$, meaning that geometrical nonlinearities do not play very significant roles. Our results also ignore the hydrodynamic effect of the bottom surface close to which the nanomotors are propelling. As we estimated experimentally the distance of the filaments to the surface to be on the order of microns, and therefore on the order of the swimmer size, we do not expect strong hydrodynamic effects from the surface, which might explain the success of our simple modelling approach. Further progress in theoretical modelling most likely have to be obtained numerically. More accurate yet complicated descriptions of the hydrodynamic interactions can be achieved using methods such as slender body theory,[50] or regularized Stokeslets.[51] Tension, self-spinning, and twist strains of the filament may also be considered for improvements.

7.3 Hybrid nanomotor: a catalytically/magnetically-powered adaptive nanoswimmer

7.3.1 Introduction

Efficient energy conversion is crucial for the successful use of synthetic artificial nanomotors.[6-10] As we discussed before, extensive recent research efforts have thus led to powerful chemically-powered nanomotors, based primarily on bisegment Pt-Au nanowires or microtube engines, that operate on a locally supplied fuel (commonly hydrogen peroxide).[6-12] Recent activity has also resulted in fuel-free nanomotors that offer efficient magnetically driven propulsion.[13-20] Several of these chemically-powered[6-8] and fuel-free nanomotors[20,52] rely on multi-segment nanowires, produced by a template electrodeposition.

In this section, we describe the design, dual-mode locomotion and advantages of a parallel hybrid nanowire motor that is powered by two sources, chemically and magnetically. Hybrid nanomotors could expand the scope of operation of man-made nanomachines into diverse and changing environments. Living/no-living hybrid devices, using biological motors or bacteria to power or propel inorganic microscale objects, have been described previously.[53,54] However, there are no reports on synthetic hybrid nanomotors capable of moving via different propulsion mechanisms. Combining different locomotion modes into a single device represents a nanoengineering challenge in view of the fundamentally different design and operational requirements associated with each propulsion mode. Taking advantages of the common use of template electrodeposition for preparing both catalytic[55] and magnetic[20] nanowire motors, our new hybrid motor relies on a multi-segment nanowire with different portions responsible for the catalytic and magnetic propulsions. Such hybrid nanowire motor is readily prepared by adding the fuel-driven propulsion capability onto a magnetically-driven flexible nanowire swimmer by simply growing a Pt segment on its Au segment to create a catalytic Pt-Au 'head' **(**Figure 7.3.1**)**.

Such 4-segment nanowires were grown by sequential template electrodeposition of the Pt, Au, Ag, and Ni segments, coupled with a partial dissolution of the Ag segment. The latter leads to the flexibility essential for breaking the system symmetry and achieving the magnetic movement under the rotating magnetic field.[20] In this section, we will evaluate the dual-mode locomotion of such flexible hybrid nanowire motor, illustrate that changes in the motor design minimally compromise either propulsion mode, demonstrate the distinct advantages of such dual operation mode, and the ability to switch the operation in response to changing conditions.

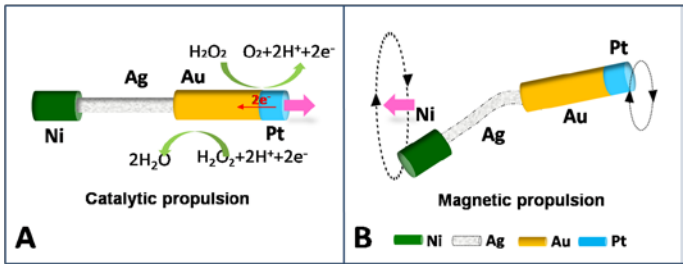

Figure 7.3.1 Catalytic (A) and magnetic (B) propulsion of the hybrid nanomotor.

7.3.2 Experimental section

The hybrid nanowire motors were prepared using the same electrodeposition protocol as Chapter 7.1.2. Copper was electrodeposited in the 'branch' area of the membrane from a $CuSO_4 \cdot 5H_2O$ (1 M) solution, using a charge of 8 C and a potential of -0.9 V (vs. Ag/AgCl reference electrode, along with a Pt-wire counter electrode); subsequently, the Pt segment was deposited galvanostatically at -2 mA for 2000 s from a commercial platinum plating solution (Platinum RTP; Technic Inc.); gold was plated next from the commercial gold plating solution (Orotemp 24 RTU RACK; Technic Inc.) at -1.0 V (vs. Ag/AgCl), using a charge of 3 C; silver was plated subsequently at -0.9 V (vs. Ag/AgCl) for a total charge of 3.5 C using a commercial silver plating solution (1025 RTU @ 4.5 Troy/gallon; Technic Inc., Anaheim, CA); finally, nickel was deposited from a nickel plating solution containing $NiCl_2 \cdot 6H_2O$ (20 g L^{-1}), $Ni(H_2NSO_3)_2 \cdot 4H_2O$ (515 g L^{-1}), and H_3BO_3 (20 g L^{-1}) at -1.0 V (vs. Ag/AgCl) for 3 C. All nanowire solutions were stored in nanopure water at room temperature. Flexibility of the central

silver segment was achieved by its partial dissolution accomplished by mixing 10 µl of the diluted Pt/Au/Ag/Ni nanowire solution with 10 µl of the hydrogen peroxide solution (16%) for 1 min. Hydrogen-peroxide residues were removed by repeated washing of the nanowires on the microscope glass slide using nanopure water (18.2 MΩ·cm) until a neutral pH was achieved.

7.3.3 Results and discussions

The ability to power the new hybrid nanomotor chemically and magnetically is illustrated in Figure 7.3.2. This figure compares the movement of the hybrid nanomotor in its catalytic (b) and magnetic (c) modes over 4 s period of time. Using its 'catalytic' mode, the hybrid nanowire motor moves (in an 8% H_2O_2 solution) towards its Pt end at a speed of 8 µm/s (Figure 7.3.2b). Similarly, an efficient magnetically-driven propulsion with a speed of 6 µm/s is observed in the absence of the H_2O_2 fuel under a rotating magnetic field (Figure 7.3.2c). As expected for such magnetic propulsion,[20] the motor moves 'backward' towards its nickel side. As will be illustrated below such opposite motion directions facilitate an on-demand change in the motor directionality. In contrast, no directed motion of the hybrid nanomotor is observed (in the control experiment of Figure 7.3.2a) in the absence of the fuel or the magnetic field.

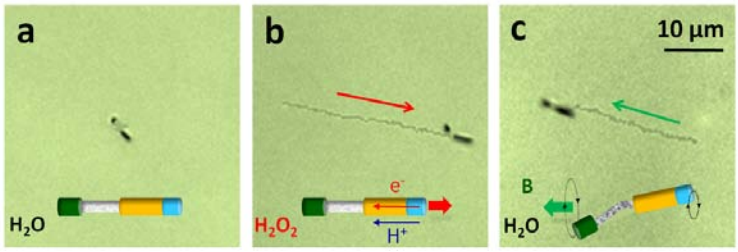

Figure 7.3.2 Movement of the hybrid nanomotor in the catalytic (b) and magnetic (c) modes. Tracking lines illustrating a typical motion in each mode over 4 s, along with the motion of the motor without fuel or magnetic field (a). The fuel-driven motion is performed in 8% H_2O_2, while the magnetic propulsion is achieved using an alternating magnetic field (10 Gauss, 15 Hz) and a perpendicular constant magnetic field (8 Gauss).

The dimension of the hybrid nanowire and the relative length of its individual segments have a profound effect upon the performance of the new nanomotor. We systematically changed the length of the individual segments of the Pt-Au-Ag-Ni nanowire and found that length of 0.5,

2.0, 3.5, 1.0 μm of the Pt, Au, Ag and Ni segments, respectively, offer the most favourable hybrid performance. Particularly important (for both propulsion modes) is the length of the Pt segment. A 0.5 μm Pt segment offered the most promising catalytic propulsion without affecting the hydrodynamics essential for the magnetic swimming. Flexibility of the silver segment was achieved by its partial dissolution in an 8% hydrogen peroxide solution.[20] The dissolution step leads to hydroxyl products that chemisorb on the Ag surface and result in AgOH and Ag_2O surface products.[20]

Critical to the success of future hybrid nanovehicles is that the change in the motor design (essential for creating the hybrid) will have minimal effect upon the individual propulsion modes. While the magnetic propulsion is not influenced much by the addition of the short catalytic Pt segment, the catalytic movement is slower in the presence of the additional long Ni and Ag segments. However, despite of the higher drag resistance associated with the significantly longer nanowire motor (6 μm vs. 2 μm), the decrease in the catalytic speed is not significant, probably due to the silver-ion 'acceleration' effect,[56] associated with the partial silver dissolution and redeposition.[57]

We also evaluated the propulsion of the hybrid nanowire in the presence of both the fuel and magnetic field, i.e., a 'dual operation mode'). We observe an initial fuel-driven motion of the hybrid motor at a speed of 8 μm/s (towards the Pt end), followed by application of the rotating magnetic field that results in a combined 'forward' motion at a slower speed of 4.5 μm/s. The slower speed at such dual operation mode is attributed to several reasons, including increased fluid drag resistance caused by the rotation process and the magnetic propulsion force in the opposite direction. In contrast, application of the magnetic field onto a slower catalytic motor (5 μm/s, at a lower peroxide level of 5.5%), leads to reversal of the motion direction towards the Ni end, with a speed of 4.5 μm/s. Such change in directionality holds prospects for an adaptive hybrid vehicle control. As will be discussed below, the movement direction of such combined

catalytic/magnetic operation depends on the dominating propulsive force, as the magnetic locomotion pulls the motor backward.

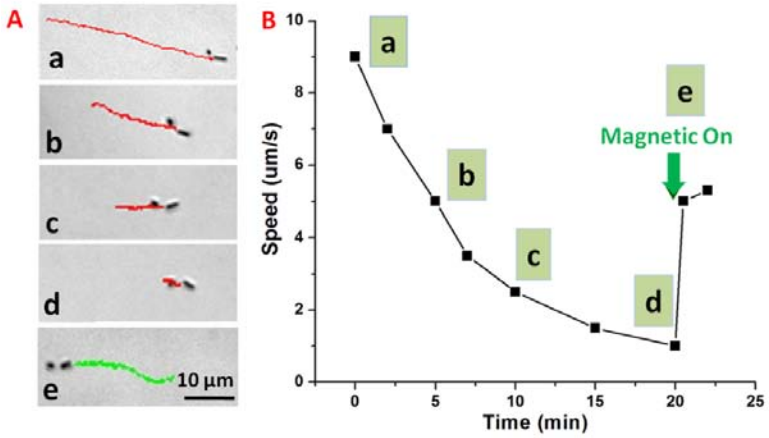

Figure 7.3.3 Switching to the magnetic mode in response to depletion of the fuel. (A) Tracking lines over 5 s showing the diminished fuel-driven motion of the hybrid nanomotor upon depletion of the fuel during a prolonged 20 min operation (a-d, 0, 5, 10, 20 min), followed by restoring the movement upon applying the rotating magnetic field (e). (B) Speed-time profile of the hybrid motor during this prolonged operation (a-e, as in A). Initial fuel level, 8% peroxide. Other conditions, as in Figure 7.3.2.

The hybrid nanomotor can address the fuel depletion during a prolonged catalytic operation, which leads to a gradually slower movement (reflecting the speed dependence upon the fuel level). Figure 7.3.3 illustrates the effect of the hydrogen-peroxide depletion upon the chemically-powered movement over a 20 min period, along with the ability to activate the motion magnetically upon consuming the fuel. While the nanomotor initially moves at a speed of around 9 µm/s in the 8% H_2O_2 solution, the speed decreases gradually to 5 and 2 µm/s after 5 and 10 min, reflecting the gradual fuel consumption (Figure 7.3.3b and 7.3.3c, respectively). The nanomotor motion nearly stops after 20 min, as indicated from its Brownian movement (observed in Figure 7.3.3d). At this point, the rotating magnetic field has been applied to resume the nanomotor motion (Figure 7.3.3e), leading to a magnetic propulsion with a speed of 5.5 µm/s. One can envision a self-regulated operation, with an autonomous magnetic actuation upon sensing the complete fuel consumption. Our experiments show, under magnetic mode, the hybrid nanomotor can swim nicely over 30 min (the sample drop almost dried up) without obvious speed

change. The hybrid nanowire motor can also address the high-ionic strength limitation of catalytic nanomotors[58] by changing on-demand its operation mode upon encountering a salt-rich environment. The speed of the nanomotor in its catalytic mode decreases rapidly upon adding 250 μM KCl. Non-directional motion is observed 20 s following the salt addition. The hybrid nanomotor can adapt to the new salt-rich environment by switching on its magnetic propulsion, rapidly reaching a speed of 5 μm/s. Eventually, such hybrid nanomotor will autonomously reconfigure its operation in response to such environmental change.

7.3.4 Conclusions

We have illustrated the fuel-driven and fuel-free propulsion of a new flexible hybrid Pt-Au-Ag_{flex}-Ni nanowire motor powered by two sources, chemically and magnetically, respectively. Template electrodeposition has been shown to be particularly attractive preparing such multi-segment nanowire motors with different portions responsible for the catalytic and magnetic propulsions. The dual propulsion mode of the new hybrid nanomotor increases the versatility and broadens the scope of operation of man-made nanomachines. The design of such hybrid nanomotor only minimally compromises the performance of the individual propulsion modes and can address the fuel depletion and salt limitation common in chemically-powered motors. Reversal of the flow direction is accomplished by switching on the magnetic propulsion. Such hybrid nanomotors hold considerable promise for designing self-regulated nanovehicles that adapt and reconfigure their operation according to the surrounding environment and unexpected events toward various important applications.

7.4 Bio-inspired helical microswimmer based on vascular plant

7.4.1 Introduction

Magnetic nanoswimmer, inspired by the motility of natural microorganisms, are particularly attractive for a variety of future biomedical applications at different scales because they can perform demanding tasks and remote operations while obviating the fuel requirement.[13-20,52,59,60] Besides the flexible artificial flagella we discussed in Chapter 7.1-7.3, the helical magnetic microswimmers which can transform the rotation around their helical axis into a translational corkscrew motion under a low-strength rotating magnetic field has also received particular attention.[13,14,18,59,60] However, the large-scale preparation of reproducible three-dimensional helical micro/nanostructures is challenging and involves complex and expensive fabrication processing techniques, including self-scrolling, glancing angle deposition, and 3-D direct laser writing.[13,14,59] The steep instrumental demands of these preparation routes restrict their production only to labs with such advanced fabrication facilities and greatly hinder their widespread use. In addition, biocompatible materials are desired for a variety of *in vivo* biomedical applications.

In contrast to the synthetic fabrication techniques, Nature has created uniquely complex patterns and elegant structures through plants over millions of years of evolution. Ranging from the natural fractal geometry of branches[61] to the formation of barbed raphide crystals[62] and thin stacks of grana thylakoids in chloroplasts,[63] plants are capable of generating a variety of highly-ordered hierarchical structures on different size scales. At the micrometer and nanometer scales, natural plant structures often have an advanced level of intricacy that rivals the sophistication of current engineered materials and systems.[64] Additional synthetic methods can be utilized to transform highly-structured plant materials into functional materials, taking advantage of their intrinsic natural morphology. These new hybrid structures can be applied to drug delivery,[65]

environmental remediation,[66] energy generation,[67] or biotemplated nanofabrication.[68] In addition, the direct incorporation of plant structures within polymeric and carbonaceous materials demonstrated high biodegradability, indicating the great promise of plant composites for biomedical[69] and biosensing[70] applications.

Here we demonstrate the first example of plant-based bio-inspired magnetically-propelled helical microswimmers. The new helical plant vessel-based microswimmers are fabricated by the simple coating of isolated spiral xylem vessel plant fibers with a thin magnetic layer. The intrinsic use of the plant material lends to the biocompatibility and ease of fabrication of the three-dimensional microswimmer, while the magnetic layer allows for high speed propulsion (over 250 μm/s) and precise directional control. The new method of using the spiral plant vessel as the major component of the helical micromotor greatly simplifies the fabrication process by utilizing the intrinsic biological microstructures that Nature provides. Due to the extremely high density of spiral vessels within the leaves, over a million individual helical swimmers can be generated from a short single segment of the plant stem.

7.4.2 Experimental section

Fabrication of the Helical Microswimmers

Various species of plants were collected from the UC San Diego campus (La Jolla, CA). To obtain unstretched spiral vessels, leaves were macerated in a 15 wt% KOH solution at 100°C. After washing off all loose plant matter with pure water, the resulting planar networks of 'feather-veins' were gently separated by tweezers to expose isolated, compressed spiral vessels. To obtain stretched spiral vessels, leaves were gently scored, and the two segments were pulled apart to a fixed length. These helical vessels were placed onto glass slides and coated with a 20 nm titanium layer at 1 Å/s, and a 80 nm nickel layer at 2 Å/s, using a Temescal BJD 1800 E-beam Evaporator. The metal-coated spiral vessels were then embedded within a layer of nail polish or S1818 photoresist and baked at 80 ºC for 2 min in order to confine the helices and to protect their

structure during dicing. The resulting photoresist film on glass was then diced to desired lengths. After dissolving the protective coating and washing the microswimmers in acetone, the microswimmers were redispersed in DI water.

7.4.3 Results and discussions

Xylem tissue extends all throughout vascular plants and transports water and nutrients from the roots to the leaves through capillary action. However, in order to support the high negative pressures involved in transpirational pull, plants developed thickened and lignin-supported xylem vessel walls.[71] These support structures can consist of chiral crystalline cellulose, resulting in distinct spiral structures of varying dimensions, depending on the type of plant. Figure 7.4.1 demonstrates the spiral microstructures from the xylem vessels of a diverse array of vascular plants. Uniform helical microstructures of various diameters can thus be isolated from ordinary plants ranging from decorative shrubs to flowering fruit-bearing trees (a-e). For example, the spiral vessels of the five plants shown in Figure 7.4.1 are characterized by different yet highly reproducible pitch and diameter. The diameters of these structures were found to vary from around 10 µm (*e.g. Raphiolepsis*) to over 60 µm (*e.g.* banana peel).

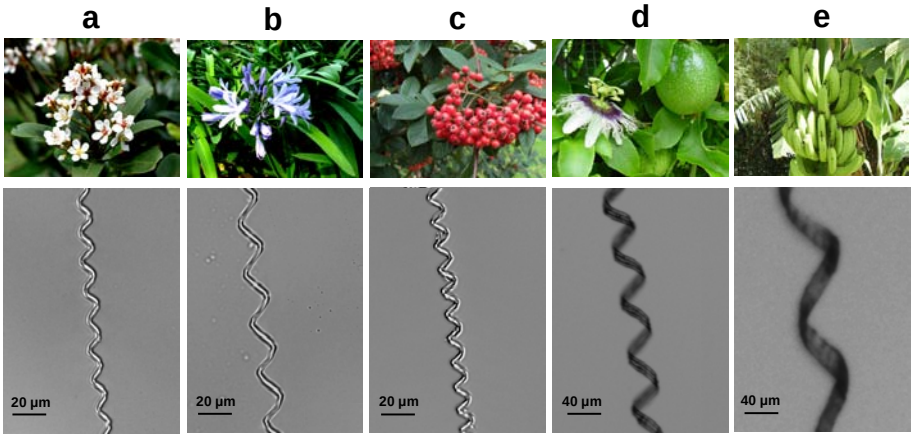

Figure 7.4.1 Photographic (upper) and microscopic (lower) images of spiral microstructures from xylem of different plants: a) *Rhaphiolepis indica*, b) *Cotoneaster lacteus*, c) *Agapanthus africanus*, d) *Passiflora edulis (passionfruit)* and e) *Musa acuminata (banana).*

Additionally, larger vessels are seen to have multiple parallel connected spiral supports, as seen in the larger vessels of the *Passiflora edulis* (passionfruit) and *Musa acuminata* (banana) plants (Figure 7.4.1(d,e)). The plants were taken from the two major classes of vascular angiosperms (flowering plants): *Liliopsida* (monocots) and *Magnoliopsida* (dicots). The distribution of stem vasculature varies between these two classes, with the distinction being drawn between sparsely scattered vascular bundles (monocots) and ring-shaped arrangements of vascular tissue (dicots). In both cases, there are numerous xylem vessels present in the bulk of the stem, allowing for the facile isolation of a large number of spiral microstructures from both dicots (Figure 7.4.1(a,c,d)) and monocots (Figure 7.4.1(b,e)). Control of geometric variables of the spiral vessels, such as the helix diameter and pitch, *via* mechanical stretching results in reproducible fabrication and performance of numerous helical microswimmers.

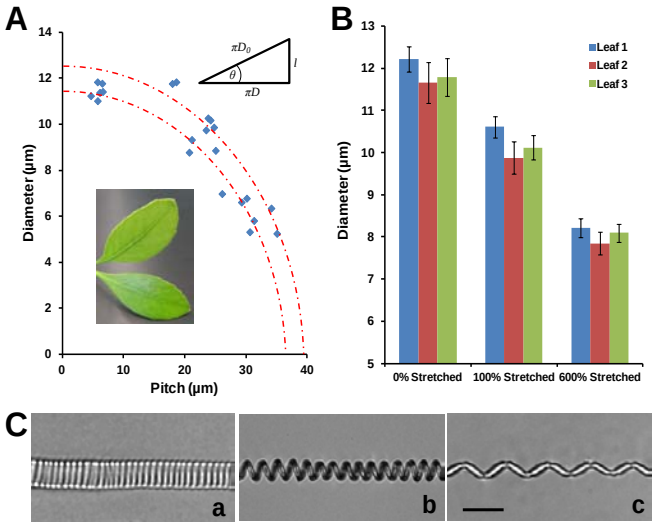

Figure 7.4.2 Stretching studies of the helical microstructure from xylem in *Rhaphiolepis indica*. A) The relationship between the pitch and diameter from a single leaf(in red: guides for the eye based on Eq. 2 for D_0 = 11.5 and 12.5 μm. B) The relationship of the stretching ratio and the helical diameter for different leaves after different stretching (0%, 100% and 600%) The error bars represent the standard deviations of the measured diameters found for a sample of 20 helices at each stretching point. C) Microscopic images of the spiral vessels isolated from the leaves before stretching (a) and at various stretching states (b,c). Scale bar, 20 μm.

The initial diameter of the unstretched spiral vessel is the most crucial dimension for determining the final shape of the helical structures. Within the leaves, the vessels are initially compressed as tightly wound coils with a characteristic diameter. This helix diameter was found to be consistent for similar leaves in plants of the same species. Isolating the compressed spiral structures from the stem regions of younger, developing leaves of *Rhaphiolepsis indica* resulted in helical coils with diameters within a narrow range of 11.5 to 12.5 μm. The individual vessel fibers are very thin with radii of 1 μm. We can model the stretching of the helical plant structure as a simple helical spring undergoing plastic deformation with a constant number of helical turns and negligible tensile stretching of the plant fiber. A geometric relationship between the diameter of the helix, *D*, and the helix angle can thus be obtained:[72]

$$\pi D = \pi D_0 \cos\theta \tag{7.4.1}$$

where θ is the helix angle and D_0 is the diameter of the helical coil at helix angle 0°. The diameter of the helix can be expressed:

$$D = \frac{1}{\pi}\sqrt{(\pi D_o)^2 - l^2} \tag{7.4.2}$$

where l is the helical pitch, or distance between consecutive turns. The diameters of the spiral plant vessels were observed to decrease with increased stretching (Figure 7.4.2A, B), following the expected behavior. Further tests on the reproducibility and consistency of the dimensions of the spiral vessels were carried out by evaluating different leaves from different plants. When stretched to 100% and 600% of their initial pitch length, the helical vessels from different leaves had similar diameters, with the small variability due to the range of initial helix diameters. The resulting stretched spiral vessels are uniform along their length and maintain their mechanical structure (Figure 7.4.2C). Thus, the crucial dimensions (*i.e.* helix diameter) of the spiral vessels can be controlled for the precise fabrication and reproducible performance of helical microswimmers.

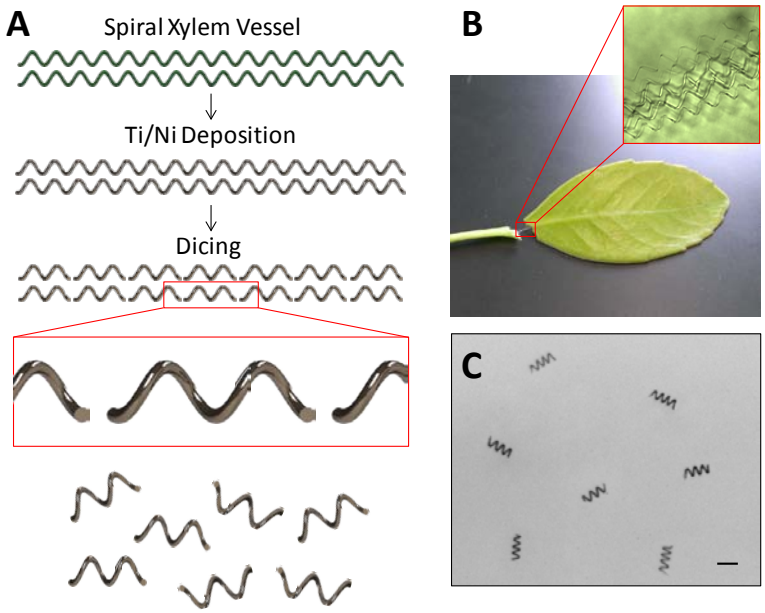

Figure 7.4.3 A) Schematic illustrating the steps involved in the preparation of the plant-based microswimmers. B) Image illustrating arbitrary stretching of the leaves to isolate the helical structure. The inset optical microscopic image illustrates the high density and uniformity of the natural helices. C) Microscope image of multiple magnetic helical microswimmers from *Agapanthus africanus*. Scale bar, 30 μm.

To overcome challenges of isolating the spiral vessels through chemical methods,[68] we developed a simple yet reproducible extraction method, illustrated in Figure 7.4.3A. Leaves of different plant species were lightly scored near the stem perpendicular to the vascular bundles, exposing the coiled spiral vessels. The two leaf segments were then carefully separated, gently drawn apart to a fixed length, and placed upon a narrow glass slide. After creating a large array of helical vessels, thin layers of Ti and Ni were sequentially deposited on the long spiral vessels for improving adhesion and magnetic actuation, respectively. These fibers were subsequently embedded within a layer of photoresist or nail polish, then diced into the desired lengths, resulting in a large quantity of identical microswimmers. The helical dimensions of the microswimmers remained constant throughout the whole fabrication process. The extremely high density of spiral vessels within the leaves (Figure 7.4.3B) provides an ideal platform for mass production of uniform functional helical microswimmers (Figure 7.4.3C). This method is thus

extremely promising for providing a simple, cost-effective, and reproducible large-scale mass-production of helical magnetic microswimmers, and offers substantial savings in material requirements and processing costs compared to the commonly used methods for fabricating helical microswimmers.[13,14,59] For example, for leaves of *Rhaphiolepis*, two segments of the lower leaf can each be stretched to obtain 9 mm long vascular fiber bundles, with each ring of vascular bundles containing over 30 spiral vessels. For *Agapanthus*, the flowering stem can have over 300 complete strands of easily extracted spiral vessels. Upon dicing the fibers to 60 μm lengths, one leaf of *Rhaphiolepis* can produce 4500 individual helical swimmers, while a 30 cm segment of *Agapanthus* stem can lead to over 1,500,000 individual helical swimmers.

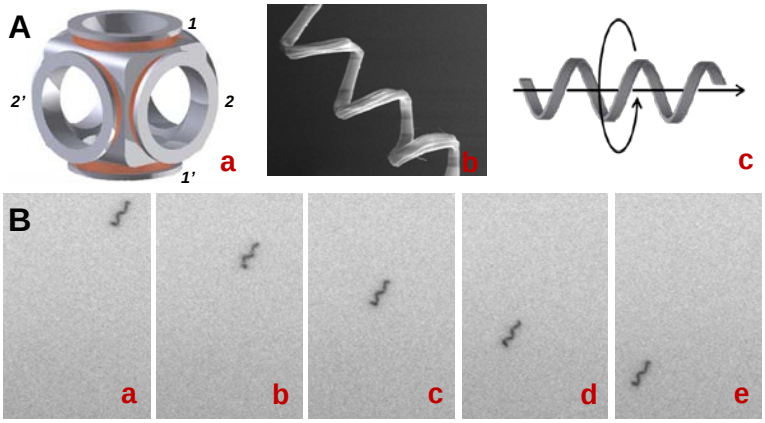

Figure 7.4.4 A) a) The triaxial Helmholtz coil used for generating the rotating magnetic field. b) SEM image of helical structure of a single microswimmer from *Rhaphiolepis indica.* c) Schematic of the corkscrew motion. Scale bar, 5 μm. B) Time lapse images depicting efficient propulsion of a helical microswimmer (from the spiral vessel of *Rhaphiolepis indica*) under rotating magnetic field (10 Gauss, 70 Hz) over 500 ms time intervals. Scale bar, 50 μm.

The precise control of the propulsion of plant-based microswimmer is achieved using three orthogonal Helmholtz coil pairs that create a uniform rotating magnetic field, as illustrated in Figure 7.4.4Aa. To characterize the locomotion behavior of the plant-based nanomotors, the helical microswimmers (from *Rhaphiolepis indica*, vessel structure shown in Figure 7.4.4Ab) were suspended in deionized (DI) water and tested under the magnetic fields with the strength of 10 Gauss and different frequencies ranging from 10 to 80 Hz. At low frequency, the helical

swimmers display a wobbling motion, rotating around the axis with a misalignment angle. As the input frequency increases, the angle gradually decreases and finally reaches 0° (corkscrew motion as shown in Figure 7.4.4Ac). The time-lapse images in Figure 7.4.4B illustrate the efficient propulsion of a helical microswimmer (from *Rhaphiolepis indica*) with a helix angle of 41° over a 2 s period at 500 ms intervals (a-e) under a rotating magnetic field with a frequency of 70 Hz. The microswimmer is propelled at a high speed of over 250 μm/s, which corresponds to a relative speed of ~5 body lengths/s. Such efficient propulsion here is comparable to magnetic microswimmers fabricated by the direct laser writing technique and higher than that of most previously reported magnetic swimmers.[13-20,52,59,60] Similarly, the helical swimmer derived from *Agapanthus africanus* also displays an efficient speed of around 140 μm/s under the rotating magnetic field with a frequency of 15 Hz.

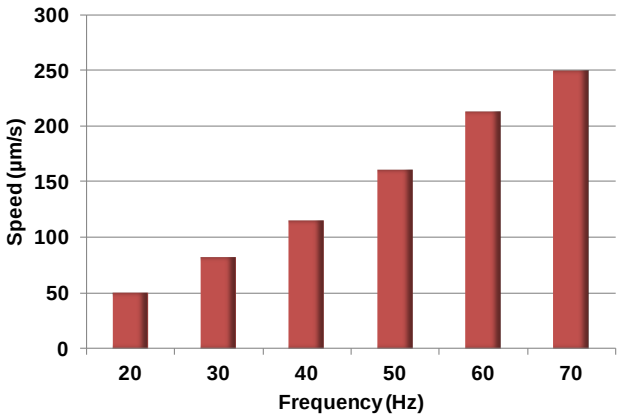

Figure 7.4.5 Dependence of the propulsion of plant-derived microswimmers (from *Rhaphiolepis indica*) upon the frequencies of the magnetic field (10 Gauss).

Based on resistive force theory from slender body dynamics, the drag coefficients of the helical microswimmer can be estimated by:[60]

$$\xi_{\parallel} = \frac{2\pi\eta}{\ln\left(\frac{2q}{R}\right)-0.5},\ \xi_{n} = \frac{4\pi\eta}{\ln\left(\frac{2q}{R}\right)+0.5} \tag{7.4.3}$$

where $\xi_{\parallel}$ and ξ_{n} are the resistive force coefficients parallel and perpendicular to the helical motor axis, q is equal to $0.09l$, R is the radius of the plant vessel fiber, and η is the kinematic viscosity of

the fluid. From the simplified model of rotational swimming of a helical motor, the relationship between the externally applied force (F) and torque (τ) and the translational (v) and rotational (ω) velocities of the motors can be expressed in terms of the propulsion matrix:

$$\begin{bmatrix} F \\ \tau \end{bmatrix} = \begin{bmatrix} a & b \\ b & c \end{bmatrix} \begin{bmatrix} v \\ \omega \end{bmatrix} \tag{7.4.4}$$

where the components of the propulsion matrix are:[60]

$$a = 2\pi nR\left(\frac{\xi_{\parallel}\cos^2(\theta) + \xi_n \sin^2(\theta)}{\sin(\theta)}\right) \tag{7.4.5}$$

$$b = 4\pi nR^2(\xi_{\parallel} - \xi_n)\cos(\theta) \tag{7.4.6}$$

$$c = 8\pi nR^3\left(\frac{\xi_{\parallel}\sin^2(\theta) + \xi_n \cos^2(\theta)}{\sin(\theta)}\right) \tag{7.4.7}$$

where θ is the helical angle and n is the number of turns of the helix. Since the entire body of the microswimmer is helical and the magnetic field is uniform, the external applied force (F) is equal to zero. As a result, for constant input frequency ω, there is a predicted linear relationship between the actuation frequencies and the translational velocity (v) of the plant-based helical microswimmers. As illustrated in Figure 7.4.5, microswimmers with a diameter of 9 μm and a pitch of 25 μm display increasing movement speeds with increasing input frequency of the applied magnetic field. The speed increases linearly from 50 μm/s to 250 μm/s with increasing the applied frequency from 20 Hz to 70 Hz. However, the microswimmer displays a greatly reduced speed at frequencies higher than 80 Hz (step-out frequency). When the frequency is increased above the step-out frequency, the fluidic drag exceeds the maximal available magnetic torque, hence leading to a decrease in velocity as the swimmer rotates out-of-sync with the magnetic field. The linear increase of the speeds of the aforementioned microswimmer matches the theoretical predictions and can be mathematically fit to the theory using the critical frequency ω_c (the frequency at which movement begins) and the step-out frequency $\omega_{s\text{-}o}$:[73]

$$U = \kappa\omega\left(1 - \frac{{\omega_c}^2}{\omega^2}\right), \qquad \omega_c < \omega < \omega_{s-o}$$

where U is the translational velocity, ω is the frequency of the applied rotating magnetic field, and κ is the dimensional coefficient which can be found from numerical data fitting ($\frac{11}{3}$ in this case). As such, for large enough values of ω, the theory predicts a linear relationship between speed and actuating frequency.

The plant-derived helical microswimmer demonstrates a very fast movement in raw biological media. Figure 7.4.6 illustrates a microswimmer (from *Rhaphiolepis indica*) moving in pure human serum at a speed of 85 μm/s under the rotating magnetic field with a frequency of 40 Hz. The absolute speed obtained here is similar to that observed in pure water (~90 μm/s), indicating that the increased viscosity of the biological fluid has negligible impact upon the propulsion behavior. This represents a major advantage of the magnetic microswimmer over the common chemically propelled micro/nanomotors whose propulsion is usually hindered by viscous biological media.[74] The microswimmer shown consists of one full helical turn (pitch length 30 μm), displaying a high relative speed of ~3 body lengths/s. Such efficient movement of magnetically-actuated swimmers in raw biological media is crucial for various relevant biomedical applications requiring precise micromanipulation. It should be noted that at higher frequencies (above 50 Hz), the movement of the plant based-microswimmers in human serum can become punctuated by periods of slower rotational and translational movement.

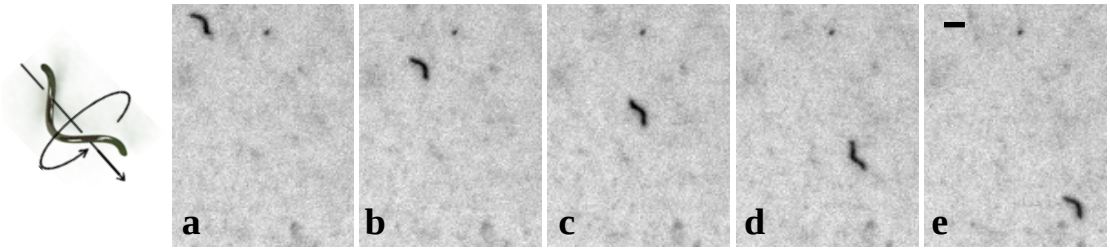

Figure 7.4.6 Time lapse images depicting the propulsion of a plant-derived helical microswimmer (from the spiral vessel of *Rhaphiolepis indica*) in pure human serum over 600 ms intervals (a-e) using a rotating magnetic field (10 Gauss, 40 Hz). Scale bar, 20 μm.

7.4.4 Conclusions

In conclusion, we have developed a novel plant-derived approach for the high-yield, cost-effective generation of magnetically-propelled helical microswimmers. The new bio-inspired microswimmers are prepared directly from isolated spiral vessels of plants followed by coating with a magnetic nickel layer. This intrinsic use of the plant material lends to the biocompatibility, biodegradability, and ease of fabrication of the microswimmer, while the magnetic layer allows for high speed propulsion and precise directional control. By harnessing the intrinsic natural structures of plant xylem vessels, and controlling geometric variables of the spiral vessels (e.g., helix diameter and pitch), this new method provides an extremely simple, cost-effective fabrication route for the large-scale mass-production of defined and effective helical magnetic swimmers compared to common methods for fabricating magnetically-actuated helical micro/microswimmers. These plant-derived helical microswimmers are able to be propelled at high speed in raw human serum, which indicates great promise for future biomedical applications.

7.5 Nanomotor-based biocatalytic patterning of helical metal microstructures

7.5.1 Introduction

Self-propelled nano/microscale machines have demonstrated considerable potential for performing diverse operations and important tasks, ranging from isolation of biomaterials,[75] nanotool-based drilling,[76] delivery of therapeutic payloads,[77] to environmental remediation.[78] This section reports on the use of flexible magnetic nanowire swimmers for biocatalytic patterning of complex surface microstructures. The preparation of well-defined surface micro/nanostructures represents an important goal of microfabrication. Tip-based scanning-probe (SP) techniques have been extremely useful for depositing chemical or biological materials onto flat substrates.[79] Such tip-based SP fabrication methods commonly rely on the controlled movement of a functionalized tip along predetermined paths for a localized surface modification. Willner et al.[80-83] have demonstrated the successful combination of Dip-Pen-Nanolithography (DPN) and biocatalytic inks for generating Au or Ag nanowires in connection to the deposition of glucose oxidase (GOx) or alkaline-phosphatase lines, respectively. However, patterning of three dimensional structures with high topological complexity of a helix represents a major fabrication challenge even with advanced lithographic techniques such as DPN.[80-83]

Recent advances in nanomotors have facilitated the realization of the new nanomotor-based direct biocatalytic patterning method. These include the ability to navigate the motors along predetermined complex paths, to control and regulate their speed, to functionalize them with different biological or chemical entities, and to move them rapidly over large areas.[84,85] Previous studies reported that HRP-functionalized catalytic nanowire motors can be used for writing localized polymeric lines.[86] However, the limited propulsion of these catalytic nanomotors in high-ionic strengths environments and the peroxide-fuel requirement hinder the applications of

these nanomotors.[58] Similar to different tip-based SP fabrication techniques,[79] nanomotors based on different propulsion and guidance mechanisms could be employed for creating a variety of surface microstructures. Various microstructures, made of different materials (polymers, metals, etc.), can thus be fabricated on conducting and insulating substrates based on a judicious choice of the reactants and the specific reaction involved. In view of the 'large' (submicrometer) size of catalytic nanomotors, compared to common SP tips, the new nanomotor 'writing' method is currently limited to the creation of microscale surface features.

This study illustrates for the first time the creation of complex helical metallic microscale surface structures based on local reaction of enzyme-functionalized artificial fuel-free magnetic nanomotors. Magnetically-controlled motion, inspired by the motility of microorganisms, represents an attractive route for addressing the challenge of nanoscale propulsion, as they can perform complex maneuvers while obviating fuel requirements.[13-20] Highly efficient flexible magnetic nanowire swimmers have been prepared recently by a simple membrane-template electrodeposition route.[20,52,87]

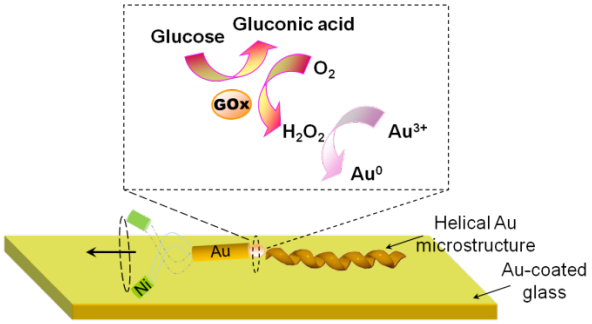

Figure 7.5.1 Schematic representation of the nanomotor-induced biocatalytic metallization of a helical Au microstructure using a GOx-Au/Ag_{flex}/Ni magnetic nanowire swimmer. Inset shows the biocatalytic reactions involved in the Au patterning.

In the following sections we will illustrate biocatalytically-induced growth of distinct helical Au microstructures during the magnetically-powered movement of GOx-functionalized flexible nanowire motors. The patterning of helical surface microstructures commonly represents a major challenge using conventional nano- and microfabrication methods. As illustrated in

Figure 7.5.1, the new nanomotor-induced surface 'writing' protocol relies on the controlled movement of an enzyme-functionalized nanomotor along a localized surface and leads to distinct helical structures due to reproducible rotation of the immobilized biocatalytic layer. This is accomplished by using magnetically-driven GOx-functionalized flexible three-segment Au-Ag_{flex}-Ni nanowire motors under a rotating magnetic field. Previously we demonstrated that such magnetically-powered nanowire motors, containing a flexible silver joint, can swim efficiently under an external rotating magnetic field.[20]

7.5.2 Experimental section

Synthesis of the flexible Au/Ag_{flex}/Ni magnetic nanowires

The Au/Ag_{flex}/Ni magnetic nanowires were prepared using the same template-directed electrodeposition protocol as 7.1.2 ('backward' mode). Nickel was plated at -1.0 V (vs. Ag/AgCl) for 3 C; silver was plated at -0.9 V (vs. Ag/AgCl) for a total charge of 3.5 C; finally, Au was plated from the commercial gold-plating solution at -1.0 V (vs. Ag/AgCl), using a charge of 3 C.

Bio-functionalization of the nanowires

Figure 7.5.2 depicts a schematic representation of the biofunctionalization process by exposing the Au ends of the nanowires (while in the membrane) to a 2.5 mM ethanolic solution of 11-Mercaptoundecanoic acid (MUA) overnight at room temperature in order to form a dense carboxylic acid-terminated SAM. The MUA-modified nanowires (still in the membrane) were subsequently treated with a solution of *N*-hydroxysuccinimide (NHS) (100 mM) and 1-(3-dimethylaminopropyl)-*N*'-ethylcarbodiimide hydrochloride (EDC) (400 mM) in ultrapure water for 2 h following by a further incubation 2 h in a 1,364 U μL^{-1} Glucose oxidase (GOx, from *Aspergillus niger*, EC 1.1.3.4) solution (prepared in 0.1 M phosphate buffer solution of pH 7.4). Finally, the membrane with the GOx-modified nanowires was washed 3 times with ultrapure water. A diluted NaOH (0.3 M) solution was used to dissolve the membrane and release the enzyme-functionalized nanowires which were washed thoroughly with ultra pure water by

repeated centrifugation at 6,000 rpm for 5 min. These GOx-functionalized nanowires were washed repeatedly with nanopure water (18.2 MΩ·cm) until a neutral pH was achieved and were stored in phosphate buffer (pH 7.4) at 4 °C until their use.

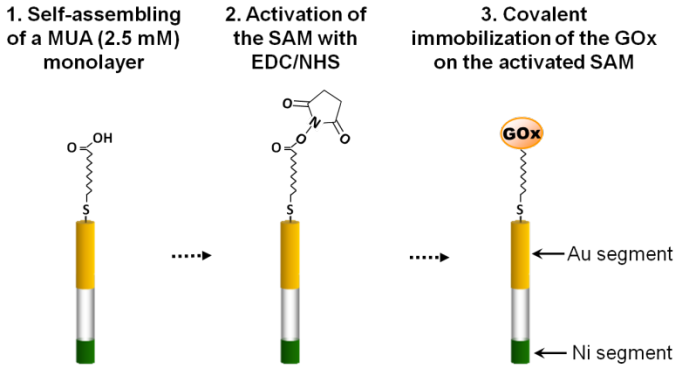

Figure 7.5.2 Schematic representation of the surface chemistry involved in the magnetic swimmer modification with GOx.

Biocatalytic patterning of helical Au microstructures using GOx-modified nanoswimmers

The flexible thinner joint is prepared by partial dissolution of the silver segment accomplished by mixing 10 µL of the diluted magnetic swimmer suspension with 10 µL of a 10% (w/w) H_2O_2 solution for 1 min. The nanowires were then washed under optical microscope using nanopure water (18.2 MΩ·cm) until a neutral pH was achieved. These thorough washings ensured complete removal of H_2O_2 used for the Ag partial dissolution. A 10 µL aliquot of freshly prepared GOx-functionalized flexible magnetic nanowire motors was mixed with the same volume of the developing solution (containing 10 mM glucose and 0.3 mM $AuCl_4^-$).

Residual GOD enzymatic activity evaluation after membrane dissolution

In order to corroborate that the enzymatic activity of the GOD immobilized on the nanomotors survived the harsh conditions during membrane dissolution we performed additional electrochemical experiments by immobilizing the enzyme, using the same protocol followed for bio-functionalization of the nanowires, on Au/SPEs. These Au/SPEs include a silver pseudoreference electrode and a gold counter electrode. After immobilization of the enzyme, the

electrodes were washed and dried and a 10 μL drop of a 0.3 M NaOH solution was placed on the GOD-modified Au/SPEs surface and incubated during 24 h at 4 ºC in an humidified chamber. After washing and drying chronoamperometric detection was performed by placing a 50 μL drop of a mixture containing 1 mM HRP substrate 3,3´,5,5´-tetramethylbenzidine (TMB, Neogen K-blue enhanced activity substrate, containing H_2O_2), 1 mM glucose and 137.4 U mL^{-1} horseradish peroxidase (HRP, Type II from *Horseradish*, EC 1.11.1.7) (in phosphate buffer 0.1 M pH 7.4) on the sensor, stepping the potential to -200 mV (vs the Ag pseudoreference electrode), and sampling the resulting current at different times.

7.5.3 Results and discussions

As illustrated in Figure 7.5.1 our new surface 'writing' concept relies on the confinement of GOx onto the Au end of a flexible Au-Ag_{flex}-Ni magnetic 5.5 μm long nanowire motor for localized biometallization through a H_2O_2-mediated deposition of helical Au microwires in the presence of glucose and $AuCl_4^-$ ions. The enzyme confinement onto the end of the Au segment was accomplished by covalent immobilization using carbodiimide/succinimide onto a carboxylic acid terminated alkanethiol thiolated self-assembled monolayer (SAM) (see Figure 7.5.2). Under rotating magnetic field, the Ni segment of the flexible Au/Ag_{flex}/Ni nanomotors generates a cone-shaped rotation which causes rotation of the Au segment on the opposite end.[20] Defined surface microstructures can thus be patterned through a controlled movement and accurate positioning of the GOx-modified nanomotor, in a manner analogous to the AFM biocatalytic lithography and H_2O_2-mediated growth of Au microstructures.[81-83] During the rotation of the GOx-functionalized Au segment, the biocatalytic oxidation of glucose leads to the formation of distinct helical plumes of the H_2O_2 product (eqn 7.5.1). The latter acts as a reducing agent for the localized catalytic reduction of $AuCl_4^-$ ions on a AuNPs-coated glass (eqn 7.5.2), leading to unique surface patterns of helical Au microstructures that reflect the rotation of the enzyme and the corresponding peroxide plume. AuNPs seeds were shown to be essential for biocatalytically induced growth of

Au nanowires on glucose oxidase.[82] Magnetically-guided motion of the GOx-modified motor thus leads to a localized biocatalytic metallization and hence to the direct 'writing' of Au microfeatures in the presence of GOx along the nanomotor path. It is expected that the modification of such magnetic swimmers with different biocatalysts will lead to motor-based patterning of different metal microstructures.

$$\text{glucose} + O_2 \longrightarrow \text{gluconic acid} + H_2O_2 \qquad (7.5.1)$$

$$AuCl_4^- + 3/2\ H_2O_2 \longrightarrow Au^0 + 4Cl^- + 3H^+ + 3/2\ O_2 \qquad (7.5.2)$$

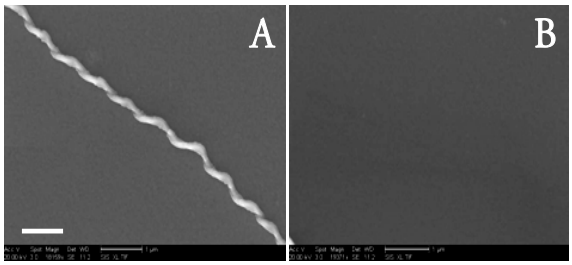

Figure 7.5.3 SEM images of a biocatalytically-generated helical Au micropattern over a Au-coated glass surface using an Au/Ag_{flex}/Ni magnetic microswimmer modified (A) and unmodified (B) with GOx on the Au side. The biometallization reaction was carried out in a solution containing 10 mM glucose and 0.3 mM $AuCl_4^-$. Magnetic field: 7.5 Hz. Scale bar, 1 μm.

Figure 7.5.3A illustrates the microscale Au helical surface microstructure created by the biocatalytic metallization reaction using a GOx-Au/Ag_{flex}/Ni nanowire. The biometallization reaction was carried out in 10 mM glucose and 0.3 mM $AuCl_4^-$ at a rotation frequency of 7.5 Hz. The controlled translational movement of the swimmer, including the defined rotation of the GOx-modified Au segment, thus results in distinct Au helical surface microstructures. In this specific case, a ~500 nm wide (~15 μm long) wire with an average height of ~500 nm, is obtained (Figure 7.5.3A). In order to confirm that the patterning is solely due to the biocatalytic process, we performed control experiments with SAM-modified flexible Au-Ag_{flex}-Ni nanowires without GOx. As expected, no such microstructure was observed in the absence of the enzyme (Figure 7.5.3B), clearly demonstrating the biocatalytic nature of the patterning process. Similarly, no surface microstructures were observed in additional control experiments without the glucose

substrate or the $AuCl_4^-$ ions in the developing solution, or using a bare glass surface without the AuNPs seeds (not shown). All of these control experiments indicate clearly that the localized biocatalytic formation of H_2O_2 is essential to induce the growth of the microstructure and corroborate that the AuNPs seeds on the glass surface act as catalysts for the reduction of $AuCl_4^-$ by H_2O_2.[80] The formation of the helical Au patterning was also confirmed using the Energy-dispersive X-ray (EDX) elemental mapping measurements.

Our results also confirm the enzymatic activity of the GOx attached to the flexible Au-Ag_{flex}-Ni nanowires, despite of the harsh alkaline conditions used for dissolving the alumina nanowires template. This was supported by additional electrochemical experiments that were carried out in order to estimate the enzymatic activity after exposure to these harsh membrane-dissolution conditions. The results of these experiments, demonstrate that the attached enzyme retains approximately the 23.5% of its original activity. This is supported by early observations of Martin and coworkers who reported that GOx nanotubes - prepared by a similar protocol – are able to catalyze the oxidation of glucose.[88]

Most favourable results were observed using 10 mM glucose, 0.3 mM $AuCl_4^-$ and following an initial 30 min incubation time. No apparent patterning was noticeable using incubation times shorter than 15 min or using glucose concentrations lower than 1 mM. These results could be attributed to the requirement for a threshold H_2O_2 level for the Au enlargement reaction to take place.[81] In view of these results, the height and width of the resulting helical microstructures appear to depend on the biocatalytic "development" time-interval[81] and the concentration of glucose. The resulting structural features can thus be tuned by a rational adjustment of these parameters, reflecting the mechanistic aspects involved in the helical biometallization patterning. Obviously, the resulting helical surface patterns are extremely unique. Creating such three dimensional surface patterning is commonly very challenging even by using state-of-the-art lithographic techniques.

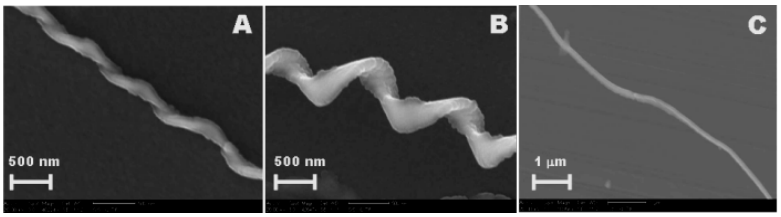

Figure 7.5.4 SEM images of the biocatalytically-generated helical Au micropatterns obtained using GOx-modified Au/Ag_{flex}/Ni magnetic swimmers at different rotation frequencies: 7.5 (A), 12 (B) and 15 (C) Hz.

Controlled nanomotor motion along predetermined paths, with a fine control over its position and rotation, is essential for generating reproducible predefined surface patterning. In particular, a judicious control of the magnetic actuation allows the fine tuning and tailoring of the resulting microstructures. For example, as clearly illustrated in Figure 7.5.4, the period and width of helical structure can be controlled by using different rotation frequencies (7.5, 12 and 15 Hz; A-C). Using the lower frequency (Figure 7.5.4A) the diameter of the helical structure created is less than 500 nm; the line width increases upon raising the frequency to 12 Hz (Figure 7.5.4B). However, the highest frequency of 15 Hz resulted in microscale lines instead of a helical microstructure (Figure 7.5.4C). A simple calculation using frequency and speed of the nanomotors indicates that the expected pitch of the helical structure (the width of one complete helix turn), when the frequency of the rotation is between 7.5 and 12 Hz, should be both around 1 μm due to the nearly linear relation between the frequency and speed.[52] Our experimental results also confirm that in both cases the pitch of the metallic helical structures is around 1 μm.

As illustrated in Figure 7.5.5, the lower the rotation frequency (7.5 Hz) induced a lower diameter of the helical structure. However, the exact rotation radius of the Au segment highly depends upon the elasticity and length of the flexible Ag joint. Accordingly, it is difficult to predict the exact correlation between the radius of the rotation of the motors and the width of the helical structures.

Our experimental data proves that there is a cut-off frequency around 15 Hz at which nanomotors stop to respond to the rotation of the external magnetic field. No obvious helical structures have been formed over 15 Hz. Instead, a fairly straight Au line deposits on the surface. This can be attributed to that at this frequency the speed of the nanomotors will increase to 12 μm s^{-1}, leading to shorter contact times of GOx with the Au surface and to a different plume dynamics of the H_2O_2 product, and hence to the absence of helical surface patterns.

Another important advantage of this new methodology, compared to DPN-based biocatalytic approaches, is that the developed nanomotor-based approach is not a self-limiting process. In the nanomotor-induced surface 'writing' strategy presented the biocatalytic reaction and hence the patterning does not come to a standstill due to the physical blocking of the enzyme observed in the biocatalytic-DPN method.[80,82] Another distinct feature of the present nanomotor-based nanofabrication strategy is that it can be readily used to prepare defined structures of finite lengths. Since the pattern is formed only when the nanomotor navigates in close proximity to the Au-coated glass surface, one can terminate the process by guiding the motor to an upper plane, thus enabling the "writing" of finite lengths microstructures.

7.5.4 Conclusions

In conclusion, we presented a new and attractive nanomotor-based biocatalytic surface patterning route approach for generating three-dimensional Au microstructures with the high topological complexity (e.g., helical shape) using enzyme modified magnetic nanomotors. This method merges the fine control over the position and translational motion of the magnetic nanowires, essential for generating reproducible predefined patterns, with the versatility of biocatalytic metal deposition reactions. Although the present study has demonstrated for the first time the use of magnetic nanowires motors along with the "biocatalytic inks" as a new paradigm for generating metallic helical nanostructures the concept could be easily extended to other "biocatalytic inks" that generate conducting, semiconducting and insulating polymers, as well

microscale magnetic or semiconductor wires. Future effort will also aim at gaining better understanding of the dynamics, dispersion and directionality of the plume of the peroxide product (in relation to the swimmer actuation) towards enhanced control of the patterning process. The ability to grow tailored metallic helical patterns and the application of different biocatalytic reactions pave the way for the generation of a variety of complex metal microstructures. A judicious selection of the experimental variables allows tuning of the exact writing patterns. The new nanomotor-based biocatalytic patterning thus holds a considerable promise for generating different surface microstructures of different materials and shapes in connection to diverse (bio)chemical reactions, towards the creation of complex surface circuitries.

7.6 Cargo-towing magnetic nanoswimmers for targeted drug delivery

7.6.1 Introduction

The proper understanding and execution of nanomotor biological functionality, i.e. pickup, transport and delivery of biologically relevant nanostructured loads,[6-11,77,89-91] is crucial for myriad future biomedical applications including drug delivery and gene therapy. Past work from both Sen's group and our team have previously demonstrated the ability of catalytic nanowire motors to pick-up, tow and release polystyrene spherical particles.[89,90] Our group has also recently demonstrated the guided transport of drug-loaded liposomes,[77] pancreatic cancer cells,[92] and nucleic acids[93] by fuel-driven nanomotors. Despite these advances in cargo-towing by catalytic nanomotors, future *ex vivo* and *in vivo* biomedical transport applications require the use of biocompatible, fuel-free nanomotors.

In this work we describe the efficient cargo-towing capabilities of magnetically-driven (fuel-free) nanomotors, elucidate the fundamental mechanism of cargo-towing by these flexible nanoswimmers, and assess to what extent they can be used to transport relevant cargos in biological media. Magnetically-driven nanomotors, which swim under externally applied magnetic fields, are particularly promising for use in a variety of biomedical applications,[12-20] as they can perform complex maneuvers while obviating fuel requirements. To examine the directed transport of payloads by these fuel-free magnetic swimmers, we rely here on our recently developed flexible nanowire motors that are prepared by a template electrodeposition approach.[20,52] These two or three segment flexible nanowire motors consist of a rotating magnetic nickel head (~1.5 μm long), along with a flexible silver segment (~4 μm long). These swimmers appear to be among the fastest fuel-free synthetic nanomotors reported to date in terms of dimensionless swimming speed (*U/Lf*, obtained by dividing the dimensional speed by the body

length and the actuation frequency to scale off the effects of motor size and frequency), allowing them to propel efficiently in biological fluids.[52] Despite the great potential for these magnetically-propelled nanoswimmers in diverse biomedical applications, their ability to carry a cargo has not yet been demonstrated.

In order to elucidate the fundamental mechanisms of cargo-towing by flexible magnetic nanomotors, we examine the transport of various-sized drug-loaded magnetic polymeric microspheres made of poly(D,L-lactic-co–glycolic acid) (PLGA). We investigate their towing performance and discuss the hydrodynamic features of these cargo-loaded motors. The effect of the iron-oxide loaded cargo size upon the swimming performance is evaluated experimentally and compared to a theoretical model emphasizing the interplay between hydrodynamic drag forces and magnetic actuation. The performance of these new fuel-free nanowire motors makes them attractive for future biomedical applications, as illustrated below for the directed delivery of drug-loaded microparticles to HeLa cells in cell culture media. Our investigations will ultimately enable us to address the performance and physical limitations of nanomotor-towing for the efficient transport of biological and therapeutic payloads.

7.6.2 Experimental section

Synthesis of Ni-Ag$_{flex}$ magnetic nanowires and magnetic driven movement: same as section 7.2.2.

Preparation of the drug-loaded, magnetic PLGA microparticles

Doxorubicin-loaded magnetic PLGA microparticles were prepared using an oil-in-water emulsion method.[94] Briefly, an excess of triethylamine was added to an aqueous solution of doxorubicin hydrochloride in order to neutralize the hydrochloride ion. The resulting free-base doxorubicin was extracted from the aqueous solution with dichloromethane. The extraction was performed three times to improve yield. The collected free-base doxorubicin was dried under argon and dissolved in chloroform at 1 mg mL^{-1}. Meanwhile, PLGA-ester (10 mg, 30 mg mL^{-1}, 50:50 lactic acid: glycolic acid, IV 0.82 dL g^{-1} from Lactel, Pelham, AL) were dissolved in

chloroform. 400 μL of the oleic-acid coated 10 nm-Fe_3O_4 nanoparticles suspension in chloroform (16.7 mg mL^{-1}) were added to the PLGA solution. To complete the oil phase of the oil-in-water emulsion, a doxorubicin solution (100 μL) was added to the PLGA–Fe_3O_4 suspension and the mixture was vortexed for complete mixing. The chloroform oil phase was then added dropwise to a water phase consisting of an aqueous solution of PVA (1.5 mL, 2% (w/v)). The PVA serves as an emulsifying agent to stabilize the oil phase in the water. The mixture was then vortexed at high speed for 3 min to create an emulsion. The emulsion was sonicated in a bath sonicator (Fisher Scientific FS30D) for 6 min to produce a more uniform emulsion, followed by gently stirring overnight with the lid off to allow the chloroform to evaporate. Finally, the solution was washed 3 times with a 100 kDa MW cut-off centrifuge filter and resuspended with water (4 mL) after the first two washes and 1 mL of water after the final wash. PLGA particles were separated using the appropriate variety of filter membranes to obtain the desired particle size fractionation.

PDMS channels preparation

Polydimethylsiloxane (PDMS) was hand-mixed in a 10:1 polymer: fixing agent ratio using the commercial Sylgard 184 Silicone elastomer kit. PDMS was poured over a glass Petri dish, degassed in a vacuum desiccator, and baked at 110°C for 15 min. Holes of ~2 mm were punched in each well using a puncher (Ted Pella, Redding, CA). An open channel of ~200 μm wide and ~10 mm in length was used to properly visualize the magnetic nanowire motors. The resultant structures and cleaned glass slides were exposed to UVO ozone (Jetline Co., Irvine, CA) at a gas flow rate of 3 sccm for 5 min, pressed together and baked for another 10 min at 110°C to complete the bonding process. The PDMS channel was washed with ultra pure water to ensure the removal of any residual dust and dried properly under nitrogen before starting the experiments. Ambient light and digital adjustments to brightness and contrast were used to visualize the magnetic nanowires with the cargo and the PDMS channel at the same time.

Cell line and culture

HeLa cells were cultured in a flask in RPMI medium supplemented with 10% fetal calf serum, penicillin (100 μg mL^{-1}), and streptomycin (100 μg mL^{-1}). The HeLa cells were incubated with 5% CO_2 at 37 °C until 80% confluent. The cells were treated with trypsin and centrifuged at 1,000 rpm for 10 minutes to form a pellet. The cells were resuspended in fresh RPMI medium and counted with a hemacytometer in order to determine the cell concentration per mL. The cells were seeded in the PDMS wells attached to slide coverslips at approximately 10^4 cells cm^{-2}. The PDMS-coverslips were placed inside a 100-mm cell culture dish and an additional coverslip was placed over the PDMS well to prevent evaporation. The cells were allowed to incubate overnight and were used in subsequent experiments.

Experiments in PDMS channels

$Ni\text{-}Ag_{flex}$ magnetic nanowires repeatedly washed (10 times) with culture media to remove the remaining peroxide residue. Then the PDMS channel was filled with culture media (500 µL) and an appropriate volume of the washed flexible $Ni\text{-}Ag_{flex}$ magnetic nanowires suspension and the drug-loaded magnetic PLGA microparticles (~10 µL of each) was added to the magnetic microparticles capture well. After capturing the magnetic microparticles, the flexible nanowires were magnetically guided across the channel to the target cells reservoir. HeLa cells were plated 24 hours earlier in the corresponding reservoir selected for a stationary delivery.

7.6.3 Results and discussion

7.6.3.1 Cargo Towing Magnetic Nanowire Motors

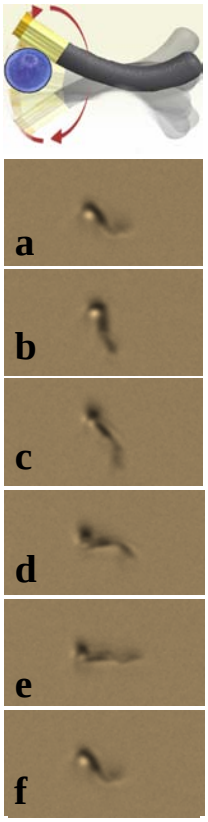

Figure 7.6.1 Time-lapse images depicting the slow motion of a magnetic nanowire motor with a 1.0 μm drug-loaded magnetic PLGA microsphere. The time interval between each image is 20 ms. Scale bar, 10 μm. Magnetic field: f=10 Hz, H_1 = 10 G and H_0 = 9.5 G.

Figure 7.6.1(a–f) shows a sequence of pictures, taken at 20 ms intervals, of the motion of a magnetic nanowire motor carrying a ~1.0 μm drug-loaded magnetic PLGA microsphere under a rotating magnetic field under a rotating magnetic field (the magnetic moment of the microsphere arises due to the encapsulation of iron-oxide nanoparticles). These images display the entire movement of the sphere-loaded flexible nanoswimmer. As clearly seen in the images, the motor rotates around the cargo (the particle is loaded inside the cone swept by the nickel), which is further shown by the disappearance of the particle during each rotation cycle. The location of the magnetic cargo towards the free end of the nickel segment also confirms that the particle is magnetically-bound, as the nickel segment poles are the strongest attraction point. The motor is actuated by the magnetic nickel segment, which follows closely the external rotating magnetic

field. Through boundary actuation, the flexible silver filament deforms in a chiral fashion to produce propulsion in the direction towards the nickel segment. The necessity of chirality in the deformation for propulsion was established in our previous work, together with a simple elastohydrodynamic model for its propulsion.[52] Using high-definition quality images, we noticed that the deformation of the flexible filament does not seem to change significantly before and after picking-up the cargo sphere. The deformation of the silver segment is very apparent in the slow motion images, which show the segment whipping and driving the propulsion of the cargo-carrying wire through the fluid. The exact shape of the silver filament is a result of the competition from magnetic actuation, elastic forces from the flexible filament and viscous forces from the fluid medium.[52] Overall, these results demonstrate that our flexible magnetic nanoswimmers are able to transport micrometer particles at high speeds, both dimensional (up to 10 μm s^{-1}) and dimensionless (up to 0.2 body lengths per revolution).

The pick-up of distinctly-sized polymeric magnetic particles of different sizes (radii ranging from 500 nm to 2.5 μm) was used to assess the influence of cargo size on the nanomotors' speed and trajectory. Figure 7.6.2A shows actual optical images highlighting the directed motion of the magnetic nanomotor towards a drug-loaded PLGA particle (0.65 μm, 1.25 μm, and 2.25 μm in diameter, representative of different particle-size groups) (red trajectories), followed by the instantaneous capture of a magnetic polymeric sphere by the nanomotor and its transport (green trajectories). This cargo loading is accomplished via the magnetic attraction between the nickel segment on the nanomotor and the iron-oxide nanoparticles encapsulated in the PLGA particle. As was illustrated in our previous work,[52] the magnetic frequency and strength have a profound influence on the speed of nanoswimmer, and should thus influence its cargo-towing ability. Similar speed – cargo-towing relationship has been reported for fuel-driven nanomotors.[95]

In previous studies on cargo transportation using catalytic fuel-driven nanomotors,[89,90] loaded particles were found to increase the hydrodynamic resistance, and led to a monotonic

decrease in propulsion speed with particle size. Upon loading, the hydrodynamic center changes only along the axis of the nanowire; since the motion of the catalytic motor is only along the axial direction, the loading process simply contributes additional hydrodynamic drag to the motor. The additional loading obeys the Stokes' law for the viscous resistance of spheres (the force (F) to speed (U) ratio is given by $F/U = 6\pi\mu a_r = R_r a_r$ where a_r is the dimensional radius of the sphere and μ is the fluid viscosity) and results in a monotonic decrease in propulsion speed upon increasing the size of the loaded particle.

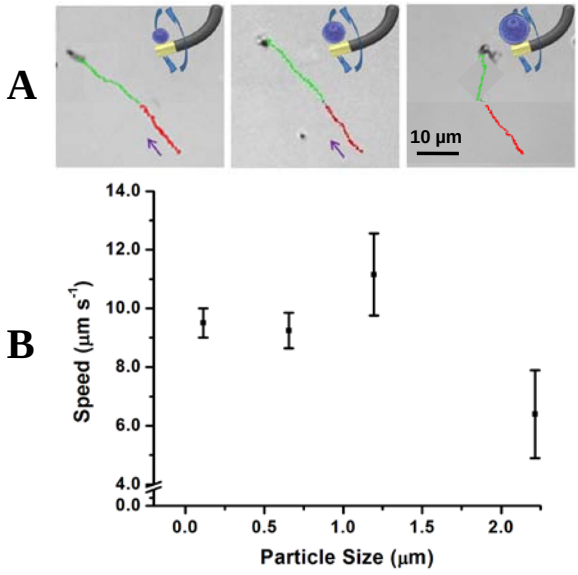

Figure 7.6.2 A) Capture and transport of different sizes of drug-loaded magnetic PLGA micro/nano particles. Time-lapse images showing the motion trajectory within 2 s before and after picking-up the different sized drug-loaded PLGA particles, respectively. B) Variation of the speed of the magnetic nanowire motors after picking-up different sizes of drug-loaded PLGA particles. Red line shows the initial average speed of the magnetic nanomotors without any cargo. Magnetic fields, as in Figure 7.6.1.

In contrast, here, we observe an unusual non-monotonic impact of the cargo loading on the speed and trajectory of the magnetic (fuel-free) nanowire motors. As shown in Figure 7.6.2B, for the small drug-loaded particle (average 0.2 and 0.65 µm in diameter), the cargo-loaded nanomotors travel at approximately the same speed (9.5 µm s^{-1}) as before the loading; for the medium size of cargo (average 1.25 µm in diameter), we observed an unexpected (~20%)

increase in the propulsion speed after pickup; however, a significant reduction in the average speed (~33%) was observed for the very large particle (average 2.25 μm in diameter). We attempt below to rationalize the physical basis for this non-monotonic velocity change.

7.6.3.2 Dynamic Considerations

An investigation into the magnetic contribution added by the iron-oxide loaded particles to the magnetic nickel segment of the motor reveals that the particle's magnetic moment is several orders of magnitude less than that of the nickel segment. The magnetic torque on the nickel segment still dominates the motion, and hence the slope of the nickel segment is still slaved to that of the external magnetic field (small Mason number limit, given by the ratio of viscous-to-magnetic forces). The observed non-monotonic propulsion is therefore not attributed to the extra magnetic moment introduced by the particle whose sole effect is to allow for the attachment of the particle to the nanomotor.

Since the particle is attached to the nickel segment via magnetic attraction, the rotation of the nickel segment leads to spinning of the particle cargo at the same rate. Therefore, the presence of the particle not only contributes additional viscous drag but also sets up a rotating flow field due to its spinning motion. Can the flow field induced by the spinning particle influence the propulsion velocity? We answer this question by extending the calculations of Ref 16 while also including a background flow field generated by the spinning particle of radius a_r, placed immediately next to the silver filament (sphere centered at $z = L + a_r$, hence maximum influence). We nondimensionalized lengths and time by using the silver filament's length, L, and the inverse of the angular frequency, $1/\Omega$, respectively. Details of the derivation are included in the Supporting Information. Expanding the deformation and swimming velocity in powers of h (ratio of the amplitude of the transverse and longitudinal magnetic fields), we have

$\vec{r}_\perp(z) = h\vec{r}_{\perp 1}(z) + h^2\vec{r}_{\perp 2}(z) + \cdots$ and $U = hU_1 + h^2U_2 + \cdots$. The first order deformation $\vec{r}_\perp = [x(z), y(z)]$ is governed by the dimensionless equations:

$$-y\left[1-\left(\frac{a}{1+a-z}\right)^3\right] = \mathrm{Sp}^{-4}\frac{d^4x}{dz^4} \tag{7.6.1}$$

$$x\left[1-\left(\frac{a}{1+a-z}\right)^3\right] = \mathrm{Sp}^{-4}\frac{d^4y}{dz^4} \tag{7.6.2}$$

where where $a = a_r/L$ is the dimensionless radius of the sphere, and the sperm number $Sp = L(\xi_\perp\Omega/A)^{1/4}$ is a dimensionless parameter comparing the viscous to elastic forces ($\xi_\perp$ is the drag coefficient of a slender filament moving perpendicular to its axis and *A* is the bending stiffness of the filament).[1,4] In the absence of the sphere (*a* = 0), the above equations reduce to the case of an unloaded motor.[52] We apply the boundary conditions $\partial^3\vec{r}_\perp/dz^3(z=0) = \partial^2\vec{r}_\perp/dz^2(z=0) = 0$ and $x(z=1) = b = 0$, $y(z=1) = \partial y/\partial z(z=1) = 0$ and $\partial x/\partial z(z=1) = 1$ as in Ref. 52, where b represents the displacement of the Ni-Ag junction. Balancing the $O(h)$ local viscous force in the longitudinal direction yields $U_1 = 0$, so swimming occurs at $O(h^2)$. Upon solving for $(x_1(z), y_1(z))$, we obtain the second order swimming velocity of the nanomotor U_2. Next, we compare in Figure 7.6.3 the case when there is no particle (*a* = 0, solid line) and when there is a large particle (2.5 μm in diameter, *a* = 0.3125, dashed line). It is observed that the effect of the flow field set up by the spinning sphere acts to reduce the propulsion speed for all sperm numbers. For a large particle of diameter 2.5 μm, the maximum reduction in speed due to the flow field is around 5%. For even larger particles (5 μm in diamater), the reduction is at most 16%, while experimentally we observed no apparent propsulsion for

larger size of particles. Therefore, for the size of particles considered in the experiment, this effect is negligible.

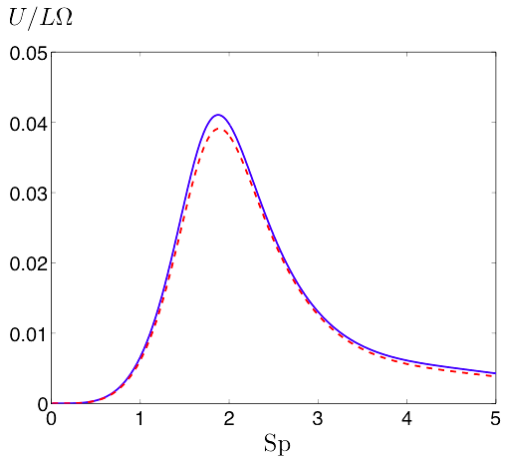

Figure 7.6.3 Dimensionless propulsion speed as a function of the sperm number (Sp) for the case when there is no particle (a=0, blue solid line) and when there is a large particle of diameter 2.5 μm (a=0.3125, red dashed line).

The non-monotonic variation of the swimming speed is actually caused by a subtle change, brought about by the loading process, in the boundary condition for the filament actuation. Unlike catalytic motors, the attachment of a spherical particle to the magnetic nickel segment of the current motor not only increases the viscous drag, but also perturbs the total force and torque balances, which in general lead to a change in the boundary actuation condition (the displacement and slope at z=1, the Ni-Ag junction) and hence the deformation of the entire silver filament. Since the propulsion speed is a function of the shape of the silver filament, a non-trivial modification of the propulsion speed is expected. The slope at the boundary is still slaved to the external magnetic field, but we believe that the location of the hinge (the point about which the filament rotation occurs) is displaced by the attachment of the particle. Consider first a simplified scenario for illustration purposes. Upon the action of a planar rotating magnetic field, a rigid magnetic nanowire of unit length should rotate about its mid-point by symmetry to maintain an overall force-free condition (Figure 7.6.4 inset A, left panel). Now imagine the center of a spherical particle of radius a (dimensionless) attached to one end of the nanowire. One would

expect the rotation point to shift towards the side with the attached particle (denote this shift by b_s) to maintain the force-free condition (Figure 7.6.4 inset A, right panel). A simple force balance reveals that $b_s = a\beta / 2(1 + a\beta)$ for this scenario, where $\beta = R_s / \xi_\perp$. For this reason, the attachment of a cargo particle to the nanowire motor in the experiment changes the location of the point of rotation, which was approximately located at the Ni-Ag junction before loading, hence $b \approx 0$, Figure 4 inset B, left panel. In order to maintain the force-free condition, the point of rotation is expected to shift towards the location where the cargo is attached. Hence, an increase in the magnitude of *b* in the boundary actuation is anticipated (Figure 7.6.4 inset B, right panel). A detailed numerical simulation including all the hydrodynamic interactions and the effect of the surface is required to determine the exact value of *b*. To illustrate qualitatively the possible effect of such a change, we use the expression of the simplified scenario described above and scale it by $\sin\theta$ (where θ is the angle made by the resultant magnetic field and the constant magnetic field) as a rough estimation for the value of the boundary condition, i.e. $x_1(z=1) = -b_s \sin\theta$. In Figure 7.6.4, we illustrate separately different effects. We first assume that the loading process amounts to no change in the boundary actuation condition, and show only the effect of the additional viscous drag from the particle. As expected from Stokes law for a sphere, the speed of the motor deceases monotonically with the size of the attached particle (dash-dotted curve). Next, we ignore the increased hydrodynamic resistance from the sphere and observe the effect of the change in boundary actuation described above: $x_1(z=1) = -a\beta \sin\theta / 2(1 + a\beta)$. Such a change in the boundary condition tends to systematically enhance the propulsion speed nonlinearly, as shown by the dashed line. The combined effect of the change in boundary actuation condition and the extra hydrodynamic resistance from the particle produces a non-monotonic variation of the propulsion speed with the particle size (solid curve). For small to medium sized loaded particles, the propulsion speed can indeed be enhanced after loading. However, for very large particles, the

increase in hydrodynamic resistance dominates and reduces the propulsion speed. This simple analysis suggests a possible mechanism for the counter-intuitive increase in propulsion upon loading shown in Figure 7.6.2. Since the boundary conditions employed are obtained from a simplified geometry and hydrodynamic interactions could also be important in this scenario,[95] we do not expect a quantitative agreement bewteen theory and experiment. Instead we aim to suggest a possible mechanism capturing qualitively this non-monotonic feature of cargo loading.

For large particles (~2 μm in diameter), in addition to the 30% reduction in speed, we also observed a significant change in the motor trajectory after loading. For unloaded motors, or when the loading particle is small, the motor propels in the direction of the axial magnetic field both before and after the loading (Figure 7.6.2A, left and middle panel). However, when the cargo is large, the new trajectory is seen to occur at an angle with respect to the axial magnetic field (Figure 7.6.2A, right panel). Such a change in the cruising angle could be attributed to hydrodynamic interactions with surfaces, which is expected to play a more significant role when the loading particle is large. The presence of a surface breaks spatial symmetry and the viscous drag experienced by a moving body is higher when located close to the bottom surface. Tierno *et al.* first exploited this type of drag anisotropy in order to convert the rotational motion of an anisotropic colloidal doublet (i.e. a small sphere attached to a larger sphere) near a surface into translational motion.[96,97] As pointed out in their work, the higher viscous drag near the surface plays a role similar to the solid friction between a rolling wheel and a solid surface. When loaded with a particle, our current nanowire motor is geometrically similar to an anisotropic doublet, and hence we suspect that the off-axis propulsion velocity after loading is due to a similar mechanism. The current nanowire motor performs thus both as a flexible swimmer (propelling in the direction of the constant magnetic field) and as a surface walker (propelling in a direction perpendicular to the constant magnetic field) when it is loaded with a large particle in the presence of a surface. For future applications close to a surface/boundary and requiring a preservation of the cruising

direction, the cargo particle has therefore to be limited in size to avoid any interference with the swimming direction of the motor.

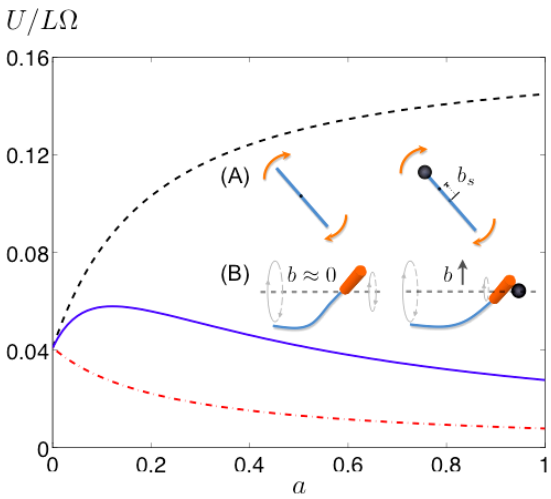

Figure 7.6.4 Dimensionless propulsion speed as a function of the dimensionless particle radius. Black dashed curve: the isolated effect of the change in boundary condition $x(z=1) = -a\beta \sin\theta / 2(1+a\beta)$, without the effect of additional hydrodynamic resistance from the particle; red dot-dashed curve: the effect of the additional hydrodynamic resistance from the particle, without change in boundary condition $x(z=1) = 0$; blue solid curve: the combined effect of the change in boundary actuation condition and the extra hydrodynamic resistance from the particle. Inset (A): the simplified scenario of a planar rotation of a nanowire, illustrating the shift of rotation center upon the attachment of a spherical particle. Inset (B): schematic illustration of the possible change in boundary actuation condition upon particle loading.

7.6.3.3 Targeted Drug Delivery

The results obtained through the former study illustrate that the iron oxide-loaded polymeric particles and the size of the nickel segment within the nanomotors are sufficient for enabling the particle's pick-up and transport. These results also demonstrate that the size of the drug-loaded spheres plays a significant role in the speed and trajectory of the cargo-loaded Ni-Ag nanowire motors. After having studied the physicochemical properties and cargo-carrying capability of the magnetic nanoswimmers, we next examine the potential practical utility of these fuel-free nanomotors by experimentally delivering drug (e.g., doxorubicin)-loaded PLGA microparticles to cancer cells in an *in vitro* setting. This active transport – which usually occurs at a rate orders of magnitude faster than diffusion[77] – takes place through a microchannel that

connects the pick-up zone to the release microwell, as illustrated schematically in Figure 7.6.5A. The corresponding experimental results are shown in the images of Figure 7.6.5B. For systemic drug delivery purpose most drug carriers (e.g. PLGA particles and liposomes) are used at a size less than 1 μm, where the flexible nanomotors do not have any obvious speed changes. In this study, in order to directly visualize the concept of delivering drug-loaded particles to target cancer cells, we used PLGA particles of around 1.25 μm in size. Experiments were conducted using HeLa cancer cells because they can readily adhere to the plasma-treated glass wells when incubated overnight in a culture medium. Repeatedly washed flexible nanowire motor and drug-loaded PLGA particles were added to a culture medium solution in the left well and the cancer cells were seeded and cultured in the right well. Figure 7.6.5 shows both a cartoon (A) and captured experimental images of a five-step *in vitro* process which is used to emulate the fuel-free motors drug delivery capabilities (B, a-e). First, the flexible nanomotor approaches the target iron-oxide/doxorubicin-encapsulated PLGA particle in a cell-free well via a precise magnetic guidance (a). As the motor passes close by the particle, the particle is magnetically attracted and picked up (b). The long-range transport capability of the flexible nanomotor is then tested while it tows and guides the PLGA particle across the channel (c) and to the open secondary well containing the HeLa cancer cells. The nanomotor is then guided to a target HeLa cancer cell (d), which is attached and spread across the bottom surface. Finally, the flexible silver segment of the nanowire non-specifically bound to the HeLa cell to enable localized drug release from the PLGA particle (e). We observed this non-specific binding several times when the motor was directed to the cancer cell and given enough time to interact. In most cases the cargo-loaded nanomotor tended to travel around or over the cell as it perpetually interacted with the cell. Future endeavors could involve nanomotors functionalized with antibodies specific for cancer cells to increase their binding efficiency once they have been directed to the target cells. This nanomotor-based targeted drug delivery system involving fuel-free nanovehicles may potentially address current challenges

of nanoparticle drug delivery, such as inevitable off-targeting of particles and the likelihood of systemic toxicity.

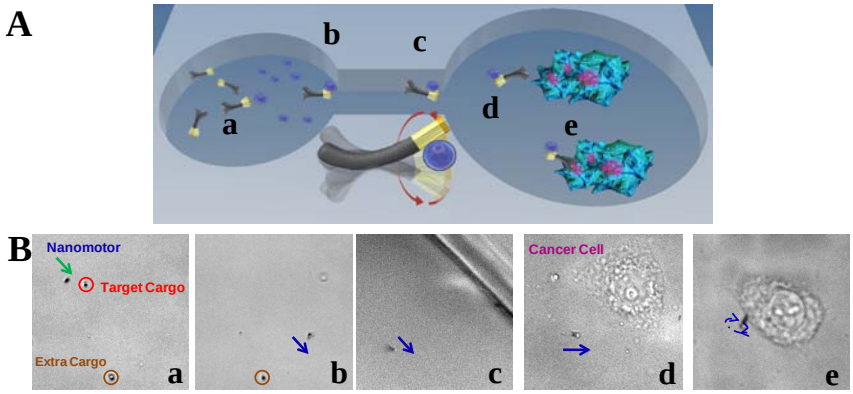

Figure 7.6.5 Drug delivery to HeLa cells using flexible magnetic nanoswimmer in cell culture media. (A) Scheme depicting the process as a flexible magnetic Ni-Ag nanowire motor (a) captures the drug-loaded magnetic polymeric particle in the loading reservoir (b); transports it through the channel (c), approaches the target cell (d); sticks onto the target cell and releases the drug (e). (B) Time-lapse images illustrating each of the previous described steps. Conditions, as in Figure 7.6.1.

7.6.4 Conclusions

In conclusion, we demonstrated the first example of directed transport of magnetic polymeric drug carriers by fuel-free flexible magnetic nanomotors, investigated both experimentally and theoretically the influence of such cargo upon the propulsion speed and trajectory of the loaded motor, and elucidated the fundamental mechanism of such cargo towing. These fuel-free nanomotors have been shown useful for the pick-up and transport of various drug carriers from a loading zone to a predetermined destination through a predefined route, and they represent a novel approach towards transporting cargos in a target specific manner. Note that the transport occurs at a rate order of magnitude faster than that expected from Brownian motion. The new understanding will ultimately enable us to address the performance and physical limitations of nanomotor-towing for the efficient transport of biological and therapeutic payloads.

Despite these significant advancements of nanomotor design and our new understanding of the ability of the flexible nanoswimmer to transport cargo, several challenges still exist for

their practical *in vivo* uses. Enhancements on the propulsive thrust and cargo attachment are necessary to overcome any additional hydrodynamic drag and shear present in the *in vivo* environment. To further improve the efficiency of nanomotor-based drug delivery, we envision the possibility of attaching drug carriers to these magnetically-driven nanoswimmers through cleavable linkers that are responsive to tumor microenvironments (e.g., enzyme and acidic pH) to enable an autonomous release of the carriers and a more accurate delivery of cargos to the target site. While eliminating the fuel requirements, attention must be given also to the preparation of more biocompatible magnetic nanowimmers. Eventually, such magnetically-driven fuel-free nanoswimmers are expected to provide a new and unique approach for rapidly delivering drug carriers to predetermined destinations in a target specific manner.

Chapter 7.1, is based, on the material as it appears in Journal of the American Chemical Society, 2010, by Wei Gao, Sirilak Sattayasamitsathit, Kalayil Manian Manesh, Daniel Weihs, Joseph Wang. Chapter 7.2, is based, on the material as it appears in Soft Matter, 2011, by On Shun Pak, Wei Gao, Joseph Wang, Eric Lauga. Chapter 7.3, is based on, the material as it appears in Small, 2011, by Wei Gao, Kalayil Manian Manesh, Joe Hua, Sirilak Sattayasamitsathit, Joseph Wang. Chapter 7.4, is based on, the material as it appears in Nano Letters, 2014, by Wei Gao, Xiaomiao Feng, Allen Pei, Christopher R Kane, Ryan Tam, Camille Hennessy, Joseph Wang. Chapter 7.5, is based on, the material as it appears in Nanoscale, 2013, by Kalayil Manian Manesh, Susana Campuzano, Wei Gao, María Jesús Lobo-Castañón, Isao Shitanda, Kiarash Kiantaj, Joseph Wang. Chapter 7.6, is based on, the material as it appears in Small, 2012, by Wei Gao, Daniel Kagan, On Shun Pak, Corbin Clawson, Susana Campuzano, E. Chuluun-Erdene, Erik Shipton, Eric E. Fullerton, Liangfang Zhang, Eric Lauga, Joseph Wang. The dissertation author was the primary investigator and author of these papers.

7.7 References

1. Purcell, E. M. *Am. J. Phys.* **1977**, *45*, 3–11.

2. Brennen, C.; Winet, H. *Annu. Rev. Fluid Mech.* **1977**, *9*, 339–398.

3. Childress, S. *Mechanics of Swimming and Flying*, Cambridge University Press, Cambridge, England, 1981.

4. Lauga, E.; Powers, T. *Rep. Prog. Phys.* **2009**, *72*, 096601.

5. Turner, L.; Ryu, W. S.; Berg, H. C. *J. Bacteriol.* **2000**, *182*, 2793–2801.

6. Mallouk, T. E.; Sen, A. *Sci. Amer.* **2009**, *5*, 72–77.

7. Wang, J. *ACS Nano* **2009**, *3*, 4–9.

8. Mirkovic, T.; Zacharia, N. S.; Scholes, G. D.; Ozin, G. A. *ACS Nano* **2010**, *4*, 1782–1789.

9. Mei, Y. F.; Solovev, A. A.; Sanchez, S.; Schmidt, O. G. *Chem. Soc. Rev.* **2011**, *40*, 2109–2119.

10. Nelson, B. J.; Kaliakatsos, I. K.; Abbott J. J. *Annu. Rev. Biomed. Eng.* **2010**, *12*, 55–85.

11. Wang, J.; Gao, W. *ACS Nano* **2012**, *6*, 5745–5751.

12. Gao, W.; Wang, J. *ACS Nano* **2014**, *8*, 3170–3180.

13. Zhang, L.; Abbott, J. J.; Dong, L.; Peyer, K. E.; Kratochvil, B. E.; Zhang, H.; Bergeles, C.; Nelson, B. J. *Nano Lett.* **2009**, *9*, 3663–3667.

14. Ghosh, A.; Fischer, P. *Nano Lett.* **2009**, *9*, 2243–2245.

15. Tierno, P.; Golestanian, R.; Pagonabarraga, I.; Sagués, F. *Phys. Rev. Lett.* **2008**, *101*, 218304.

16. Tierno, P.; Güell, O.; Sagués, F.; Golestanian, R.; Pagonabarraga, I. *Phys. Rev. E: Stat., Nonlinear, Soft Matter Phys.*, **2010**, *81*, 011402.

17. Sing, C. E.; Schmid, L.; Schneider, M. F.; Franke, T.; Alexander-Katz, A. *Proc. Natl. Acad. Sci. U. S. A.* **2010**, *107*, 535–540.

18. Zhang, L.; Abbott, J. J.; Dong, L. X.; Kratochvil, B. E.; Bell, D.; Nelson, B. J. *Appl. Phys. Lett.* **2009**, *94*, 064107.

19. Dreyfus, R.; Baudry, J.; Roper, M. L.; Fermigier, M.; Stone, H. A.; Bibette, J. *Nature* **2005**, *437*, 862–865.

20. Gao, W.; Sattayasamitsathit, S.; Manesh, K. M.; Weihs, D.; Wang, J. *J. Am. Chem. Soc.* **2010**, *132*, 14403–14405.

21. Geranio, L.; Heuberger, M.; Nowack. B. *Environ. Sci. Technol*., **2009**, *43*, 8113-8118.

22. Sun, X. M.; Li, Y. D. *Adv. Mater*. **2005**, *17*, 2626–2630.

23. Mirkovic, T.; Foo, M. L.; Arsenault, A. C.; Fournier-Bidoz, S.; Zacharia, N. S.; Ozin, G. A. *Nature Nanotechnol*. **2007**, *2*, 565–569.

24. Goszner, K.; Korner, D., Hite, R. *J Catal*. **1972,** *25*, 245–253.

25. Goszner, K.; Bischof H. *J. Catal.* **1974**, *32*, 175–182.

26. Zhang, Q.; Cobley, C. M.; Zeng, J.; Wen, L.-P.; Chen, J.; Xia, Y. *J. Phys. Chem. C* **2010**, *114*, 6396–6400.

27. Hatwalne, H., Ramaswamy, S., Rao, M., and Simha, R. A. *Phys. Rev. Lett.* **2004**, 92, 118101.

28. Paxton, W. F., Baker, P. T., Kline, T. R., Wang, Y., Mallouk, T. E., and Sen, A. *J. Am. Chem. Soc.* **2006**, *128*, 14881– 14888.

29. Kim, Y. W.; Netz, R. R. *Phys. Rev. Lett.* **2006**, *96*, 158101.

30. Manghi, M.; Schlagberger, X.; Netz, R. R. *Phys. Rev. Lett.* **2006**, *96*, 068101.

31. Wada, H.; Netz, R. R. *Europhys. Lett.* **2006**, *75*, 645.

32. Coq, N.; du Roure, O.; Marthelot, J.; Bartolo, D.; Fermigier, M. *Phys. Fluids* **2008**, *20*, 051703.

33. Coq, N.; du Roure, O.; Fermigier, M.; Bartolo, D. *J. Phys.: Condens. Matter* **2009**, *21*, 204109.

34. Qian, B.; Powers, T. R.; Breuer, K. S. *Phys. Rev. Lett.* **2008**, *100*, 078101.

35. Coq, N.; Ngo, S.; du Roure, O.; Fermigier, M.; Bartolo, D. *Phys. Rev. E: Stat., Nonlinear, Soft Matter Phys.* **2010**, *82*, 041503.

36. Downton, M. T.; Stark, H. *Europhys. Lett.* **2009**, *85*, 44002.

37. Keaveny, E. E.; Maxey, M. R. *J. Fluid Mech.* **2008**, *598*, 293–319.

38. Machin, K. E. *J. Exp. Biol.* **1958**, *35*, 796–806.

39. Wiggins, C. H.; Goldstein, R. E. *Phys. Rev. Lett.* **1998**, *80*, 3879–3882.

40. Wiggins, C. H.; Riveline, D.; Ott, A.; Goldstein, R. E. *Biophys. J.* **1998**, *74*, 1043–1060.

41. Lowe, C. P. *Philos. Trans. R. Soc. London, Ser. B* **2003**, *358*, 1543–1550.

42. Powers, T. R. *Phys. Rev. E: Stat. Phys., Plasmas, Fluids, Relat. Interdiscip. Top.* **2002**, *65*, 040903.

43. Yu, T. S.; Lauga, E.; Hosoi, A. E. *Phys. Fluids* **2006**, *18*, 091701.

44. Lauga, E. *Phys. Rev. E: Stat., Nonlinear, Soft Matter Phys.* **2007**, *75*, 041916.

45. Landau, L. D.; Lifshitz, E.M. *Theory of Elasticity*, Pergamon Press, Oxford, 1986.

46. Gray, J.; Hancock, G. J. *J. Exp. Biol.* **1955**, *32*, 802.

47. Becker, L. E.; Koehler, S. A.; Stone, H. A. *J. Fluid Mech.* **2003**, *490*, 15–35.

48. Fujime, S.; Maruyama, M.; Asakura, S. *J. Mol. Biol.* **1972**, *68*, 347–354.

49. Hoshikawa, H.; Kamiya, R. *Biophys. Chem.* **1985**, *22*, 159–166.

50. Tornberg, A.-K.; Shelley, M. J. *J. Comput. Phys.* **2004**, *196*, 8–40.

51. Cortez, R.; Fauci, L.; Cowen, N.; Dillon, R. *Comput. Sci. Eng.* **2004**, *6*, 38–45.

52. Pak, O. S.; Gao, W.; Wang, J.; Lauga, E. *Soft Matter* **2011**, *7*, 8169–8181.

53. Soong, R. K.; Bachand, G. D.; Neves, H. P.; Olkhovets, A. B.; Craighead, H. G.; Montemagno, C. D. *Science* **2000**, *290*, 1555.

54. Behkam, B.; Sitti, M. *Proceedings of IEEE 2006 International Conference of Engineering in Medicine and Biology* **2006**, 2421.

55. Paxton, W. F.; Kistler, K. C.; Olmeda, C. C.; Sen, A.; Angelo, St. S. K.; Cao, Y.; Mallouk, T. E.; Lammert, P. E.; Crespi, V. H. *J. Am. Chem. Soc.* **2004**, *126*, 13424.

56. Kagan, D.; Calvo-Marzal, P.; Balasubramanian, S.; Sattayasamitsathit, S.; Manesh, K. M.; Flechsig, G. U.; Wang, J. *J. Am. Chem. Soc.*, **2009**, *131*, 12082.

57. Sattayasamitsathit, S.; Gao, W.; Calvo-Marzal, P.; Manesh, K. M.; Wang, J. *ChemPhysChem* **2010**, *11*, 2802.

58. Paxton, W. F.; Baker, P. T.; Kline, T. R.; Wang, Y.; Mallouk, T. E.; Sen, A. *J. Am. Chem. Soc.* **2006**, *128*, 14881.

59. Tottori, S.; Zhang, L.; Qiu, F.; Krawczyk, K. K.; Franco-Obregon; A.; Nelson, B. J. *Adv. Mater.* **2012**, *24*, 811–816.

60. Peyer, K. E.; Zhang, L.; Nelson, B. J. *Nanoscale* **2013**, *5*, 1259–1272.

61. Morse, D. R.; Lawton, J. H.; Dodson, M. M.; Williamson, M. H. *Nature*, **1985**, *314*, 731–733.

62. Franceschi, V.; Nakata, P. *Annu. Rev. Plant Biol.* **2005**, *56*, 41–71.

63. Staehalin, L. *Photosynth. Res.* **2003**, *76*, 185–196.

64. Zhou, H.; Fan, T.; Zhang, D. *ChemSusChem* **2011**, *4*, 1344–1387.

65. Hall, S.; Bolger, H.; Mann, S. *Chem. Commun.* **2003**, 2784–2785.

66. Bessekhouad, Y.; Robert, D.; Weber, J. V. *J. Photochem. Photobiol. A* **2004**, *163*, 569–580.

67. Zhao, Y.; Wei, M.; Lu, J.; Wang, Z. L.; Duan, X. *ACS Nano* **2009**, *3*, 4009–4016.

68. Kamata, K.; Suzuki, S.; Ohtsuka, M.; Nakagawa, M.; Iyoda, T.; Yamada, A. *Adv. Mater.* **2011**, *23*, 5509–5513.

69. Shibata, M.; Oyamada, S.; Kobayashi, S.; Yaginuma, D. *J. Appl. Polym. Sci.* **2004**, *92*, 3857–3863.

70. Wang, J.; Lin, M. S. *Anal. Chem.*, **1988**, *60*, 1545–1548.

71. Sperry, J. *Int. J. Plant Sci.* **2003**, *164*, S115–S127.

72. Johnson, W.; Yu, T. X. *J. Strain Anal. Eng.* **1981**, *16*, 111–121.

73. Morozov, K. I., Leshansky, A. M. *Nanoscale*, **2013**, 6, 1580-1588.

74. Wang, J. *Nanomachines: Fundamentals and Applications*; Wiley-VCH: Weinheim, Germany, **2013**.

75. Campuzano, S.; Orozco, J.; Kagan, D.; Guix, M.; Gao, W.; Sattayasamitsathit, S.; Claussen, J. C.; Merkoçi, A.; Wang, J. *Nano Lett.* **2012**, *12*, 396.

76. Solovev, A. A.; Xi, W.; Gracias, D. H.; Harazim, S. M.; Deneke, C.; Sanchez, S.; Schmidt, O. G. *ACS Nano* **2012**, *6*, 1751.

77. Kagan, D.; Laocharoensuk, R.; Zimmerman, M.; Clawson, C.; Balasubramanian, S.; Kang, D.; Bishop, D.; Sattayasamitsathit, S.; Zhang, L.; Wang, J. *Small* **2010**, *6*, 2741.

78. Guix, M.; Orozco, J.; García, M.; Gao, W.; Sattayasamitsathit, S.; Merkoçi, A. A.; Escarpa, A.; Wang, J. *ACS Nano* **2012**, *6*, 4445.

79. Soh, H. T.; Guarini, K. W.; Quate, C. F. *Scanning Probe Lithography*, Kluwer Academic Publishers, Norwell, 2001.

80. Zayats, M.; Baron, R.; Popov, I.; Willner, I. *Nano. Lett.* **2005**, *5*, 21.

81. Basnar, B.; Weizmann, Y.; Cheglakov, Z.; Willner, I. *Adv. Mater.* **2006**, *18*, 713.

82. Willner, I.; Baron, R.; Willner, B. *Adv. Mater.* **2006**, *18*, 1109.

83. Basnar, B.; Willner, I. *Small* **2009**, *5*, 28.

84. Wang, J.; Manesh, K. M. *Small* **2010**, *6*, 338.

85. Campuzano, S.; Kagan, D.; Orozco, J.; Wang, J. *Analyst* **2011**, *136*, 4621.

86. Manesh, K. M.; Balasubramanian, S.; Wang, J. *Chem. Commun.* **2010**, *46*, 5704.

87. Gao, W.; Manesh, K. M.; Hua, J.; Sattayasamitsathit, S.; Wang, J. *Small* **2011**, *7*, 2047.

88. Hou, S. F.; Wang, J. H.; Martin, C. R. *Nano. Lett.* **2005**, *5*, 231.

89. Burdick, J.; Laocharoensuk, R.; Wheat, P. M.; Posner, J. D.; Wang, J. *J. Am. Chem. Soc.* **2008**, *130*, 8164.

90. Sundararajan, S.; Lammert, P. E.; Zudans, A. W.; Crespi, V. H.; Sen, A. *Nano Lett.* **2008**, *8*, 1271.

91. Sanchez, S.; Solovev, A. A.; Schulze, S.; Schmidt, O. G. *Chem. Commun.* **2011**, *47*, 698-700.

92. Balasubramanian, S.; Kagan, D.; Hu, C-M.; Campuzano, S.; Lobo-Castañon, M. J.; Lim, N.; Kang, D. Y.; Zimmerman, M.; Zhang, L.; Wang, J. *Angew. Chem. Int. Ed.* **2011**, *50*, 4161-4164.

93. Kagan, D.; Campuzano, S.; Balasubramanian, S.; Kuralay, F.; Flechsig, G. U.; Wang, J. *Nano Lett.* **2011** *11*, 2083-2087.

94. Chaisri, W.; Hennink, W. E.; Okonogi, S. *Curr. Drug Deliv.* **2009**, *6*, 69.

95. Raz, O.; Leshansky, A.M. *Phys. Rev. E* **2008**, *77*, 055305(R).

96. Tierno, P.; Güell, O.; Sagués, F.; Golestanian, R.; Pagonabarraga, I. *Phys. Rev. E* **2010**, *81*, 011402.

97. Tierno, P.; Golestanian, R.; Pagonabarraga, I.; Sagués, F. *Phys. Rev. Lett*. **2008**, *101*, 218304.

Chapter 8 Conclusions and Future Perspectives

8.1 To make nanomotor moving more efficiently and more effectively

These miniature man-made machines have arisen from the fictional world of the *Fantastic Voyage* and are approaching initial proof-of-concept biomedical or environmental studies. While impressive progress has been made over the past decade toward developing a wide range of synthetic fuel-driven and fuel-free nano/microscale machines, the realization of practical applications requires further improvement in their efficiency, power and performance. The control and increase of the speed of catalytic micro/nanomotors has received considerable attention since the introduction of these man-made machines. The speed record for current catalytic micro/nanomotor is 10 mm s^{-1} (over 1400 body lengths s^{-1}) obtained with the newly developed polymer based microengines (Chapter 3) at 37 °C,[1] which corresponds to a maximum relative speed/H_2O_2 concentration of 140 body lengths s^{-1} $\%^{-1}$.[2] These amazing speed records of synthetic nanomotors compare well with those of other natural or man-made objects. For example, the maximum relative speeds of the fastest human and of the fastest land animal (Cheetah) are 'only' around 6 and 20 body lengths s^{-1}, respectively. Even the fastest-moving vehicles, the new Chinese bullet train and the Italian 'Ferrari' car, offer maximum relative speeds of ca. 0.5 and 21 body lengths s^{-1}, respectively.[2]

As we can see from the thesis, artificial micro/nanomotor can have the ultrafast speed (of over 1000 body lengths s^{-1}), comparable to some of the fastest nature bacteria reported.[3,4] Achieving such remarkably high speed and power has been accomplished through fundamental understanding and rationale optimization of key factors governing the propulsion behavior,

including composition of the motor and fuel, the motor morphology and various external stimuli. Among these, particular attention should be given to the identification of new and efficient catalytic materials for the fuel decomposition reactions. Coupled with optimal surface morphology and microporosity, these efficient electrocatalytic materials should result with new ultrafast nanomotors and lead to new world records. The increase in nanomotor power and speed should facilitate more demanding tasks such as pickup and transport of 'heavy' cargo (e.g., cellular or therapeutic payloads). Equally important, the improved fuel economy should lower the fuel concentration requirements. We hope that our discussion will lead to new nanotechnological advances and will serve as a useful guide the rationale design of even faster and more efficient nanomotors, with speed limits that are limited only by our imagination.

8.2 To design biocompatible and environmentally-friendly nanomotors

The requirement of the common hydrogen peroxide fuel hinders some practical biomedical applications of catalytically propelled micro/nanomotors. A wide range of such applications, particularly *in vivo* applications, thus require other fuel sources. Extending the scope of chemically powered nanomotors to diverse biomedical operations and different biological fluids would require the identification of new *in situ* fuels in connection with new catalytic materials and reactions. Ultimately, it would be beneficial to explore the sample matrix itself as the fuel source, thus obviating the need for adding external fuels and not compromising the viability of the biological target.

In Chapter 7, I demonstrated that acid or water driven micromotors could be possible to address the problem of propulsion in biological environments. However, the lifetime of such acid or water driven micromotors is limited. Extending the lifetime of water driven micromotors remains a major challenge. One possible way is using photocatalytic reactions instead of

corrosion reactions to power the micromotors. For example, TiO_2, ZnO, ZnS or other catalysts could be used as the new material to build the next generation micro/nanomotors.[5,6] Under the light stimuli, such micromotors could display bubble propelled locomotion due to the photocatalytic water splitting reactions.

Biocatalytic propulsion, powered by ensembles of multiple enzymes, has shown promise for moving microobjects in the presence of glucose fuel.[7,8] The abundant presence of glucose in body fluids makes it an attractive biocompatible fuel. For example, Feringa's group[7] described autonomously moving carbon nanotubes, functionalized with a dual-enzyme (glucose-oxidase/catalase) assembly, which relied on glucose fuel to generate hydrogen peroxide and oxygen gas for their propulsion. Mano and Heller[8] demonstrated rapid propulsion at the water–oxygen interfaceof carbon-fibers containing (on their opposite ends) a redox-polymer wired glucose oxidase and an oxygen-reducing bilirubin oxidase. Such a terminal glucose-oxidizing microanode and an oxygen-reducing microcathode resulted in a power-generating glucose–oxygen reaction and efficient bioelectrochemical locomotion. Other biocompatible fuels are *via* different biocatalytic reactions.

Magnetically powered nanoswimmers (Chapter 6) hold great promise for medical applications. Further improvements on the efficiency/speed of magnetic nanoswimmers are highly desired. The ultrasound could be another possible biocompatible energy transduction mechanism that can power micromotors. Ultrasound is the most widely used clinical cross-sectional imaging technique for viewing internal body organs.[9] Hoyos and Mallouk describe exciting experiments in which ultrasonic acoustic waves can propel template-grown metallic nanowires in fast axial directional motion and in-plane rotation.[10] Parallel efforts by Esener and Wang at UCSD have illustrated powerful ultrasound-driven microbullets, possessing sufficient force to penetrate, to cleave, and to deform cellular tissue.[11] The significance of these findings indicate exciting possibilities for ultrasound-driven motors in medicine.

8.3 Challenge and opportunities toward biomedical applications

As new capabilities are further developed and future nanomachines become more functional, these tiny devices are expected to perform more diverse and demanding tasks, and benefit different important medical areas (See Chapter 4).[12] These miniature machines are likely to have profound impact upon diverse biomedical applications, including directed drug delivery, nanosurgery, biopsy, cell sorting, artery cleaning, or microchip bioassays. Micro/nanoscale machines thus offer considerable promise to change various aspects of medicine by navigating through bodily fluids, cleaning clogged arteries, and performing targeted therapy and localized diagnosis in hard-to-reach places.

The sophistication of man-made nano/microscale machines has been increasing at a fast pace to provide unlimited biomedical opportunities. Although significant progress over the past 10 years has greatly advanced the capabilities of these tiny man-made machines, much more work is required before real biomedical benefits are realized. Artificial nanomotors are thus expected to advance from current initial proof-of-concept studies into practical *in vitro* and *in vivo* biomedical applications for further evaluation. Given the enormous interest in this cutting-edge research field, we anticipate exciting new ideas and applications in the future.

For practical environmental or biomedical applications, proper attention should also be given to control issues; integration of electronics, communication, software, and mechanics; and related scaling-down and packaging issues. Performing demanding biomedical tasks may also require an autonomous self-adaptive operation with machines cooperating and communicating with each other. For example, such collective action holds particular promise toward multiple-motor driven transport of “heavy” therapeutic payloads. Improved understanding of the physical limitations of such nanomotor-towing ability is desired for effective drug-delivery applications.

With such innovations and developments, along with careful attention to key challenges and requirements, nano/microscale motors are expected to have tremendous impact on diverse biomedical applications, providing unlimited opportunities limited only by one's imagination. These remarkable developments will eventually revolutionize disease treatment and diagnosis, lead to major improvements in the quality of our life, and facilitate the realization of the *Fantastic Voyage* vision.

8.4 Challenge and opportunities toward environmental applications

In Chapter 5, I have described the use of nanomachines for a variety of applications in the environmental field, ranging from accelerated decontamination to *in situ* water toxicity screening. These early developments indicate that nanomachines enable novel environmental applications and that the movement of such tiny machines adds a new and powerful dimension to such remediation and sensing procedures. While the proof-of-concept of different potential applications has also been demonstrated lately by several research groups, and new environmental capabilities of nanomachines have emerged, significant efforts are required before large-scale environmental benefits are realized.[13] These recent accomplishments are thus only the first step towards the design of functional and sophisticated nanomachines, swimming in natural water environments and performing demanding sensing and cleanup activities. It is hoped that future efforts, in close collaboration with environmental scientists and engineers, along with new technological breakthroughs and greater sophistication of micro/nanoscale machines, will lead to rapid translation of the above research activity into practical environmental applications, hence contributing further to the environmental benefits of nanotechnology. Given the immense interest and the competitive cutting-edge research in the field of nanomachines, we anticipate exciting

new ideas and applications in the future. Recent initial proof-of-concept studies are thus expected to advance into practical environmental applications.

Translating these recent and exciting advances to widespread environmental applications would require major attention to key challenges. Particular attention should be given to scale-up issues towards coverage of large contaminated areas and large volumes of wastewater. This would require additional advances and innovations and pilot studies involving different sample sizes. Larger (micrometer-to-millimeter scale) motors, swimming over long distances, and the coordinated action of swarms of numerous micromotors hold promise for dynamic action over larger scales and for transporting larger payloads of remediation agents. Many practical applications involve small samples sizes, *e.g.*, *ex-situ* water toxicity screening or cleanup of contaminated pipes or capillaries. Attention should be given also to the influence of the environmental medium upon the propulsion behavior. While environmental samples can result in decreased speed of tubular microengines, such bubble-propelled micromotors maintain efficient propulsion in most natural water media.[14] Finally, the potential toxicity of micro/nanoscale motors needs to be evaluated to prevent potential adverse environmental impacts. Recent efforts in this direction have also been devoted for designing environmentally-friendly and self-degradable nanomachines based on green materials (*e.g.*, Zn or Mg) (Chapter 7). Selecting nanomachines for specific environmental applications would depend on the complexity of the problem and economic costs, and require comparison to traditional technologies. Where do we go from here? The ability of nanomachines to address environmental problems is just beginning to be explored. In the not-so-distant future, we anticipate to see self-regulated multi-functional nanomachines, capable of performing multiple tasks, ‘sensing, isolating and destroying’ toxic pollutants and chemical threats, searching for sources of hazardous chemicals, or delivering nanosensors and nanosamplers to remote hostile locations. Swarms of micromachines could be assembled in response to hazardous conditions, used for mapping the spread of a toxic pollutant

over a large area or for accelerating environmental cleanup. Our preliminary data demonstrated the organized schooling of micromotors in the presence of a hazardous material.[15] These and similar developments will have a significant impact upon the environmental field, hence addressing the environmental sustainability challenges facing our world.

Chapter 8 is based, in part, on the material as it appears in ACS Nano, 2012, by Joseph Wang, Wei Gao; in part on the material as it appears in The Chemical Record, 2012, by Wei Gao, Sirilak Sattayasamitsathit, Joseph Wang; in part on the material as it appears in ACS Nano, 2014, by Wei Gao, Joseph Wang. The dissertation author was the primary investigator and author of these papers.

8.5 References

1. Gao, W.; Sattayasamitsathit, S.; Uygun, A.; Pei, A.; Ponedal, A.; Wang, J. *Nanoscale* **2012**, *4*, 2447.

2. Gao, W.; Sattayasamitsathit, S.; Wang, J. *Chem. Rec.* **2012**, *12*, 224.

3. Stocker, R.; Seymour, J. R.; Samadani, A.; Hunt, D. E.; Polz, M. F. *Proc. Natl. Acad. Sci. U.S.A.* **2008**, *105*, 4209–4214.

4. Mitchell, J. G.; Pearson, L.; Bonazinga, A.; Dillon, S.; Khouri, H.; Paxinos, R. *Appl. Environ. Microbiol.* **1995**, *61*, 877–882.

5. Maeda, K.; Domen, K. *J. Phys. Chem. Lett.* **2010**, *1*, 2655.

6. Ni, M.; Leung, M. K. H.; Leung, D. Y. C.; Sumathy, K. *Renewable Sustainable Energy Rev.* **2007**, *11*, 401–425.

7. Pantarotto, D.; Browne, W. R.; Feringa, B. L. *Chem. Commun.* **2008**, 1533–1535.

8. Mano, N.; Heller, A. *J. Am. Chem. Soc.***2005**, *127*, 11574–11575.

9. Liang, H. D.; Blomley, M. J. K. *Br. J. Radiol.***2003**, *76*, S140–S150.

10. Wang, W.; Castro, L. A.; Hoyos, M.; Mallouk, T. E. *ACS Nano* **2012**, 6, 6122–6132.

11. Kagan, D.; Benchimol, M. J.; Claussen, J. C.; Chuluun-Erdene, E.; Esener, S; Wang, J. *Angew. Chem. Int. Ed.* **2012**, 51, 7519–7522.

12. Wang, J.; Gao, W. *ACS Nano* **2012**, *6*, 5745–5751.

13. Gao, W.; Wang, J. *ACS Nano* **2014**, *8*, 3170–3180.

14. Gao, W.; Sattayasamitsathit, S.; Orozco, J.; Wang, J. *Nanoscale* **2013**, 5, 8909–8914.

15. Gao, W.; Pei, A.; Dong, R.; Wang, J. *J. Am. Chem. Soc.* **2014**, 136, 2276– 2279.